DENSITY-FUNCTIONAL THEORY: CHEMICAL TESTS AND EVALUATION OF EXCHANGE–CORRELATION FUNCTIONALS

A Thesis

Presented to

The Faculty of Graduate Studies

of

The University of Guelph

by

WEI QUAN TIAN

In partial fulfillment of the requirements

for the degree of

Doctor of Philosophy

March, 2001

ABSTRACT

DENSITY-FUNCTIONAL THEORY: CHEMICAL TEST AND EVALUATION OF EXCHANGE–CORRELATION FUNCTIONALS

Wei Quan Tian — Advisor:

University of Guelph, 2001 — Professor John D. Goddard

This thesis reports an investigation of density functional based methods for the study of selected organic reactions and simple atomic and molecular systems to evaluate and rationalize the role of exact (Hartree-Fock) exchange in hybrid density functional methods and the performance of density functional methods in the prediction of chemical property. The performance of density functional methods has been compared with certain conventional *ab initio* methods: HF, MP2 and CCSD, and available experimental results. The chemical systems and density functional methods investigated were:

(1) The Reactions of a Triplet Oxygen Atom (^{3}P) with C_{60} Fragments. The structures of C_{60} fragments and their oxides were studied at the HF, BHandHLYP, and B3LYP levels with the 6-31G* basis set. The reaction barrier and the transition state structure for the initial reaction of a triplet oxygen atom with these fragments were investigated theoretically. The nucleus-independent chemical shifts (NICSs) of Schleyer were adopted as criteria of aromaticity in polycyclic aromatic hydrocarbons (PAHs) and used to study the reactivity and properties of the C_{60} fragments. The initial reaction of a triplet oxygen atom with C_{60} fragments is exothermic with a low reaction barrier.

(2) Reaction of Triplet Oxygen Atom (^3P) with Benzene and Isomerization of Benzene Oxides. The reaction of a triplet oxygen atom and the potential energy surfaces for isomerization of the benzene oxides were studied to explore the reaction mechanism and find the reaction pathways. For these reactions, the role of exact exchange (Hartree-Fock (HF) exchange) was examined through the performances of the HF, BHandHLYP, B3LYP, B1LYP, BLYP and mPW1PW91 methods in the prediction of the reaction barrier and in potential energy surface modeling in comparison to the results from MP2. The 6-31G* basis set was used throughout. The theoretical predictions were compared with available experimental results when possible.

(3) Numerical Examination of Density Functional Methods. The exchange functionals B, PW91, mPW91, LG, G96 and the correlation functionals LYP and PW91 were examined numerically in combination with HF exchange to scrutinize the role of HF exchange in hybrid density functional theory. Both energy and electronic properties were studied for the simple atomic systems H, He and Li. One-electron systems (H, H_2^+, He^+) were employed to investigate the self-interaction error in the exchange and correlation functionals. The highest occupied orbital energies of these systems were examined with the various exchange correlation functionals. A new combination of exchange and correlation functionals within the one-parameter protocol of the hybrid method, mPW1LYP, was evaluated on the reduced G2 data for geometric and thermodynamic predictions. This new method was employed in studies on some inert gas dimers, weakly interacting complexes, low barrier reactions, and the electronic spectra of some small molecules. The overall performance of mPW1LYP is promising.

Acknowledgements

I would like to thank the fellow members of my quantum chemical research group: Dr. Galina Orlova, Robert Mawhinney, and Xiaoqing Chen. Special thanks go to my advisor Professor John D. Goddard, during my studies for my PHD. He gave me tremendous opportunities and freedoms in quantum chemical research and showed extreme patience and gave me inspirations in guiding me through the way to a potential scientific researcher. He also rendered me lots of care and help in my setting-up in the new environment. I would like to thank my advisory committee members: Professor Ian Hamilton, Professor Glenn Penner and Professor Dan F. Thomas for their advice on my study and research. Professor William Tam's help in naming some of the benzene oxides in Chapter 4 is much appreciated.

I would thank my wife Lei, who has cared my life during my study. I would also thank my elder sister Wei Jū, elder brother Wei Qin and families. They always helped and encouraged me through my grow-up. Finally I would give my deep thanks to my dear parents who have always been behind me for years.

Table of Contents

Chapter 1 Introduction 1

1.1 Quantum Chemistry.....2

1.1.1 Conventional ab initio theory.....3

1.1.2 Density functional theory.....5

1.1.3 A comparison between conventional ab initio theory and density functional theory 7

1.2 Organic Chemistry.....9

1.3 Analysis of exchange correlation functionals.....9

1.4 References.....11

Chapter 2 Overview of Quantum Chemistry 13

2.1 Overview of Conventional Ab Initio Theory.....14

2.1.1 The adiabatic and Born-Oppenheimer approximations.....14

2.1.2 Hartree-Fock theory and electron correlation.....16

2.1.2.1 Hartree-Fock theory 16

2.1.2.2 Electron correlation.....17

2.1.3 Many-body perturbation theory.....20

2.1.4 Quadratic configuration interaction(QCI).....22

2.1.5 Multi-configuration self-consistent field: complete active space self-consistent field (CASSCF) and complete active space plus perturbation theory to second-order (CASPT2).....24

2.1.5.1 Complete active space self-consistent field (CASSCF).....24

2.1.5.2 Complete active space plus perturbation theory to second-order (CASPT2).....26
2.2 Overview of Density Functional Theory.....27
2.2.1 Local spin density approximation.....29
2.2.2 General gradient approximation.....30
2.2.3 Hybrid density functional theory.....36
2.2.4 Time-dependent density functional theory.....39
2.2.4.1 Time-dependent Hartree-Fock theory.....39
2.2.4.2 Time-Dependent density functional theory.....40
2.3 Computational Details.....46
2.3.1 Programs and facilities.....46
2.3.2 Methods, basis sets, geometry optimizations, and vibrational frequencies.....47
2.3.3 Potential energy surfaces.....48
2.3.4 Thermochemistry and structural data for systems.....49
2.3.5 Excitation energies.....49
2.4 References.....50
Chapter 3 Critical Evaluation of Density Functional Methods: Theoretical Characterization of Fragments of C_{60}: Bonding, Reactivity and Aromaticity.....57
3.1 Introduction.....58
3.2 Theoretical Methods and Computational details.....62

3.3 Theoretical Results.....64

3.3.1 C_2H_4.....64

3.3.1.1 Initial barrier to reaction 64

3.3.1.2 Intersystem crossing.....69

3.3.1.3 Overall reaction of triplet oxygen with ethylene 73

3.3.2 C_6H_6.....73

3.3.3 $C_{10}H_8$.....81

3.3.3.1 Previous studies.....81

3.3.3.2 Results and discussion.....82

3.3.4 $C_{14}H_{10}$.....88

3.3.5 $C_{18}H_{12}$.....92

3.3.6 $C_{26}H_{12}$.....96

3.3.7 Aromaticity (Nucleus Independent Chemical Shifts, energetics and structures).....101

3.4 Closing Remarks.....107

3.5 References.....109

Chapter 4 Tests of Density Functional Methods: Theoretical Investigations of the Reaction of O (^{3}P) with Benzene and the Isomerization of Benzene Oxide

.....116

4.1 Introduction.....117

4.2 Computational Details.....119

4.3 Theoretical Results and Discussion 122

4.3.1 Initial reaction of oxygen with C_6H_6.....122

4.3.1.1 Initial reaction barrier.....124

4.3.1.2 The triplet intermediate, 4-3.....130

4.3.1.3 Intersystem crossing.....132

4.3.2 Isomerization pathway from epoxide to 7-Oxa-norbornadiene 139

4.3.2.1 Relative stability of benzene epoxide and oxepin.....139

4.3.2.2 Isomerization of oxepin.....145

4.3.3 Isomerization pathway from epoxide to Dewar benzene oxide.....151

4.3.4 Isomerization pathway from oxepin to bicyclo[2.1.0]-2-pentene-5-carbaldehyde.....159

4.3.5 Isomerization pathway from epoxide to bicyclo[3.1.0]hex-3-en-2-one.....164

4.3.6 The Isomerization pathway from hexadienone to 2,5-cyclo-hexadienone 172

4.3.7 Isomerization pathway for C_2 benzene epoxide 177

4.3.8 Performance of the functionals 182

4.3.8.1 Structure and property prediction.....182

4.3.8.1.1 Benzene.....182

4.3.8.1.2 Triplet intermediate, 4-3.....183

4.3.8.1.3 Region of singlet intermediate, 4-4.....185

4.3.8.2 Electronic properties.....197

4.4 Concluding Remarks 198

4.4.1 Chemical applications.....198

4.4.2 Performance of the density functional methods 200

4.5 References.....202

Chapter 5 Numerical Examination of Density Functional Methods: Aspects of Exchange and Correlation Functionals.....207

5.1 Introduction.....208

5.2 The Role of Exact Exchange and of the Self-Interaction Error: Numerical Examination of the Atoms and Ions of H, He, Li and of the Ion-Molecule H_2^+ 209

5.2.1 Theoretical background.....209

5.2.1.1 Adiabatic connection mechanism-ACM.....209

5.2.1.2 Rationale of exact exchange in the exchange-correlation functional 212

5.2.1.3 Self-interaction error.....213

5.2.2 Previous studies.....215

5.2.2.1 Exchange functionals.....215

5.2.2.2 Correlation functionals.....217

5.2.3 Computational details.....218

5.2.4 Results and discussion.....219

5.2.4.1 Formulas for the exchange and correlation functionals.....219

5.2.4.1.1 Exchange functionals.....219

5.2.4.1.2 Correlation functionals.....222

5.2.4.2 One-electron systems – H, He^+ and H_2^+.....223

5.2.4.2.1 H and He^+.....224

5.2.4.2.2 H_2^+.....233

5.2.4.2.3 Self-interaction error, SIE 237

5.2.4.3 Two-electron systems – H^-, He and Li^+ 244

5.2.4.3.1 H^- 245

5.2.4.3.2 Singlet He 251

5.2.4.3.2.1 Total energy of He 251

5.2.4.3.2.2 The decomposition of the total energy of helium.....252

5.2.4.3.2.3 The energetic contributions from correlation functionals 257

5.2.4.3.3 Triplet He 261

5.2.4.3.3.1 Total energy of triplet He 261

5.2.4.3.3.2 The decomposition of the total energy of triplet helium 263

5.2.4.3.3.3 The energetic contributions from correlation functionals 268

5.2.4.4 Three-electron systems – He^- and Li 271

5.2.4.5 Contribution of the kinetic and potential energy from correlation functionals.....276

5.2.5 The contribution from LSDA (local spin density approximation) 277

5.2.6 Concluding remarks.....279

5.2.6.1 Exchange functionals 280

5.2.6.2 Correlation functionals.....281

5.3 Role of Correlation: Numerical Examination of a New Exchange-Correlation

Functional mPW1LYP 282

5.3.1 Introduction 282

5.3.1.1 A modified PW91 exchange functional and the performance of mPW1PW91.....283

5.3.1.2 The reduced G2 data set.....284

5.3.1.3 The basis set superposition error (BSSE) 284

5.3.2 Computational details 286

5.3.3 Results and discussion 286

5.3.3.1 The reduced G2 data 286

5.3.3.2 Noncovalent interactions (inert gas dimers, water dimer, and $C_2H_4\cdots Cl_2$).....295

5.3.3.3 Proton transfer in malonaldehyde.....300

5.3.3.4 The Walden inversion 302

5.3.3.5 Reaction barrier of oxygen (^3P) with ethylene (C_2H_4) and benzene (C_6H_6).....306

5.3.3.6 Electronic spectra.....312

5.3.4 Concluding remarks 318

5.4 References 319

Chapter 6 Conclusions.....324

6.1 Chemical Applications 325

6.1.1 The reactions of a triplet oxygen atom with C_{60} fragments.....325

6.1.2 Reaction of triplet oxygen atom (^3P) with benzene and the isomerization of benzene oxides.....325

6.1.2.1 Reaction of a triplet oxygen atom, $O(^3P)$, with benzene.....325

6.1.2.2 Isomerization of benzene oxides.....327

6.2 Evaluation of Exchange-Correlation Functionals.....332

6.2.1 The evaluation of exchange-correlation predictions for chemical reactions 332

6.2.2 Detailed analysis of exchange and correlation functionals 333

6.2.3 A new hybrid exchange-correlation functional, mPW1LYP 334

6.3 General Conclusions and Suggestions for the Improvement of Density Functional Methods 334

6.4 References.....337

Appendices.....338

List of Tables

Table 3-1 The energy difference (kcal/mol) between the reactants ($O(^3P) + C_2H_4$) and product C_2H_4O and the $<S^2>$ of the triplet transition states and diradicals.....67

Table 3-2 The energy difference (kcal/mol) between the reactants ($O(^3P) + C_6H_6$) and product C_6H_6O and the $<S^2>$ of the triplet transition states and diradicals.....77

Table 3-3 The energy difference (kcal/mol) between the reactants ($O(^3P) + C_{10}H_8$) and product $C_{10}H_8O$ and the $<S^2>$ of the triplet transition states and diradicals.....86

Table 3-4 The energy difference (kcal/mol) between the reactants ($O(^3P) + C_{14}H_8$) and product $C_{14}H_8O$ and the $<S^2>$ of the triplet transition states and diradicals.....91

Table 3-5 The energy difference (kcal/mol) between the reactants ($O(^3P) + C_{18}H_{12}$) and product $C_{18}H_{12}O$ and the $<S^2>$ of the triplet transition states and diradicals.....95

Table 3-6 The energy difference ΔE (kcal/mol) between the reactants ($O(^3P) + C_{26}H_{12}$) and product $C_{26}H_{12}O$ and the $<S^2>$ of the triplet transition states and diradicals.....100

Table 3-7 GIAO-SCF/6-31G* calculated nucleus independent chemical shifts (ppm) for the set of molecules.....104

Table 4-1 Relative energies of the isomers in Fig. 1 (in kcal/mole) ($[\Delta E=E_n-(E_{oxygen}+E_{benzene})]$).....128

Table 4-2 $<S^2>$ of the triplet transition state 2 and the triplet intermediate 3.....129

Table 4-3 Relative energies (in kcal/mole) between structures 3 and 4 in their singlet and triplet electronic states calculated with 6-31G*.....134

Table 4-4 Energy of the (C_s) epoxide-5 and (C_s) oxepin-7 (in kcal/mole)

($\Delta E=E_{oxepin}-E_{epoxide}$).....141

Table 4-5 Relative energies of the isomers on the isomerization path from epoxide to 7-Oxa-norbornadiene (in kcal/mole)[$\Delta E=E_n-(E_{oxygen}+E_{benzene})$].....147

Table 4-6 $<S^2>$ and HOMO-LUMO gaps (in a.u.) for the open shell singlet 9'.....148

Table 4-7 Relative energies of the isomers on the isomerization pathway from epoxide to Dewar benzene oxide (in kcal/mole)[$\Delta E=E_n-(E_{oxygen}+E_{benzene})$].....154

Table 4-8 HOMO-LUMO gaps Δ (in Hartree) the of the closed shell singlet, open shell singlet and triplet of 16 and $<S^2>$ for the open shell singlet and triplet of 16...157

Table 4-9 Relative energies of the isomers on the isomerization path from oxepin to Bicyclo[2.1.0]-2-pentene-5-carbaldehyde (in Kcal/mole) [$\Delta E=E_n-(E_{oxygen}+E_{benzene})$] 163

Table 4-10 Relative energies of the isomers for the isomerization path from epoxide to bicyclo[3.1.0]hex-3-en-2-one (in kcal/mole)[$\Delta E=E_n-(E_{oxygen}+E_{benzene})$].....169

Table 4-11 Relative energies of the isomers on the isomerization pathway from hexadienone to 2,5-cyclo-hexadienone (in kcal/mole) [$\Delta E=E_n-(E_{oxygen}+E_{benzene})$].....176

Table 4-12 Relative energies of the isomers on the isomerization pathway from C_2 epoxide to (C_2)3-Oxa-bicyclo-[3.2.0]hept-6-ene, 37 (in kcal/mole) [$\Delta E=E_n-(E_{oxygen}+E_{benzene})$].....180

Table 4-13 The HOMO- LUMO gap (in Hartree) of triplet intermediate 3 as predicted by BxHFyLYP.....184

Table 4-14 Relative energies of the stationary points near structure 38 (in kcal/mole) [$\Delta E=E_n-(E_{oxygen}+E_{benzene})$].....190

Table 4-15 $<S^2>$ and HOMO-LUMO gaps (in a.u.) of the open shell singlet 39 and 40.....193

Table 4-16 Relative energies of the isomers on the reaction pathway from the "walk" transition states 4 and 40 to 7-oxa-norbornadiene (in kcal/mole) [$\Delta E=E_n-(E_{oxygen}(^3P) + E_{benzene})$].....196

Table 5-1 The electron-electron interaction energy (in a.u.) in He predicted by B, BLYP, PW91 and PW91PW91 with the cc-pv5Z basis set 257

Table 5-2 The kinetic and potential energies (in a.u.) of He predicted by the B, BLYP, PW91 and PW91PW91 functionals with the cc-pv5Z basis set.....258

Table 5-3 Kinetic, potential and electron-electron interaction energies (in a.u.) in triplet He predicted by B, BLYP, PW91 and PW91PW91 with the cc-pv5Z basis set.....270

Table 5-4 The total energy, potential, kinetic, and electron-electron interaction energies (in a.u.) predicted by the B, BLYP, HF, PW91, and PW91PW91 with the cc-pv5Z basis set.....277

Table 5-5 Theoretical and experimental geometries of the diatomic molecules in the reduced G2 data set. Bond lengths in angstroms. All theoretical values were obtained with the 6-311G(d,p) basis set 289

Table 5-6 Theoretical and experimental geometries of the polyatomic molecules in the reduced G2 data set. Bond lengths in angstroms, angles in degree. All theoretical values were obtained with the 6-311G(d,p) basis set.....290

Table 5-7 Theoretical and experimental atomization energies (kcal/mol) for the 32 molecules in the reduced G2 data set. All theoretical values were obtained with

the 6-311G++G(3df,3pd) basis set at the 6-311G(d,p) geometries. The atomization energies include ZPVE corrections for the molecules.....292

Table 5-8 Mean absolute deviations of different methods for the properties of 32 molecules in the G2 data set. Bond lengths (Å), and harmonic frequencies (in cm^{-1}) are computed using the 6-311G(d,p) basis set. Atomization energies (D_0) (in kcal/mol) and dipole moments (D) are evaluated with the 6-311++G(3df,3pd) basis set.....294

Table 5-9 Bond lengths and interaction energies for He_2 and Ne_2.....295

Table 5-10 Selected geometrical parameters (Å), harmonic Cl-Cl frequencies (cm^{-1}) and the binding energy (kJ/mol) of the $C_2H_4\cdots Cl_2$ complex.....300

Table 5-11 Selected geometrical parameters (Å) and relative energies (kJ/mol) for the minimum (M) and saddle points (SP) of malonaldehyde.....301

Table 5-12 Selected geometrical parameters of the ion-complex $Cl^-\cdots CH_3Cl$ and the corresponding transition state for the Walden inversion. All values are obtained with the 6-311+G(d,p) basis set.....305

Table 5-13 Complexation energies of the ion-molecule complex Cl^--CH_3Cl ΔE_{comp}, activation energy $\Delta E^{\#}$, and overall activation energy relative to reactants ΔE_{ovr} for the Walden inversion.....306

Table 5-14 Activation barrier (kJ/mol) of C_6H_6 reacting with triplet oxygen. The activation energy is calculated by 6-311++G(3df,3pd) basis set at 6-311G** geometries including ZPVE correction.....309

Table 5-15 The main geometrical features of the C_2H_4O transition state and the activation barrier (kJ/mol) of C_2H_4 reacting with triplet oxygen by 6-311++G(3df,3pd) with

ZPVE correction.....310

Table 5-16 Transition energies (in eV) of formaldehyde (H_2CO) predicted with the 6-311++G** basisi set.....315

Table 5-17 Transition energies (in eV) of acetaldehyde (H_3CHCO) predicted with the 6-311++G** basis set.....316

Table 5-18 Transition energies (in eV) of acetone (H_3CCOCH_3) predicted with the 6-311++G** basisi set.....317

List of Figures

Figure 3-1 Illustration of the reaction of the triplet oxygen atom with the central CC bond of selected hydrocarbons.....65

Figure 3-2 Structures of ethylene, of the transition states, of the intermediate diradicals, and of the singlet epoxide product (bond lengths and bond angles) 68

Figure 3-3 A schematic illustration of the intersystem crossing of the singlet and triplet states during the ring closure to form the epoxide.....71

Figure 3-4 Structures of benzene and benzene oxides.....80

Figure 3-5 Structure of naphthalene and naphthalene oxides.....84

Figure 3-6 Structure of pyracylene and pyracylene oxides 90

Figure 4-1 Geometries of the transition state and intermediates for the initial reaction and of the epoxide.....125

Figure 4-1A Illustration of the energies of the initial reaction of oxygen (^{3}P) with benzene.....126

Figure 4-2 Isomerization pathway from epoxide to 7-Oxa-norbornadiene.....140

Figure 4-2A Geometries of oxepin and transition states.....143

Figure 4-2B Geometries of isomer 10, the transition state to 3-Oxa-quadricyclane, 3-Oxa-quadricyclane and 7-Oxa-norbornadiene.....144

Figure 4-3 Geometries of Dewar benzene epoxide and the transition states.....152

Figure 4-3A Isomerization pathway from epoxide to Dewar benzene oxide.....153

Figure 4-4 Geometries of 2-oxa-bicyclo[3,2,0]hepta-3,6-diene, the transition states and

bicyclo[2.1.0]-2-pentene-5-carbaldehyde(4-20).....161

Figure 4-4A Isomerization path from oxepin to bicyclo[2.1.0]-2-pentene-5-carbaldehyde.....162

Figure 4-5 Geometries of butadienylketene, cyclohexadienone and transition states....165

Figure 4-5A Geometries of bicyclo[3.1.0]hex-3-en-2-one and its transition state.....166

Figure 4-5B Isomerization path from epoxide to bicyclo[3.1.0]hex-3-en-2-one.....167

Figure 4-6 Geometries of phenol and the related transition states.....173

Figure 4-6A Geometries of 2,5-cyclo-hexadienone and its related transition state.....174

Figure 4-6B The isomerization pathway from hexadienone to 2,5-cyclo-hexadienone..175

Figure 4-7 The isomerization pathway for C_2 epoxide 178

Figure 4-7A Geometries of C_2 epoxide, oxepin, related transition states and isomers ..179

Figure 4-8 Geometries and vibrational modes for the two imaginary frequencies of 38 187

Figure 4-8A The isomerization pathway near transition state 4-4.....188

Figure 4-9 Geometries of transition states 4-39 and 4-40.....192

Figure 4-9A The reaction pathway from transition states 4-4 and 4-40 to 7-Oxa-norbornadiene 195

Figure 5-1 Energy of H predicted by BxHFy, G96xHFy, PW91xHFy, mPW91xHFy and LGxHFy.....225

Figure 5-2 Energy of He^+ predicted by BxHFy, G96xHFy, PW91xHFy, mPW91xHFy and LGxHFy.....227

Figure 5-3 Kinetic energy of H predicted by BxHFy, G96xHFy, PW91xHFy, mPW91xHFy and LGxHFy.....228

Figure 5-4 Kinetic energy of He^+ predicted by BxHFy, G96xHFy, PW91xHFy, mPW91xHFy and LGxHFy.....229

Figure 5-5 Potential Energy of H predicted by BxHFy, G96xHFy, PW91xHFy, mPW91xHFy, LGxHFy.....231

Figure 5-6 Potential energy of He^+ predicted by BxHFy, G96xHFy, PW91xHFy, mPW91xHFy and LGxHFy.....232

Figure 5-7 Energy of H_2^+ at 4 Å predicted by BxHFy, G96xHFy, PW91xHFy, mPW91xHFy and LGxHFy.....234

Figure 5-8 Kinetic energy of H_2^+ (R=4Å) predicted by BxHFy, G96xHFy, PW91xHFy, mPW91xHFy and LGxHFy.....235

Figure 5-9 Potential energy of H_2^+ (R=4Å) predicted by BxHFy, G96xHFy, PW91xHFy, mPW91xHFy and LGxHFy.....236

Figure 5-10 Self-interaction error of H_2^+ (R=4Å) predicted by BxHFy, G96xHFy, PW91xHFy, mPW91xHFy and LGxHFy.....238

Figure 5-11 Self-interaction error of H predicted by BxHFy, G96xHFy, PW91xHFy, mPW91xHFy and LGxHFy.....239

Figure 5-12 Self-interaction error in He^+ predicted by BxHFy, G96xHFy, PW91xHFy, mPW91xHFy and LGxHFy.....240

Figure 5-13 Self-interaction error in H_2^+ (R=4Å) predicted by PW91xHFy and PW91xHFyPW91.....243

Figure 5-14 Energy of H^- predicted by BxHFx, G96xHFy, PW91xHFy, mPW91xHFy and LGxHFy.....246

Figure 5-15 Energy of the highest occupied orbital of H^- predicted by BxHFy, G96xHFy,

PW91xHFy, mPW91xHFy and LGxHFy.....247

Figure 5-16 Energy of the highest occupied orbital of H^- predicted by BxHF and BxHFyLYP.....249

Figure 5-17 Energy of the highest occupied orbital of H^- predicted by PW91xHFy and PW91xHFyPW91.....250

Figure 5-18 Energy of He Predicted by BxHFy, G96xHFy, PW91xHFy, mPW91xHFy and LGxHFy.....252

Figure 5-19 Kinetic energy of He predicted by BxHFy, G96xHFy, PW91xHFy, mPW91xHFy and LGxHFy.....254

Figure 5-20 Potential energy of He predicted by BxHFy, G96xHFy, PW91xHFy, mPW91xHFy and LGxHFy.....255

Figure 5-21 Electron-electron interaction energy of He predicted by BxHFy, G96xHFy, PW91xHFy, mPW91xHFy and LGxHFy.....256

Figure 5-22 The highest occupied orbital energy of He predicted by BxHFy, G96xHFy, mPW91xHFy, PW91xHFy and LGxHFy.....260

Figure 5-23 Total energy of triplet He predicted by BxHFy, G96xHFy, PW91xHFy, mPW91xHFy and LGxHFy.....262

Figure 5-24 Kinetic energy of triplet Helium predicted by BxHFy, G96xHFy, PW91xHFy, mPW91xHFY and LGxHFy.....264

Figure 5-25 Potential energy of triplet Helium predicted by BxHFy, G96xHFy, PW91xHFy, mPW91xHFy and LGxHFy.....265

Figure 5-26 Electron-electron interaction energy in He predicted by BxHFy, G96xHFy, PW91xHFy, mPW91xHFy and LGxHFy.....266

Figure 5-27 Total energy of triplet He predicted by PW91xHFy and PW91xHFyPW91.....269

Figure 5-28 Total energies of Li Predicted by BxHFy, G96xHFy, PW91xHFy, mPW91xHFy and LGxHFy.....272

Figure 5-29 Kinetic energies of Li predicted by BxHFy, G96xHFy, PW91xHFy, mPW91xHFy and LGxHFy.....273

Figure 5-30 Potential energies of Li predicted by BxHFy, G96xHFy, PW91xHFy, mPW91xHFy and LGxHFy.....274

Figure 5-31 Electron-electron interaction energies of Li predicted by BxHFy, G96xHFy, PW91xHFy, mPW91xHFy and LGxHFy.....275

Figure 5-32 Energy of H predicted by SxHFy.....278

Figure 5-33 Energy of He predicted by SxHFy.....279

Figure 5-34 Energy of Li predicted by SxHFy.....279

Figure 6-1 Illustration of the initial reaction of triplet oxygen atom (^{3}P) with benzene.....327

Figure 6-2 Illustration of the isomerization pathways of benzene oxides.....329

Figure 6-3 Illustration of the isomerization pathway for benzene oxide with C_2 symmetry.....331

List of schemes

Scheme 3-1 Illustration of the imaginary vibrational frequencies of the C_s (orthogonal) diradical as predicted by HF/6-31G*.....72

Scheme 3-2 Possible approaches for the reaction of oxygen with benzene.....75

Scheme 4-1 Possible pathways for the reaction of oxygen (^3P) with benzene.....123

Scheme 4-2 The relative energy of the singlet and triplet states of 4-3 and 4-4 136

Scheme 4-3 Reaction pathways from oxepin to isomer 4-10 and an illustration of the spin distribution in the open shell singlet structure (C_s, TS).....149

Scheme 4-4 Illustration of oxygen migration in Dewar benzene epoxide.....158

Chapter 1

Introduction

1.1 Quantum Chemistry

With the development of quantum mechanics, an amazing change occurred in chemistry. The application of quantum mechanics to chemistry leads to a new subdiscipline in chemistry - quantum chemistry, as foretold by Dirac's famous statement:

" The underlying physical laws necessary for the mathematical theory of a large part of physics and the whole of chemistry are thus completely known, and the difficulty is only that the exact application of these laws leads to equations much too complicated to be soluble. It therefore becomes desirable that approximate practical methods of applying quantum mechanics should be developed, which can lead to an explanation of the main features of complex atomic systems without too much computation." [1]

The development of quantum chemistry enables us to study larger and larger chemical systems with the aid of computational tools. As the fundamental basis of quantum chemistry, Schrödinger's equation uses the N-electron wave function $\Psi(x_1, x_2, \ldots x_N)$ of the system, which is very complicated. The wave function contains all the information we can possibly know about the system it describes. The solution of Schrödinger's equation with a wave function approach leads to conventional *ab initio* theory.

However, there is a remarkable theory that allows us to replace the complicated N-electron wave function and the associated Schrödinger equation by the much simpler electron density $\rho(r)$ and its associated computational scheme, which is known as density functional theory.

1.1.1 Conventional *ab initio* theory

After the Born-Oppenheimer approximation, the Schrödinger equation, for an N-electron system in a stationary state is:

$$\hat{H}_{elec}|\Psi_{elec}\rangle=E_{elec}|\Psi_{elec}\rangle \qquad 1.1$$

$\hat{H}_{elec}$: electronic Hamiltonian operator (in atomic units)

$$\hat{H}_{elec}=-\sum_{i=1}^{N}\frac{1}{2}\nabla_i^2-\sum_{i=1}^{N}\sum_{A=1}^{M}\frac{Z_A}{r_{iA}}+\sum_{i=1}^{N}\sum_{j>i}^{N}\frac{1}{r_{ij}} \qquad 1.2$$

$|\Psi_{elec}\rangle$: total electronic wave function

E_{elec}: total electronic energy

Because of the interelectronic repulsion terms $1/r_{ij}$ for a multielectron atom or molecule this equation is not separable. Only for the hydrogen atom and hydrogen like ion is the exact solution of the Schrödinger equation known. The Schrödinger equation would separate into N one-electron hydrogenlike equations with zeroth-order wave function as the hydrogen atomic orbital if the electron repulsion were ignored. The zeroth-order wave function would be a product of the N hydrogenlike (one-electron) orbitals:

$$|\Psi(0)\rangle=|\varphi_1(r_1,\theta_1,\phi_1)\,\varphi_2(r_2,\theta_2,\phi_2)\ldots\varphi_N(r_N,\theta_N,\phi_N)\rangle \qquad 1.3$$

where the hydrogenlike orbitals are

$$\varphi=R_{nl}(r)Y_l^m(\theta,\phi) \qquad 1.4$$

The *central-field approximation* is adopted in this procedure which is known as the *Hartree self-consistent-field (SCF) method*, and the interaction between electrons is averaged. With the modification due to Fock that the wave function be anti-symmetric, we obtain the *Hartree-Fock SCF method.*

In the Hartree-Fock SCF method, there is a single-electron operator $\hat{f}$:

$$\hat{f}\ (\mathrm{i})\ \varphi\ (\mathrm{i})=\varepsilon_i\varphi\ (\mathrm{i}) \qquad 1.5$$

$$f(\mathrm{i})=-\frac{1}{2}\nabla_i^2-\sum_A\frac{Z_A}{r_{iA}}+\sum_{j=1}^{N}[\hat{j}_j(i)-\hat{k}_j(i)] \qquad 1.6$$

The total energy of the system is:

$$\mathrm{E}=\sum_i\varepsilon_i-\sum_i\sum_{j>i}(J_{ij}-K_{ij}) \qquad 1.7$$

where the average repulsion of the electrons in the Hartree-Fock orbitals are subtracted from the sum of the orbital energies, and where the J_{ij} are the Coulomb integrals.

In the Hartree-Fock method, the instantaneous electron-electron interaction or correlation is not considered. Electron correlation accounts for about 0.5% to 1% of the total energy of a system, which is of the magnitude of a single-bond energy, and thus although small in absolute value, is very important in considering chemistry [2].

Improvement of the Hartree-Fock solution leads to post-Hartree-Fock theory. MP2 (*Möller-Plesset*) is the simplest correction for electron correlation, though higher order perturbation is desirable. *Configuration Interaction* is another way of including electron correlation, which involves the excitation of electrons from the reference state. The first order correction *is configuration interaction with single and double substitutions* (CISD). The *Coupled-cluster* (CC) method is an accurate but very expensive method, while *quadratic configuration interaction* (QCI) method is intermediate between the CC and CI methods, but is usually considered to be a variant of CC.

A linear combination of several *configuration state functions* (CSF) produces a *multi-configuration self-consistent field* (MCSCF) approach. The popularly used MCSCF

method involves *complete active space self-consistent field* (CASSCF), in which several highest occupied orbitals are optimized by varying both the coefficients of the configuration state functions and the orbitals. A further improvement on CASSCF with perturbation theory results in *Multi-configurational Second-order Perturbation Theory* (CASPT2).

Although high level *ab initio* methods (for example CC or CASPT2) can give very accurate predictions in chemistry, their prohibitive computer resource requirements prevent such methods being widely applied. CCSD scales as about O^3V^4 for CPU time and N^4 for disk space. A single SCF scales about N^4 for CPU time. MP2 (conventional) energies and gradients scale as about ON^4 for CPU time and N^4 for disk space. N is the total number of basis functions, O is the number of occupied orbitals and V is number of unoccupied orbitals. New accurate methods which demand less computer resources for their application are required. Density functional theory is such a method.

1.1.2 Density functional theory

Density functional theory considers the particle density to be the fundamental variable to describe the state of a system in an external potential. The external potential itself may result from particles obeying classical or quantum mechanics [3].

Historically, the density functional approach was initiated with the idea that locally the behavior of a collection of particles, the electron cloud, could be represented and approximated by a free electron gas of the same density at that point [3].

The Thomas-Fermi (TF) model [4,5], an early density functional theory, showed the basic steps to obtain the density functional for the total energy by using standard quantum

mechanics based on the wave function. From a well-defined model (and some extra assumptions, averages and practical simplifications guided by physical considerations) a direct relation, a functional, between the total energy and the density was obtained. The TF model allows for the direct determination of a charge density for a given external potential. It was the first method to exploit the idea of a *local density functional theory* when it considered a functional depending on the variables at only one point in space. The TF theory provides a differential equation for the self-consistent determination of the charge density without the intermediate use of a wave functions. It stands as an important model for the study of an atomic system without the use of wave functions [4].

Later, Dirac included a local density functional for the electron-electron exchange energy [6] and Wigner in 1934 included a local electron-electron correlation energy functional [7], which made it clear that density functional theory was computationally feasible.

The formalization of density functional theory began with the existence theorem of Hohenberg and Kohn[8]. The total energy of a many particle system in its ground state is a unique functional of its particle density and there exists a variational principle for the energy functional. Kohn and Sham invented, in 1965, an ingenious approach to the kinetic-energy functional T[ρ], the Kohn-Sham method[9]. They proposed introducing orbitals into the problem in such a way that the kinetic energy can be computed simply but to good accuracy. A small residual correction is handled separately. Thereby they turned density functional theory method into a practical tool for rigorous calculations. Thereafter, many approximations to the exchange-correlation functional have been proposed, which roughly can be classified into three types:

1 Local Spin Density Approximation (LSDA), the functional depends only on the density (ρ) at a point in the space, such as SVWN[10,11].

2 Generalized Gradient Approximation (GGA), the functional depends both on the density itself and its gradient.

3 Hybrid Density Functional Method, which involves the mixing of exact exchange into the functional. A typical approach is Becke's 1993 three parameter exchange functional B3 [12].

Previous studies indicated that DFT can predict molecular properties comparable to those from MP2 at a lower computational cost [13].

1.1.3 A comparison between conventional *ab initio* theory and density functional theory

Although there exists fundamental differences between conventional *ab initio* theory and density functional theory, these two theories are conceptually complementary. The following scheme shows a formal comparison between the two theories with respect to their Hamiltonian, fundamental variable, approximations made, reference system, and starting point for improvement.

The HF calculation formally scales as O^4 for computing time, O is the size (usually the number of basis functions) of the system studied. DFT methods scale as O^3. Higher level *ab initio* methods such as CCSD scale to much higher powers of O.

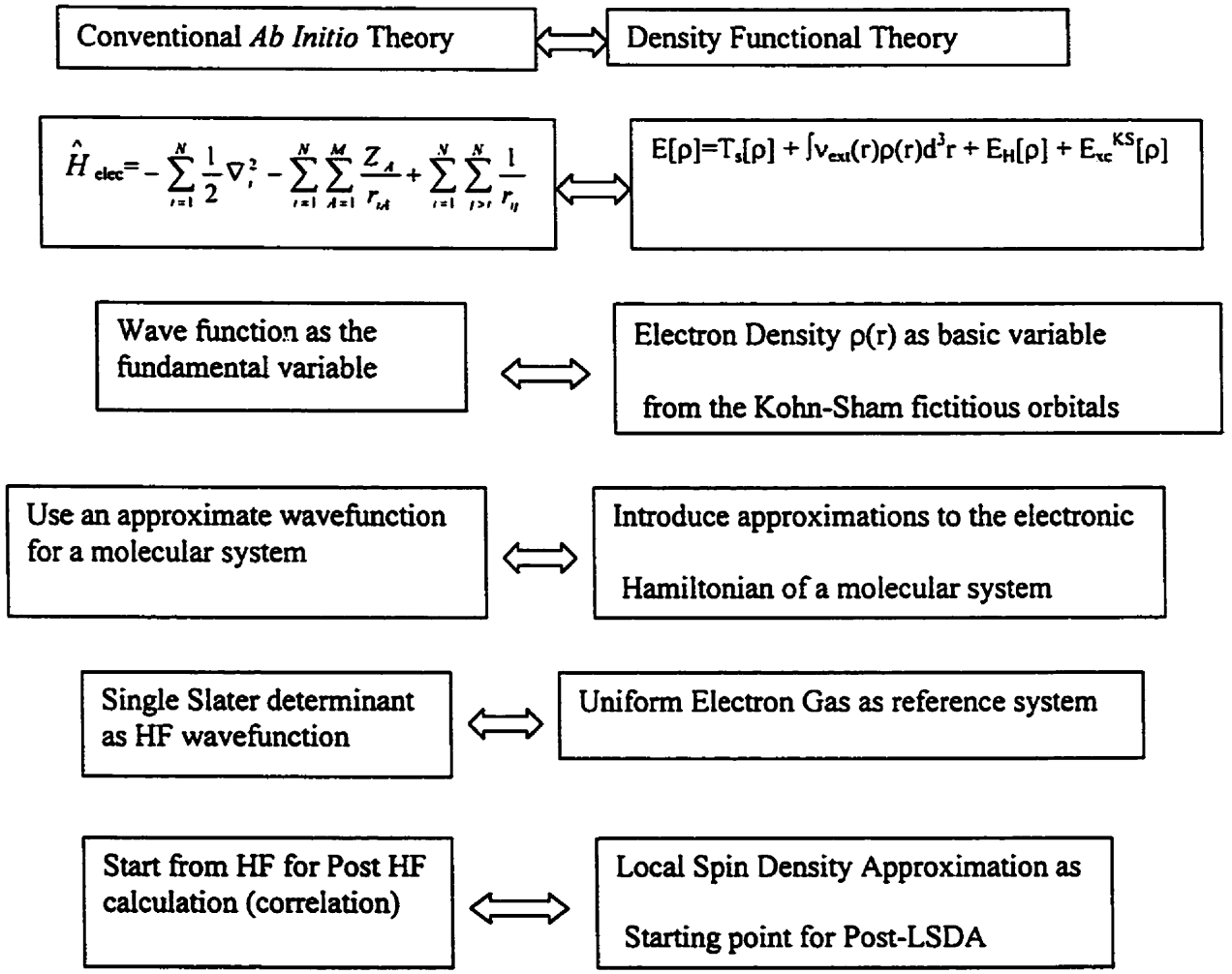
Conventional *Ab Initio* Theory
Density Functional Theory
$\hat{H}_{elec} = -\sum_{i=1}^{N} \frac{1}{2}\nabla_i^2 - \sum_{i=1}^{N}\sum_{A=1}^{M} \frac{Z_A}{r_{iA}} + \sum_{i=1}^{N}\sum_{j>i}^{N} \frac{1}{r_{ij}}$
$E[\rho]=T_s[\rho] + \int v_{ext}(r)\rho(r)d^3r + E_H[\rho] + E_{xc}^{KS}[\rho]$
Wave function as the fundamental variable
Electron Density ρ(r) as basic variable from the Kohn-Sham fictitious orbitals
Use an approximate wavefunction for a molecular system
Introduce approximations to the electronic Hamiltonian of a molecular system
Single Slater determinant as HF wavefunction
Uniform Electron Gas as reference system
Start from HF for Post HF calculation (correlation)
Local Spin Density Approximation as Starting point for Post-LSDA

1.2 Organic Chemistry

The reaction of an oxygen atom with aromatic organic molecules plays an important role in atmospheric chemistry [14,15], photochemical air pollution, and in combustion processes. Earlier experimental studies on C_{60} indicated that this new type of carbon molecule has new chemical properties with three-dimensional π electron conjugation and a unique structure [16,17,18]. In Chapter 3 of this work, the reactivity of the double bond in C_{60} will be studied through examining the reactivity towards an oxygen atom of its fragments ($C_{14}H_8$, $C_{18}H_{12}$ and $C_{26}H_{12}$) along with other systems (C_2H_4, C_6H_6, and $C_{10}H_8$). Benzene, a typical aromatic molecule, serves as a prototypical model for aromatic molecules. The reaction of benzene with a triplet oxygen atom, which is important in atmospheric chemistry, is studied in Chapter 4 along with the isomerization of the benzene oxide. There have been no extensive studies on this reaction or on the isomerization of benzene oxide.

1.3 Analysis of exchange correlation functionals

Becke's three-parameter exchange protocol (B3) [12], which was inspired by the adiabatic connection mechanism (ACM) [19] in combination with the LYP [20] correlation functional has been very successful in chemical applications. It serves as a standard density functional method for much chemical modeling. Although the role of exact exchange (HF exchange in terms of computation) has been rationalized [21], the behavior of hybrid DFT methods for property prediction with variation in the weight of the HF exchange is not so clear. The different behaviors of the functionals and the role of HF exchange are examined in the isomerization of benzene oxides. In Chapter 5, the

available exchange and correlation functionals are studied by varying the weight of HF exchange in the hybrid method to determine the total energies for simple atomic systems (H, He and Li) and for H_2^+. The total energy is decomposed further into its energy components (kinetic, potential and electron-electron interaction energies) to examine the contributions of the exchange and correlation functional to each component of the total energy. The orbital energies of these systems predicted by the various exchange and correlation functionals are examined. These studies are expected to give insight into the detailed behavior of the functionals. They should provide preliminary guides to future improvement of the hybrid method and the construction of new functionals.

At the end of Chapter 5, the new method mPW1LYP (a combination of exchange (mPW [22]) and correlation functionals (LYP [20]) along with Becke's one-parameter protocol [23]) is examined. Results for the reduced G2 data [24] and other chemical systems were computed and compared with those from other methods [22]. The purpose of this work is to check the role of the correlation functional in predictions of chemical phenomena and to seek the best combination of existing exchange and correlation functionals.

1.4 References

1. P. A. M. Dirac, Proc. Roy. Soc., (London) **123,** 714 (1929)
2. I. N. Levine, Quantum Chemistry, 4th Ed, Prentice Hall Inc., 1991
3. J. Keller and J. L. Gázquez Eds., Lecture Notes in Physics: Density Functional Theory, Springer-Verlag, Berlin, 1983
4. L. H. Thomas, Proc. Cambridge Philos. Soc., **23,** 542 (1927)
5. E. Fermi, Z. Phys., **48,** 73 (1928)
6. P. A. M. Dirac, Proc. Cambridge Philos. Soc., **26** 376 (1930)
7. E. Wigner, Phys. Rev., **46,** 1002 (1934)
8. P. Hohenberg, and W. Kohn, Phys. Rev., B **136,** 864 (1964)
9. W. Kohn, and L. J. Sham, Phys. Rev., **140,** A1133 (1965)
10. J. C. Slater, Quantum Theory of Molecular and Solids. Vol.4: The Self-Consistent field for Molecules and Solid (McGraw-Hill, New York, 1974).
11. S. H. Vosko, L. Wilk and M. Nusair, Can. J. Phys., **58,** 1200 (1980)
12. A. D. Becke, J. Chem. Phys., **98,** 5648 (1993)
13. J. B. Foresman, and Æ. Frisch: Exploring Chemistry with Electronic Structure Methods, Second Edition, Gaussian Inc., Pittsburgh, PA, 1996
14. T. H. Lay, J. W. Bozzelli, and J. H. Seinfeld, J. Phys. Chem., **100,** 6543 (1996)
15. B. Klotz, I. Barnes, K. H. Becker, and B. T. Golding, J. Chem. Soc., Faraday Trans., **93**(8), 1507 (1997)
16. J. M. Hawkins, A. Meyer, T. A. Lewis, S. Loren, F. J. Hollander, Science, **252,** 312 (1991)
17. L. Isaacs, A. A. Wehrsig, F. Diederich, Helv. Chim. Acta, **76,** 1231 (1993)

18. A. Pasquarello, M. Schlüter, R. C. Haddon, Science, **257**, 1660 (1992)

19. J. Harris, and R. O. Jones, J. Phys. **F 4**, 1170 (1974); O. Gunnarsson, and B. I. Lundqvist, Phys. Rev. **B 13**, 4274 (1976); D. C. Langreth, and J. P. Perdew, Phys. Rev. **B 15**, 2884 (1997); J. Harris, Phys. Rev. **A, 29**, 1648 (1984)

20. C. Lee, W. Yang, and R. G. Parr, Phys. Rev. **B 37**, 785 (1988)

21. J. P. Perdew, M. Ernzerhof, and K. Burke, J. Chem. Phys., **105**, 9982 (1996)

22. C. Adamo, and V. Barone, J. Chem. Phys., **108**, 664 (1998)

23. A. D. Becke, J. Chem. Phys., **104**, 1040 (1996)

24. B. G. Johnson, P. M. W. Gill, and J. A. Pople, J. Chem. Phys., **98**, 5612 (1993)

Chapter 2

Overview of Quantum Chemistry

2.1 Overview of Conventional *Ab Initio* Theory

This chapter will discuss general aspects of conventional *ab initio* and density functional methods, the computer resources used and the programs involved. More detail on the computational methods and procedures will be found in the "Computational Details" section of the following chapters. Since density functional methods are most important to this work, conventional *ab initio* theories will be introduced and briefly discussed in a way that helps the understanding of density functional theory. Electron correlation is the central problem in quantum chemistry and will be discussed in both the *ab initio* and density functional approaches.

2.1.1 The adiabatic and Born-Oppenheimer approximations

The total Hamiltonian of a system can be written as the kinetic and potential energies of the nuclei and electrons [1]:

$$H_{tot} = T_n + T_e + V_{ne} + V_{ee} + V_{nn} \qquad 2.1$$

For the system transformed to center of mass coordinates:

$$H_{tot} = T_n + H_e + H_{mp} + V_{nn} \quad \text{and} \quad H_e = T_e + V_{ne} + V_{ee} \qquad 2.2$$

$$H_{mp} = -\frac{1}{2M_{tot}}\left(\sum_{i=1}^{N}\nabla_i\right)^2, \quad T_n = \sum_{i=1}^{N} -\frac{1}{2M_a}\nabla_a^2 = \nabla_n^2$$

H_e is the electronic Hamiltonian and H_{mp} is called mass-polarization, M_{tot} is the total mass of all the nuclei and the sum is over all electrons. H_e depends only on the nuclear position (*via* equation (1.2)) and not on their momenta.

For H_e, the electronic Hamiltonian, the Schrödinger equation is:

$$H_e(R)\Psi_i(R,r) = E_i(R)\Psi_i(R,r), \quad i = 1,2\ldots\infty \qquad 2.3$$

R denotes nuclear positions and **r** electronic coordinates. Without introducing any approximation, the total wave function can be written as an expansion in the complete set of electronic functions, with the expansion coefficients being functions of the nuclear coordinates.

$$\Psi_{tot}(R,r) = \sum_{i=1}^{\infty} \Psi_{ni}(R)\Psi_i(R,r) \qquad 2.4$$

After derivation [1], we obtain:

$$\sum_{i=1}^{\infty} \{\Psi_i(\nabla_n^2\Psi_{ni}) + (\nabla_n\Psi_i)(\nabla_n\Psi_{ni}) + \Psi_{ni}\nabla_n^2\Psi_i + \Psi_{ni}E_i\Psi_i + \Psi_{ni}H_{mp}\Psi_i\}$$

$$= E_{tot}\sum_{i=1}^{\infty} \Psi_{ni}\Psi_i \qquad 2.5$$

or after multiplying Ψ_j^* and integrating under orthonormality,

$$\nabla_n^2\Psi_{ni} + E_j\Psi_{ni} + \sum_{i=1}^{\infty} \{2\langle\Psi_j|\nabla_n|\Psi_i\rangle(\nabla_n\Psi_{ni}) + \langle\Psi_j|\nabla_n^2|\Psi_i\rangle\Psi_{ni}$$

$$+ \langle\Psi_j|H_{mp}|\Psi_i\rangle\Psi_{ni}\} = E_{tot}\Psi_{nj} \qquad 2.5'$$

The first two terms are the first- and second-order non-adiabatic coupling elements from which the electronic wave function has been removed, while the last one is the mass polarization. The non-adiabatic coupling elements are important for systems involving more than one electronic surface, such as photochemical reactions [1].

In the adiabatic approximation the form of the total wave function is restricted to one electronic surface, i.e. all coupling elements in equation 2.5 are neglected (only the terms with i = j survive). Except for spatially degenerate wave functions, the diagonal first-order non-adiabatic element is zero.

$$(\nabla_n^2 + E_j + \langle\Psi_j|\nabla_n^2|\Psi_j\rangle + \langle\Psi_j|H_{mp}|\Psi_j\rangle)\Psi_{nj} = E_{tot}\Psi_{nj} \qquad 2.6$$

Neglecting the mass polarization and reintroducing the kinetic energy operator gives

$$(T_n + E_j + \langle\Psi_j|\nabla_n^2|\Psi_j\rangle)\Psi_{nj} = E_{tot}\,\Psi_{nj} \qquad 2.7$$

or

$$(T_n + E_j(R) + U(R))\Psi_{nj}(R) = E_{tot}\,\Psi_{nj}(R) \qquad 2.8$$

U(R) is the diagonal correction, and is smaller than $E_j(R)$ by a factor roughly equal to the ratio of the electronic and nuclear masses. It is usually a slowly varying function of R, and therefore the shape of the energy surface is determined almost exclusively by $E_j(R)$[2].

In the Born-Oppenheimer approximation the diagonal correction is neglected, and the resulting equation takes on the usual Schrödinger form, where the electronic energy plays the role of a potential energy.

$$(T_n + E_j(R))\Psi_{nj}(R) = E_{tot}\,\Psi_{nj}(R) \qquad 2.9$$

The Born-Oppenheimer (and adiabatic) approximation is usually a good approximation, but breaks down when two (or more) solutions to the electronic Schrödinger equation come close together energetically.

2.1.2 Hartree-Fock theory and electron correlation

2.1.2.1 Hartree-Fock theory

In Hartree-Fock theory (as described in Chapter 1), if each spatial orbital is restricted to have two electrons with opposite spin (one with α and one with β spin), Restricted Hartree-Fock (RHF) results. If no restriction on the form of the spatial orbital is made, then Unrestricted Hartree-Fock (UHF) is obtained. As the restricted wave functions constrain various parameters, the energy of the UHF wave function is always lower than

or equal to the corresponding restricted wave function. However, the UHF description has the disadvantage that the wave function is not normally an eigenfunction of the S^2 operator (unless it is equal to the RHF solution). S^2 evaluates the total electron spin angular momentum squared, and the UHF suffers from spin contamination from higher multiplicity states.

2.1.2.2 Electron correlation

As mentioned in Chapter 1, the Hartree-Fock method generates solutions to the Schrödinger equation where the real electron-electron interaction is replaced by an average interaction due to the introduction of a single Slater determinant as the wave function. With a complete basis set, the HF wave function is able to account for up to ~99% of the total energy. The remaining energy, which is the electron correlation energy, is often very important for describing chemical phenomena. The electron correlation energy has almost the same order of magnitude as a single bond energy. For practical purposes, we adopt the definition of the *Electron Correlation* (EC) energy as the difference in energy between the HF and the lowest possible energy in a given basis set within the framework of conventional *ab initio* methods [3]. Physically the electron correlation corresponds to (and results from) the instantaneous Coulombic interactions that keep the electrons further apart than the average interaction in HF, causing the energy for a correlated method to be lower than the HF value. Unrestricted Hartree-Fock (UHF) does introduce some relaxation relative to restricted HF. The E_{HF} below is the general Hartree-Fock energy and,

$$E_{corr} = E_{exact} - E_{HF} \qquad 2.10$$

Although the correlation between pairs of electrons belonging to the same spatial molecular orbital (MO) is large, as the size of a molecule increases, the number of electron pairs belonging to different spatial MOs grows faster than those belonging to the same MO. So the inter-pair correlation is often comparable to the intra-pair contribution. Since the correlation between opposite spins has both intra- and inter-orbital contributions, it will be larger than the correlation between electrons having the same spin in a restricted reference state.

The opposite spin correlation is sometimes called *Coulomb correlation*, while the same spin correlation is termed *Fermi correlation*. The Coulomb correlation is the larger contribution. There is a reduced probability of finding one electron in the immediate vicinity of another electron, the *Coulomb hole* for opposite spins, and the *Fermi hole* for the same spins.

In full CI (including all possible excitations in configuration interaction) there are three (not mutually exclusive) categories of correlation corrections relative to the reference wave function (usually the HF solution) that should be distinguished [3c]:

Category 1 is called dynamic correlation because it enables the electrons to stay further apart. It usually represents the largest part of the total correlation energy.

Category 2 occurs for an open-shell singlet such as H_2 (the correct separation of H_2 requires two determinants $C_1|1\sigma_g\alpha 1\sigma_g\beta| \pm C_2|1\sigma_u\alpha 1\sigma_u\beta|$ where $C_1=C_2$ at ∞ separation but $C_1>>C_2$ at R_e). This is called static correlation, or symmetry required correlation. Generalized valence bond (GVB) theory includes this static correlation.

Category 3 is often called nondynamic correlation and is perhaps best described by considering the simplest possible correlated function for F_2 that can correctly dissociate.

For F_2, the wave function consists of two determinants $C_1|core2p\sigma_g\alpha 2p\sigma_g\beta| \pm C_2|core2p\sigma_u\alpha 2p\sigma_u\beta|$ in GVB theory. UHF predicted that two F atoms are lower in energy than is the F_2 molecule (UHF can not describe the correct wave function for F_2), thus UHF does not predict the existence of the F_2 molecule [3c]. Correct description of the wave function of F_2 by GVB ensures that GVB correctly predict bonding in F_2.

However, electron correlation can be divided into two parts [4]: dynamic correlation and non-dynamic correlation. Dynamic correlation was described above, and occurs with a 'tight pair' of electrons as in He or in the $(2p_z)^2$ in Ne, etc. Non-dynamic correlations arise from degeneracies or near-degeneracies. Categories 2 and 3 can be assigned to non-dynamic correlation. Non-dynamic and dynamic correlation occur in the sequence:

$$HF \rightarrow CASSCF \rightarrow CASPT2$$

CASSCF [5] introduces non-dynamic correlation (also including some dynamic correlation), and CASPT2 [6] improves the CASSCF results by including dynamic correlation. Such theories were developed to overcome the deficiencies of the Hartree-Fock method i.e. the lack of electron correlation.

However, the definitions of exchange and correlation in DFT are not completely equivalent to their wave mechanical counterparts [1]. The correlation energy in wave function theory is usually defined as the difference between the exact energy and the corresponding Hartree-Fock value. The exchange energy is the total electron-electron repulsion energy minus the Coulomb energy. These energies have both short- and long-range parts (in term of the distance between two electrons). The long-range correlation is essentially the "static" correlation energy (i.e. the "multi-reference" part for the appropriate description of the electronic state) while the short-range part is the

"dynamical" correlation. The definitions of exchange and correlation in DFT are local (short range). They only depend on the density at a given point and in its immediate vicinity (*via* derivatives of the density). This is at least true for the GGA and LSDA.

2.1.3 Many-body perturbation theory (Møller-Plesset perturbation theory)

The idea in perturbation theory is that the problem at hand only differs slightly from a problem that has already been solved (exactly or approximately). So the solution should be close to that for the already solved system. The Hamiltonian consists of two parts, a reference (H_0) and a perturbation (H'), and H' which in electronic structure theory introduces the electron correlation is much smaller than H_0. Perturbation theory can be used for adding corrections to solutions that employ an independent particle approximation, resulting in *Many-Body Perturbation Theory* (MBPT). If we choose the unperturbed Hamiltonian as a sum of Fock operators, then we obtain Møller-Plesset Perturbation Theory (MP) [7].

The total unperturbed wave function is $|\Psi\rangle = |\chi_1\chi_2\cdots\chi_n\rangle$, χ_n is the single electron wave function, or orbital, and the wave function of the system Φ is a linear combination of the unperturbed wave functions:

$$\Phi = C_0\Psi^0 + C_1\Psi^{(1)} + C_2\Psi^{(2)} + \cdots \qquad 2.11$$

Energy $E = C_0E^0 + C_1E^{(1)} + C_2E^{(2)} + \cdots$

$$H_0 = \sum_{i=1}^{N} f(i) \qquad 2.12$$

$$f(i)\chi(i) = \varepsilon_i\chi(i), \qquad 2.13$$

$$f(i) \equiv -\frac{1}{2}\nabla_i^2 - \sum_A \frac{Z_A}{r_{iA}} + \sum_{j=1}^{N}[\hat{j}_j(i) - \hat{k}_j(i)], \quad f(i) \text{ is the Fock operator} \qquad 2.14$$

$H_0 |\Psi_i\rangle = E_i^{(0)} |\Psi_i\rangle$ 2.15

E_i is the eigenvalue of the unperturbed wave function

$|\Psi_i\rangle = |i\rangle$ is the unperturbed wave function. 2.16

$H = H_0 + \lambda v$ λ is an ordering parameter 2.17

$H|\Phi_i\rangle = (H_0+v)|\Phi_i\rangle = E_i|\Phi_i\rangle$ 2.18

$$H = -\sum_{i=1}^{N} \frac{1}{2}\nabla_i^2 - \sum_{i=1}^{N}\sum_{A=1}^{M} \frac{Z_A}{r_{iA}} + \sum_{i=1}^{N}\sum_{j>i}^{N} \frac{1}{r_{ij}} \qquad 2.19$$

H is the electronic Hamiltonian of the system.

So,

$$v = \sum_{i=1}^{N}\sum_{j>i}^{N} \frac{1}{r_{ij}} - \sum_{i=1}^{N} \sum_{j=1}^{N} [\hat{j}_j(i) - \hat{k}_j(i)] \qquad (\lambda=1) \qquad 2.20$$

substituting 2.11 and 2.17 into 2.18, and since all the terms are linearly independent, each order m should only relate to itself. Then multiplying from the left by Ψ^0 for each order and using intermediate normalization results in

$$(E^0 - H_0)\,\Psi^{(m)} = (v - E^{(1)})\,\Psi^{(m-1)} - \sum_{k=2}^{m} E^{(k)}\Psi^{(m-k)} \qquad 2.21$$

and

$$E^{(m+1)} = \langle \Psi^0 | v | \Psi^{(m)} \rangle \qquad 2.22$$

Actually, the HF energy is correct to first order; thus, the perturbation contribution starts at second order. Since the Hamiltonian contains only one- and two-electron terms, only single and double excitations can contribute *via* direct mixing with Ψ^0 in the lowest orders. However, the self-consistent optimization of the HF wave function prevents direct mixing between single excitations and Ψ^0 (Brillouin's theorem). Thus, the second- and third-order energies have contributions only from double excitations. In higher orders,

there is indirect coupling *via* double excitations and thus the fourth- and fifth-order energies have contributions from single, double, triple and quadruple excitations.

Perturbation theory truncated at any order is size-consistent. The most important contribution in MPn comes from the second order correction [3d]. Due to its low computational cost and consideration of the size of the second order correlation correction, MP2 is by far the most commonly used conventional *ab initio* method for the treatment of electron correlation.

2.1.4 Quadratic configuration interaction(QCI)

Among many schemes introduced to address the electron correlation problem, perhaps the most simple and general technique is the method of *configuration interaction* (CI) [8]. The CI wave function mixes the Hartree-Fock wave function with single, double, triple quadruple, ... excited configurations, and the coefficients which determine the amount of mixing are computed variationally. If all possible excited configurations are included, the method gives the exact solution within the space spanned by a given basis set and is referred to as full configuration interaction (FCI). Clearly, FCI results are not practical for many-electron systems. However, used with modest basis sets, FCI aids in evaluating the inherent errors due to the deficiency of electron correlation methodology. In practice, only truncated CI schemes are applied to many-electron systems with large basis sets. The most common treatment is CI with single and double excitations (CISD) [8] where triple and higher excitations are neglected. Double excitations contribute dominantly to the electron correlation energies. Single excitations contribute relatively little to the correlation energies, although they appear to be important for the accurate evaluation of

certain molecular properties. However, CISD is not size-consistent which is a very important drawback to the successful application of this method on molecular complexes.

Quadratic configuration interaction (QCI) is a technique suggested by Pople *et al.*[9] which introduces size consistency exactly into CISD theory. It can be viewed as intermediate between configuration interaction and coupled cluster theory (CC) [10]. Quadratic configuration interaction uses the substitution operator T that generates new configurations and the HF wave function as the reference wave function.

$$T_1 = \sum_{ia} a_i^a \hat{t}_i^a \qquad 2.23$$

$$T_2 = \frac{1}{4}\sum_{ijab} a_{ij}^{ab} \hat{t}_{ij}^{ab} \qquad 2.24$$

$$T_3 = \frac{1}{36}\sum_{ijkabc} a_{ijk}^{abc} \hat{t}_{ijk}^{abc} \qquad 2.25$$

$\hat{t}_i^a, \hat{t}_{ij}^{ab}, \hat{t}_{ijk}^{abc}$ ... are elementary substitution operators, the *a* arrays involve coefficients to be determined. The wave function is,

$\Psi = f(T_1, T_2, \ldots)\Psi_0$ Ψ_0 is HF wave function. 2.26

$\overline{H} = H - E_{HF}$ Hamiltonian 2.27

$$\langle \Psi_0 | \overline{H} | T_2\Psi_0 \rangle = E_{corr} \qquad 2.28$$

$$\langle \Psi_i^a | \overline{H} | (T_1 + T_2 + T_1T_2)\Psi_0 \rangle = a_i^a E_{corr} \qquad 2.29$$

$$\langle \Psi_{ij}^{ab} | \overline{H} | (1 + T_1 + T_2 + \frac{1}{2}T_2^2)\Psi_0 \rangle = a_{ij}^{ab} E_{corr} \qquad 2.30$$

The T_2^2 and T_1T_2 terms make the QCISD (quadratic configuration interaction single and double excitation) method size-consistent. These terms are needed for size consistency in the CISD method. It has been shown that these equations are identical to CCSD (coupled cluster with single and double substitution) where some of the terms have been omitted [11]. In practice, QCISD and CCSD often give similar results [12]. QCISD scales as O^2V^4,

O is the number of occupied orbitals and V is the number of virtual orbitals. The same scaling occurs with CCSD.

2.1.5 Multi-configuration self-consistent field: complete active space self-consistent field (CASSCF) and complete active space plus perturbation correction to second-order (CASPT2)

2.1.5.1 Complete active space self-consistent field (CASSCF)

The HF method is a single-determinant based method. By the aid of natural orbital [13] analysis and unrestricted HF methods, UHF can simulate multi-configuration character in some problems. Intrinsically, it is still a single-determinant method and can not handle fully problems with degeneracies, or near-degeneracies between different electronic configurations, where non-dynamic correlation is especially important. Nondynamic correlation is important, for example, in the transition state for symmetry-forbidden chemical reactions and in the dissociation of a molecule especially when the fragments are at a large distance. In such cases, the electronic state can only be described by several electronic configurations.

The multi-configuration self-consistent field (MCSCF) model is an attempt to generalize the HF method to the problem of degeneracies or near-degeneracies. The molecular wave function is written as a linear combination of configuration state functions (CSFs) Φ_i and not only the expansion coefficients a_i in $\Psi=\Sigma_i a_i \Phi_i$, but also the forms of the orbitals in the CSFs are optimized. One of the most popular MCSCF methods is the complete active space self-consistent field model (CASSCF) [5]. In

CASSCF, the molecular orbitals are divided into three subspaces: inactive, active, and external orbitals [14]. The active and inactive subspaces constitute the internal (occupied) orbital subspace and the external orbitals are unoccupied. The CASSCF wave function is formed as a linear combination of configuration state functions (CSFs) generated from these orbitals in the following way [14],

1 The inactive orbitals are doubly occupied in all CSFs.

2 The remaining (active) electrons occupy the active orbitals. The CASSCF wavefunction is written as a linear combination of all the CSFs constructed from the electrons and orbitals in the active space, which comprises a complete expansion in the active orbital subspace.

The CASSCF configuration space becomes unmanageably large when the number of active orbitals is increased. At present more than 12 to14 orbitals cannot be handled within CASSCF [15]. For the case of degeneracies or near-degeneracies, CASSCF studies these effects without bias, since the only decision made by the user is the selection of the inactive and active orbitals and the atomic orbital basis set. In fact, studies on C_2, N_2, BH and N_2O_4 show the success of CASSCF in problems with multi-configuration character [14]. CASSCF can give a correct zeroth-order description of the wavefunction in situations where the single determinant based methods fail. In spite of its success, CASSCF cannot describe the bonding in Cr_2 properly and other transition metal dimers in which dynamic correlation is also important. CASSCF emphasizes the description of non-dynamic correlation.

2.1.5.2 Complete active space plus perturbation correction to second-order (CASPT2)

Complete Active Space plus Perturbation Theory in Second-order (CASPT2) [6,15] is a correction to CASSCF accounting for the dynamic correlation of electrons. The idea of treating dynamic correlation in CASPT2 is similar to using a low-order perturbation approach to the correct Hartree-Fock result. The CASSCF wavefunction acts as the zeroth-order approximation. A perturbation term $\lambda \hat{H}_1$ is added to the unperturbed Hamiltonian $\hat{H}_0$ to form the total Hamiltonian $\hat{H}$. In terms of $\hat{H}$, the eigen-equation can be expanded in a Taylor series. In CASPT2, the series expansions are truncated to first order in the wavefunctions, and second order in the energy,

$$|\hat{H}_1> = \sum_{i=1}^{M} C_i |i>, \quad |i> \in V_{SD} \qquad 2.31$$

V_{SD} is a subspace spanned by single and double replacement states, which forms the total configuration space with the other subspace [15].

$\{C_i, i = 1,\ldots, M\}$ is a solution of the system of linear equations,

$$\sum_{i=1}^{M} C_i < j | \hat{F} - E_0 | i > = -< i | \hat{H} | 0 >, \quad j = 1, \ldots, M \qquad 2.32$$

obtained from,

$$(\hat{H}_0 - E_0)| \hat{H}_1> = -(\hat{H} - \hat{H}_0)| 0 > \qquad 2.33$$

and $\hat{F}$ is a one-particle operator.

CASPT2 has been shown to give an accurate description of molecular structures in both ground and excited states. A large number of applications have shown that CASPT2 can be applied with good accuracy in calculating excited state properties and excitation

energies [15]. The error in predicting excitation energies is usually 0.5eV or less. In general, CASPT2 is comparable to MRCI or CCSD(T) in property prediction. The time consuming calculation and the limitation of the active space (number of orbitals included in active space) are major problems for the application of CASPT2 in chemistry.

2.2 Overview of Density Functional Theory

Over the past 30 years, density functional theory has become the physicist's method of choice for describing the electronic structure of solids, the original purpose behind its development [16]. More recently, chemists have also used DFT extensively to study molecules.

Density functional theory is primarily a theory of electronic ground state structure, couched in terms of the electronic density distribution $\rho(r)$. It has become increasingly useful for the understanding and calculation of the ground state density, $\rho(r)$, and energy, E, of molecules, clusters and solids. It is an alternative, and complementary, approach to the traditional methods of quantum chemistry which emphasize the many-electron wave function $\Psi(r_1,r_2,\ldots,r_n)$. Although both the Thomas-Fermi (TF) [17] and the Hartree-Fock-Slater [18] ($X\alpha$) method can be regarded as ancestors of modern density functional theory (DFT), those models are intrinsically approximate, while modern DFT is in principle exact [16,19].

A wave function for an N-electron system contains 3N coordinates, three for each electron (four if spin is included). The electron density is the square of the wave function. In the Kohn-Sham version [16b], the fictitious single-particle orbitals φ_j^{KS} are integrated over N-1 electron coordinates to calculate the density. This density depends only on three

coordinates independent of the number of electrons. Kohn-Sham theory [16b] is a rigorous *ab initio* framework for multi-electron calculations that has the appearance of an independent-particle model. It thus holds great promise for applications to large chemical systems beyond the reach of wave function based methods [20].

Although the ground-state electronic energy of the system is determined completely by the electron density $\rho(r)$, i.e. there exists a one-to-one correspondence between the electron density and the energy [16a], the exact functional connecting the electron density with the energy is not known. Thus many approximations to the functional have been proposed [19].

According to Kohn-Sham theory [16b], the general DFT energy functional can be written as:

$$E[\rho]=T_s[\rho] + \int v_{ext}(r)\rho(r)d^3r + E_H[\rho] + E_{xc}^{KS}[\rho]=\int v_{ext}(r)\rho(r)d^3r + F[\rho] \qquad 2.34$$

and

$$F[\rho]=T_s[\rho] + E_H[\rho] + E_{xc}^{KS}[\rho]$$

is an unknown but universal functional of the density $\rho(r)$ only. $v_{ext}(r)$ is the external potential. The non-interacting reference system is a system of independent non-interacting electrons in a common one-body potential V_{KS} yielding the same density as the "real" fully-interacting system. In mathematical terms, the one-body potential V_{KS} generates independent orbitals φ_i through the one-body Schrödinger equation

$$-\frac{1}{2}\nabla^2\varphi_i + V_{KS}\varphi_i = \varepsilon_i\varphi_i \qquad 2.35$$

such that, by construction, the total independent-particle density is

$$\rho = \sum_i |\varphi_i|^2 \qquad 2.36$$

We obtain $T_s[\rho]$, the kinetic energy of the non-interacting reference system, as

$$T_s[\rho] = \frac{1}{2}\sum_i |\nabla\varphi_i|^2 \qquad 2.37$$

$\int v_{ext}(r)\rho(r)d^3r$ is the potential energy of interaction with the external field. $E_H[\rho]$ is the classical Coulomb self-interaction energy, and everything else is called the Kohn-Sham exchange-correlation energy $E_{xc}^{KS}[\rho]$. The scheme is motivated [16b] by the supposition that E_{XC} is a relatively small part of the total energy. Since $T_s[\rho]$ is not the kinetic energy of the real system, E_{XC} contains a kinetic energy correlation term as well.

At the heart of DFT is the exchange-correlation functional V_{XC} whose exact form is not known. Many different approximate functionals have been proposed. It is customary to separate the E_{XC} unto two parts, an exchange E_X and a correlation part E_C, although no rigorous grounds have been given for such a separation. The exchange energy is by far the largest contributor to E_{XC} [1,19]. According to the dependence of the exchange-correlation functional on the electron density, the functionals can roughly be classified into two categories: local and non-local. Both the local density approximation and generalized gradient approximation (GGA) are based on localized model exchange-correlation holes. Though the GGA also depends on the electron derivatives, it is still a local DFT. Hybrid DFTs which incorporate the exact-exchange are non-local [19].

2.2.1 Local density approximation (LDA)

The simplest method is the local density approximation (LDA) [16b] which is:

$$E_{XC}^{LDA}[\rho(r)] \equiv \int \varepsilon_{XC}[\rho(r)]\rho(r)d^3r \qquad 2.38$$

$\varepsilon_{XC}(\rho(r))$ is the exchange-correlation energy density of a uniform interacting electron gas of density ρ. The LDA becomes exact when the length scale l over which $\rho(r)$ varies is

large, i.e. the density change is very slow. When introducing the spin into LDA, we get the local spin density approximation for E_{XC}^{LSDA}. The LSDA depends only on the electron density ρ.

$$E_{XC}^{LDA}[\rho_\alpha(r), \rho_\beta(r)] \equiv \int \varepsilon_{XC}[\rho_\alpha(r), \rho_\beta(r)]\rho(r)d^3r \qquad 2.39$$

$$\rho(r) = \rho_\alpha(r) + \rho_\beta(r) \qquad 2.40$$

The most popular LSDA correlation functional was constructed by Vosko, Wilk and Nusair(VWN) [16c] and the accompanying exchange functional is often the simple Slater exchange S [21]. LSDA might be expected to be a crude approximation, since the electron density varies rapidly in atoms and molecules and thus the LSDA is a poor description. In tests on atoms, the LSDA typically underestimates the exchange energies by a few percent and overestimates correlation energies by a factor of roughly two. In tests on molecules, the LSDA yields very good geometries (at least for main-group molecules). Vibrational frequencies, densities, and ionization potentials tend to agree well with experiment [22,23] for normal chemical bonds. Hydrogen bonds and Van der Waals interactions are not well treated in the LSDA functional. The LSDA has notorious overbinding tendencies [20].

2.2.2 Generalized gradient approximation (GGA)

Due to the rapid change of the electron density in atoms and molecules, the next logical step to correct the LSDA is to introduce the electron density gradient into the functional. This results in the so-called generalized gradient approximation

$$E_{XC}^{GGA} = \int f(\rho(r), |\nabla\rho(r)|)dr \qquad 2.41$$

GGA is considered to be a local DFT model since the functional depends only on the

density and its derivatives at a given point, and not on a space volume as for example does the Hartree-Fock exchange energy. In other words, properties at a point in space as described by GGA do not depend on any other points in space.

Perdew and Wang [24] proposed a GGA for the exchange energy based on the gradient expansion of the exchange hole, with real-space cutoffs chosen to guarantee that the hole is negative everywhere and represents a deficit of one electron,

$$\varepsilon_X^{PW86} = \varepsilon_X^{LDA} (1 + ax^2 + bx^4 + cx^6)^{1/15} \qquad 2.42$$

$$x = \frac{|\nabla \rho|}{\rho^{4/3}} \qquad 2.43$$

x is a dimensionless gradient variable[24], and a , b and c are constants (summation over equivalent expressions for the α and β densities is implicitly assumed). a=1.296, b=14 and c=0.2. The PW86 exchange functional is a parameter-free coordinate-space model for an inhomogeneous system. Its performance is much better than that of LSDA [24].

Becke [25] proposed a one-parameter exchange functional (B) motivated by the lowest-order gradient correction (LGC) to the local-density approximation

$$E_X^{LGC} = E_X^{LDA} - \beta \sum_\sigma \int \frac{(\nabla \rho)^2}{\rho_\sigma^{4/3}} d^3r \text{, where } \beta \text{ is a constant.} \qquad 2.44$$

determined on semi-empirical grounds [26] as,

$$E^X = E^X_{LSDA} - \beta \sum_\sigma \int \rho_\sigma^{4/3} \frac{x_\sigma^2}{(1 + 6\beta x_\sigma \sinh^{-1} x_\sigma)} d^3r \qquad 2.45$$

β is determined by a least squares fit to the exact atomic Hartree-Fock exchange energy and β=0.0042 best fits the six noble gas atoms helium through radon.

$x_\sigma = \frac{|\nabla \rho_\sigma|}{\rho_\sigma^{4/3}}$ σ: spin either "up" or "down"

$$E^{X}_{LSDA}=-C_X\sum_{\sigma}\int\rho_{\sigma}^{4/3}d^3r \qquad C_X=\frac{3}{2}(\frac{3}{4\pi})^{1/3} \qquad 2.46$$

Test calculations with B of thermochemistry on the G1 [27, 28] database indicate that the gradient correction improves the performance of the new functional. Further calculations with B indicated that DFT does not discriminate between molecules containing light atoms and those containing heavy atoms[29].

Perdew and Wang [30] proposed an exchange functional PW91 similar to Becke's 1988 exchange functional [25] to be used with the PW91 correlation functional [30,31],

$$\varepsilon_X^{PW91}=\varepsilon_X^{LDA}\left(\frac{1+xa_1\sinh^{-1}(xa_2)+(a_3+a_4e^{-bx^2})x^2}{1+xa_1\sinh^{-1}(xa_2)+a_5x^2}\right) \qquad 2.47$$

where $a_{1\text{-}5}$ and b are suitable constants and x is the same variable as in equation (2.45).

Recently, Gill introduced a new gradient-corrected exchange functional (G96) [32] with a semi-empirical parameter chosen to fit the exchange energy of the argon atom,

$$E^{X}_{G96}=\int\rho^{4/3}\left(\alpha-\frac{|\nabla\rho|^{3/2}}{137\rho^{2}}\right)dr \qquad 2.48$$

$$\alpha=-\frac{3}{2}(\frac{3}{4\pi})^{1/3}$$

While similar to Becke's B functional, it is simpler and its potential in a finite system is asymptotically unbounded. Combined with the LYP [33, 34] correlation functional, it performs similarly to BLYP on the standard G2 [35] benchmark set of molecules.

Along with the approximate exchange functionals, there have been many approximations for the correlation functional. Perdew proposed a gradient correction to the LSDA (P86) [36],

$$\varepsilon_C^{P86}=\varepsilon_C^{LDA}+\Delta\varepsilon_C^{P86} \qquad 2.49$$

$$\Delta\varepsilon_C^{P86}[\rho] = \frac{e^{\Phi} C(\rho)|\nabla\rho|^2}{f(\zeta)\rho^{7/3}}$$

$\zeta = (\rho_\alpha - \rho_\beta)/\rho$

$r_s = (3/4\pi\rho)^{1/3}$

$$f(\zeta) = 2^{1/3}\sqrt{\left(\frac{1+\zeta}{2}\right)^{5/3} + \left(\frac{1-\zeta}{2}\right)^{5/3}}$$

$$\Phi = 0.19195\frac{C(\infty)|\nabla\rho|}{C(\rho)\rho^{7/6}}$$

$C(\rho) = \delta_1 + (\delta_2 + \delta_3 r_s + \delta_4 r_s^2) / (1 + \delta_5 r_s + \delta_6 r_{s2} + \delta_7 r_s^3)$

$\delta_1 = 0.001667$ $\delta_2 = 0.002568$ $\delta_3 = 0.023266$ $\delta_4 = 7.389\times10^{-6}$ $\delta_5 = 8.723$

$\delta_6 = 0.472$ $\delta_7 = 0.007389$

This functional was later modified by Perdew and Wang in 1991 [30, 31]

$$\Delta\varepsilon_C^{PW91}[\rho] = \rho[H_0(t,r_s,\zeta) + H_1(t,r_s,\zeta)] \qquad 2.50$$

$H_0(t,r_s,\zeta) = a^{-1} f(\zeta)^3 \ln[1 + b(t^2 + At^4)/(1 + At^2 + A^2t^4)]$

$H_1(t,r_s,\zeta) = (16/\pi)(3\pi^2)^{1/3}[C(\rho) - c]\, f(\zeta)^3 t^2 e^{-ax^2/f(\zeta)^2}$

$$f(\zeta) = \frac{1}{2}((1+\zeta)^{2/3} + (1-\zeta)^{2/3})$$

$$t = (192/\pi^2)^{1/6}\frac{|\nabla\rho|}{2f(\zeta)\rho^{7/6}}$$

$A = b[e^{-a\varepsilon_c(r_s,\zeta)/f(\zeta)^3} - 1]^{-1}$

x is as defined in equation (2.43) and $C(\rho)$ is defined above, where $\epsilon(r_s,\zeta)$ is the PW91 parameterization of the LSDA correlation energy,

$$\epsilon_C^{PW91}(x) = -2a\rho(1+\alpha x^2)\ln\{1 + 1/[2a(\beta_1 x + \beta_2 x^2 + \beta_3 X^3 + \beta_4 x^4)]\} \qquad 2.51$$

a,α, β_1, β_2, β_3, and β_4 are constants.

Another popularly used correlation functional is due to Lee, Yang and Parr (LYP) [33],

$$E^C = -a\int \frac{1}{1+d\rho^{-1/3}}\left\{\rho + b\rho^{-2/3}[C_F\rho^{5/3} - 2t_W + (\frac{1}{9}t_W + \frac{1}{18}\nabla^2\rho)]e^{-c\rho^{-1/3}}\right\}\gamma(r)dr \qquad 2.52$$

a,b,c are the same as in the Colle-Salvetti (CS) functional [37] by fitting data for the helium atom.

$\gamma = 2[1-(\rho_\alpha^2+\rho_\beta^2)/\rho^2]$

$$t_W^{\ \sigma} = \frac{1}{8}\frac{|\nabla\rho_\sigma(r)|^2}{\rho_\sigma(r)} - \frac{1}{8}\nabla^2\rho_\sigma \qquad 2.53$$

the t_w functional is known as the Weizsacker kinetic energy density. Note that the γ-factor becomes zero when all the spins are aligned ($\rho=\rho_\alpha,\rho_\beta=0$), i.e. the LYP functional does not predict any parallel spin correlation in such a case (e.g. the LYP correlation energy in triplet He is zero)[1].

Recently Becke proposed certain "minimal" requirements for functionals [38]. The CS [33, 37] functionals incorrectly give zero correlation energy in a ferromagnetic system (i.e. all spins aligned). Both P86 and PW91 give small but nonzero correlation energies for the hydrogen atom where the value should be zero. These errors are unfortunately large if the goal of density-functional thermochemistry is precision on the order of a few kcal/mol or a few milli-Hartree. Becke's B and CS do not attain the exact uniform electron gas limit [38]. Thus Becke proposed a new gradient correction correlation functional B96 adopting the uniform electron gas model (UEG) [39]:

$$E^C = E^C_{opp} + E^C_{\alpha\alpha} + E^C_{\beta\beta} \qquad 2.55$$

$$E^C_{opp} = [1 + C_{opp}(\chi_\alpha^2+\chi_\beta^2)]^{-1}E_{Copp}^{UEG}$$

$$E^{C}_{\alpha\alpha}=[1+C_{\alpha\alpha}\chi_{\alpha}^{2}]^{-2}\frac{D_{\sigma}}{D_{\sigma}^{UEG}}E_{C\alpha\alpha}^{UEG}$$

$$x_{\sigma}=\frac{|\nabla\rho_{\sigma}|}{\rho_{\sigma}^{4/3}}$$

$$D_{\sigma}=\tau_{\sigma}-(\nabla\rho_{\sigma})^{2}/(4\rho_{\sigma}) \quad \text{and} \quad \tau_{\sigma}=\sum_{i}|\nabla\Psi_{i\sigma}|^{2}$$

$$D_{\sigma}^{UEG}=\frac{3}{5}(6\pi^{2})^{2/3}\rho_{\sigma}^{3/5}$$

E_{Copp}^{UEG} and $E_{C\alpha\alpha}^{UEG}$ are from Stoll, Pavlidou and Preuss [39]. $C_{\alpha\alpha}$, C_{opp} are fit to the correlation energy of the helium atom (C_{opp}), and neon ($C_{\alpha\alpha}$) atoms. $C_{\alpha\alpha}$=0.038 C_{opp}=0.0031. B96 satisfies all four requirements for exchange and correlation functionals [38]. However, no asymptotic scaling condition [40] has been considered. Combined with the new one parameter exchange functional B1 [38], B1B96 performs better than the BB96 combination in a test of thermochemistry on the G2 molecules [35]. 56 atomization energies, 42 ionization potentials, and 8 proton affinities are included in the fit used in constructing the new functional. Electron affinity is omitted from the G2 data set due to the instability of negative ions in LSDA [38].

Depending on what constraints and criteria are used in the construction of a new functional, the functionals can be classified into two categories. One has a semi-empirical parameterization, e.g. LYP, B, G96, and the new Becke functionals. The other contains non-empirical functionals which include only fundamental constants, e.g. P86, PW91.

Usually, the functional contains only exchange or correlation parts (although not pure exchange or correlation). There is another type of functional which includes both exchange and correlation, e.g. Perdew, Burke, and Ernzerhof's 1996 generalized gradient approximation (PBE) [41].

These authors analyzed the problems with PW91 [41] and the derivation is long and depends on a mass of detail. Levy's uniform scaling to the high-density limit is not satisfied. They suggested a new exchange-correlation functional,

$$E_{XC}^{GGA}[\rho_\alpha,\rho_\beta]=\int d^3r\rho\epsilon_x^{unif}(\rho)F_{XC}(r_s,\zeta,s) \qquad 2.56$$

$\zeta=(\rho_\alpha-\rho_\beta)/\rho$, is the relative spin polarization. $F_{XC}(r_s,\zeta,s)$ is an enhancement factor over the local exchange. r_s is the local Seitz radius $\rho=3\pi r_s^3/4$. Without semi-empirical fitting, PBE is expected to predict molecular properties without regard to the elements and to be a new approach to creating functionals.

2.2.3 Hybrid density functional theory

A Hamiltonian is written in the following form with $0\leq\lambda\leq1$ [1].

$$H_\lambda = T + V_{ext}(\lambda) + \lambda V_{ee} \qquad 2.57$$

The V_{ext} operator is equal to V_{ne} for $\lambda=1$. For an intermediate λ value, it is assumed that the external potential V_{ext} is adjusted so that the same density is obtained for both $\lambda=1$ (real system) and $\lambda=0$ (the reference system: a hypothetical system with non-interacting electrons). The general DFT energy expression can be written as

$$E_{DFT}[\rho]=T_s[\rho] + E_{ne}[\rho] + J[\rho] + E_{XC}[\rho] \qquad 2.58$$

By equating E_{DFT} to the exact energy, we can define the exchange-correlation energy E_{XC} in density functional theory. It is the part which remains after subtraction of the non-interacting kinetic energy, and the E_{ne} and J (electron self-interaction) potential energy terms,

$$E_{XC}[\rho] = (T[\rho]-T_s[\rho]) + (E_{ee}[\rho]-J[\rho]) \qquad 2.59$$

E_{XC} contains, buried within it, all the details of two-body exchange and dynamical

correlation and a kinetic-energy component as well [42]. From equation (2.57), (2.58) and (2.59), an exact connection can be made between the exchange-correlation energy and the corresponding potential connecting the non-interacting reference and the actual system. The Adiabatic Connection Formula (ACF) [43] results and involves an integration over the parameter λ which "turns on" the electron-electron interaction.

$$E_{XC} = \int_0^1 \langle \Psi_\lambda | V_{XC}(\lambda) | \Psi_\lambda \rangle d\lambda \qquad 2.60$$

Based on such a connection, Becke [42], in 1993, suggested a functional marrying the exact-exchange Kohn-Sham theory and the local spin-density approximation,

$$E_{XC} \cong \frac{1}{2} E_X + \frac{1}{2} U_{XC}^{LSDA} \qquad 2.61$$

which is referred to as "Becke's Half-and-Half or BHandH" functional. We should note that E_X is not, strictly speaking, the conventional Hartree-Fock exchange energy, since Kohn-Sham and Hartree-Fock orbitals are not the same. From a practical perspective, however, there is little numerical difference. The models that include exact exchange are often called hybrid methods.

Equation 2.61 is an average of the exact-exchange energy at λ=0 (non-interacting model) and the LSDA for the exchange-correlation potential energy at λ=1. Thus, it employs the electron-gas model at full interaction strength only and discards the problematic λ=0 limit of LSDA (for example the left-right correlation in H_2) [44].

However, BHandH is just a crude approximation since the coefficients are given by intuition rather than on sound theoretical grounds. Thus Becke suggested another exact-exchange mixed exchange functional, a three-parameter exchange functional (B3) [44] and studied the role of exact-exchange,

$$E_{XC}=E_{XC}^{LSDA}+a_0(E_X^{exact}-E_X^{LSDA})+a_X\Delta E_X^{B88}+a_C\Delta E_C^{PW91} \qquad 2.62$$

a_0, a_X, a_C are semi-empirical coefficients from a linear least-squares fit to the G1 Data set $a_0=0.20$, $a_X=0.72$, $a_C=0.81$

E_X^{exact} is the exact exchange energy, ΔE_X^{B88} is Becke's 1988 exchange, ΔE_C^{PW91} is the 1991 gradient correction for correlation of Perdew and Wang. The E_{XC}^{LSDA} functions is the leading term. The second term replaces some electron-gas exchange with exact exchange to capture the proper small λ limit of equation 2.59. ΔE_X^{B88} is the gradient correction. E_C^{PW91} is included to account for the flexibility of the functional. It is worth noting that G1 includes the 56 atomization energies, 42 ionization potentials, 8 proton affinities, and the 10 first-row total atomic energies [27, 28]. However, the electron affinities were not considered because the LSDA exchange-correlation potential does not bind negative ions, a well-known failure of the local-spin-density-approximation [44].

In 1996, Becke reviewed the role of exact exchange in Kohn-Sham DFT, and introduced a new one-parameter functional (B1) [38].

Given any local exchange-correlation DFT, the simple correction for the $\lambda=0$ problem [38] is,

$$E_{XC} = E_{XC}^{DFT} + a_0(E_X^{Exact} - E_X^{DFT}) \qquad 2.63$$

Replacing the qualitatively incorrect DFT behavior near $\lambda=0$ (namely, the DFT pure exchange part) with exact $\lambda=0$ behavior (namely, the exact exchange energy of the Kohn-Sham Slater determinant) properly represents the $\lambda=0$ region of the Adiabatic Connection Formula (Equation 2.60). Or in another form,

$$E_{XC}=\frac{1}{2}\iint\frac{\rho(r_1)}{r_{12}}\left[\int_0^1 h^{\lambda}_{XC}(r_1,r_2)d\lambda\right]d^3r_1d^3r_2 \qquad 2.64$$

$$h^{\lambda}_{XC}(r_1,r_2) = \frac{P_2^{\lambda}(r_1,r_2)}{\rho(r_1)} - \rho(r_2) \qquad 2.65$$

The parameter a_0, reflecting a system's "Hartree-Fock character", controls the amount of this replacement, and is determined by fitting to the G2 thermochemical data. In conjunction with BB96, the best value for a_0 is 0.28, and the method is B1B96.

2.2.3 Time-dependent density functional theory

2.2.3.1 Time-dependent Hartree-Fock theory

Solving the time-dependent Schrödinger equation, one can obtain molecular properties that change with time. Dirac [45] and Frenkel [46] derived the time-dependent Hartree-Fock equations, which are also known as the random phase approximation (RPA)[47]. Karplus and Kolker [48] extended the theory to include external perturbation in the uncoupled approximation. McLachlan and Bell [49] extended it to a coupled approximation in 1964. Dalgarno and Victor [50] reformulated the coupled Hartree-Fock approximation for describing the effects of time-dependent perturbations on many-electron systems. This became the working model for later time-dependent Hartree-Fock methods (TD-HF) [51, 52], in which the time-dependent part is treated as a perturbation V(r,t),

$$V(r,t)=\lambda\{\exp(i\omega t) + \exp(-i\omega t)\}\sum_{i=1}^{N} \upsilon_i(r_i) \qquad 2.66$$

Starting from the Hartree-Fock approximation, we solve the perturbed time-dependent equation 2.66 to first order,

$$[F+V-i\hbar\frac{\partial}{\partial t}]\Phi(r,t)=0 \qquad 2.67$$

$$F=\sum_{i=1}^{N} H_i - \sum_{i<k} \sum\int u_i^{(0)}(r_i)[\beta_{ik}-\alpha_{ik}]u_i^{(0)}(r_i)dr_i \qquad 2.68$$

$$\Phi^{(i)}(r,t)=\Psi^{(i)}(r)\exp(-iE_F^{(i)}t/\hbar), \quad \Psi^{(i)}(r_1,r_2,\ldots,r_N)=A\prod_{j=1}^{N}u_j^{(i)}(r_j)$$

H_i is a single-electron HF operator.

and results in,

$$(H_i-\varepsilon_i(0)\pm\hbar\omega)u_{i\pm}^{(1)}(r_i)+[V_{i\pm}^{(1)}(r_i)+v_{i\pm}^{(1)}(r_i)-\langle u_i^{(0)}|V_{i\pm}^{(1)}|u_i^{(0)}\rangle K\hbar\omega\langle u_i^{(0)}|u_{i\pm}^{(1)}\rangle]u_i^{(0)}(r_i)=0 \qquad 2.69$$

the ± comes from the $\exp(\pm i\omega t)$.

With different perturbations V, Equation 2.69 can be applied to different phenomena[49, 51, 52]. However, time-dependent Hartree-Fock approximation neglects correlation effects. Inclusion of such effects in DFT would require the time-dependent analog of the Kohn-Sham stationary equations.

2.2.3.2 Time-dependent density functional theory

Density functional theory was originally developed for stationary systems [16]. However, with the development of the theory, it was successfully applied to time-dependent problems: Atomic [53] and nuclear [54] scattering processes, photoabsorption in atoms [55], and the dynamical response of an inhomogeneous metallic system [56, 57] were considered. Starting with the time-dependent Schrödinger equation, Runge and Gross gave a complete and general formalism for time-dependent density functional theory [58]. A time-dependent version of Thomas-Fermi theory was proposed as early as 1933 by Bloch[59].

The first, and rather successful, steps towards time-dependent Kohn-Sham theory were taken by Peuckert [60] and by Zangwill and Soven [61]. The authors took the linear density response of rare-gas atoms to a time-dependent external potential as the response

of the non-interacting electron to an effective time-dependent potential. By analogy to stationary KS theory, this effective potential was assumed to contain an exchange-correlation part, $v_{xc}(rt)$, in addition to the time-dependent external and Hartree terms:

$$v_{eff}(rt) = v(rt) + \int \rho(r't)/|r-r'| d^3r' + v_{xc}(rt) \qquad 2.70$$

Zangwill and Soven adopted the functional form of the static exchange correlation potential,

$$v_{xc}(rt) = \delta E_{xc}[\rho(r't)]/\delta\rho(rt), \qquad 2.71$$

where $E_{xc}[\rho(r',t)]$ is the exchange-correlation energy functional of ordinary density functional theory. For this functional, Zangwill and Soven employed the local density approximation,

$$E_{xc}[\rho(r't)] = \int \epsilon_{xc}[\rho(r't)]\ \rho(r't)\ d^3r', \qquad 2.72$$

where $\epsilon_{xc}[\rho(r't)]$ is the exchange-correlation energy per particle of a static uniform electron gas of density of ρ. The static approximation is obviously valid only if the time-dependence of $\rho(r,t)$ is sufficiently slow [62].

Runge and Gross [58] provided a novel feature of the formalism for time-dependent density functional theory not present in ground-state density functional theory, the dependence of the respective density functionals on the initial (many-particle) state $\Psi(t_0)$. Also they proved that the exact time-dependent density $\rho(rt)$ of the system can be computed from the single-particle orbitals $\phi(r,t)$,

$$\rho(rt) = \Sigma\phi_j^*(rt)\ \phi_j(rt), \qquad 2.73$$

while the single-particle orbitals $\phi_j(rt)$ satisfy the time-dependent Schrödinger equation,

$$(i\partial/\partial t + \tfrac{1}{2}\nabla^2)\phi_j(rt) = v_{eff}[rt, \rho(rt)]\ \phi_j(rt) \qquad 2.74$$

with an effective one-particle potential given by

$$v_{eff}[r t, \rho(r t)] = v(r t) + \int d^3 r' \rho(r t) w(r r') + \delta A_{XC}/\delta \rho(r t) \qquad 2.75$$

A_{XC} is the "exchange-correlation" part of the action integral,

If the functional $A_{XC}[\rho]$ is known, then the corresponding densities can be calculated from equations 2.73 to 2.75. This provides a quantum mechanical structure in the most natural way [58].

Further, Gross and Kohn [62] gave a one-to-one mapping between time-dependent potentials and time-dependent densities for a given initial many-particle wave function Ψ_0,

$$\Psi_0 = \Psi(t_0) \qquad 2.76$$

So the time-dependent density determines the external potential uniquely within an additive purely time-dependent function. The potential uniquely determines the time-dependent wave functional, which can therefore be considered as a functional of the time-dependent density,

$$\Psi(t) = \Psi[\rho](t), \qquad 2.77$$

where $\Psi[\rho]$ is unique to within a purely time-dependent phase factor. As a consequence, the expectation value of any quantum mechanical operator $\hat{O}(t)$ is a unique function of the density which implicitly depends on the initial state Ψ_0,

$$O(t) = \langle \Psi[\rho](t) | \hat{O}(t) | \Psi[\rho](t) \rangle \equiv O[\rho](t)$$

With the initial condition by Equation 2.77, the solution of the time-dependent Schrödinger equation corresponds to a stationary point of the quantum mechanical action integral,

$$A[\rho] = \int_{t_0}^{t_1} dt \; \langle \Psi[\rho](t) | i \frac{\partial}{\partial t} - \hat{H}(t) | \Psi[\rho](t) \rangle$$

$$= B[\rho] - \int_{t_0}^{t_1} dt \int d^3r\, \rho(rt)v(rt) \qquad 2.78$$

$B[\rho]$ is a universal (Ψ_0 dependent) functional, defined as

$$B[\rho] = \int_{t_0}^{t_1} dt \ \langle \Psi[\rho](t)| i\frac{\partial}{\partial t} - \hat{T} - \hat{U} |\Psi[\rho](t)\rangle \qquad 2.79$$

Starting from the non-interacting electron model and solving the Euler equation

$$\frac{\delta A_s[\rho]}{\delta \rho(rt)} = 0 = \frac{\delta B_s[\rho]}{\delta \rho(rt)} - v(rt) \qquad 2.80$$

$$A_s[\rho] = B_s[\rho] - \int_{t_0}^{t_1} dt \int d^3r\, \rho(rt)v(rt)$$

$$B_s[\rho] = \int_{t_0}^{t_1} dt \ \langle \Psi[\rho](t)| i\frac{\partial}{\partial t} - \hat{T} |\Psi[\rho](t)\rangle \quad (U \equiv 0)$$

where s denotes the non-interacting particle model ($U \equiv 0$), the time-dependent Kohn-Sham scheme can be derived. A single-particle potential $v_s(r,t)$ exists such that the interacting density is identical with the density

$$\rho(rt) = \sum_{n=1}^{N} |\varphi_n(r,t)|^2 \qquad 2.81$$

of the non-interacting system described by the Schrödinger equation

$$i\frac{\partial}{\partial t}\varphi_n(r,t) = (-\nabla^2/2 + v_s(rt))\,\varphi_n(r,t) \qquad 2.82$$

Define $A_{XC}[\rho]$, the "exchange-correlation" part of the action functional, as,

$$A_{XC}[\rho] = B_s[\rho] - \frac{1}{2}\int_{t_0}^{t_1} dt \int d^3r \int d^3r' \frac{\rho(rt)\rho(r't)}{|r-r'|} - B[\rho] \qquad 2.83$$

Employing the variational principle for the interacting system and by comparison, we can obtain the explicit representation for $v_s(rt)$,

$$v_s(rt) = v(rt) + \int d^3r' \frac{\rho(r't)}{|r-r'|} + \frac{\delta A_{XC}[\rho]}{\delta\rho(rt)} \qquad 2.84$$

Equations (2.81), (2.82) and (2.84) constitute the time-dependent KS scheme. Compared with the time-dependent Hartree-Fock method, this scheme has two advantages:

a. The time-dependent effective potential $v_s(rt)$ is local (i.e. a multiplication operator in real space).

b. Correlation effects are included.

When we consider the ground-state responses of the electronic system, most cases fall in the regime of linear response. The initial density $\rho_0(r)$ resulting from the potential $v_0(r)$ can be calculated from the ordinary (ground state) Kohn-Sham scheme. At $t=t_0$ a time-dependent perturbation $v_1(rt)$ is switched on, i.e. the total external potential is given by

$$v(rt) = \begin{cases} v_0(r) & for \quad t<t_0 \\ v_0(r)+v_1(r,t) & for \quad t\geq t_0 \end{cases} \qquad 2.85$$

The linear density response $\rho_1(r,t)$ is conventionally expressed in terms of the full response function χ as

$$\rho_1(rt) = \int d^3r' \int_{t_0}^{\infty} dt' \chi(rt,r't') v_1(r't') \qquad 2.86$$

Since the time-dependent Kohn-Sham equations (2.81), (2.82), (2.84) provide a formally exact way of calculating the time-dependent density, the exact linear density response of the interacting system can alternatively be calculated as the density response of the non-interacting Kohn-Sham system:

$$\rho_1(rt) = \int d^3r' \int_{t_0}^{\infty} dt' \chi_{KS}(rt,r't') v_s^{(1)}(r't') \qquad 2.86$$

$v_s^{(1)}(rt)$ is the time-dependent Kohn-Sham potential (2.84), calculated to first order in the perturbating potential. It can be written in the form

$$v_s^{(1)}(rt) = v_1(rt) + \int d^3r' \frac{\rho_{1(r't)}}{|r-r'|} + \int d^3r' \int dt' f_{xc}(rt,r't')\rho_1(r't') \qquad 2.87$$

f_{xc} denotes the exchange-correlation response kernel which is formally defined as the functional derivative of the time-dependent exchange-correlation potential

$$v_{xc}(rt) = \frac{\delta A_{xc}[\rho]}{\delta \rho(rt)}$$

$$f_{xc}(rt,r't') = \frac{\delta v_{xc}[\rho](rt)}{\delta \rho(r't')} \Big| \rho=\rho_0 \qquad 2.88$$

calculated at the initial ground-state density $\rho_0(r)$.

Equations 2.86 and 2.87 constitute the Kohn-Sham equations for the linear density response. χ_{KS} is relatively easy to calculate [63]. Given some approximation for the exchange-correlation kernel f_{xc}, these equations provide a self-consistent scheme to calculate the density response $\rho_1(rt)$. If an approximate expression for $A_{XC}[\rho]$ satisfies

$$A_{XC}[\rho] = (t_1-t_0)\cdot E_{xc}[\rho] \qquad 2.89$$

for all ground-state densities $\rho(r)$ and is local in time, then it has the form

$$\int_{t_0}^{t_1} dt \; E_{xc}[\rho] \Big| \rho=\rho(rt). \qquad 2.90$$

In practical applications, the action functional $A_{XC}[\rho(rt)]$ is approximated by E_{XC} – the exchange-correlation functional of time-independent Kohn-Sham theory and $\rho(rt)$ is a function of space at fixed time t . This local approximation in time is usually referred to as the adiabatic approximation and works best for low-lying excited states of valence type when used in conjunction with standard functionals [64].

TD-DFT has been shown to be very useful in the prediction of the excitation energies of molecular system [65,66,67], it includes substantial double excitation character and is a

significant improvement over HF-based theories such as TD-HF and single excitation configure interaction (CIS) [68].

2.3 Computational Details

2.3.1 Programs and facilities

All calculations are carried out with the Gaussian quantum chemistry package versions G94 and G98 (A.5 and A.7) [69]. Spartan Plus and Spartan Pro were used to produce initial geometries [70]. For visualizing the resultant geometries and vibrational modes, Molekel [71] and Molden [72] were employed.

The calculations in Chapter 3 were run mainly on a Silicon Graphics (SGI) Octane (R10000 processor with 256MB memory and 4 GB hard drive) under IRIX 6.4 and on an Indigo2 (R4000 processor with 96MB memory and 5GB hard drive) under the IRIX 5.3 operating system. These workstations are in our quantum chemical research laboratory. Some of the larger calculations such as $C_{26}H_{12}O$ were performed on the computer from the former Numerically Intensive Computing (NIC) facility at the University of Guelph. This SGI server has 8 R4400 processors with 512MB memory and a 6 GB hard drive. This facility was moved to the Department of Chemistry and Biochemistry at the University of Guelph and renamed the Guelph Research Intensive Numerical Computing Hub (GRINCH) and brought up with the IRIX 6.5 system.

Most of the calculations in Chapter 4 were performed on the SGI Origin 2000 server of 4 R12000 processors with 4GB memory and a 100GB hard drive at the University of Waterloo. Gaussian A.7 was implemented on this server under the IRIX 6.5 operating system. Some calculations in Chapter 4 were run on the Octane workstation or an Intel

Pentium II 300 MHz computer with 128MB memory and 9 GB hard drive under Linux in our research laboratory. The Linux operating systems installed were Red Hat 5.2 (for Gaussian A.5) and then Mandrake 6.0 (for Gaussian A.7), Gaussian A.7 was compiled with the Portland Group Fortran compiler version 3.1 (Version 1.7 for Gaussian A.5) on this computer.

Most of the calculations for Chapter 5 were run on the Origin 2000 server at the University of Waterloo and the Pentium II computer under Linux. Some calculations of Chapter 6 were performed on another SGI Indigo 2 workstation with an R10000 processor with 384 MB memory and a 4GB hard drive running IRIX 6.5 in our research laboratory.

2.3.2 Methods, basis set, geometry optimizations, and vibrational frequencies

The Hartree-Fock [73] method was employed as a starting point in all calculations. The density functional methods were then used for more reliable calculations. The density functionals methods employed were BHandHLYP [42], B3HLYP [33, 34, 44], B1LYP [38], BLYP [25] and mPW1PW91[74]. The IOP options in Gaussian allow the user to use self-defined hybrid density functional methods [75], and this technique was used in Chapter 5 for the studies of the density functionals. For open shell species, unrestricted density functional methods were used. For comparison, MP2 [7] was employed when computer resources allowed. In some situations requiring a more accurate energy determination, the coupled cluster methods including triple contributions (CCSD-T) [10, 76] were used. Basis sets used included 6-31G* [77], 6-311G** [78], 6-311++G** [78, 79], and 6-311++G(3df,3pd) [78,79]. Dunning's cc-pV5Z [80] (for Ne, cc-pV5Z has been modified)

has been also used in Chapter 5. The application of post-HF methods and density functional methods ensured that electron correlation is included in the calculation to improve the results.

Geometry optimizations were carried out in internal or Cartesian coordinates with analytic energy gradient methods and the algorithms of Schlegel [81] for both the conventional *ab initio* and density functional methods. For all optimized geometries, harmonic vibrational frequency analyses with second-order analytic energy gradient were performed to determine if the stationary points were minima or saddle points on the potential energy surfaces. A minimum has no imaginary vibrational frequencies, while saddle points have at least one imaginary vibrational frequency (for a transition state one, a second order saddle point (SOSP) has two imaginary vibrational frequencies). The minimum is a minimum in energy in all directions on the potential energy surfaces. A transition state is a maximum along one coordinate and a minimum on along the remaining coordinates on potential energy surface going through the point. A transition state connects two stationary points (usually but not necessary minima) of lower energy on the potential energy surfaces. A second order saddle point is a maximum on two potential curves that are orthogonal to each other, and is a minimum on all other potential curves. When any questions arise about the minima connected to a specific transition state, the intrinsic reaction coordinate (IRC) [82] calculation was performed at the same level as the frequency calculation. This calculation starts at the transition state and follows the vector of the imaginary vibrational mode down towards the relevant stationary points.

2.3.3 Potential energy surface

It is almost impossible with quantum chemical methods to explore completely the potential energy surface of a system with more than three nuclei. Such calculations are computationally prohibitive. The total number of acceptable points which should be calculated on the potential surface is on the order of $(3n-6)^{10}$ (or $(3n-5)^{10}$ for linear system). The portion of the surfaces of greatest interest is the potential energy curve along a particular direction in which a reaction takes place. For a vibrational frequency calculation, the zero-point vibrational energies (ZPVE) were included in any energy prediction. No scaling factor has been used for this ZPVE correction. The use of scaling factor arises from a systematic error of a quantum chemical method in vibrational frequency prediction in comparison experiment. For some single point energy calculations with larger basis sets, the ZPVE correction from a smaller basis set calculation with the same quantum chemical method has been used.

On a potential curve, minimum and saddle points with up to two imaginary vibration frequencies have been examined for the reaction of a triplet oxygen atom with the fragments of C_{60}, the reaction of the triplet oxygen atom with benzene, and the isomerizations of benzene oxides.

2.4 References

1. F. Jensen, *Introduction to Computational Chemistry*, John Wiley & Sons, Chichester (1999)
2. N. C. Handy and A. M. Lee, Chem. Phys. Lett., **252**, 425 (1996)
3. a) P. -O, Löwdin, Adv. Chem. Phys., **2**, 207 (1959); b) A. Szabo and N. S. Ostlund, *Modern Quantum Chemistry*, McGraw-Hill, 1982; c) R. J. Bartlett and J. F. Stanton, Rev. Comput. Chem., **5**, 65 (1994); d) K. Raghavachari and J. B. Anderson, J. Phys. Chem., **100**, 12960 (1996)
4. a) D. K. W. Mok, R. Neumann and N. C. Handy, J. Phys. Chem., **100**, 6225 (1996); b) O. Sinanoğlu, Adv. Chem. Phys., **6**, 358 (1964)
5. B. O. Roos, Adv. Chem. Phys., **69**, 339 (1987)
6. B. O. Roos, K. Andersson, M. P. Fülscher, P. –Å. Malmqvist, L. Serrano-Andres, K. Pierloot and Merchan, Adv. Chem. Phys., **93**, 219 (1996)
7. C. Møller and M. S. Plesset, Phys. Rev., **46**, 618 (1934)
8. I. Shavitt, *Modern Theoretical Chemistry*, H. F. Schaefer, Ed., Plenum Press, New York, Vol. **3**, 189 (1977)
9. J. A. Pople, M. Head-Gordon, K. Raghavachari, J. Chem. Phys., **87**, 5968 (1987)
10. Z. He, E. Kraka, D. Cremer, Int. J. Quantum Chem., **57**, 157 (1996); J. Cizek, J. Chem. Phys., **45**, 4256 (1966); Adv. Chem. Phys., **14**, 35 (1969)
11. G. E. Scuseria and H. F. Schaefer III, J. Chem. Phys., **90**, 3700 (1989)
12. T. J. Lee, A. P. Rendall and P. R. Taylor, J. Phys. Chem., **94**, 5463 (1990)
13. P. –O, Löwdin, Rev. Mod. Phys., **32**, 328 (1960)
14. B. O. Roos, in *Ab Initio Methods in Quantum Chemistry II*, K. P. Lawley Ed., John

Wiley & Sons Ltd., New York (1987) 399

15. K. Andersson, and B. O. Roos, in *Modern Electronic Structure Theory* (Advanced Series in Physical Chemistry, 12), D. R. Yarkony Ed., World Scientific Publishing Co. Pte. Ltd., Singapore (1995) 55

16. a) P. Hohenberg, and W. Kohn, Phys. Rev. B, **136,** 864 (1964); b) W. Kohn, and L. Sham, Phys. Rev. A, **140,** 1133 (1965); c) S. H. Vosko, L. Wilk, and M. Nusair, Can. J. Phys., **58,** 1200 (1980)

17. a) L. H. Thomas, Proc. Cambridge Philos. Soc., **23**, 542 (1927); b) E. Fermi, Z. Phys., **48**, 73 (1928)

18. J. C. Slater, Phys. Rev., **81**, 385 (1951)

19. W. Kohn, A. D. Becke, and R. G. Parr, J. Phys. Chem., **100**, 12974 (1996)

20. A. D. Becke, In *Modern Electronic structure Theory*, D. R. Yarkony Ed., World Scientifc Publisher Co. Pte. Ltd., Singapore, 1995

21. J. C. Slater, Quantum Theory of Molecular and Solids. 4: *The Self-Consistent filed for Molecular and Solids*, McGraw-Hill, New York, 1974

22. B. Delley, J. Chem. Phys., **94**, 7245 (1991); J. Andzelm, E. Wimmer, J. Chem. Phys. **96**, 1280 (1992)

23. B. G. Johnson, P. M. W. Gill, J. A. Pople, J. Chem. Phys., **98**, 5612 (1993)

24. J. P. Perdew and Y. Wang, Phys. Rev. **B, 33**, 8800 (1986)

25. A. D. Becke, Phys. Rev. **A, 38**, 3098 (1988)

26. A. D. Becke, J. Chem. Phys., **84**, 4524 (1986)

27. J. A. Pople, M. Head-Gordon, D. J. Fox, K. Raghavachari, and L. A. Curtiss, J. Chem. Phys., **90**, 5622 (1989)

28. L. A. Curtiss, C. Jones, G. W. Trucks, K. Raghavachari, and, J. A. Pople, J. Chem. Phys., **93**, 2537 (1990)

29. A. D. Becke, J. Chem. Phys., **96**, 2155 (1992)

30. J. P. Perdew, and Y. Wang, Phys. Rev. **B**, **45**, 13244 (1992)

31. J. P. Perdew, J. A. Chevary, S. H. Vosko, K. A. Jackson, M. R. Pederson, D. J. Singh, and C. Fiolhais, Phys. Rev. **B**, **46**, 6671 (1992)

32. P. M. W. Gill, Mol. Phys., **89**, 433 (1996)

33. C. Lee, W. Yang, and R. G. Parr, Phys. Rev. **B**, **37**, 785 (1988)

34. B. Miehlich, A. Savin, H. Stoll, and H. Preuss, Chem. Phys. Lett., **157**, 200 (1989)

35. L. A. Curtiss, K. Raghavachari, G. W. Trucks, and J. A. Pople, J. Chem. Phys., **94**, 7221 (1991)

36. J. P. Perdew, Phys. Rev. **B**, **33**, 8822 (1986)

37. R. Colle and D. Salvetti, Theor. Chim. Acta, **37**, 329 (1975)

38. A. D. Becke, J. Chem. Phys., **104**, 1040 (1996)

39. H. Stoll, C. M. Pavlidou, and H. Preuss, Theor. Chim. Acta, **49**, 143, (1978); H. Stoll, E. Golka, and H. Preuss, Theor. Chim. Acta, **55**, 29 (1980)

40. M. Levy, and J. P. Perdew, Int. J. Quantum Chem., **49**, 539 (1994)

41. J. P. Perdew, K. Burke, and M. Ernzerhof, Phys. Rev. Lett., **77**, 3865 (1996); **78**, 1396 (1997)

42. A. D. Becke, J. Chem. Phys., **98**, 1372 (1993)

43. J. Harris, Phys. Rev. **A**, **29**, 1648 (1984)

44. A. D. Becke, J. Chem. Phys., **98**, 5648 (1993)

45. P. A. M. Dirac, Proc. Camb. Phil. Soc., **26**, 376 (1930)

46. J. Frenkel, *Wave Mechanics, Advanced General Theory*, Clarendon Press, Oxford, 1934

47. P. Noziéres, and D. Pines, Nouvo Cimento, **9**, 470 (1958); D. J. Thouless, Nucl. Phys., **21**, 225 (1960); **22**, 78 (1961)

48. M. Karplus, and H. J. Kolker, J. Chem. Phys., **39**, 2987 (1963)

49. A. D. McLachlan, and M. A. Bell, Rev. Mod. Phys., **36**, 844 (1964)

50. A. Dalgarno, and G. A. Victor, Proc. Roy. Soc. London A, **291**, 291 (1966)

51. H. Sekino and J. Bartlett, J. Chem. Phys., **85**, 976 (1986)

52. S. P. Karna, and M. Dupuis, J. Comput. Chem., **12**,487 (1991)

53. M. Horbatsch, and R. M. Dreizler, Z. Phys., A **300**,119 (1982); **308**, 329 (1982)

54. G. Holzwarth, Phys. Lett., **66B**, 29 (1977)

55. P. Malzacher, and R. M. Dreizler, Z. Phys. **A**, **307**, 211 (1982)

56. S. C. Ying, Nuovo Cimento **B**, **23**, 270 (1974)

57. G. Mukhopadhyay, and S. Lundqvist, Nuovo Cimento **B**, **27**, 1 (1975)

58. E. Runge, and E. K. U. Gross, Phys. Rev. Lett., **52**, 997 (1984)

59. F. Bloch, Z. Phys., **81**, 363 (1933)

60. V. Peuckert, J. Phys. C, **11**, 4945 (1978)

61. A. Zangwill, and P. Soven, Phys. Rev. **A**, **21**, 1561 (1980)

62. E. K. U. Gross, and W. Kohn, in: *Advances in Quantum Chemistry*, **21**, 255 (1990)

63. A. Zangwill, and P. Soven, Phys. Rev. **A 21**, 1561 (1980); N. Iwamoto, and E. K. U. Gross, Phys. Rev. **B**, **35**, 3003 (1987)

64. R. E. Stratmann, G. E. Scuseria, and M. J. Frisch, J. Chem. Phys., **109**, 8218 (1998)

65. R. Bauernschmitt, and R. Ahlrichs, Chem. Phys. Lett., **256**, 454 (1996)

66. M. E. Casida, C. Jamorski, K. C. Casida, and D. R. Salahub, J. Chem. Phys., **108**, 4439 (1998)

67. M. J. Allen, and D. J. Tozer, J. Chem. Phys., **113**, 5185 (2000)

68. S. Hirata, M. Head-Gordon, Chem. Phys. Lett., **302**, 375 (1999)

69. a) Gaussian 94, (Revision B.1), M. J. Frisch, G. W. Trucks, H. B. Schlegel, P. M. W. Gill, B. G. Johnson, M. A. Robb, J. R. Cheeseman, T. Keith, G. A. Petersson, J. A. Montgomery, K. Raghavachari, M. A. Al-Laham, V. G. Zakrzewski, J. V. Ortiz, J. B. Foresman, J. Cioslowski, B. B. Stefanov, A. Nanayakkara, M. Challacombe, C. Y. Peng, P. Y. Ayala, W. Chen, M. W. Wong, J. L. Andres, E. S. Replogle, R. Gomperts, R. L. Martin, D. J. Fox, J. S. Binkley, D. J. Defrees, J. Baker, J. P. Stewart, M. Head-Gordon, C. Gonzalez, and J. A. Pople, Gaussian, Inc., Pittsburgh PA, 1995. b). Gaussian 98 (Revision A.5), M. J. Frisch, G. W. Trucks, H. B. Schlegel, G. E. Scuseria, M. A. Robb, J. R. Cheeseman, V. G. Zakrzewski, J. A. Montgomery, R. E. Stratmann, J. C. Burant, S. Dapprich, J. M. Millam, A. D. Daniels, K. N. Kudin, M. C. Strain, O. Farkas, J. Tomasi, V. Barone, M. Cossi, R. Cammi, B. Mennucci, C. Pomelli, C. Adamo, S. Clifford, J. Ochterski, G. A. Petersson, P. Y. Ayala, Q. Cui, K. Morokuma, D. K. Malick, A. D. Rabuck, K. Raghavachari, J. B. Foresman, J. Cioslowski, J. V. Ortiz, B. B. Stefanov, G. Liu, A. Liashenko, P. Piskorz, I. Komaromi, R. Gomperts, R. L. Martin, D. J. Fox, T. Keith, M. A. Al-Laham, C. Y. Peng, A. Nanayakkara, C. Gonzalez, M. Challacombe, P. M. W. Gill, B. G. Johnson, W. Chen, M. W. Wong, J. L. Andres, M. Head-Gordon, E. S. Replogle and J. A. Pople, Gaussian, Inc., Pittsburgh PA, 1998. c) Gaussian 98,

(Revision A.7), M. J. Frisch, G. W. Trucks, H. B. Schlegel, G. E. Scuseria, M. A. Robb, J. R. Cheeseman, V. G. Zakrzewski, J. A. Montgomery, Jr., R. E. Stratmann, J. C. Burant, S. Dapprich, J. M. Millam, A. D. Daniels, K. N. Kudin, M. C. Strain, O. Farkas, J. Tomasi, V. Barone, M. Cossi, R. Cammi, B. Mennucci, C. Pomelli, C. Adamo, S. Clifford, J. Ochterski, G. A. Petersson, P. Y. Ayala, Q. Cui, K. Morokuma, D. K. Malick, A. D. Rabuck, K. Raghavachari, J. B. Foresman, J. Cioslowski, J. V. Ortiz, A. G. Baboul, B. B. Stefanov, G. Liu, A. Liashenko, P. Piskorz, I. Komaromi, R. Gomperts, R. L. Martin, D. J. Fox, T. Keith, M. A. Al-Laham, C. Y. Peng, A. Nanayakkara, C. Gonzalez, M. Challacombe, P. M. W. Gill, B. Johnson, W. Chen, M. W. Wong, J. L. Andres, C. Gonzalez, M. Head-Gordon, E. S. Replogle, and J. A. Pople, Gaussian, Inc., Pittsburgh PA, 1998

70. Spartan Plus and Spartan Pro, Wavefunction, Inc., Irvine, CA

71. Molekel on UNIX, Peter F. Flükiger, and Stefan Portmann, Switzerland

72. G.Schaftenaar and J.H. Noordik, "Molden: a pre- and post-processing program for molecular and electronic structures", J. Comput.-Aided Mol. Design, **14** (2000) 123-134

73. a) D. R. Hartree, Proc. Cambridge Phil. Soc., **24**, 89, 111, 246 (1928). b) V. Z. Fock, Physik, **61**, 126 (1930). c) C.C. J. Roothann, Rev. Mod. Phys., **23**, 69 (1951)

74. C. Adamo, and V. Barone, Chem. Phys. Lett. **274**, 242 (1997)

75. Æ. Frisch, and M. J. Frisch, Gaussian 98 User's Reference, Gaussian Inc., Pittsburgh, 1998

76. J. A. Pople, M. Head-Gordon, and K. Raghavachari, J. Chem. Phys., **87**, 5968 (1987)

77. a) R. Ditchfield, W. J. Hehre, and J. A. Pople, J. Chem. Phys., **54**, 724 (1971). b) W. J. Hehre, R. Ditchfeld, and J. A. Pople, J. Chem. Phys., **56**, 2257 (1972). c) P.C. Hariharan, and J. A. Pople, Theor. Chim. Acta, **28**, 213 (1973). d) M. S. Gordon, Chem. Phys. Lett., **76**, 163 (1980)

78. a) A. D. McLean, and G. S. Chandler, J. Chem. Phys., **72**, 5639 (1980). b) R. Krishnan, J. S. Binkley, R. Seeger, and J. A. Pople, J. Chem. Phys., **73**, 650 (1980).

79. a) T. Clark, J. Chandrasekhar, G. W. Spitznagel, and P. v. R. Schleyer, J. Comp. Chem., **4**, 294 (1983). b) M. J. Frisch, J. A. Pople, and J. S. Binkley, J. Chem. Phys., **80**, 3265 (1984)

80. R. A. Kendall, T. H. Dunning, and R. J. Harrison, J. Chem. Phys., **96**, 6796 (1992); D. E. Woon, and T. H. Dunning, J. Chem. Phys., **98**, 1358 (1993); K. A. Peterson, D. E. Woon and T. H. Dunning Jr., J. Chem. Phys. **100**, 7410 (1994), PNNL at http://www.emsl.pnl.gov:2080/forms/basisform.html

81. H. B. Schlegel, J. Comp. Chem., **3**, 214 (1982)

82. C. Gonzalez, H. B. Schlegel, J. Phys. Chem., **90**, 2154 (1989)

Chapter 3

Critical Evaluation of Density Functional Methods: Theoretical Characterization of Fragments of C_{60}: Bonding, Reactivity and Aromaticity

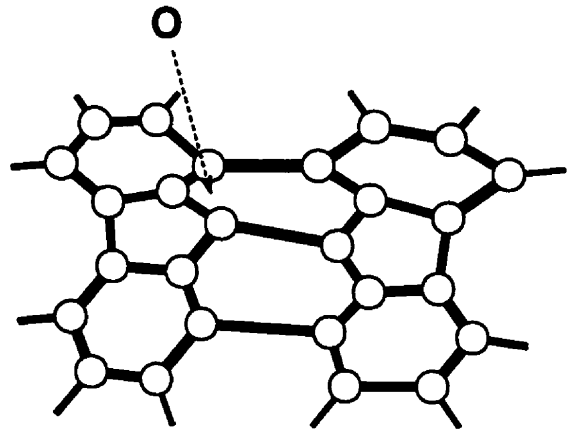

3.1 Introduction

The isolation of C_{60} in large quantities [1,2] in the last several years triggered the investigation of its reactions. The C_{60} molecule has 12 pentagons, each of which is surrounded by 5 hexagons. It has 30 6-6 bonds (at the junctions between two six-membered rings) and 60 6-5 bonds (at the junction between a six- and a five-membered ring). X-ray crystal structure determinations of transition-metal derivatives of C_{60} indicate significant bond alternation in this fullerene [3,4]. The 6-6 bond has significantly higher double-bond character (as evidenced by the bond length of 1.38 to 1.40Å) than the 6-5 bond (bond length ~ 1.45Å). Theoretical calculations of the electronic structure of C_{60} [5,6] predicted an energetically low-lying, threefold-degenerate lowest unoccupied molecular orbital (LUMO), which should readily accept up to six electrons in electrochemical reductions or, in chemical conversions, should be occupied by the electrons transferred from the lone pair of an attacking nucleophile [5]. The reactivity of C_{60} appears to be that of a strained, electron-deficient poly-alkene with rather localized double bonds [7,8]. It forms adducts readily with radicals, various nucleophiles, and carbenes, participates as the electron-deficient dienophilic component in a variety of thermal cycloaddition reactions, and undergoes photochemical cycloadditions [9]. In addition to the many conversions in which C_{60} acts as an electrophile, C_{60} can be oxidized with dimethyldioxirane in toluene [10] or photochemically by dioxygen in benzene [11] to give $C_{60}O$ with an oxirane ring fused at a 6-6 bond.

However, the conjugation of the π electrons in C_{60} could make C_{60} a three-dimensional aromatic compound. The aromaticity of C_{60} is considered to be a balance between the diamagnetic contribution from the six membered rings and a paramagnetic

contribution from the five membered rings. Hydrogens located above the five membered rings in fullerene derivatives are shifted downfield while the hydrogens above the six membered rings are shifted upfield [12]. This balance of diamagnetic and paramagnetic behavior produces the unusual reactivity of fullerenes. Schleyer *et al* [12] confirmed the expected "antiaromatic-aromatic" nature of C_{60} [13]. In C_{60}, paramagnetic currents flow within the pentagons and weaker diamagnetic currents flow all round the C_{60} molecule, and the overall effects of the diamagnetic and paramagnetic contributions result in the "antiaromatic-aromatic" nature of C_{60} [13].

The reactions of atomic oxygen O (^{3}P) with alkenes play important roles in combustion and in atmospheric chemistry. Detailed information on the elementary chemical steps is essential for a thorough understanding of the overall reactions of such complex systems. The reaction of the O (^{3}P) atom with ethylene acts as a prototypal system for the addition of oxygen atom across a carbon-carbon double bond, which is important in a wide variety of areas ranging from atmospheric chemistry to the metabolic activation of potentially carcinogenic hydrocarbons [14]. There are extensive studies on the reaction of oxygen with ethylene both experimentally [15-20] and theoretically [21-27]. The oxidation of C_{60} also has attracted extensive attention from chemists [10,11,28-37]. The structure and properties of the monoxide $C_{60}O$ [38,39,40] and higher oxides $C_{60}O_2$, $C_{60}O_3$ have been studied theoretically [41]. However, the details of the oxidation mechanism are not clear and no systematic theoretical study on the reactivity of the central double bond with O(^{3}P) in systems ranging from ethylene to C_{60} has been performed. The daunting size of the fullerenes or even of the fragments of these cages prohibits the use of the very most sophisticated *ab initio* treatments. The computationally efficient density functional

theory (DFT) has become a popular method to study larger molecules. It has the advantage that it includes electron correlation, which is often important to describe correctly molecular properties.

There are many sites in C_{60} at which reaction with an oxygen atom could take place and both monoadducts and higher adducts can be obtained under different reaction conditions. As there are two different bonds in C_{60}, two possibilities exist for the reaction of oxygen with C_{60}: at the 6-5 bond or at the 6-6 bond. Depending on whether the C-C bond breaks or not, there are four possible structures for the CCO ring: the 6-6 closed ring (epoxide), 6-6 open ring, 6-5 closed ring and 6-5 open ring. Although relatively low level *ab initio* and DFT calculations (Hartree-Fock and Local Spin Density Approximation) showed that the 6-5 open structure is more stable than the 6-6 closed isomer, inclusion of a gradient correction in the exchange correlation functional switches the stability of these two isomers [38]. The calculated electronic spectra of these two isomers confirmed that the 6-6 closed structure is the ground state [40]. Experiments showed that the 6-5 open structure is a kinetic intermediate which can rearrange into the thermodynamically more stable 6-6 closed isomer [4,8,42,43,44,45].

Intrigued by the reaction of $O(^3P)$ with C_{60} but recognizing the computational difficulty inherent in treating a system of this size, we sought a simpler model of C_{60} to investigate the addition of $O(^3P)$ to double bonds. Polycyclic aromatic hydrocarbons (PAHs) may serve as suitable candidates and are smaller and thus easier examined computationally. Like fullerene, the PAHs consist of five- and six-membered rings, and the five-membered rings surrounded by six-membered rings provide some curvature to the overall molecular structure [46]. NMR experiments indicated that the carbon-13 NMR

in PAHs (142.0 and 145.4ppm) is very close to that in fullerene (143ppm in C_{60}) [46]. Also there is a similarity in that the bowl-shaped PAHs and fullerenes represent compromises between strain from the curvature and stabilization due to conjugation of the π electrons. Potentially the PAHs can serve as good models for fullerene structure and reactivity. It will be interesting to observe the progression from smaller to larger fragments of the C_{60} fullerene to determine if the chemical and molecular properties of the selected PAHs become fullerene-like. In addition, accessibility to both the concave and convex faces once curvature occurs may allow for both endo and exo complexation of reagents. Further, both fullerenes and curved PAHs show a compromise between strain and conjugation and there will be of interest in the study of aromaticity. The PAHs may play a role as a bridge between planar aromatic compounds and ball-shaped fullerenes [46].

Among PAHs, $C_{26}H_{12}$ is the smallest bowl-shaped fragment that contains a central double bond in an environment that clearly at first glance resembles that in C_{60}. This double bond might be expected to display fullerene-like chemistry toward a variety of reagents [47]. Reactions such as alkylations *via* nucleophilic attack, osmylation, cycloaddition with pyrollidine, and dibromocarbene that occur with C_{60} were successfully carried out on $C_{26}H_{12}$. However, considering cyclopropanation and Diels-Alder reactions, the central double bond of $C_{26}H_{12}$ is not as reactive as the bond in C_{60} and it was suggested that this bond may be more electron rich [48]. AM1 calculations on the Diels-Alder cycloaddition of 1,3-butadiene to $C_{26}H_{12}$ indicated that it retains most of the characteristic reactivity of C_{60} as seen in the analysis of the reaction energetics [49]. Thus we chose $C_{26}H_{12}$ as a model for C_{60}. In order to study how the reactivity and properties change with the size of the fragment, we investigated the reactivity and properties of

$C_{10}H_8$ (naphthalene), $C_{14}H_8$ (pyracylene) and $C_{18}H_{10}$ as well. For comparison, we included ethylene and benzene in our study.

Aromaticity and antiaromaticity are fundamental but complex concepts in chemistry [50]. Aromatic systems are cyclic systems having a large resonance energy in which all the atoms in the ring take part in a single conjugated system. There are various criteria for aromaticity emphasizing [51] energetic, structures, and magnetic properties. Schleyer *et al.* [12] established a relationship between aromaticity and nucleus-independent chemical shifts, NICSs, for a wide-ranging set of aromatic and antiaromatic five-membered heterocyclic rings. NICSs correlate with the up-field chemical shifts of protons located inside aromatic rings and are local. NICSs have been shown to be a reliable criterion of aromaticity and to show a good correlation with structural variations [12]. We employ NICSs as measures of aromaticity in our present study.

3.2 Theoretical Methods and Computational Details

Ab initio and density functional predictions were made with the Gaussian 94 [52] or Gaussian 98 [53] packages. Although the Hartree-Fock (HF) method does not include electron correlation, it often provides a reasonable starting point for higher level theoretical investigation. It is well known that the Hartree-Fock method overestimates the activation energy for reactions, while Generalized Gradient Approximation (GGA) density functional methods frequently underestimate this quantity [54]. We sought a compromise through the use of hybrid density functional methods. We could avoid the shortcomings of HF and GGA with respect to the over- or under-estimation of the reaction barrier through the hybrid methods. We retain the strengths of DFT: low

computational cost and reliable performance in geometry prediction. Another strength of DFT is the relatively small spin contamination for open shell systems. Starting with the Hartree-Fock optimized structures for any stationary point, B3LYP [55], Becke's three parameter hybrid exchange functional [56] along with Lee, Yang, and Parr's gradient corrected correlation functional [57], was employed. The B3 functional earlier was shown to yield generally excellent performance in thermodynamic calculations [56] and structural characterizations [58]. However, for the reaction of an oxygen atom with the double bond of ethylene [26], B3LYP gives an average error in the classical barrier height [59] (-4.7±2.6kcal/mol in which the error is ±2.6kcal) larger than the reaction barrier (~2 kcal/mol).

Another hybrid density functional BHandHLYP [55] (Becke's half and half exchange functional [60] along with the LYP [57] correlation functional), which has only a -0.8±2.7 kcal/mol average error for the same classical barrier height [59], reproduces the reaction barrier and locates the transition state in the low barrier reaction. Previous studies have shown that BHandHLYP can be a good tool for reaction characterization [59,61,62].

For the NICS calculations, the Hartree-Fock method was used since no systematic improvements were observed with DFT in earlier calculations of NMR properties [55]. The NICS, the negative of the absolute magnetic shielding, was calculated by the GIAO-SCF/6-31G* approach at the various ring centers determined as the non-weighted mean of the heavy atom coordinates of the ring. Negative NICS denotes aromaticity (e.g. -11.5 for benzene), and positive NICSs denote antiaromaticity (e.g. 28.8 for cyclobutadiene). A nonaromatic ring has a very small value for this quantity (e.g. -2.2 for cyclohexane) [12]. The NICS is less dependent than other criteria [12] on the ring size and can be employed to

assess the aromaticity of individual rings in polycyclic systems.

For comparison, MP2 [63] was employed to determine the NICS for benzene, naphthalene and for the products of the reactions of benzene with the oxygen atom. Based on a compromise between the desired accuracy of the calculations and the size of and thus computational effort for the molecule, Pople's 6-31G* split valence plus polarization basis set was used throughout this portion of the study. The discussion of energetics below includes zero point vibrational energy (ZPVE) corrections unless specified otherwise.

It was decided not to employ the gradient corrected exchange functional, Becke's 1988 exchange functional (B or B88), since this generalized gradient approximation (GGA) has been observed to underestimate activation energies in earlier studies [54].

3.3 Theoretical Results

3.3.1 C_2H_4

3.3.1.1 Initial barrier to reaction

The reaction of oxygen $O(^3P)$ with ethylene has been studied extensively [15-27]. It has been assumed that the $O(^3P)$ atom, when allowed to react with olefins, first adds to one of the olefinic carbons (one end of the double bond) to form a triplet diradical [20,64]. The triplet diradical undergoes intersystem crossing due to Spin-Orbit Coupling (SOC) involving the oxygen atom [27] to reach the singlet state. On this singlet surface an epoxide structure forms with spin inversion and the loss of excess energy takes place very rapidly. This mechanism agrees with experiment [24,64]. There may exist another possible pathway for the formation of the epoxide. For example, the oxygen may attack the double

bond directly followed by a rapid intersystem crossing to the electronic ground state of the epoxide structure. The diradical mechanism is the main channel for the reaction of oxygen O(^{3}P) with the double bond in the systems of interest, as illustrated at the top of Figure 3-1.

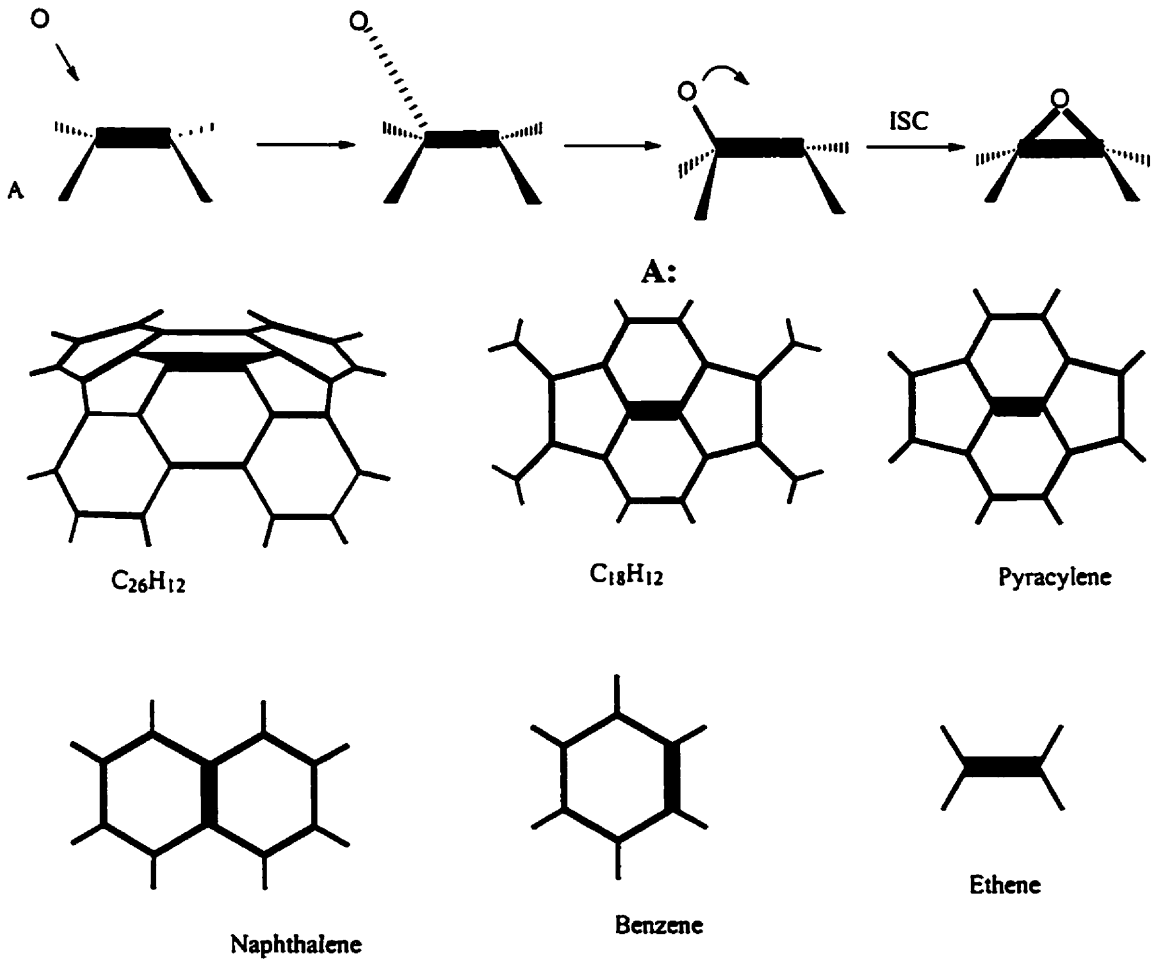

Figure 3-1 Illustration of the reaction of the triplet oxygen atom with the central CC bond (▬) of selected hydrocarbons

Reaction of the oxygen atom, $O(^3P)$, with ethylene is studied with the HF, BHandHLYP, B3LYP and MP2 methods. When the triplet oxygen $O(^3P)$ approaches one of the carbon atoms in ethylene, it faces a reaction barrier to the formation of a triplet diradical. The transition state and the diradical for this reaction are shown in Figures 3-1 and 3-2.

Previous MCSCF studies predicted that the transition state for the addition of $O(^3P)$ to ethylene has C_s rather than C_{2v} symmetry [23,26]. With UMP and APUMP (approximate projected Møller-Plesset) calculations, a C_s symmetric transition state was indicated [24]. In that study [24], the authors pointed out that the influence of spin contamination on geometry is not so serious in the case of these triplet species. However spin contamination greatly effects the predicted barrier heights. With HF, BHandHLYP and MP2, we have located both symmetric (C_s), **1a** in Figure 3-2, and asymmetric (C_1), **1b** in Figure 3-2, transition states. The structures of the two transition states are almost identical in energy as shown in Table 3-1 and Figure 3-2. No transition state could be located with B3LYP. The C_s and C_1 transition states are essentially identical in structure especially for BHandHLYP and MP2, for example the two dihedral angels D_{OCCH} (the same DOOCH as shown in structure **3-2**) are 87.2725 and –87.2742 at MP2 level. The largest and only significant difference from HF is the OC bond length (0.002Å). The bond angles show very small differences of only 0.1° in the two transition states at this level.

In the transition state for the reaction of $O(^3P)$ with ethylene, the ethylene fragment essentially retains its geometry as in the separated species. The CC bond has a slightly longer distance than the typical double bond and the ethylene skeleton remains roughly

planar. From the OCC angle, 106.4° in the HF structure and 99.5° to 99.7° in the BHandHLYP and MP2 structures, we note that oxygen attacks the carbon atom from above along a nearly orthogonal path. The reaction barrier of the transition state relative to reactants is 1.2±0.7 kcal/mol from experiment [26b]. At the HF level, this barrier is 11.8

Table 3-1 The Energy (kcal/mol) difference between the reactants ($O(^3P)$ + C_2H_4) and product C_2H_4O and the $<S^2>$ of the triplet transition states and diradicals

	Transition State	Diradical		Epoxide
		C_s*	C_l	
HF	11.8	-7.8	-7.2	-27.7
BHandHLYP	1.0	-25.4	-25.6	-71.0
B3LYP	-[a]	-30.4	-30.6	-82.7
MP2	12.9	-18.9	-19.1	-82.6

$<S^2>$ of the triplet transition states and diradicals

	Transition State	Diradical	
		C_s	C_l
HF	2.275	2.022	2.023
BHandHLYP	2.076	2.010	2.011
B3LYP	-[a]	2.007	2.008
MP2	2.250	2.022	2.024

a. Transition state could not be located with B3LYP; * transition state

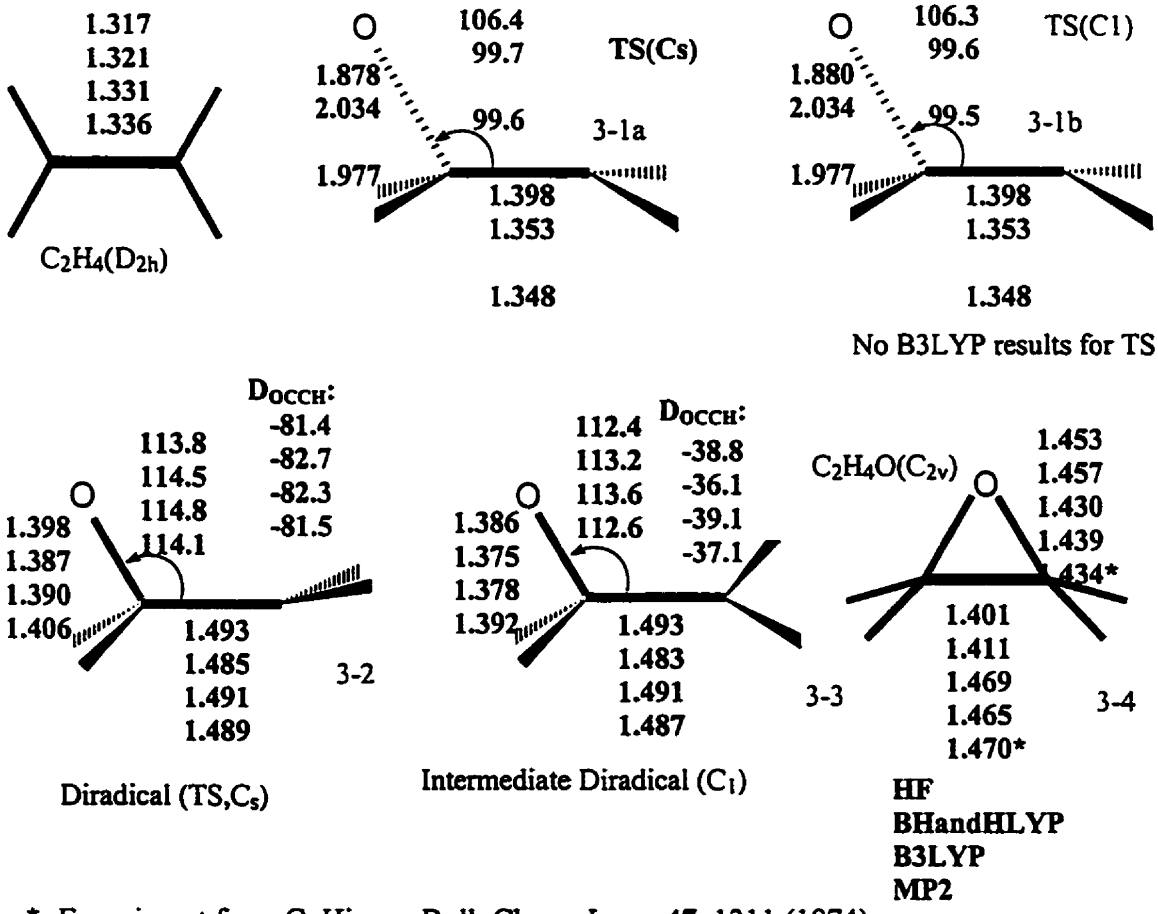

*: Experiment from C. Hirose, Bull. Chem. Japan 47, 1311 (1974)

Figure 3-2 Structures of ethylene, of the transition states, of the intermediate diradicals, and of the singlet epoxide product (bond lengths and bond angles)

kcal/mol. This quantity becomes 12.9 kcal/mol at the UMP2 level. This barrier at the BHandHLYP level (1.0 (actually 1.04) kcal/mol for C_s symmetry and 1.1(actually 1.06) kcal/mol for C_1 symmetry) is in much better agreement with experiment. The similarity in the energies and structures of the C_s, **3-1a**, and C_1, **3-1b**, transition states indicate that a symmetry constraint of C_s does not play an important role in the structure of this transition state. Retaining the symmetry plane, we located a C_s diradical transition state, **3-2** in Figure 3-2, that lies between two equivalent asymmetric C_1 diradical intermediates **3-3**. In this transition state, the imaginary vibrational mode involves the rotation of the end methylene group about the C-C bond. The C-O distance is approximately 1.4 Å and the C-C bond 1.5 Å in length in the transition state with all four theoretical methods. The two hydrogens on the methylene group which is not attacked lie slightly above the C-C bond as indicated by the OCCH dihedral angle in Figure 3-2. A spin density analysis shows that the two unpaired electrons are mainly at the two ends of the open structure, i.e. on the oxygen atom and on the methylene carbon in the diradical. The interaction of the σ-σ orbitals (we use the same notation as in reference [23]) causes the end methylene to rotate about the C-C bond and drives the distortion from C_s symmetry during the bonding of the oxygen to the carbon atom.

3.3.1.2 Intersystem Crossing

Distortion along the imaginary vibrational mode of the C_s diradical results in a C_1 diradical intermediate, **3-3**. The dihedral angle of the methylene group with the hydrogens above the CC bond to the OCC plane is about 40° compared to 80° in the C_s structure. The C-C bond distance lengthens (from 1.331 Å in ethylene to 1.491 Å in the

C_1 diradical intermediate with B3LYP) and allows free rotation of the terminal methylene group. The OCC angle is almost unchanged as the oxygen approaches ethylene. Comparing the structures of the C_1 and C_s diradicals, only the dihedral angle changes significantly during the rotation of the methylene group.

Keeping the other structural parameters fixed and varying only the OCC angle in the C_s diradical intermediate, we predicted using B3LYP the energies of closely spaced points along this ring closure coordinate for both the singlet and triplet states. The OCC angle is expected to be the most important coordinate in the OCC ring closure process. At an OCC angle of about 100.8°, we located a crossing point of the singlet and triplet potential energy curves. Spin-orbit coupling most probably takes place [27] in this region as shown schematically in Figure 3-3. In the ring closure, the methylene group experiences a rotation with a low barrier [23] to meet the oxygen atom. The final product ethylene epoxide (or oxirane), **3-4** in Figure 3-2, is a three-membered ring with C_{2v} symmetry. At different levels of theory, the CC and CO bond distances differ somewhat. At the HF and BHandHLYP levels, the CC bond is shorter than the CO bond by about 0.05Å and both the CC and CO are single bonds. B3LYP predicts the CC bond (1.469Å) to be longer than the CO bond (1.430Å). MP2 shows the same trend as B3LYP, but with a slightly shorter CC bond (1.465Å) and slightly longer CO bond (1.439Å). The experimental value for CC bond is 1.470 Å and CO bond is 1.434 Å as shown in Figure 3-2.

However, for the diradicals, there are two extremes for the relative orientation of the methylene group: one has the terminal methylene group orthogonal to the OCC plane, the other has this group in the OCC plane. Both structures have C_s symmetry. The in-plane

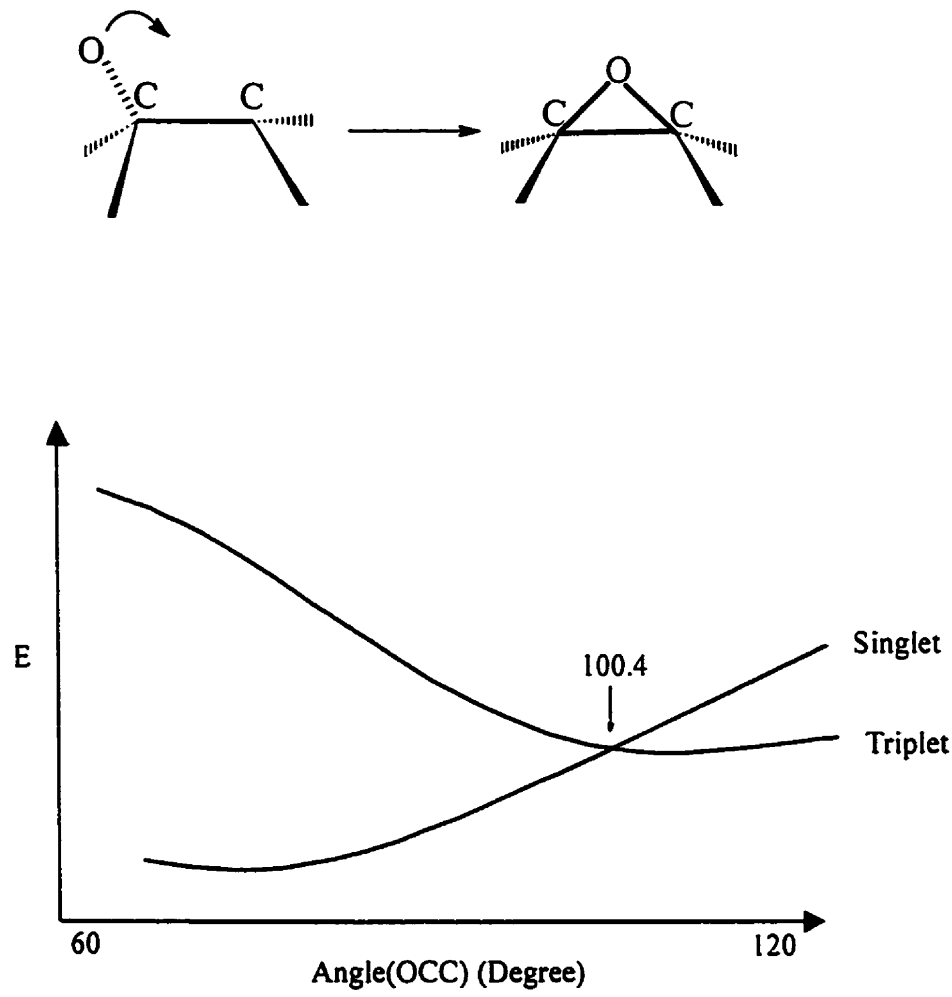

Figure 3-3 A schematic illustration of the intersystem crossing of the singlet and triplet states during the ring closure to form the epoxide

structure is the transition state described above. The orthogonal structure is a second order saddle point with two imaginary vibrational modes at the HF level. The smaller imaginary vibrational frequency (i103cm^{-1} a") involves an out-of-plane (the C_s symmetry plane) motion of the hydrogens on the methylene group which was not attacked.

The second imaginary frequency at the HF level (i1324cm^{-1}) involves a rocking of the two methylene groups about the C-C bond axis to destroy the symmetry plane. The two imaginary vibrational modes are displayed in Scheme 3-1. At the BHandHLYP, B3LYP and MP2 levels, this structure becomes a transition state between two distorted diradical intermediates with C_1 symmetry. The imaginary frequency from the BHandHLYP method is obviously much larger than that of the B3LYP and MP2 approaches, while the later two methods predict very similar frequencies.

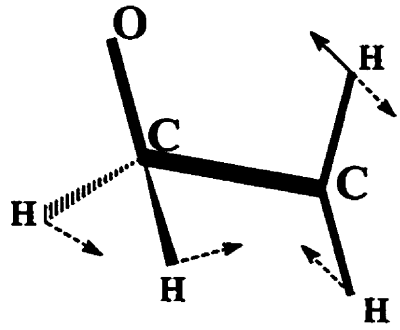

Dashed arrow: vibration modes for 1130cm^{-1}i
Solid arrow: vibration modes for 103cm^{-1}i

Scheme 3-1. Illustration for the imaginary vibration frequencies of the C_s (orthogonal) diradical predicted by HF/6-31G*

3.3.1.3 Overall reaction of triplet oxygen with ethylene

The overall reaction of oxygen (^3P) with ethylene to yield the triplet diradical is predicted to be exothermic at all four levels of theory. For the energetics, including ZPVE correction, all four methods show the same trend for the relative energies of these species. The energy differences are reported in Table 3-1. The HF energy difference is smaller than the other three methods. MP2 and HF predict similar, much higher reaction barriers than experiment for the approach of oxygen to ethylene. This might be due to spin contamination from an electronic state of higher multiplicity [24]. We note that the expectation value of S^2 with the HF and MP2 methods for the transition state is much larger than in the diradicals as shown in Table 3-1. Also the expectation value for S^2 in HF and MP2 for all triplet species are much larger than those from BHandHLYP and B3LYP which indicates the highly spin contamination of HF and MP2 on open shell species. In the following studies, only the results of the BHandHLYP calculations for spin density are shown in each figure and discussed. Only BHandHLYP (although B3LYP has been tried) could be used to locate all the transition states for all systems studied.

3.3.2 Benzene, C_6H_6

The reaction of oxygen atoms with benzene plays an important role in atmospheric chemistry, in combustion processes, and in photochemical air pollution. Also benzene serves as a realistic model for the reaction of an oxygen atom with other aromatic molecules. However, there has not been any extensive theoretical investigation of this reaction. Here, we investigate one possible pathway for the addition of an oxygen atom to one C-C bond in the benzene ring. Other possible modes of reaction of oxygen with

benzene are shown in Scheme 3-2 [65]. When an oxygen atom approaches the benzene ring (here we consider approach to a C-C bond), there are at least four possible paths for the reaction of the atom with the ring. First, the oxygen atom approaches the center of the ring and forms a complex. Second, in the plane of the benzene ring, the oxygen atom can approach the C-C bond experiencing an interaction with the two hydrogens connected to the two nearest carbons. Depending on the relative positions of the two hydrogen atoms, there are two paths. One has the two hydrogens in the plane of the benzene ring, while in the other the two hydrogens are on different sides of the oxygen and slightly out of the plane. Third, from above the benzene ring, an oxygen atom can add to one carbon atom of the C-C bond. A fourth approach has the oxygen atom add to the center of the C-C bond from directly above. Only the third case will be discussed in this chapter.

In the case of attack by oxygen on one carbon atom, a diradical with C_s symmetry forms before the OCC ring closure take place resulting in the formation of an epoxide with C_s symmetry. With all four methods, a transition state **3-6** (see Figure 3-4) was located between the separated reactants and this diradical intermediate. At the HF level, the oxygen atom attacks one carbon atom with a CO distance of 1.801Å in the transition state. Due to the attack of the oxygen, the benzene ring distorts to C_s symmetry. There are small alterations in the various CC bond lengths. At the HF level, all CC bonds lengthen compared with the reactant benzene. The CC bonds connecting the carbon atom which is attacked become conjugated single bonds, while the other four bonds keep typical aromatic bond lengths of 1.387 Å (or 1.409 Å at the HF level). The CO distance in this transition state lengthens to 1.859Å with BHandHLYP, 1.910Å with B3LYP and 1.879Å at the MP2 level. The CC bonds shorten to typical aromatic bond lengths

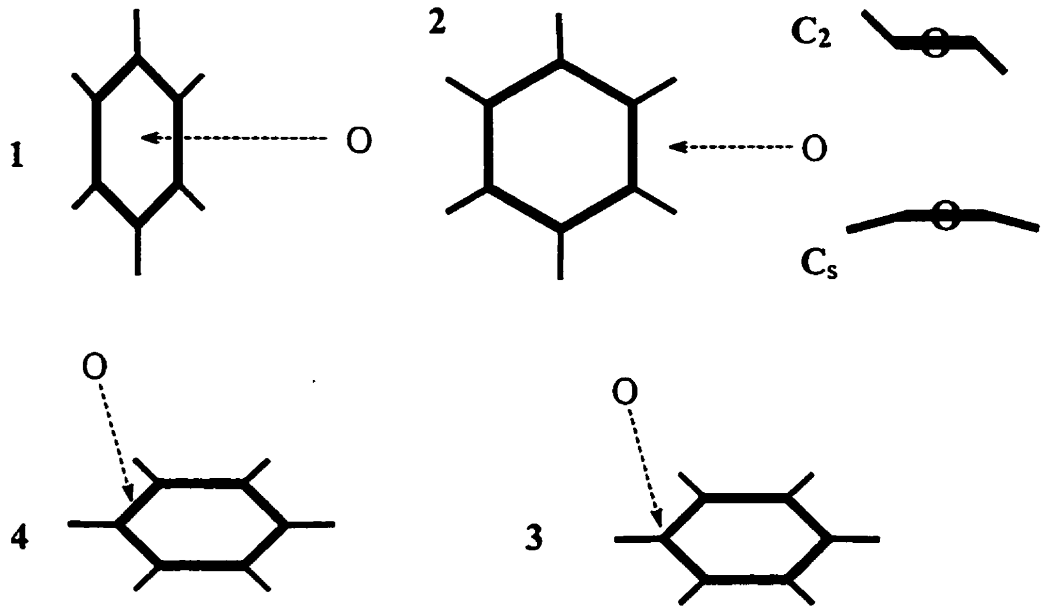

Scheme 3-2. Possible modes of reaction of oxygen with benzene

although the differences among the CC bond distances remain similar to changes observed with HF on the transition state. There is serious spin contamination in this transition state at the HF and MP2 levels. The expectation values of S^2 are 2.6891 and 2.6326 for HF and MP2 respectively. Spin contamination increases the barriers due to the mixture of higher energy electronic states of higher spin multiplicity. In relative terms, BHandHLYP and B3LYP have much smaller spin contamination (2.1257 for S^2 with BHandHLYP and 2.0354 with B3LYP) as reported in Table 3-2. The two unpaired electrons are located principally on the oxygen atom (due to the severe spin contamination with HF and MP2, only the spin densities from the BHandHLYP and the B3LYP method are discussed here). 1.56 of the unpaired spin density at the BHandHLYP level and 1.76 at the B3LYP level is located on the oxygen atom. The interaction of oxygen with the benzene ring allows a partial transfer of the unpaired electrons from oxygen to the benzene ring. The activation energy is higher than in the case of oxygen plus ethylene presumably due to the greater difficulty in disrupting the electronic structure of the aromatic molecule. This barrier is 13.5 kcal/mol at the HF level, and it decreases to 7.9 kcal/mol at the BHandHLYP level. It is interesting that the barrier height for the transition state at the B3LYP level is zero although a transition state was located by the geometry optimization and verified by the vibrational frequency analysis with this method. The reactants face no energetic barrier to the formation of the diradical intermediate at this level. The imaginary vibrational mode ($i454cm^{-1}$) at the B3LYP level involves mainly a back-and-forward motion of the oxygen atom and the carbon atom undergoing attack. Such a mode obviously connects the separated reactants and the diradical intermediate. The reaction barrier increases to 18.1 kcal/mol at the MP2 level

Table 3-2 The energy difference (kcal/mol) between the reactants ($O(^3P)$ + C_6H_6) and the C_6H_6O products, epoxide and oxepin, the transition structure between them, and the $<S^2>$ of the triplet transition states and diradicals

	C_6H_6O				
	Transition State 3-6	Diradical Triplet 3-7	Epoxide 3-8	Oxepin 3-10	Transition State 3-9
HF	13.5	3.7	4.4	1.0	17.3
BHandHLYP	7.9	-6.7	-38.7	-40.0	-31.1
B3LYP	0.0	-11.2	-51.8	-53.1	-46.7
MP2	35.4	18.1	-51.1	-48.3	-45.7
	$<S^2>$ of the triplet transition states and triplet diradicals				
HF	2.689	2.480			
BHandHLYP	2.126	2.101			
B3LYP	2.035	2.033			
MP2	2.633	2.409			

with its large spin contamination as shown in Table 3-2.

In the diradical intermediate, **3-7**, the oxygen atom forms a single bond to one carbon. This CO bond is about 1.4Å at the HF, BHandHLYP and B3LYP levels, but lengthens by 0.02Å at the MP2 level (see Figure 3-4). During the approach of oxygen to the carbon, the OCC angle changes very little as indicated by the structures of transition state **3-6** and intermediate **3-7** in Figure 3-4. While the bonding of the oxygen with the carbon atom causes the spin density to redistribute among the atoms, one electron remains mainly on the oxygen atom and the other on the benzene ring. As shown in Table 3-2, both at the HF and MP2 levels, the formation of the triplet diradical relative to triplet oxygen atom and singlet benzene is endothermic (3.7 kcal/mol and 18.1 kcal/mol at HF and MP2 respectively). However strong spin contamination makes these energetic predictions unreliable. The reaction to form the triplet diradical is exothermic at the BHandHLYP and B3LYP levels (6.7 kcal/mol and 11.2 kcal/mol) as reported in Table 3-2. The addition of an oxygen atom destroys the π electron ring current around the benzene ring which is viewed as stabilizing this aromatic molecule. Thus it is expected that the formation of the diradical would not be strongly exothermic due to this reduction of aromatic character upon reaction.

If subjected to a small perturbation, the oxygen atom will swing to one of the neighboring carbon atoms and bond to it without breaking the C-C bond. This involves an intersystem crossing from the triplet to the singlet electronic state. Since the hydrogen atoms attached to the two carbon atoms bonding to the oxygen are on the same side, this epoxide structure has C_s symmetry. The structure appears to be "diene like" rather than an aromatic compound when the CC bond lengths are examined. The CC bond in the

epoxide ring and the two other CC bonds connecting to the carbon in the three membered ring are single bonds judging from their bond lengths. The CC bond opposite to the epoxide ring is a conjugated single bond as well (1.464Å at the HF and 1.444Å at the MP2 levels, Figure 3-4). The remaining two equivalent carbon-carbon bonds have lengths typical of a double bond (1.329Å at the HF and 1.360Å at the MP2 level). At the HF level the formation of the singlet epoxide product relative to reactants is predicted to be endothermic (4.4 kcal/mol). The other three methods, all of which include electron correlation, predict the formation of the epoxide from triplet oxygen atom and singlet benzene to be strongly exothermic (38.7kcal/mol at BHandHLYP, 51.8 kcal/mol at B3LYP and 51.1 kcal/mol at MP2)(See Table 3-2).

Due to the strain in the three membered epoxide ring, the CC bond in the epoxide is easily broken to form an oxepin, a seven-membered heterocyclic ring, **3-9**. Hückel's 4n+2 rule for an eight π-electron system and thus an anti-aromatic ring rationalizes the distortion in the geometry from planar to non-planar. The oxygen atom lies out of the plane of the carbon atoms, and the oxepin has a relatively flat but boat like shape. From the bond lengths, oxepin appears structurally to be a triene. The nonplanarity of the oxepin does not change greatly compared with the epoxide structure [66]. The CC distance of the two carbon atoms bonding to the oxygen lengthens from about 1.5Å in the epoxide ring to about 2.3Å in the oxepin isomer. Obviously the carbons are bonded in the epoxide and this bond is broken in the oxepin. There exists a transition state which connects the CC bonded epoxide and the CC open oxepin structure, in which the distance between the two carbon atoms connected by oxygen lies between the distances in the epoxide and the

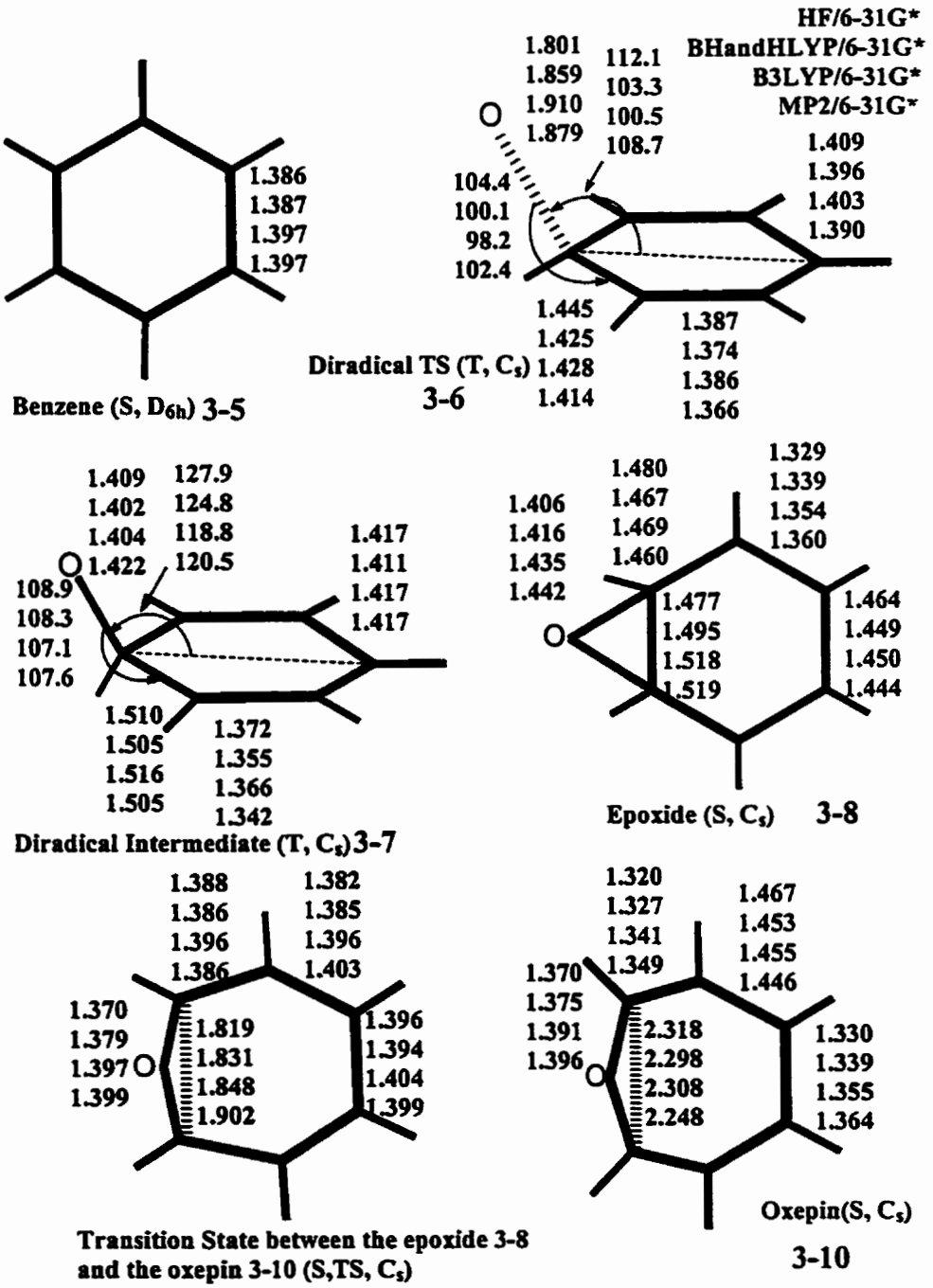

Figure 3-4 Structures of benzene and benzene oxides

oxepin (ranging from 1.819Å at the HF level to 1.902Å at the MP2 level as shown in Figure 3-4). The reaction barrier relative to the epoxide structure is 12.9 kcal/mol at the HF level, 7.6 kcal/mol at the BHandHLYP level, 5.1 kcal/mol at B3LYP and 5.4 kcal/mol at the MP2 level. At the HF, BHandHLYP, and B3LYP levels, the oxepin is slightly more stable than the epoxide (3.4 kcal/mol at HF, 1.3 kcal/mol at BHandHLYP and 1.3kcal/mol at B3LYP). The order switches at the MP2 level (the oxepin is 1.8 kcal/mol higher in energy than the epoxide). For oxepin, inversion to the equivalent nonplanar isomer through a planar structure is a relatively easy process energetically. The inversion barrier of the oxepin is only 3.0 kcal/mol at HF, 3.3 kcal/mol at BHandHLYP, 3.4 kcal/mol at B3LYP and 6.1 kcal/mol at MP2. There are no large changes in the bond distances in the planar transition state compared with the oxepin. The imaginary vibrational mode involves mainly bending of the oxygen atom out of plane in the planar transition state. All these structures are shown in Figure 3-4.

3.3.3 Naphthalene, $C_{10}H_8$

3.3.3.1 Previous Studies

The first PAH which contains a central 6-6 bond which could be attacked by an oxygen atom is naphthalene. Sondheimer *et al.* [67] synthesized naphthalene oxide and characterized it by UV, IR and NMR spectroscopy. Experimentally [68] the carbon-carbon bond lengths are nearly equal indicating electron delocalization in the most stable ring structure [67]. Bock *et al.* [69] studied different possible oxides of naphthalene with the AM1 and HF/6-31G methods. They found that at both the AM1 and HF/6-31G levels, the localized C_s symmetric 1,6-oxido-[10]annulene in which the central CC bond is broken is most stable, the delocalized C_{2v} symmetric structure with the central CC bond broken is

slightly higher in energy than the localized C_s symmetric one (by 0.6 kcal/mol), while the epoxide structure is the most unstable, and is higher in energy than the delocalized form by 7.9 kcal/mol(see the structures in Figure 3-5). There are extensive investigations on the methano-bridged analogues both experimentally [70] and theoretically [71,72,73,74]. Experimentally, the isomer with the open central CC bond i.e. the delocalized species is favored over the closed tricyclic epoxide by 5.7±2 kcal/mol, although the tricyclic epoxide is known to be an intermediate [70]. Earlier lower level calculations [71,73,74] favor the open central CC bond localized species over the delocalized open structure and the epoxide. With the inclusion of electron correlation, MP2 calculations [72] indicated that the delocalized open central bond species is more stable than the localized open central bond structure by 1.5 kcal/mol. In addition, it is more stable than the epoxide (norcaradienic isomer) by 15.6 kcal/mol. These authors [72] used the optimized structures from HF for the MP2 single point energy calculations. However, at low temperature, the 11,11-dicyano derivative is known to exist in the tricyclic norcaradiene form in the solid state as determined by x-ray crystallographic analysis [50b]. This derivative also adopts a tricyclic structure in solution at low temperature [50b]. However no theoretical work has been undertaken on the reaction of oxygen atom, $O(^3P)$, with naphthalene.

3.3.3.2 Results and discussion

We report in this study results for the reaction of an oxygen atom with the central CC bond in naphthalene. From the results on the reaction of ethylene and benzene with an oxygen atom using the HF, BHandHLYP, B3LYP and MP2 methods, we recall that there exists serious spin contamination for the triplet species with the HF and MP2 approaches.

This contamination adversely effects the energetics of these species. Also we note that the MP2 results for the molecular structures and energetics are generally similar to those from B3LYP. However, the MP2 calculations require much more disk space and CPU time. The disk space requirement can become a critical limiting factor for calculations on these large molecules. Thus we have used BHandHLYP and/or B3LYP to calculate the properties of $C_{18}H_{12}$, $C_{26}H_{12}$ and related species but not MP2. The HF method is employed only for closed shell stationary point calculations hereafter.

The oxygen atom approaches one carbon atom of the central CC bond within the symmetry plane containing the central CC bond and overcomes a barrier of 14.3 kcal/mol (BHandHLYP) to reach a triplet diradical intermediate (**3**). This barrier decreases to 5.3 kcal/mol at the B3LYP level. The relative energy differences of the structures are listed in Table 3-3. The distance from the oxygen to the carbon atom under attack is 1.755Å at the BHandHLYP level and 1.776Å at the B3LYP level in the transition state (**3-12**)(See Figure 3-4). In this transition state, the oxygen attacks the carbon atom in a similar direction as it does with benzene relative to the molecular plane. The angle of the oxygen to the central CC bond is about 103° at BHandHLYP and 106° at B3LYP. The central CC bond distance undergoes a relatively large change in the transition state compared with to this distance in naphthalene. This central CC bond lengthens to 1.459Å at BHandHLYP and 1.467Å at B3LYP in the transition state. The CC bonds closest to the oxygen are about 0.04Å longer than those in the parent molecule, naphthalene. The CC bonds farther away from the oxygen are nearly unchanged in length during the initial reaction with the oxygen atom.

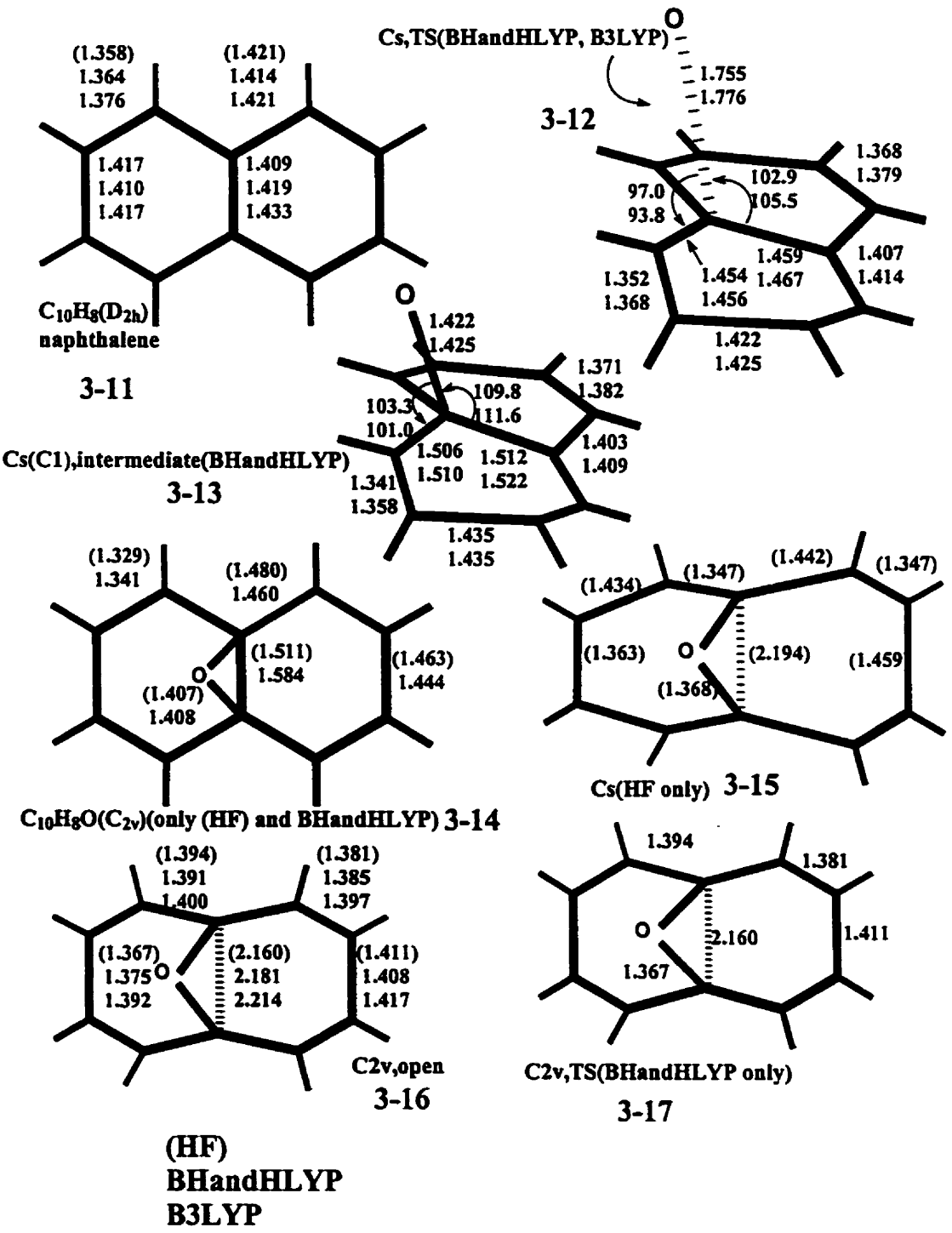

Figure 3-5 Structure of naphthalene and naphthalene oxides

The diradical of C_s symmetry is a transition state for which the imaginary frequency involves the bending of the oxygen out of the symmetry plane at the BHandHLYP level. Distortion along the vibrational mode for the imaginary frequency results in an asymmetric diradical intermediate. The structure of the asymmetric diradical does not change much compared with the symmetric diradical except for the loss of the C_s symmetry plane. The total energy of the asymmetric diradical is only 0.3kcal/mol above the symmetric diradical at the BHandHLYP level. This symmetry related problem will be discussed further in the next chapter [65].

At the HF level, there are three isomers for the oxide in which the oxygen attacks the central CC bond. One is the epoxide structure (norcaradienic isomer **3-14**). The two central carbon atoms in this epoxide structure form a CC bond (1.511Å). Stretching of this CC bond leads to a C_{2v} bicyclic structure with a central CC distance of 2.160Å which is obviously a non-bonded distance and thus an open structure results. The C_{2v} bicyclic structure, **3-16**, in Figure 3-5, is delocalized judging from the CC bond lengths. The longest CC distance is 1.411Å and the shortest is 1.381Å. However, from the vibrational analysis, this C_{2v} bicyclic structure is a transition state structure between two localized bicyclic structures with C_s symmetry at the HF level. The C_s bicyclic localized structure, **3-15** in Figure 3-5, has a longer central CC distance (2.194Å) than does the C_{2v} structure. The CC bond length on one side of the C_s structure resembles hexadiene while on the other side it resembles a hexatriene considering the CC bond lengths. The CO bond distances in the C_{2v} and C_s structures are almost identical. Energetically, the C_s structure is favored over the epoxide structure by a small amount, about 3.5 kcal/mol. However, both the bicyclic

Table 3-3 The energy difference (kcal/mol) between the reactants ($O(^3P)$ + $C_{10}H_8$) and the product $C_{10}H_8O$. The $<S^2>$ for the triplet transition states and triplet diradicals

	$C_{10}H_8O$			
	3-12 Triplet Transition State	3-13 Triplet Diradical	3-14 or 3-16 C_{2v} Product	3-15 C_s Product
HF	-[a]	-[a]	25.4	21.9
BHandHLYP	14.3	7.1	*	-
B3LYP	5.3	-1.1	-44.3	-
$<S^2>$ of the triplet transition states and triplet diradicals				
BHandHLYP	2.185	2.180		
B3LYP	2.039	2.033		

a: Not located; *: The value for the epoxide C_{2v} is –18.1 kcal/mol, for open CC C_{2v} –27.7 kcal/mol, and the value for the transition state between these two C_{2v} isomers is -18.4 kcal/mol

structures are lower in energy than the epoxide by approximately 3.5 kcal/mol. The inversion of the two C_s structures should be very fast at room temperature since the barrier associated with the C_{2v} transition state is very close to zero (0.1 kcal/mol). Even at the HF level, we note that the C_{2v} bicyclic delocalized structure (**3-16**) is favored over the C_{2v} tricyclic epoxide isomer (**3-14**) in energy even though the C_{2v} bicyclic delocalized structure is a transition state. With BHandHLYP, the C_s bicyclic stationary point disappears and the C_{2v} delocalized bicyclic structure becomes a minimum. The C_{2v} bicyclic delocalized structure is lower in energy than the epoxide (the tricyclic structure) by 9.6 kcal/mol. It is very interesting that the transition state between the epoxide structure (norcaradienic isomer) and the C_{2v} bicyclic structure is lower in energy than the epoxide by 0.3 kcal/mol at the BHandHLYP level. Such an energy difference (0.3kcal/mol) is beyond the accuracy of existing methods (even BHandHLYP in reaction barrier prediction). The explanation for the lower energy transition state is that the epoxide isomer faces no barrier to breaking the central CC bond and isomerizing to the C_{2v} minimum. This is in agreement with the experimental findings that the epoxide is an intermediate [70]. Decreasing the percentage of exact exchange in the functional on going from BHandHLYP to B3LYP, only the C_{2v} bicyclic delocalized structure is predicted to be a minimum even starting from the closed epoxide structure. All the bonds involving heavy atoms lengthen at the B3LYP level as shown in Figure 3-5. At the HF and BHandHLYP levels, the C_{2v} bicyclic delocalized structures are lower in energy than the epoxide isomer. In this case, we note that with a different mixture of exact exchange [56,60], the hybrid density functional methods predict different structures, i.e. there is a significant role for exact exchange in predicting the molecular structure in this example.

3.3.4 Pyracylene, $C_{14}H_8$

Pyracylene (**3-18**) could be viewed as the smallest fragment of C_{60} that contains both five- and six-membered rings with a central double bond. However, it is a planar molecule. The surrounding rings make the central CC bond appear superficially like that in C_{60}. However, the central CC bond length has a typical CC double bond distance rather than an aromatic CC bond length even at the B3LYP level (See Figure 3-6). The CC bonds in the six-membered ring do not alternate between single and double. Except for the CC bonds parallel to the central CC bond which are nearly single bonds judged from their lengths, the remaining CC bonds in the six-membered ring are double bonds (the central CC bond) or typical aromatic CC bonds. In the five-membered rings, there are two essentially single CC bonds of length 1.49Å. Any superficial similarity of this molecule to C_{60} decreases with the closer observation of these distances.

When an oxygen atom approaches one carbon of the CC central bond in pyracylene, our earlier results would suggest that it should face an energy barrier. However, only a second order saddle point was located by BHandHLYP with the 6-31G* basis set in which the CO distance is 1.830Å. The larger imaginary vibrational frequency (i576 cm^{-1}, a') involves a backward and forwards motion of the oxygen atom relative to the carbon atom being attacked. The second imaginary vibration (i365 cm^{-1}, a") mode involves a motion of the oxygen out of the symmetry plane. At the B3LYP/6-31G* level, these two imaginary vibrational frequencies change order although the geometry does not vary much. Starting from the distorted geometry along the second imaginary vibration mode from the BHandHLYP results, a triplet diradical, **3-21**, was located with UB3LYP in which the oxygen atom was attached to one carbon atom connected to the carbon atom

which originally attacked. The vibrational frequency calculation showed that it is a minimum. There may exist several different mechanisms for the reaction of an oxygen atom (^3P) with pyracylene judging from the B3LYP results. However, the details of the reaction mechanisms of oxygen with CC bonds other than the central CC bond were not considered in the present study. Distortion along the out-of-plane mode results in a distorted transition state both at the B3LYP and BHandHLYP levels. The imaginary vibrational mode involves the back and forward motion of the oxygen and the carbon atom being attacked. The structure of the distorted transition state is generally similar to the C_s second-order saddle point except for the lack of a C_s symmetry plane. At the BHandHLYP/6-31G* level, a triplet diradical intermediate in which the oxygen attacks one carbon atom of the central CC bond was located. The attack of oxygen causes the CC bonds connected to the carbon atom under attack to lengthen at the BHandHLYP level as shown in Figure 3-6. The structure **3-21** is more stable than the reactants and the C_s diradical. It is 28.7 kcal/mol more stable than the reactants, triplet oxygen atom plus pyracylene, while the C_s diradical lies only 0.8 kcal/mol above reactants. The structure of the naphthalene fragment in the pyracylene oxide resembles the fragment in the naphthalene oxide. The pyracylene epoxide, **3-22**, has C_{2v} symmetry and the epoxide structure leads to a bowl-shape for this molecule. At the HF level, the formation of the epoxide structure is endothermic (16.1 kcal/mol above the reactants), but it is exothermic at both the BHandHLYP (27.9 kcal/mol below reactants) and the B3LYP levels (42.1 kcal/mol lower than reactants). The relative energies of the structures and $<S^2>$ of the open shell species are reported in Table 3-4. Compared with the benzene or naphthalene analogues, the CC bond length of the epoxide structure in $C_{14}H_8O$ decreases.

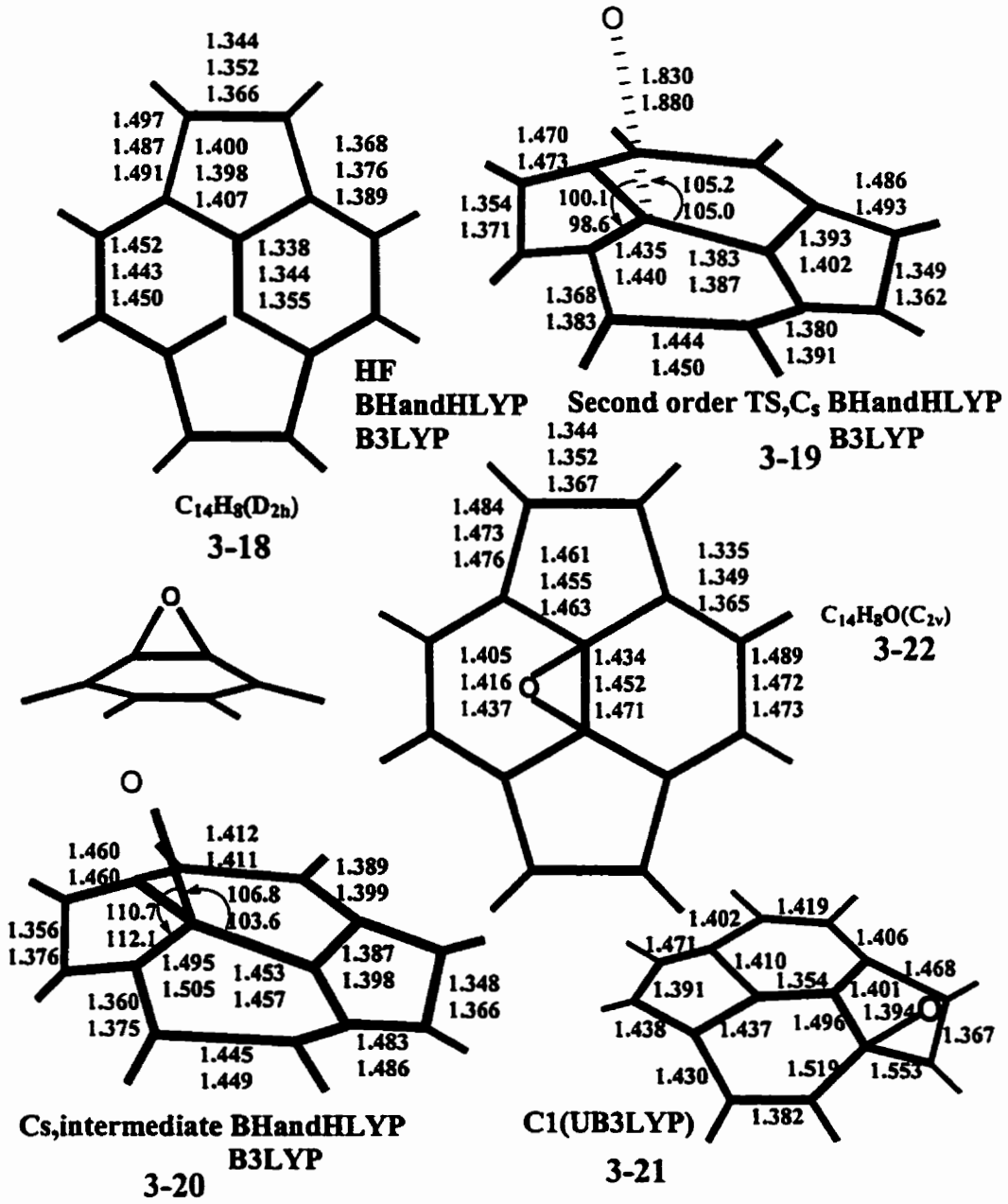

Figure 3-6 Structures of pyracylene and pyracylene oxides

Table 3-4 The energy difference between the reactants ($O(^3P) + C_{14}H_8$) and product $C_{14}H_8O$ and the $<S^2>$ of the triplet transition states and diradicals

	$C_{14}H_8O$			
	3-19 Triplet Transition State	3-20 Triplet Diradical	3-21 Triplet diradical	3-22 C_{2v} epoxide
HF	-	-	-	16.1
BHandHLYP	8.7	-2.4	-	-27.9
B3LYP	0.8	-7.4	-28.7	-42.1
	$<S^2>$ of the triplet transition states and diradicals			
BHandHLYP	2.180	2.244	-	
B3LYP	2.037	2.052	2.044	

At all three levels of theory only the epoxide structure and thus no "annulene-like" structures have been located. Even starting from a structure with a broken CC bond for the two carbon atoms connected to oxygen, only a closed structure, i.e. an epoxide, could be located. Strain from the two five-membered rings may prevent the opening of the central CC bond to form the annulenes.

3.3.5 $C_{18}H_{12}$

In order to reduce any edge effects on the central CC bond, we added four methylene groups to the four carbon atoms of the two five-membered rings to examine the change of the structure and properties as compared to pyracylene. The structures of $C_{18}H_{12}$, **3-23**, and its oxides are shown in Figure 3-7.

The addition of the four methene groups lengthens the two CC bonds connected to them in the two five-membered rings to single bond distances. The CC bonds connected to the central CC bond are still shorter than a typical CC single bond and the two CC bonds parallel to the central CC bond also decrease a little in length. The structure is closer to that of C_{60} than that of pyracylene. However, it remains a planar molecule.

For this molecule, the diradical oxide, **3-24**, in which the oxygen atom attacks one carbon atom of the central CC bond is a minimum at the BHandHLYP/6-31G* level. The formation of this diradical from a triplet oxygen atom and singlet $C_{18}H_{12}$ is endothermic at this level. In the triplet diradical, the bond lengths of the CC bonds next to oxygen and the angle of the oxygen with the central CC bond (as shown in Figure 3-7) are essentially the same as in the triplet diradical intermediates found for ethylene, benzene, naphthalene and pyracylene. The interaction of the oxygen atom with the carbon leads to that carbon atom moving out of the former $C_{18}H_{12}$ plane to bond to the oxygen. The remainder of the structure does not change much in this diradical. One of the two unpaired electrons lies on the oxygen atom, while the other is distributed over the carbon skeleton. At the UB3LYP level, the C_s diradical **3-24**, is a transition state. The imaginary vibrational mode involves motion of the oxygen out of the C_s plane. Following along this mode, a triplet diradical minimum, **3-25**, was located, in which an epoxide structure is formed at

one of the 6-5 bonds. The formation of this triplet epoxide structure is predicted to be exothermic.

We located a transition state, **3-26**, connecting the separated reactants and the diradical at the BHandHLYP/6-31G* level. The portion of the $C_{18}H_{12}$ molecule attacked by the oxygen atom changes its structure only a little in this transition state. The CC bonds in this region lengthen and the carbon atom which was attacked moves slightly out of the $C_{18}H_{12}$ plane. The bond distance between oxygen and the carbon atom under attack is 1.8Å. The two unpaired electrons mainly lie on the oxygen atom (the total spin density on oxygen is 1.54). There is a partial electron transfer from the oxygen atom to the $C_{18}H_{12}$ fragment in the transition state. At the UB3LYP level, in the $C_{18}H_{12}O$ transition state for with C_s symmetry, the OC bond lengthens by 0.036Å and the rest of structure is similar to that found for the UBHandHLYP transition state. The UB3LYP reaction barrier decreases considerably compared with that found at the UBHandHLYP level.

At the HF level, the formation of the epoxide $C_{18}H_{12}O$, **3-27**, is exothermic by 25.0 kcal/mol relative to oxygen O (^3P) and singlet $C_{18}H_{12}$. This reaction also is predicted to be exothermic at the BHandHLYP and B3LYP levels. The reaction energies and activation energies of these systems are reported in Table 3-5.

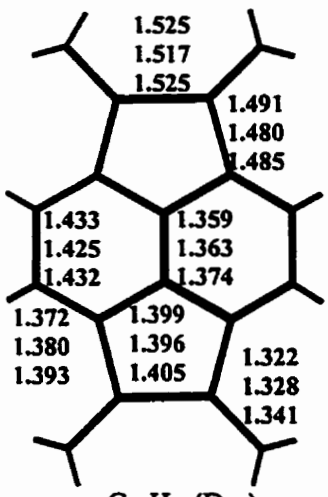

$C_{18}H_{12}(D_{2h})$

3-23

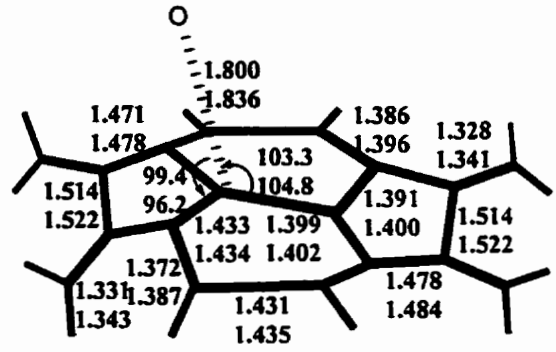

Cs,TS(BHandHLYP)
B3LYP

3-26

HF/6-31G*
BHandHLYP/6-31G*
B3LYP/6-31G*

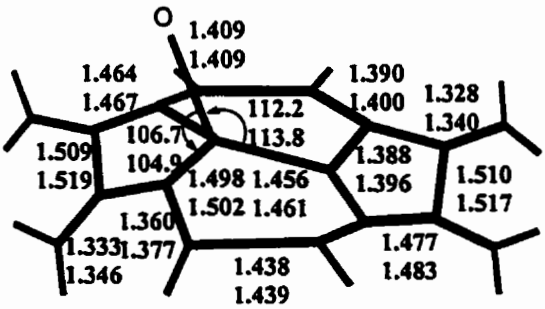

Cs,intermediate(BHandHLYP)
B3LYP

3-24

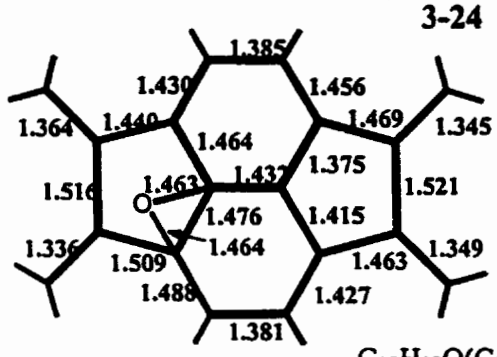

$C_{18}H_{12}O(C_1)$ UB3LYP

3-25

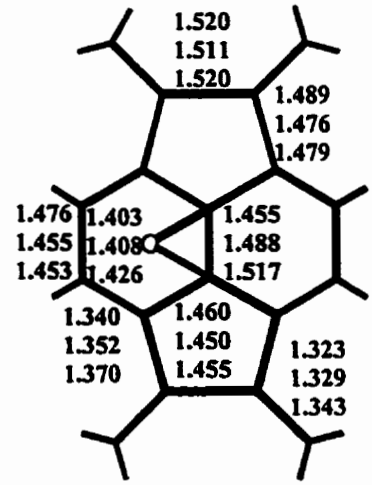

$C_{18}H_{12}O(C_{2v})$

3-27

Figure 3-7 Structures of $C_{18}H_{12}$ and its oxides

Table 3-5 The energy difference between the reactants ($O(^3P)$ + $C_{18}H_{12}$) and product $C_{18}H_{12}O$ and the $<S^2>$ of the triplet transition states and diradicals

	$C_{18}H_{12}O$			
	3-26 Triplet Transition State	3-24 Triplet Diradical	3-25 65 Epoxide	3-27 C_{2v} Epoxide
HF	-	-	-	25.0
(u)BHandHLYP	11.5	0.9		-20.1
(u)B3LYP	3.4	-6.9	-14.8	-35.0
$<S^2>$ of the triplet transition states and triplet diradicals				
		$C_{18}H_{12}O$		
(u)BHandLYP	2.292	2.337	-	
(u)B3LYP	2.039	2.046	2.064	

3.3.6 $C_{26}H_{12}$

Further addition of eight carbon atoms to the edges of $C_{18}H_{12}$ results in the formation of $C_{26}H_{12}$, **3-28**. $C_{26}H_{12}$ is a bowl-shaped structure, **3-29**, with the formation of the bowl probably due to the strain from the formation of four six-membered rings. The structures of $C_{26}H_{12}$ and its oxides are shown in Figures 3-8 and 3-9. The central CC bond length in $C_{26}H_{12}$ is still that of a typical CC double bond. It lengthens from the value 1.313Å (HF) to 1.337Å at the (B3LYP) level. In other C_{60} fragments the analogous bond lengths are 1.36 and 1.38Å [75]. The structures of the two six-membered rings at both sides of the central CC bond are similar to those in $C_{18}H_{12}$. From the bond length, we note that the structure of the six-membered rings in $C_{26}H_{12}$ does not alternate as in the single and double bond picture of C_{60}. The four outer six-membered rings in $C_{26}H_{12}$ are structurally rather more like those in benzene. Clearly a still larger model is necessary to completely mimic the structure of C_{60}. Previous studies showed that $C_{26}H_{12}$ is the smallest bowl-shaped molecule that has (some) "C_{60}-like" properties [47,48]. Constraining $C_{26}H_{12}$ to be planar, we located a transition state for the inversion between two equivalent bowl-shaped isomers. The bond lengths in the planar $C_{26}H_{12}$ decrease slightly.

The barrier to inversion connecting the two bowl-shaped isomers is similar at all three levels of theory and is about 5 kcal/mol. Biedermann *et al.* [76] investigated the inversion barrier of this molecule by AM1, PM3, HF and B3LYP methods. Only HF/3-21G and B3LYP/STO-3G vibrational frequency calculations were performed in that study. The zero point vibration energy (ZPVE) correction is smaller comparing the barrier (5.24kcal/mol) without ZPVE correction in Bidermann's study [75] to the present results. The vertical distance from the top carbon to the bottom carbon (depth of the bowl) is

1.35Å for this molecule at the B3LYP/6-311G** level [76] and is 1.30Å at the B3LYP/6-31G* level.

In the triplet diradical intermediate of $C_{26}H_{12}O$, **3-30**, as shown in Figure 3-9, the portion attacked by oxygen is similar to that in the $C_{18}H_{12}O$ diradical. The four six-membered outer rings remain nearly the same as in the bowl-shaped $C_{26}H_{12}$. There is a slightly greater transfer of unpaired electron density from the oxygen atom to the carbon skeleton than in the $C_{18}H_{12}O$ diradical. Still, one unpaired electron (0.99) remains on the oxygen, while another distributes itself over the carbon skeleton but mainly (0.64) on the carbon atom of the central CC bond which was not attacked by oxygen. The formation of the $C_{26}H_{12}O$ diradical is exothermic, in contrast to the slightly endothermic formation of the $C_{18}H_{12}O$ diradical at the BHandHLYP level. Vibrational frequency calculations demonstrate that the $C_{26}H_{12}O$ C_s diradical (1) is a transition state at the BHandHLYP level. The imaginary vibrational frequency involves an out-of-plane motion of the oxygen. The distortion along this imaginary mode did not change significantly the geometry of this diradical. Both the structure and energy are quite similar to these of the undisorted transition state.

At the BHandHLYP level, a transition state, **3-31** in Figure 3-9, connecting the separated reactants ($O(^3P)$ and singlet $C_{26}H_{12}$)) and the $C_{26}H_{12}O$ triplet diradical was located. Due to the loose structure of this transition state, the $C_{26}H_{12}$ part retains essentially the same geometry as in $C_{26}H_{12}$ itself, i.e. the transition state is more like reactant than product and thus is an "early" transition state [77]. This early nature is also true for the transition state in the reaction of an oxygen atom, $O(^3P)$, with ethylene. The

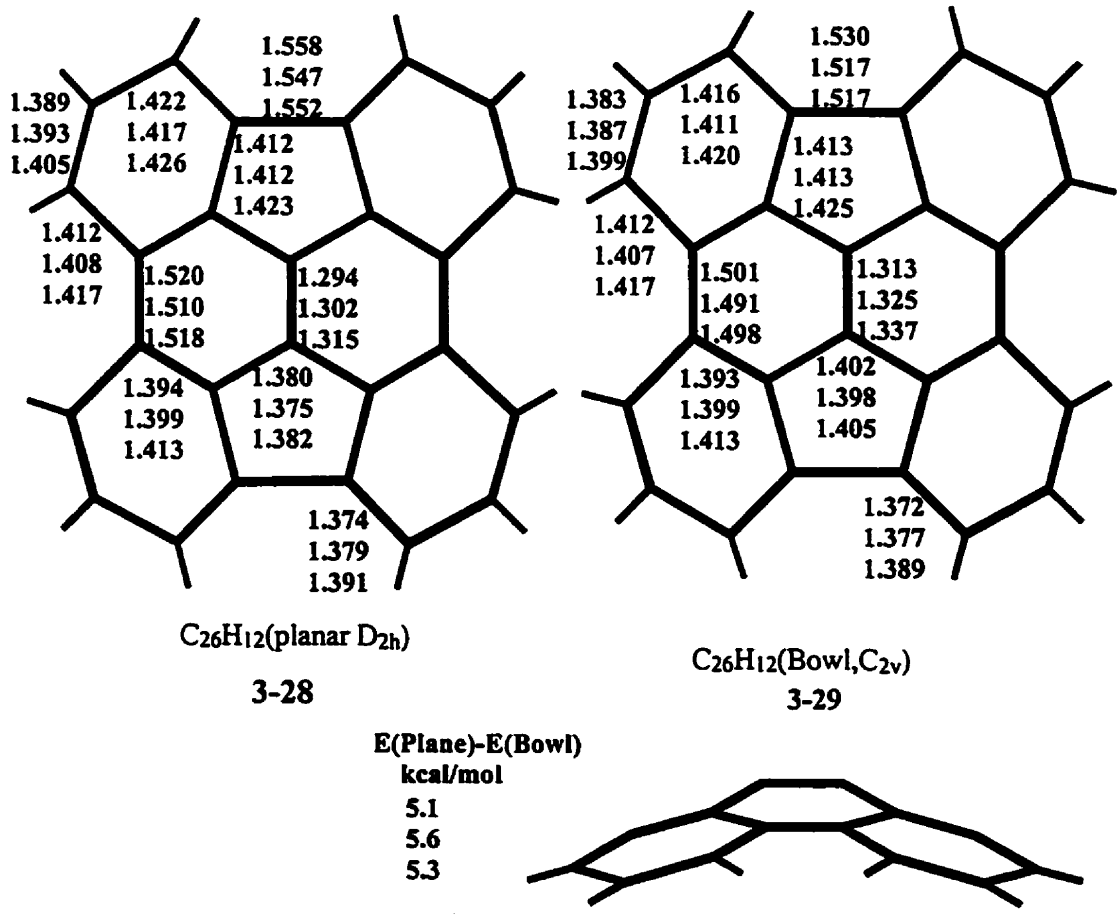

Figure 3-8 Structures of $C_{26}H_{12}$

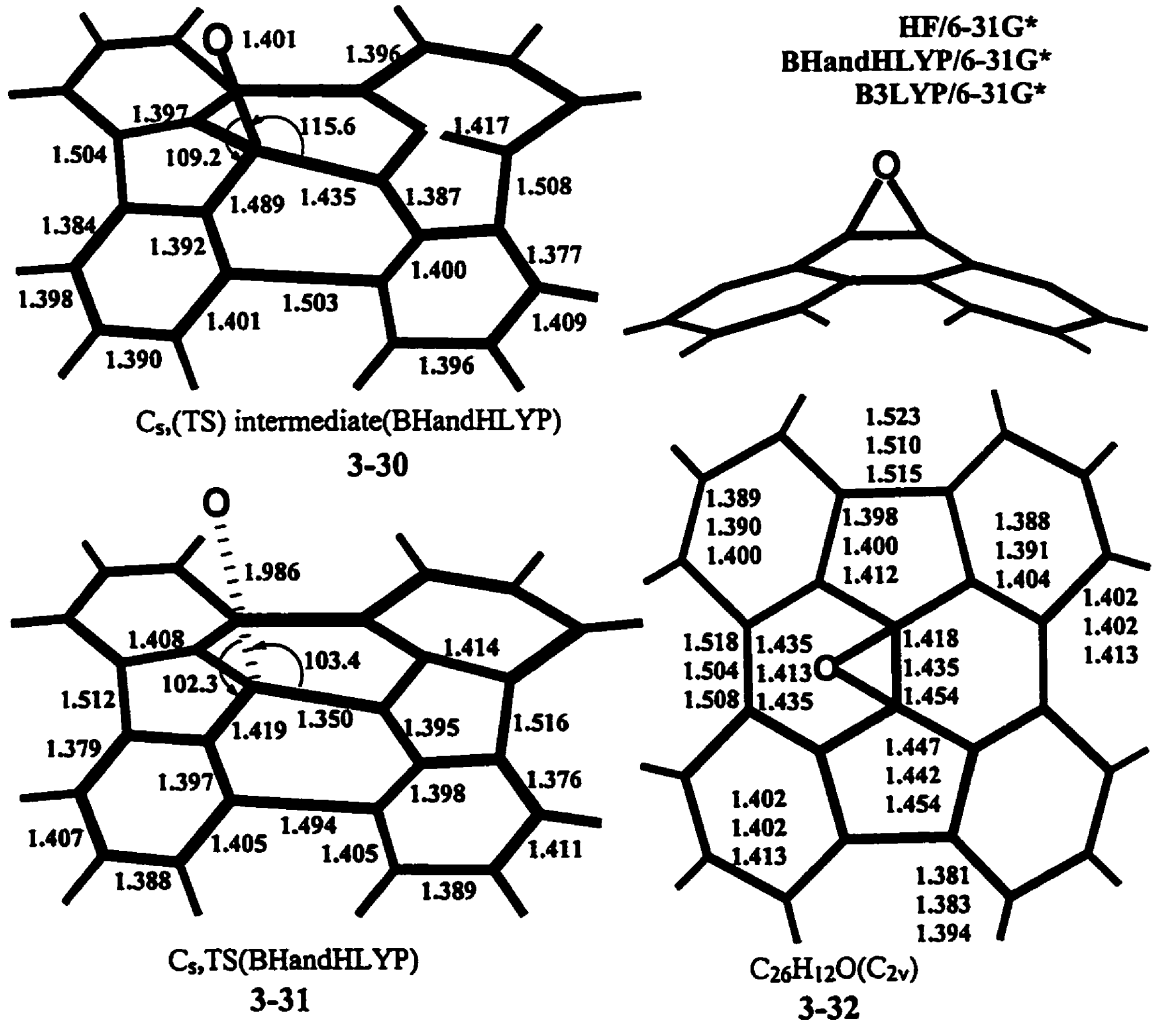

Figure 3-9 Structures of $C_{26}H_{12}$ oxides

Table 3-6 The energy difference ΔE (kcal/mol) between the reactants ($O(^3P)$ + $C_{26}H_{12}$) and product $C_{26}H_{12}O$ and the $<S^2>$ of the triplet transition states and diradicals

	ΔE			$<S^2>$	
	3-31 Triplet Transition State	3-30 Triplet Diradical	3-32 C_{2v} Epoxide	3-31 Triplet Transition State	3-30 Triplet Diradical
HF	-	-	-7.4	-	-
(u)BhandHLYP	2.2	-19.3	-50.3	2.143	2.109
(u)B3LYP	-	-	-62.1	-	-

reaction barrier for the reaction of $O(^3P)$ with $C_{26}H_{12}$ is very small at the BHandHLYP level, and is similar to that of ethylene with $O(^3P)$, as shown in Table 3-1. The two unpaired electrons lie largely on the oxygen atom in the transition state of $C_{26}H_{12}O$.

The formation of an epoxide structure from oxygen $O(^3P)$ reacting with $C_{26}H_{12}$, **3-29** in Figure 3-8, is more exothermic than the comparable reactions of oxygen with benzene, naphthalene, pyracylene and $C_{18}H_{12}$ at the same theoretical levels. It is less exothermic than the reaction of oxygen with ethylene. The energy difference between two $C_{26}H_{12}$ structures are reported in Figure 3-8 and the relative energy of the $C_{26}H_{12}$ oxides are reported in Table 3-6. No heat of formation data for the reaction products of oxygen $O(^3P)$ with C_{60} are available from experiment or from high level theory. The one value for the heat of formation was predicted by the AM1 semiempirical method [78]. This method predicted that the reaction is exothermic (by about 80 kcal/mol). Our calculations

showed that the heat formation for the reaction of oxygen with ethylene and $C_{26}H_{12}$ is of the same order of magnitude as that of oxygen with C_{60}.

The structure of the $C_{26}H_{12}O$ epoxide, **3-32**, was shown in Figure 3-9. In the three-membered ring of $C_{26}H_{12}O$, the CO bond length is longer than the CC bond at the HF and BHandHLYP levels, while this order switches with the B3LYP method. This resembles the C_2H_4O epoxide structure as shown in Figure 3-3. At all theoretical levels the CO bond length is shorter than the CC bond in the three-membered ring of the epoxide structures of benzene, naphthalene, pyracylene and $C_{18}H_{12}$. In the crystal structure of the $C_{60}O$ epoxide complex [34], the CO bond is slightly shorter than the CC bond in the three-membered ring. Also we note that the difference between the CO and CC bond lengths in the three-membered ring is much smaller in C_2H_4O and $C_{26}H_{12}O$ than in the benzene, naphthalene, pyracylene and $C_{18}H_{12}$ epoxides. The addition of oxygen further increases the height of the bowl from the bottom carbon atoms to the two central carbon atoms of the $C_{26}H_{12}$ fragment in $C_{26}H_{12}O$. This height is 1.76Å at the B3LYP/6-31G* level, so the curvature of the $C_{26}H_{12}$ bowl has increased. Comparing these structures, we note that there is a greater similarity in structure and reactivity of $C_{26}H_{12}$ to C_{60} than to the other molecules. However, the reactivity of $C_{26}H_{12}$ is rather closer to ethylene than to aromatic molecules such as benzene and naphthalene.

3.3.7 Aromaticity, nucleus-independent chemical shifts (NICSs), energetics and structures

Aromaticity, resulting from cyclic conjugation, is an important concept in organic chemistry. There are a number of criteria used to characterize this property: geometric (bond length alternation, bond order, and ring current indices [13]), energetics (aromatic

stabilization energies), and magnetic (^{1}H NMR chemical shift, diamagnetic susceptibility anisotropy). A new family of criteria for aromaticity directly related to the electronic structure of the system has been developed by Parr *et al* [79]. The derivatives of the molecular valence as a measure of aromaticity have been formulated by Komorowski *et al* [80]. Among those criteria, the NICSs, the negative values of the "nucleus-independent chemical shifts", simply and efficiently characterize the aromaticity of molecules. The concept originates in the unusual upfield chemical shifts of protons located "inside" aromatic rings [12,51,58]. The NICSs for the systems at the ring centers, defined as the un-weighted mean of the heavy atom coordinates of the ring, were predicted and are reported in Table 3-7. Negative NICSs imply aromatic character, positive implies antiaromatic character and near zero values mean nonaromatic character. In order to see the effect of oxygen on the aromaticity of the ring in the oxides, the oxygen of the epoxides has been included in the heavy atom ring for the NICSs calculation. Geometric criteria for aromaticity also are discussed for the systems of greatest interest.

If the CC bond length in benzene (~1.4Å) is adopted as the standard aromatic CC bond distance, the aromaticity of a molecule can be analyzed through the changes in its CC bond length relative to that in benzene. The alternation of the CC bond lengths in naphthalene is very small and the CC bond lengths are very close to those in benzene. In pyracylene, the strain from the two five-membered rings leads to an increase in the differences among the CC bond distances. The central CC bond shortens to 1.355Å and the CC bonds parallel to it lengthen to 1.450Å at the B3LYP level. The largest difference in the CC bond distances for pyracylene is 0.095Å between the central CC bond and the parallel CC bonds at the B3LYP level of theory. It is expected that the aromaticity of the

six-membered rings is weaker than in naphthalene or benzene due to the effects of the five-membered rings. The further addition of the four methylene groups to pyracylene reduces the differences among the CC bond length in the six-membered rings of $C_{18}H_{12}$. Thus the aromaticity of this molecule appears to be enhanced. The CC bond length of the methene groups is still that of a typical double bond. In the C_{2v} structure of $C_{26}H_{12}$, the two inner six-membered rings have similar structures to those in $C_{18}H_{12}$, although the maximum difference in the CC bond lengths is larger (0.058Å for $C_{18}H_{12}$ and 0.161Å for C_{2v} $C_{26}H_{12}$ at the B3LYP level). The central bond shortens and the bonds parallel to it lengthen. However, the outer six-membered rings have more typical aromatic distances and the largest CC bond length difference is only 0.036Å at the B3LYP level. In C_{60}, the bond length alternation of the two kinds of CC bonds is about 0.06Å.

The NICSs confirm the aromatic features of these molecules. The NICSs at the center of benzene is -11.5, which is a typical value for an aromatic molecule. Although pyracylene satisfies the 4n+2 rule, the formation of the two five-membered rings weakens the aromaticity of the six-membered ring. In pyracylene, the five-membered ring is anti-aromatic, while the six-membered ring is slightly aromatic, which is in agreement with a previous study [81]. Further additions of diffuse functions (6-31+G*) to the carbon atoms showed that the six-membered ring is non-aromatic in pyracylene [12], which indicates that these diffuse functions can change the description of aromaticity in a molecule. The degree of aromaticity changes greatly in $C_{18}H_{12}$. The five-membered rings are almost non-aromatic and the six-membered rings are aromatic even compared to benzene. Due to the different structures of the inner and outer six-membered rings in C_{2v} $C_{26}H_{12}$, the

Table 3-7: GIAO-SCF/6-31G* Calculated NICSs(ppm) for the set of molecules

Compound	Point group	NICS
Benzene	D_{6h}	-11.5
Benzene epoxide	C_s	-4.7[a]
		-5.9[b]
	C_2	-0.8[a]
		-8.0[b]
Oxepin	C_s	0.9
	C_{2v}	15.1
	C_2	49.0
Naphthalene	D_{2h}	-11.4
Naphthalene epoxide	C_{2v}	-6.4[c,a]
		-7.2[b]
1,6-oxo-[10]annulene	C_{2v}	-15.9
	C_s[d]	-8.2[e]
		-11.9[f]
$C_{14}H_8$	D_{2h}	12.0[5]
		-4.2[a]
$C_{14}H_8O$	C_{2v}	10.6[5]
		3.38[a]
		1.21[b]
$C_{18}H_{12}$	D_{2h}	2.3[5]
		-10.7[a]
C_{60}[g]	I_h	5.4[5]
		-6.8[a]
$C_{18}H_{12}O$	C_{2v}	-1.0[5]
		-6.8[a]
		-7.8[b]
$C_{26}H_{12}$	D_{2h}	4.9[5]
		-4.5[a,1]
		-10.3[a,2]
	C_{2v}	4.1[5]
		-5.0[a,1]
		-10.4[a,2]
$C_{26}H_{12}O$	C_{2v}	2.6[5]
		-1.4[a,1]
		-3.1[b,1]
		-9.9[a,2]

Geometry from B3LYP/6-31G*. [a] NICS at the center of six carbon ring. [b] NICS at the center of seven member ring. [c] BHandHLYP/6-31G* optimized geometry. [d] HF/6-31G* optimized geometry. [e] For the hexadiene. [f] For the hexatriene. [g] From P. v. R. Schleyer *et al.* J. Am. Chem. Soc. 118 (1996) 6317. [5] five membered ring. [1] inner six membered ring. [2] outer six membered ring.

aromaticity of these two kinds of rings should be different. The inner rings are weakly aromatic while the outer ones are more typically aromatic. The NICSs in planar $C_{26}H_{12}$ have nearly the same values as in the C_{2v} bowl-shaped $C_{26}H_{12}$. From the NICSs of these fragments and of C_{60}, we note that $C_{26}H_{12}$ is much closer to the value in C_{60} for this property. The NICSs of C_{60} were predicted earlier by a GIAO-SCF/3-21G calculation at the HF/3-21G optimized geometry [12]. In order to check the effect of basis set (3-21G versus 6-31G*) on the NICSs, we calculated the NICSs of benzene with the 3-21G basis set at the B3LYP geometry. The NICS at the 3-21G level is -10.0, a 10% difference from the result with the 6-31G* basis set (-11.5) for benzene. So the NICSs of C_{60} should not change by more than about 10% when the 6-31G* basis set is employed rather than the 3-21G basis set.

The NICSs in the oxides also were calculated. In the oxepin structure, in which the CC bond of the oxygen-connected carbon atoms is broken, the oxygen was included in determining the center at which to perform the NICSs calculation, i.e. the NICSs are calculated at the center of a seven atom ring. In the epoxide with the three-membered ring, the NICSs at both the center of the six carbon atom ring and the seven heavy atom ring including the oxygen were determined.

In the benzene epoxides, the C_s isomer is weakly aromatic as judged by the NICSs evaluated at both the center of the six-membered ring and of the seven-membered ring. Aromaticity increases slightly based on the NICSs determined at the six-membered ring center compared to the seven-membered ring reference point in benzene epoxide. The change in the NICSs is even more dramatic for the C_2 epoxide isomer. The structures of C_2 epoxide and oxepin will be discussed in detail in the next chapter. The C_2 structures

have one hydrogen atom of the oxygen-connected carbons on each side of the benzene ring. Without considering the oxygen, the NICSs at the center of the six-membered ring is nearly zero which means a nonaromatic system. Inclusion of the oxygen atom in calculating the point at which to evaluate the NICSs raises the value to -8.0, which indicates aromatic character. So the effect of oxygen on aromaticity is significant. The C_s oxepin isomer is nearly non-aromatic. The electronic interaction moves the oxygen atom out of the plane of the carbon skeleton in C_s oxepin, which stabilizes this structure. Planar oxepin (a transition state between two C_s oxepins isomers) is antiaromatic as judged from the NICSs values. The C_2 oxepin is a strongly anti-aromatic species with a very large positive NICS.

The naphthalene epoxide with C_{2v} symmetry is a slightly aromatic molecule. Its NICS at the six-membered ring center is -6.4, which increases to -7.2 when the oxygen atom is included in the calculation of the ring center. For the C_{2v} annulene like oxide, the aromaticity is stronger. Even for the C_s annulene oxide obtained at the HF level there are large NICSs values, which can rationalize the preference of naphthalene oxide for the annulene structure over the three-membered ring epoxide.

In the oxide of $C_{14}H_8$, the NICSs in the five-membered rings decreases to 10.6, the NICSs in the six-membered ring (3.38 without the oxygen) indicates only weak anti-aromaticity. The inclusion of oxygen in the definition of the ring center reduces this value to 1.2, i.e. non-aromatic. It is interesting that the addition of oxygen to $C_{18}H_{12}$ causes the five-membered rings to become non-aromatic or even very weakly aromatic rings. The six-member carbon ring and the seven-membered heavy atom ring are weakly aromatic in $C_{18}H_{12}O$ compared to those in $C_{18}H_{12}$. From the NICSs in $C_{14}H_8$, $C_{18}H_{12}$ and their oxides,

we note the different aromatic characters of these two molecules. In $C_{26}H_{12}O$, the NICSs do not change much compared with the C_{2v} $C_{26}H_{12}$. The absolute values of the NICSs in $C_{26}H_{12}O$ decrease overall though the outer six-membered rings keep their aromatic character and the inner six-membered ring are still weakly aromatic if the effect of oxygen is considered. Due to the prohibitive computational cost for the NICSs calculation on C_{60} and its epoxide $C_{60}O$, no attempt to determine NICSs for these two molecules was made.

From the NICSs of the oxides, we note the contribution of oxygen to the aromaticity of the systems. This may be due to the lone pair electrons in oxygen atom, which contributes to the π electron conjugation of carbon skeleton. The position of the center for NICS (for example with or without the oxygen counted in the ring) also may affect the values of the NICSs.

3.4 Concluding Remarks

Density functional theory has been applied for the first time to study the bonding and reactivity of selected fragments derived from C_{60}. The comparison of the energetics of the reaction of the oxygen atom with the C_{60} fragments and of the aromaticity of these fragments and their oxides leads to a preliminary conclusion that the C-C central bond in $C_{26}H_{12}$ (as in C_{60}) is a constrained carbon-carbon double bond.

The open CC bond structure is due to the greater structural freedom in the naphthalene oxides. Aromaticity plays a role in the relative stability of the epoxide and oxepin products from the addition of an oxygen atom to benzene. Geometric constraints cause the CC bond in the closed epoxide in $C_{14}H_8O$, $C_{18}H_{12}O$, $C_{26}H_{12}O$ and $C_{60}O_n$ to be

more favorable. From the study of the reactivity of these C_{60} fragments, it is probable that steric strain causes the particular properties of the fullerenes. This view partially confirms the conclusion that with increasing curvature there is increasing reactivity [82]. The electronic structure of C_{60} fragments may also contribute to their unusual properties[83]. In the oxides of the systems studied, the oxygen contributes to the aromaticity of the molecule as analyzed by determining the NICSs. The contribution from the geometric site of reference point for NICSs is relatively small since the centers of six membered ring and the seven membered ring are found to be very close to each other.

Based on the reaction barriers for oxygen $O(^3P)$ plus the hydrocarbons, a conclusion could be drawn that HF overestimates the activation energy, BHandHLYP does well in characterizing the activation energy, and is especially a good tool for low barrier reactions. B3LYP underestimates the activation energy, although B3LYP may be best for structural characterization. The inclusion of exact exchange increases the reaction barrier as judged from the performance of HF, BHandHLYP and B3LYP on the prediction of this quantity. The inclusion of some fraction of exact exchange decreases excessive conjugation shown by DFT [84]. For the structural predictions on the PAHs, HF favors more localized structures, while electron correlation favors delocalization.

3.5 References

1. W. Krätschmer. L. D. Lamb, K. Fostiropoulos, D. R. Huffman, Nature, **347**, 354 (1990)
2. W. A. Scrivens, P. V. Bedworth, J. M. Tour, J. Am. Chem. Soc., **114**, 7917 (1992)
3. J. M. Hawkins, A. Meyer, T. A. Lewis, S. Loren, F. J. Hollander, Science, **252**, 312 (1991)
4. L. Isaacs, A. A. Wehrsig, F. Diederich, Helv. Chim. Acta, **76**, 1231 (1993)
5. R. C. Haddon, L. E. Brus, K. Raghavachari, Chem. Phys. Lett., **125**, 459 (1986)
6. J. K. Feng, J. Li, Z. Z. Wang, M. C. Zerner, Int. J. Quantum Chem., **37**, 599 (1990)
7. R. C. Haddon, Science **261**, 1545 (1993)
8. F. Diederich, and C. Thilgen, Science, **271**, 317 (1996)
9. A. Hirsch, *The Chemistry of the Fullerenes*, Thieme, Stuttgart, New York 1994
10. Y. Elemes, S. K. Silverman, C. Sheu, M. Kao, C. S. Foote, M. M. Alvarez, R. L. Whetten, Angew. Chem., Int. Ed. Engl., **31**, 351 (1992)
11. K. M. Greegan, J. L. Robbins, W. K. Robbins, J. M. Millar, R. D. Sherwood, P. J. Tindall, D. M. Cox, A. B. Smith III, J. P. McCauley Jr., D. R. Jones, and R. T. Gallagher, J. Am. Chem. Soc., **114**, 1103 (1992)
12. P. v. R. Schleyer, C. Maerker, A. Dransfeld, H. Jiao, N. J. R. v. E. Hommes, J. Am. Chem. Soc., **118**, 6317 (1996) and reference therein
13. A. Pasquarello, M. Schlüter, R. C. Haddon, Science **257**, 1660 (1992)
14. S. Roszak, R. J. Buenker, P. C. Hariharan, J. Kaufman, J. Chem. Phys., **147**, 13 (1990)
15. M. G. Moss, J. W. Hudgens, and J. D. McDonald, J. Chem. Phys., **72**, 3486 (1980)

16. J. Kleinermanns and A. C. Luntz, J. Phys. Chem., **85**, 1966 (1981)

17. J. C. Loison, C. Dedonder-Lardeux, C. Jouvet, and D. Solgadi, J. Phys. Chem., **95**, 9192 (1991)

18. J. C. Loison, C. Dedonder-Lardeux, C. Jouvet, and D. Solgadi, Ber. Bunsenges. Phys. Chem., **96**, 1142 (1992)

19. J. C. Loison, C. Dedonder-Lardeux, C. Jouvet, and D. Solgadi, Faraday Discuss., **97**, 379 (1994)

20. O. K. Abou-Zied, and J. D. McDonald, J. Chem. Phys., **109**, 1293 (1998)

21. B. Bigot, A. Sevin, and A. Devaquet, J. Am. Chem. Soc., **101**, 1095 (1979)

22. K. Yamaguchi, S. Yabushita, and T. Fueno, Chem. Phys. Lett., **70**, 27 (1980)

23. M. Dupuis, J. J. Wendoloski, T. Takada, and W. A. Lester Jr., J. Chem. Phys., **76**, 481 (1982)

24. T. Fueno, Y. Takahara, and K. Yamaguchi, Chem. Phys. Lett., **167**, 291 (1990)

25. B. J. Smith, M. T. Nguyen, W. J. Bouma, and L. Radom, J. Am. Chem. Soc., **113**, 6452 (1991)

26. a) R. E. Huie, and J. T. Herron, J. Phys. Chem. Ref. Data **2**, 467 (1973); b) A. R. Clemo, F. E. Davidson, G. L. Duncan and R. Grice, Chem. Phys. Lett., **84**, 509 (1981)

27. S. Knuts, B. F. Minaev, O. Vahtras, and H. Ågren, Int. J. Quantum Chem., **55**, 23 (1995)

28. G. H. Kroll, P. J. Benning, Y. Chen, T. R. Ohno, J. H. Weaver, L. P. F. Chibante, and R. E. Smalley, Chem. Phys. Lett., **181**, 112 (1991)

29. J. M. Wood, B. Kahr, S. H. II Hoke, L. Dejarme, R. G. Cooks, D. Ben-Amotz, J.

Am. Chem. Soc., **113**, 5907 (1991)

30. A. L. Balch, D. A. Costa, J. W. Lee, B. C. Noll, and M. M. Olmstead, Inorg. Chem., **33**, 2071 (1994)

31. J. P. Deng, D. D. Ju, G. R. Her, C. Y. Mou, C. J. Chen, Y. Y. Lin, and C. C. Han, J. Phys. Chem., **97**, 11575 (1993)

32. T. Hamano, T. Mashino, and M. Hirobe, J. Chem. Soc., Chem. Commun., 1537 (1995)

33. A. L. Balch, D. A. Costa, J. W. Lee, B. C. Noll, and M. M. Olmstead, J. Am. Chem. Soc., **117**, 8926 (1995)

34. A. L. Balch, D. A. Costa, J. W. Lee, B. C. Noll, and M. M. Olmstead, Inorg. Chem., **35**, 458 (1996)

35. T. Sommer, and P. Roth, J. Phys. Chem. **A 101**, 6238 (1997)

36. D. I. Schuster, P. S. Baran, R. K. Hatch, A. U. Khan, and S. R. Wilson, J. Chem. Soc., Chem. Commun., 2493 (1998)

37. H. He, N. Swami, and B. E. Koel, J. Chem. Phys., **110**, 1173 (1999)

38. K. Raghavachari, Chem. Phys. Lett., **195**, 221 (1992); **209**, 223 (1993)

39. M. Menon, and K. R. Subbaswamy, Chem. Phys. Lett., **201**, 321 (1993)

40. Q. W. Teng, J. K. Feng, C. C. Sun, and M. C. Zerner, Int. J. Quantum Chem., **55**, 35 (1995)

41. A. M. Ren, J. K. Feng, W. Q. Tian, M. F. Ge, Z. R. Li, C. C. Sun, and X. Zheng, Int. J. Quantum Chem., **76**, 23 (2000)

42. M. Prato, T. Suzuki, H. Foroudian, Q. Li, K. Khemani, F. Wudl, J. Leonetti, R. D. Little, T. White, B. Rickborn, S. Yamago, and E. Nakamura, J. Am. Chem. Soc.,

115, 1594 (1993)

43. W. Eiermann, F. Wudl, M. Prato, M. Maggini, J. Am. Chem. Soc., **116**, 8364 (1994)

44. R. A. J. Janssen, J. C. Hummelen, F. Wudl, J. Am. Chem. Soc., **117**, 544 (1995)

45. Z. Li, and P. B. Shevlin, J. Am. Chem. Soc., **119**, 119 (1997)

46. P. W. Rabideau, and A. Sygula, Acc. Chem. Res., **29**, 235 (1996)

47. H. E. Bronstein, L. T. Scott, quoted in R. Baum, Chem. Eng. News, **75**, 28 (1997)

48. E-mail private communication with H. E. Bronstein of Boston College

49. J. Mestres, and M. Solà, J. Org. Chem., 63, 7556 (1998)

50. a) V. J. Minkin, M. N. Glukhovtsev, B. Y. Simkin, *Aromaticity and Antiaromaticity*, Wiley, New York, 1994; b) P. J. Garratt, *Aromaticity*, Wiley, New York, 1986

51. P. v. R. Schleyer, P. K. Freeman, H. Jiao, and B. Goldfuss, Angew. Chem. Int. Ed. Engl., **34**, 337 (1995)

52. Gaussian 94, Revision B.1, M. J. Frisch, G. W. Trucks, H. B. Schlegel, P. M. W. Gill, B. G. Johnson, M. A. Robb, J. R. Cheeseman, T. Keith, G. A. Petersson, J. A. Montgomery, K. Raghavachari, M. A. Al-Laham, V. G. Zakrzewski, J. V. Ortiz, J. B. Foresman, J. Cioslowski, B. B. Stefanov, A. Nanayakkara, M. Challacombe, C. Y. Peng, P. Y. Ayala, W. Chen, M. W. Wong, J. L. Andres, E. S. Replogle, R. Gomperts, R. L. Martin, D. J. Fox, J. S. Binkley, D. J. Defrees, J. Baker, J. P. Stewart, M. Head-Gordon, C. Gonzalez, and J. A. Pople, Gaussian, Inc., Pittsburgh PA, 1995

53. Gaussian 98 (Revision A.5), M. J. Frisch, G. W. Trucks, H. B. Schlegel, G. E. Scuseria, M. A. Robb, J. R. Cheeseman, V. G. Zakrzewski, J. A. Montgomery, R. E. Stratmann, J. C. Burant, S. Dapprich, J. M. Millam, A. D. Daniels, K. N. Kudin, M.

C. Strain, O. Farkas, J. Tomasi, V. Barone, M. Cossi, R. Cammi, B. Mennucci, C. Pomelli, C. Adamo, S. Clifford, J. Ochterski, G. A. Petersson, P. Y. Ayala, Q. Cui, K. Morokuma, D. K. Malick, A. D. Rabuck, K. Raghavachari, J. B. Foresman, J. Cioslowski, J. V. Ortiz, B. B. Stefanov, G. Liu, A. Liashenko, P. Piskorz, I. Komaromi, R. Gomperts, R. L. Martin, D. J. Fox, T. Keith, M. A. Al-Laham, C. Y. Peng, A. Nanayakkara, C. Gonzalez, M. Challacombe, P. M. W. Gill, B. G. Johnson, W. Chen, M. W. Wong, J. L. Andres, M. Head-Gordon, E. S. Replogle and J. A. Pople, Gaussian, Inc., Pittsburgh PA, 1998

54. C. Adamo, and V. Barone, in Recent Advances in Density Functional Methods, Part II, D. P. Chong ed. World Scientific Co. Pte. Ltd., Singapore, 1997, p115

55. Æ. Frisch, and M. J. Frisch, Gaussian 98 User's Reference, Gaussian Inc., Pittsburgh, 1998

56. A. D. Becke, J. Chem. Phys., **98**, 5648 (1993)

57. C. Lee, W. Yang, and R. G. Parr, Phys. Rev. **B 37**, 785 (1988)

58. M. Nendel, K. N. Houk, L. M. Tolbert, E. Vogel, H. Jiao, and P. v. R. Schleyer, J. Phys. Chem. **A 102**, 7191 (1998)

59. J. L. Durant, Chem. Phys. Lett., **256**, 595 (1996)

60. A. D. Becke, J. Chem. Phys., **98**, 1372 (1993)

61. B. M. Rice, S. V. Pai, and C. F. Chabalowski, J. Phys. Chem. **A 102**, 6950 (1998)

62. H. M. Sulzbach, M. S. Platz, H. F. Schaefer III, and C. M. Hadad, J. Am. Chem. Soc., **119**, 5682 (1997)

63. C. Møller, and M. S. Plesset, Phys. Rev., **46**, 618 (1934)

64. R. J. Cvetanović, Adv. Photochem., **1**, 155 (1963); J. Phys. Chem., **74**, 2730 (1970)

65. Depending on the mode of approach of the oxygen atom to benzene, there should be several reactive channels and thus, several different products. A detailed study including symmetry problems will be discussed in Chapter 4.

66. C. C. Pye, J. D. Xidos, R. A. Poirier, and D. J. Burnell, J. Phys. Chem., A **101**, 3371 (1997)

67. F. Sondheimer, and A. Shani, J. Am. Chem. Soc., **86**, 3168 (1964)

68. N. A. Bailey, and R. Mason, Chem. Commun., 1039 (1967)

69. C. W. Bock, P. George, and J. P. Glusker, J. Mol. Struct. (Theochem) **234**, 227 (1991)

70. G. R. Stevenson, and S. S. Ziegler, J. Phys. Chem., **87**, 895 (1983)

71. L. Farnell, and L. Radom, J. Am. Chem. Soc., **104**, 7650 (1982)

72. R. C. Haddon, and K. Raghavachari, J. Am. Chem. Soc., **107**, 289 (1985)

73. M. Sironi, M. Raimondi, D. L. Cooper, and J. Gerratt, J. Mol. Struct. (Theochem) **338**, 257 (1995)

74. C. Mealli, A. Ienco, E. B. Hoyt, Jr., and R. W. Zeollner, Chem. Eur. J., **3**, 958 (1997)

75. a) The bond length of C13-C14 at the junction of the two six-membered rings in $C_{30}H_{12}$, is 1.36Å in the crystal structure of its complex: R. M. Shaltout, R. Sygula, A. Sygula, F. R. Fronczek, G. G. Stanley, and P. W. Rabideau, J. Am. Chem. Soc., **120**, 835 (1998) b) The C1-C2A bond length in the crystal structure of $C_{36}H_{12}$ is 1.379Å: D. M. Forkey, S. Attar, B. C. Noll, R. Koerner, M. M. Olmstead, and A. L. Balch, J. Am. Chem. Soc., **119**, 5766 (1997)

76. P. U. Biedermann, S. Pogodin, and I. Agrantat, J. Org. Chem., **64**, 3655 (1999)

77. G. S. Hammond, J. Am. Chem. Soc., **77**, 334 (1955)

78. M. Manoharan, Chem. Phys. Lett., **296**, 429 (1998)

79. Z. Zhou, R. G. Parr, J. F. Garst, Tetrahedron Lett., **29**, 4843 (1988)

80. R. Balawender, L. Komorowski, F. De Proft, and P. Geerlings, J. Phys. Chem. A **102**, 9912 (1998)

81. P. W. Fowler, R. Zanasi, B. Cadioli, E. Steiner, Chem. Phys. Lett., **251**, 132 (1996)

82. K. Choho, W. Langenaeker, G. Van De Woude, and P. Geerlings, J. Mol. Struct. (TheoChem) **338**, 293 (1995)

83. L. T. Scott, H. E. Bronstein, D. V. Preda, R. B. M. Ansems, M. S. Bratcher, and S. Hagen, Pure and Appl. Chem., **71**, 209 (1999)

84. C. Adamo, and V. Barone, J. Chem. Phys., **108**, 664 (1998)

Chapter 4

Tests of Density Functional Methods: Theoretical Investigations of the Reaction of O (^{3}P) with Benzene and The Isomerization of Benzene Oxide

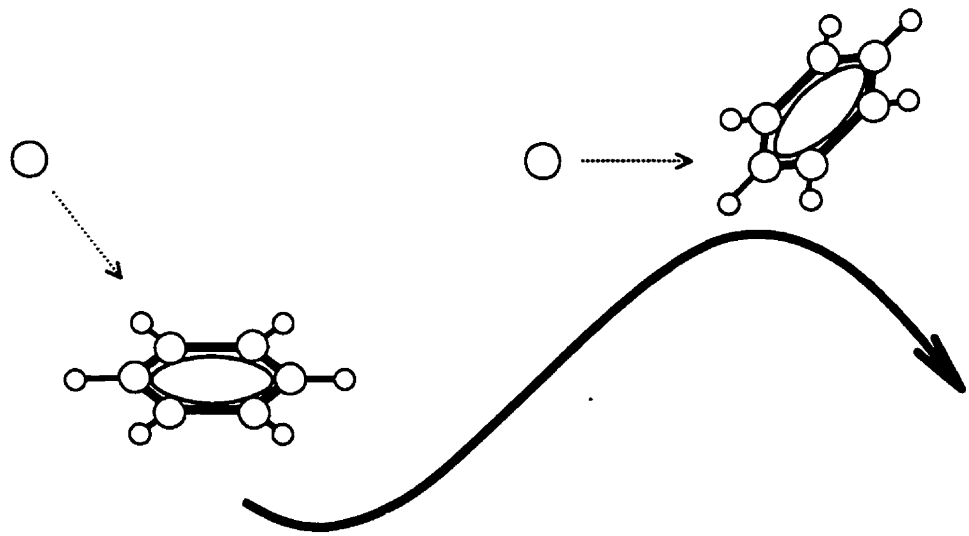

4.1 Introduction

The reaction of an oxygen atom with benzene plays an important role in atmospheric chemistry [1,2], photochemical air pollution and in combustion processes. It also serves as a realistic model for the reaction of an oxygen atom with other aromatic hydrocarbons[3,4]. It is necessary to investigate further this fundamental reaction mechanism. There have been experiments on the relative reaction rates for O (^{3}P) and benzene using static photolysis techniques [5,6], pulsed radiolysis [7], discharge flow [8,9,10], and modulation-phase shift [11,12] techniques which have determined the absolute reaction rate constants for this reaction. The mechanism of this reaction also has been studied with molecular beam mass spectroscopy [13]. In the mass spectroscopic study [13], two paths were identified: formation of a long-lived complex, and formation of carbon monoxide, CO, and a C_5H_6 hydrocarbon that is probably 3-penten-1-yne. A complex of C_{6v} symmetry and epoxide products of C_{2v} symmetry were proposed by the author. During the reaction, a spin transition was assumed to take place since the reaction changes from the lowest triplet to the ground singlet electronic state [13]. In a later crossed molecular beam experiment, the formation of phenol and the phenol radical resulted from the main reaction channel [14], CO elimination. If this reaction occured at all, it was a relatively minor reaction pathway. A microwave-discharge-fast-flow experiment found channels producing CH ($A^2\Delta$) and OH ($A^2\Sigma^+$) through observation of the emission spectra [15]. The C_5H_6 pathway was proposed to produce cyclopentadiene rather than 3-pent-1-yne in this experiment. In summary, the reaction of triplet oxygen with singlet benzene involves the following pathways:

$O(^3P) + C_6H_6 \rightarrow C_6H_6 \cdots O$ (complex)

$\rightarrow CO + C_5H_6$

$\rightarrow$ phenol + C_6H_5O + ···

$\rightarrow CH\ (A^2\Delta) + OH\ (A^2\Sigma^+)$ + ···

$\rightarrow C_6H_6O$ (oxides)

The activation energy for the initiation reaction of the O + C_6H_6 system was determined to be 4.4±0.5 kcal/mol [15]. Another crossed-molecular-beam study measured this initial reaction barrier to be 4.1±0.5kcal/mol [16]. The spin uncoupling model of Bader *et al.* [17] was proposed for the O + C_6H_6 initial reaction rather than the charge-transfer model of Cvetanović [18] on the basis of a comparison with the initial reaction barriers of O + C_2H_2, C_2H_4 and C_6H_6 [16]. Most recently, photolysis of ozone with benzene in an argon matrix at 12K has been studied [19]. A diradical intermediate was suggested in this study. Through this diradical, phenol, 2,4-cyclohexdienone, benzene oxide and butadienylketene all were produced [19]. No extensive theoretical studies of the reactions of the oxygen atom with benzene exist. The most frequently postulated structures for benzene oxide in both theoretical and experimental studies are the C_s epoxide and the C_s oxepin. The tautomerism of the epoxide and oxepin was examined by ^1H NMR [20]. The energy of the epoxide is slightly, 1.7 kcal/mol, lower than that of the oxepin according to an equilibrium constant measurement [20]. However, at room temperature the entropy gain associated with this rearrangement was predicted to cause a considerable displacement of the equilibrium toward oxepin [20].

There also are a few theoretical investigations of the structures and the tautomerism of

the benzene epoxide-oxepin at both the semi-empirical and *ab initio* Hartree-Fock levels [21]. At lower levels of theory, the geometries and enthalpies were poorly predicted [21d]. Recently, Pye *et al.* [22] studied the valence isomers benzene epoxide and oxepin with both HF and MP2 methods and included higher level MP3, MP4 and QCISD single point energy calculations. In that report [22], the authors explored the tautomerism of benzene epoxide/oxepin, and also located a transition state for the inversion which connects two equivalent non-planar oxepin isomers. However, zero point vibrational energy (ZVPE) corrections were not included explicitly in their discussions on the results from the MP3, MP4 and QCISD methods.

Until the present investigation, there have not been any extensive theoretical studies of the reaction mechanism of the triplet oxygen atom with benzene or of the isomerizations of benzene oxides.

Based on a review of previous studies, we have considered all possible pathways for an oxygen atom reacting with benzene and all the various possible products. A reasonable mechanism for the isomerization of benzene oxide is determined. In this investigation, we have employed both conventional *ab initio* (Hartree-Fock, MP2, MP3, MP4 and CCSD) and density functional theories (BHandHLYP, B1LYP, B3LYP, BLYP and MPW1PW91) with at least split valence plus polarization basis sets.

4.2 Computational Details

Ab initio and density functional computations were performed with the Gaussian 94[23] or Gaussian 98 packages [24]. The Hartree-Fock (HF) method does not include electron correlation, but is the starting point for most higher level calculations. It is well known

that in almost all cases the Hartree-Fock method overestimates the activation energies for reactions. Generalized Gradient Approximation (GGA) density functional methods frequently underestimate activation energies [22]. We chose hybrid density functional methods (mixing exact exchange, i.e. HF exchange, into the density functionals) to avoid the known shortcomings of these two methods, while maintaining their strengths: namely low computational cost and generally good performance in structural and energetic predictions. Another strength of DFT is the small spin contamination for many open shell systems especially conjugated ones, which is crucial in correctly determining the molecular energy. Starting from the Hartree-Fock optimized structures for a stationary point, B3LYP [26], Becke's three parameter hybrid exchange functional [27] along with the Lee, Yang, and Parr gradient corrected correlation functional [28], was employed in geometry optimization and in vibrational frequency analysis. However, in spite of the excellent performance of the B3 functional in the prediction of thermodynamic properties [27] and structural characterizations[29], the B3LYP average error in predicting classical barrier heights [30] is often relatively large.

Another hybrid density functional BHandHLYP [26] (Becke's half and half exchange functional [31] along with the LYP [28] correlation functional), gave an average error of -0.8±2.7 kcal/mol for a number of reaction barrier heights [30], and was employed to better reproduce the height of barriers and presumably the transition state geometries. Previous studies showed that the BHandHLYP method is a reasonable tool for the characterization of reactions [30,32,33]. In the present study, BHandHLYP also was used for predictions with a larger 6-311++G** basis set.

Inspired by Becke's one parameter protocol [34] and Perdew and Ernzerhof's rationale

for mixing exact exchange into DFT [35], Adamo and Barone [36] proposed new adiabatic connection methods (ACMs): B1LYP and B1PW91. The tests of B1LYP and B1PW91 on the reduced G2 data set show that B1LYP gives essentially the same performance as the B3LYP model but with no fitting of parameters. Considering the similarity and the simplicity of BHandHLYP and B1LYP, B1LYP also was employed in the present study. Aside from the improvements due to PW91PW91 in the description of van der Waals complexes, mPW1PW91 [37] also was shown to be one of the best density functional approaches for structure and thermochemistry. This new approach was employed along with the B1LYP method in the present study. Discussions of thermodynamics in the present study mainly are based on the BHandHLYP, B1LYP, B3LYP, MPW1PW91, and MP2 results. The gradient corrected exchange functional, Becke's 1988 exchange functional (B) [38], was used without the inclusion of exact exchange in the present study to study the role of exact exchange in the prediction of molecular properties.

For comparison of DFT with traditional *ab initio* methods, MP2 [39] was employed in this study. As a compromise between accuracy and computational complexity, Pople's split polarization valence basis set 6-31G* was used in nearly all predictions. For the triplet and singlet intermediates for the initial reaction of oxgen with benzene, the coupled cluster (CC) method with single and double substitutions and non-iterative triple excitations [40] (CCSD(T)) for all electrons were employed in single point energy calculations. Møller-Plesset perturbation theory (MP) [39] up to fourth order and CCSD(T) with the 6-311G** basis set were used for the relative energies of the epoxide and oxepin isomers.

Most calculations were performed with the Gaussian 98 A.7 program on a Silicon

Graphics Origin 2000 server with 4 R12000 processors located at the University of Waterloo. Computational facilities also included a Pentium II 300 MHz personal computer under Linux with the PGI group Fortran compiler used to set up for Gaussian 98 and an 8-processor SGI Challenge server with Gaussian 98 A.5 in the Department of Chemistry and Biochemistry at the University of Guelph.

4.3 Theoretical Results and Discussion

4.3.1 The initial reaction of oxygen with C_6H_6

When an oxygen atom approaches benzene, there are at least six different possible pathways for reaction of the atom with the ring as shown in Scheme 4-1. From above the triplet oxygen atom could add to one carbon atom to form a radical intermediate. The oxygen atom could approach the center of the ring to form a highly symmetric complex. Within the plane of the benzene ring, the oxygen atom may approach a C-C bond but first will interact with the two hydrogen atoms connected to these two carbons. In this approach, depending on the positions of the two hydrogen atoms, two paths exist. One has the two hydrogens in the symmetry plane and a C_{2v} structure results; another has the two hydrogen atoms on different sides of the oxygen in a C_2 structure. A fourth route involves an oxygen atom adding directly to the center of the C-C bond from above to form an epoxide structure. Oxygen also could attack directly a hydrogen and abstract it from the benzene to form the OH and C_6H_5 radicals. Finally, oxygen could insert into a CH bond and thus directly produce phenol. Only the pathways which produce stable benzene oxides will be discussed, i.e., the pathways for formation of the radical intermediate and of the C_2 structure.

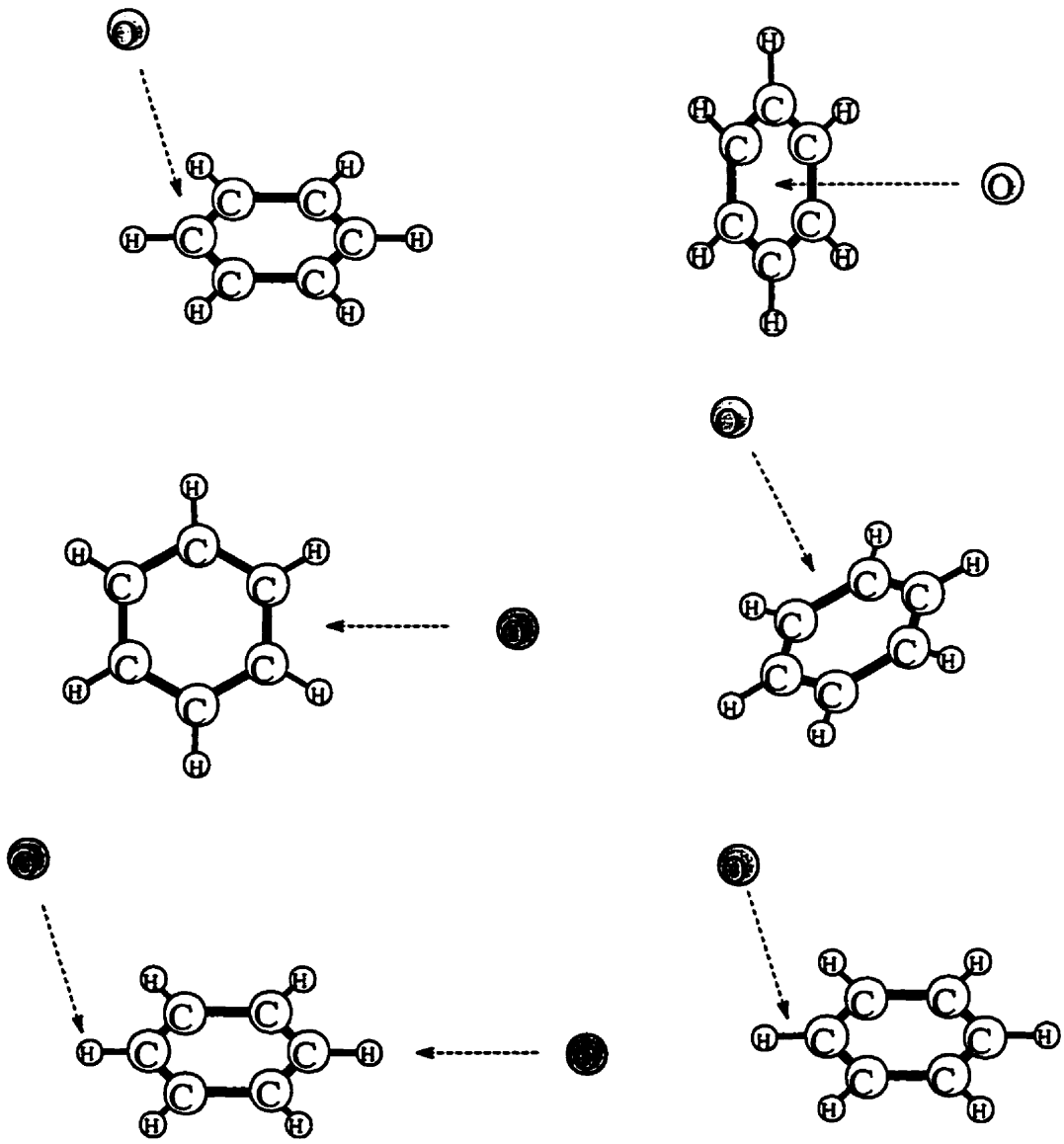

Scheme 4-1 Possible pathways for the reaction of the oxygen atom (^{3}P) with benzene

4.3.1.1 Initial reaction barrier

In the case of attack by oxygen on one carbon atom, a diradical (**4-3**) with C_s symmetry forms before inter-system crossing and the subsequent OCC ring closure to form an epoxide of C_s symmetry. The geometries of isomers are presented in Figure 4-1 and the reaction pathway is shown in Figure 4-1A. With all methods, a transition state (**4-2**) was located between the separated reactants and the diradical product. The harmonic vibrational frequency calculations verified that this stationary point is a transition state with only one imaginary vibrational mode that involves the backwards and forwards motion of the oxygen and the carbon atom under attack. In the transition state, there are small alternations among the CC bonds and all CC bonds lengthen compared with benzene. The CC bonds connecting the carbon atom which was attacked lengthen while the other four bond lengths are close to typical aromatic bond lengths. The oxygen atom forms a weak bond with the carbon atom which is attacked. From the HF, BHandHLYP, B1LYP, B3LYP to the BLYP methods, the distance between these two atoms increases from 1.801 Å at the HF level to 2.052 Å at the BLYP level. The CO distance at the MP2 level lies between those of BHandHLYP and B1LYP, while MPW1PW91 predicts a similar structure to that of B1LYP and B3LYP.

At the HF level, the activation barrier is 13.5 kcal/mol, which is obviously rather higher than the experimental value of 4.4±0.5kcal/mol [15] (or 4.1±0.5kcal/mol [16]). This activation barrier decreases to 7.9 Kcal/mol at the BHandHLYP level. As the weight of exact exchange decreases from B1LYP (0.25) [36] and B3LYP (0.21) [27] to BLYP (0.00), the activation barrier decreases further. The barrier is zero at B3LYP and negative at the BLYP level. MPW1PW91 behaves similarly to B1LYP for the prediction of the

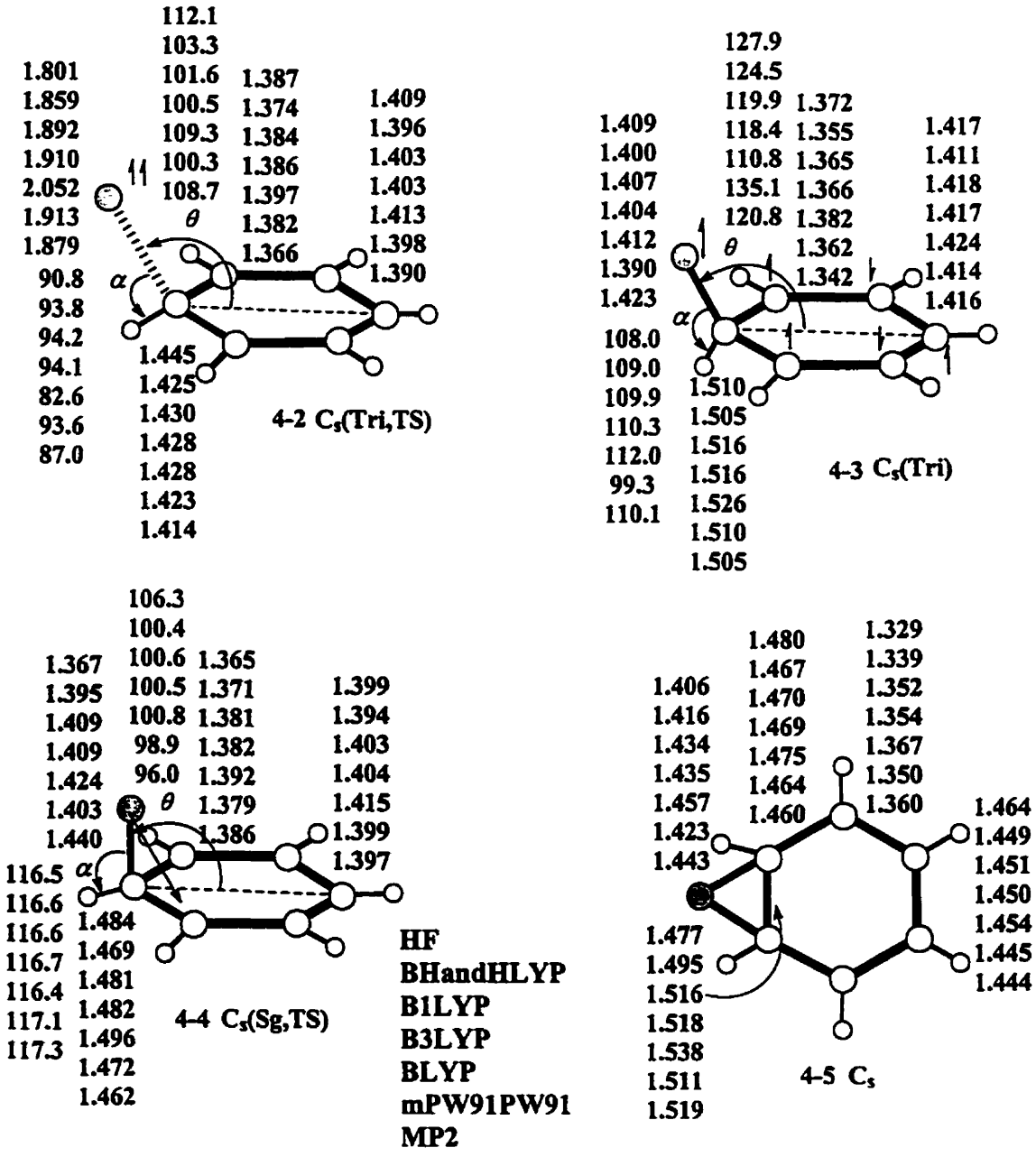

Figure 4-1 Geometries of the triplet transition state 4-2, triplet intermediates of initial reaction 4-3, the singlet "walk" transition state 4-4 and epoxide 4-5

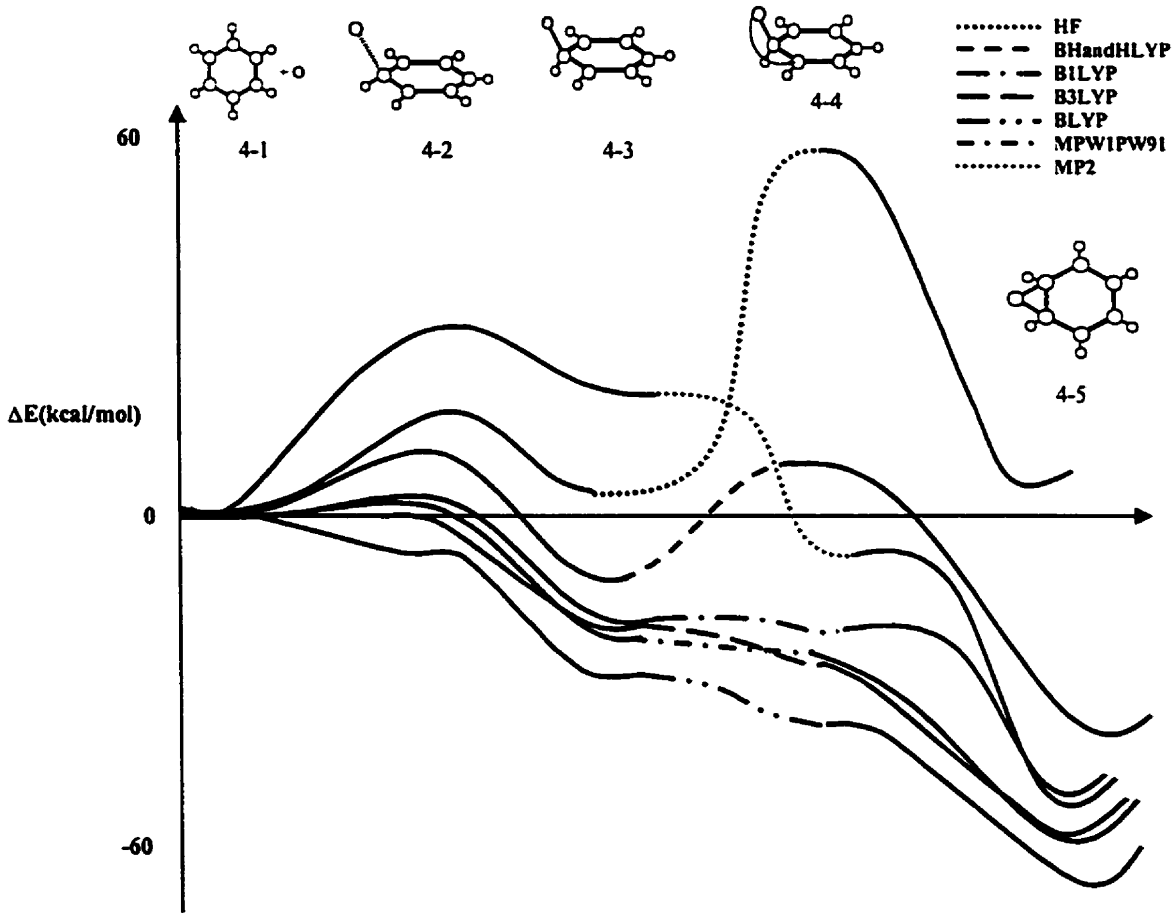

Figure 4-1A Illustration of the energies of the initial reaction of oxygen (^{3}P) with benzene

activation barrier. Due to high spin contamination in the MP2 calculations on open shell species, MP2 predicts a much higher activation barrier than the other methods. All the energies of the isomers relative to the energy of the reactants (triplet oxygen and benzene) are given in Table 4-1. Judging from the activation barrier, only the BHandHLYP, B1LYP and mPW1PW91 functionals well characterize the transition state. B1LYP and mPW1PW91 predict activation barriers closer to experiment than does BHandHLYP. B1LYP and mPW1PW91 have smaller barriers than experiment while BHandHLYP has a larger barrier than experiment. To decide which method should be chosen for other calculation, the 6-311G**, 6-311G(2df,2p), 6-311++G(2df,2p) basis sets were used with the BHandHLYP and mPW1PW91 functionals (B1LYP appears to have similar behavior to mPW1PW91) to calculate the activation barrier at the transition state. The predicted barriers from BHandHLYP are 9.3 kcal/mol, 8.8 kcal/mol, and 8.0 kcal/mol, with the three basis sets respectively. mPW1PW91 predicted the barrier to be 2.4 kcal.mol, 1.9 kcal/mol and 1.3 kcal/mol respectively. Although mPW1PW91 predicted results closer to the experimental value than BHandHLYP, the barriers approach the experimental value from below. As the basis set becomes larger, the barrier continually decreases. So mPW1PW91 (and presumably B1LYP) shows incorrect direction of convergence for this barrier with respect to basis set convergence, while BHandHLYP does show the correct trend in convergence as the basis set increases to its limit.

Table 4-1. Relative energies of the isomers in Figure 4-1 (in kcal/mole)([$\Delta E=E_n-(E_{oxygen}+E_{benzene})$])

Isomers	HF	BHandH LYP	BHandH LYP*	B1LYP	B3LYP	BLYP	mPW1PW91	MP2
4-1	0.0	0.0	0.0	0.0	0.0	0.0	0.0	0.0
4-2	13.5	7.9	8.8	1.7	0.0	-6.3	1.4	35.4
4-3	3.7	-6.7	-5.1	-10.0	-11.2	-21.8	-12.9	18.1
4-4	52.7	5.1	4.6	-10.5	-15.9	-29.6	-13.2	-5.2
4-5	4.4	-38.7	-35.9	-47.4	-51.8	-58.2	-53.7	-51.1

Basis set (except for BHandHLYP*): 6-31G*

BHandHLYP*: BHandHLYP/6-311++G**

The barrier predicted by BHandHLYP would be expected to approach the experimental result from above based on the barriers from BHandHLYP with the basis sets used. Based on this test, BHandHLYP was chosen for further predictions for this reaction. The 6-311++G** set was used to examine the effects of both diffuse functions and polarization functions on the activation barrier. BHandHLYP/6-311++G** predicted a barrier of 8.8kcal/mol, the same as BHandHLYP/6-311G(2df, 2p). Diffuse functions and polarization functions have similar effects on this quantity i.e. lowering the activation barrier. As a compromise between the probable accuracy and the CPU and other computational demands, BHandHLYP/6-311++G** was chosen for the higher level predictions on all species. For the unrestricted open shell methods, which are the defaults in the Gaussian code, the energy of an open shell system includes effects due to spin

Table 4-2 $<S^2>$ of the triplet transition state 4-2 and the triplet intermediate 4-3

Species	HF	BHandH LYP	BHandH LYP*	B1LYP	B3LYP	BLYP	mPW1PW91	MP2
4-2	2.6891	2.1257	2.1172	2.0489	2.0354	2.0149	2.0499	2.6326
4-3	2.4800	2.1014	2.0912	2.0436	2.0325	2.0108	2.0509	2.4086

BHandHLYP*: BHandHLYP/6-311++G**

$<S^2>$(pure triplet)=2.0000

contamination. An increase in spin contamination exaggerates the activation barrier [41]. Table 4-2 lists the $<S^2>$ of the transition states and intermediates with all eight methods. Obviously HF and MP2 show serious spin contamination. It is not unexpected that UMP2 has a large spin contamination since its starting point is the strongly spin contaminated UHF wavefunction. From BHandHLYP to BLYP, as the weight of exact exchange decreases in the functionals, spin contamination decreases. Exact or Hartree Fock exchange appears to be the cause of spin contamination in the current hybrid density functional methods. Compared with HF and MP2, BHandHLYP shows less spin contamination although it still has larger spin contamination than BLYP which does not include exact exchange. An increase in basis set size (from 6-31G* to 6-311++G**) reduces the spin contamination.

4.3.1.2 The triplet intermediate, 4-3

The system goes through the transition state to form a triplet state intermediate before the stable singlet benzene oxides can form. In the triplet intermediate, the oxygen binds *via* a single bond to the carbon atom which is attacked. The structure of this intermediate is similar to the transition state, however, the hydrogen connected to the carbon atom under attack by oxygen is bent further out of plane with respect to the benzene skeleton in the intermediate. The differences among the CC bond lengths are larger in the intermediate than in the transition state with respect to the CC bond length in benzene. The two CC bonds at the carbon which is attacked and the other two CC bonds farthest from that attacked carbon lengthen (to about 1.510 Å for the first two bonds and 1.420 Å for the second two). The CC bonds connecting these two sets of CC bonds decrease (to 1.360 Å). These changes result from the unpaired electron distribution among the heavy atoms. In the transition state, the two unpaired electrons remain mostly on the oxygen atom. Given the long CO distance, the interaction between the oxygen and the benzene moiety is relatively weak. Thus there is only a small change in the structure of the benzene. In the triplet intermediate, one electron remains on the oxygen atom, while the other localizes mainly on the carbon across from the carbon which was attacked by the oxygen. This spin density distribution produces two CC bonds with mostly double bond character. The CC bonds of the carbon with one unpaired electron on it have typical aromatic bond characteristics (the unpaired electron on the carbon is in conjugation with other four π electrons) and the other two CC distances are single bonds.

The triplet intermediate is a minimum with all methods except BLYP. BLYP predicted this structure to be a transition state, that is, the harmonic frequency

calculations indicated exactly one imaginary vibrational mode which involved the out-of-plane motion of the oxygen out of the symmetry plane. With distortion along the mode of the imaginary frequency, a minimum was located with the BLYP method. The structure of this minimum has changed very little compared to the transition state except for the loss of the symmetry plane. The minimum is 1.5 kcal/mol lower in energy than the symmetric structure. Larger basis sets (6-311G(2df,2p)) or a larger grid for numerical integration (500 for radial shell, 974 for angular points per shell, the default is 75, 302 respectively) with the 6-31G* basis set were use to check the effect of basis set and grid size in the DFT on the qualitative (minimum or transition state) structural prediction [41]. The calculations (larger basis set, larger grid with 6-31G*) indicated that the C_s symmetric structure is a transition state. The further addition of diffuse functions (6-311++G(2df,2p) on both heavy atoms and hydrogens did not change this prediction. Further when local DFT (SVWN/6-311++G**) was used to model the symmetric structure, the results indicated that the triplet intermediate is a minimum. Other GGA, namely PW91PW91, mPWPW91, and G96LYP [24] were employed to check the effects of the gradient correction in particular functionals. All three approaches predicted this C_s triplet structure to be a transition state. The imaginary vibrational mode is the rocking of the oxygen out of the symmetry plane. The behavior of the GGA, local and hybrid functionals, manifests the roles of gradient correction and exact exchange. The weight of exact exchange in a hybrid method, BxLYP, was set to x=0.0001, 0.010, 0.1000, 0.1500 and 0.2000 to check the role of exact exchange in the modeling of this structure. The new factorized functionals predicted this triplet species to be a transition state until the weight of exact exchange was increased to 0.2000. At 0.2000, the transition state takes on the

character of a minimum. As the weight factor of the exact exchange increases from 0.0001 to 0.1500, the magnitudes of the relative motions of the atoms in the imaginary mode change although the overall picture of the mode remains roughly the same. These changes reflect the change in the imaginary frequency as it increases from (i) 307 cm^{-1} with 0.0001 exact exchange to (i) 1683 cm^{-1} with 0.1500 exact exchange. We note that HF predicts a different potential surface from DFT around some critical points. This will be discussed later for a second order saddle point.

The addition of the oxygen atom destroys the π electron ring current around the benzene skeleton which stabilizes this typical aromatic molecule. Thus it is expected that the formation of the diradical will not be strongly exothermic as was observed in Table 4-1.

4.3.1.3 Intersystem crossing

An inter-system crossing must occur since the reactants are in a triplet state while the benzene oxides are in their ground state - singlet electronic states. Optimization of the triplet intermediate in its singlet electronic state resulted in a stationary point with C_s symmetry on the potential surface and the harmonic vibrational frequency calculations verified that this stationary point is a transition state with only one imaginary frequency. The mode of this imaginary frequency involves the "walk" of the oxygen atom around the benzene ring (as sketched in Figure 4-1): the oxygen migration from one CC bond to another, and so on, i.e. the epoxide undergoes a degenerate rearrangement. This process has a similar activation energy [43] to the previously studied migration of a methylene group around the benzene ring. There is no symmetry forbidden nature to this reaction as

there is for a methylene group migration in cycloheptatriene. With no hydrogens attached to the oxygen atom, the lone pair electrons on oxygen can smoothly adjust themselves to the geometry of the structure. This mechanism was confirmed through the technique of H labeling [3c] in an early experiment studying the photolysis of benzene oxide. The geometric structure of the singlet transition state is similar to the triplet intermediate especially in the region of the ring attacked by the oxygen. The major difference is the bond angle formed by the oxygen, the carbon attacked and the carbon atom within the symmetry plane as illustrated in structures **4-2**, **4-3**, and **4-4** of Figure 4-1. The structures of these species will be discussed later. The OCC angle within the symmetry plane becomes smaller in **4-4**, i.e. the oxygen atom approaches more closely to the benzene ring. The hydrogen on the carbon attacked by oxygen is bent further out of plane in **4-4**. The geometry change in 4 facilitates the closure of the OCC three-membered ring in the epoxide (**4-5**) and the oxygen migration within this epoxide. There is also more conjugation among the other carbon atoms in **4-4**, which makes the three CC bonds more aromatic as manifested by their bond lengths (ranging from 1.365 at HF to 1.415 at BLYP). This similarity in singlet and triplet geometries and energies inspired us to postulate an intersystem crossing mechanism through spin-orbit coupling. The spin-orbit coupling probably involves the oxygen atom and the coupling is important although the constant is relatively small [44].

The rationale of intersystem crossing necessitates the accurate prediction of the energy difference between the triplet and singlet states. At the MP2/6-31G* optimized geometries of the triplet and singlet states, CCSD(T) with all electrons correlated and the 6-31G* basis set was applied in single point energy calculations. Coupled cluster (CC)

Table 4-3 Relative energies (in kcal/mole) between structures 4-3 and 4-4 in their singlet and triplet electronic states calculated with 6-31G*

	MP2	PMP2	MP3	PMP3	MP4D	MP4DQ	MP4SDQ	MP4SDTQ	CCSD	CCSD(T)	B1LYP[a]
A	-22.5	-10.8	2.8	11.0	-2.8	2.9	-3.5	19.3	6.2	-3.9	0.6
B	-4.2	7.6	13.6	22.5	10.9	15.0	11.5	0.7	15.6	-23.6	6.0[b]
C	-47.8	-34.2	-25.2	-14.6	-29.8	-24.6	-15.1	-44.0	-15.5	-22.5	-17.1

CCSD(T)(full) with MP2/6-31G* optimized structures

A: $\Delta E=E_{4\text{-}4}-E_{4\text{-}3}$

B: $\Delta E=E_{4\text{-}3singlet}-E_{4\text{-}3triplet}$

C: $\Delta E=E_{4\text{-}4singlet}-E_{4\text{-}4triplet}$

a: 6-311++G** b: -1.6kcal/mol(UB1LYP)

theory has been shown to be one of the most reliable methods for structures [45] and energetics [46]. The energy differences of these two species in both their singlet and triplet electronic states are listed in Table 4-3. MPn up to the level of MP4SDQ were performed along with the CCSD(T) approach. The energy differences predicted by these methods are listed in Table 4-3 as well. CCSD predicted that **4-4** is higher in energy than **4-4** while the addition of triple excitations in CCSD(T) switched the energetic order of the two structures. A divergent behavior in MPn [47] for the energy differences was observed. In order to check the effects of the triple contributions, MP4SDTQ also was employed to predict the relative energies of these species. Similar to the triples contribution in CCSD(T), the addition of triple substitutions in MP4SDTQ switched the energetic order of **4-3** and **4-4** predicted by MP4SDQ, although the difference is small. A preliminary

conclusion can be drawn from this observation that there could be multiconfiguration character in this region. The vertical energy difference between the lowest triplet and singlet states of **4-3** and **4-4** with MP2 optimized geometries were predicted by MP4 and CCSD(T). For isomer **4-3**, except for MP2 and CCSD(T), all methods predicted the singlet state is above the triplet state on the potential surfaces. MP2 predicted that the singlet state is 4.2 kcal/mol below the triplet state. CCSD(T) predicted an even larger gap between these two states, with the singlet 23.6 kcal/mol lower than the triplet. The predicted energy changes very for these two states (almost 40 kcal/mol) from CCSD to CCSD(T). Although this change from MP4SDQ to MP4SDTQ is large, it is still much smaller than that from CCSD to CCSD(T). For isomer **4-3**, the energy differences between the singlet and triplet states predicted by all methods are consistent i.e. the singlet is about 20 to 30 kcal lower in energy than the triplet electronic state.

Scheme 4-2 illustrates the relative energetic order of the singlet and triplet states of **4-3** and **4-4**. With MPn and CC, no definitive conclusion regarding the relative stability can be drawn from the calculations on **4-3**. The relative order of the singlet and triplet state of isomer **4-4** appears to be established clearly. Further calculations are necessary to clarify the relative energies of singlet and triplet **4-3**. Unrestricted HF solutions with high spin contamination make MPn and apparently in the case of **4-3** even CC predict the energy of the open shell triplet electronic states inaccurately due to spin contamination. For conjugated systems such as **4-3** with a high degree of electron delocalization, caution is advised in the application of CC and MPn.

Scheme 4-2 Illustration of the relative energy of the singlet and triplet states of 4-3 and 4-4

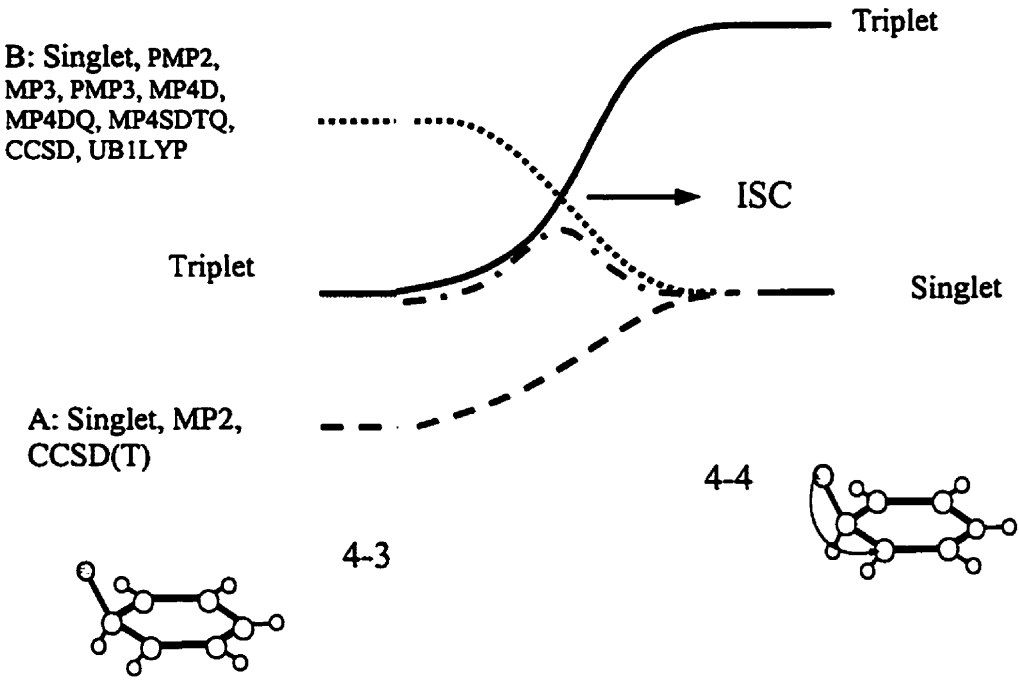

Previous studies [48,49] with DFT on some situations where multiconfiguration character was anticipated showed DFT is capable of describing some critical points with multiconfiguration electronic character. B1LYP was used here to perform unrestricted natural orbital (UNO) analysis and energetic predictions due to comparable performance to B3LYP with even better results in some difficult cases. Its simpler parameterization (without any empirical fitting) is also noteworthy [36]. Although the active space involves 2 electrons and 2 orbitals at UB1LYP, the calculation showed that the singlet of isomer **4-3** is likely to be an open shell singlet, i.e. a singlet biradical with inherent multiconfiguration character. The energy difference predicted by B1LYP/6-311++G** is also listed in Table 4-3, both at the restricted and unrestricted levels. The energy difference between the singlet and triplet states of isomer **4-3** and the energy difference between isomer **4-3** in the triplet state and isomer **4-4** in its singlet state are small. So it is plausible that inter-system crossing takes place in this region. The order of the states changes from the restricted B1LYP to the unrestricted B1LYP due to the release of the constraint on the alpha and beta Kohn-Sham orbitals.

Unrestricted B1LYP overestimates the energy of the singlet state compared with the triplet electronic state. BHandHLYP predicted that isomer **4-3** was lower in energy than isomer **4-4**, while other DFT methods predicted 4 to be lower than **4-3**, although the energy difference was small. Such a result could be due to the large component of exact exchange in BHandHLYP. HF still predicted that isomer **4-3** was 49 kcal/ higher in energy than isomer **4-4** (much higher than with other methods).

After an inter-system crossing, the system is in the singlet electronic ground state. Through transition state **4-4**, the first stable epoxide product **4-5** could be formed. The

overall formation of this epoxide is highly exothermic (about 40 to50 kcal/mol) at all theoretical levels except HF. The energy released is sufficient for the system to overcome the first barrier as well as provide the activation energy for ring closure in the next step. By all methods except HF, the ring closure transition state (**4-4**) is lower (2.8 kcal/mol at BHandHLYP/6-31G* to 40.6 kcal/mol at MP2/6-31G*) in energy than the first triplet transition state **4-2**. This energy release allows the reaction to proceed.

HF predicts that the overall reaction is endothermic and all the intermediates and product are higher in energy than the initial reactants. The relative energies are shown in Table 4-1. This performance is no doubt due to the well-known bias of HF for high spin states due to its lack of inclusion of opposite spin correlation.

The potential curves for the B1LYP, B3LYP, BLYP and mPW1PW91 functionals are similar to those illustrated in Figure 4-1A. Due to serious spin contamination, the potential curves from HF, MP2 and BHadnHLYP appear different. The different behavior of different methods is clearly obvious for the relative energy of **4** and the reactants.

4.3.2 Isomerization pathway from epoxide to 7-Oxa-norbornadiene

4.3.2.1 Relative stability of benzene epoxide and oxepin

Epoxide **4-5** isomerizes easily to oxepin by breaking the CC bond in the three-membered ring. This bond is weakened due to the constraint of the three membered ring. The epoxide-oxepin valence tautomerism was studied experimentally in the 1960s. The epoxide **4-5** is 7 kJ/mol (1.67 kcal/mol) lower in enthalpy than the oxepin **4-7** as measured by ^{1}H NMR [20]. Previous single point calculations by MP2, MP3, MP4 and QCISD(T) at the MP2 optimized geometries (all with the 6-31G* basis set) favor **4-5** but with a very small energy difference. At HF, BHandHLYP, B1LYP, B3LYP and BLYP levels, **4-5** is about 1.6 kcal/mol higher in energy than **4-7**, while MP2 and mPW1PW91 predict that **4-5** is (2.5 and 1.8 kcal/mol respectively) lower in energy than **4-7**. In addition to these predictions, single point calculations, MP4SDTQ(full) and CCSD(T)(full) with the 6-31G* and 6-311G** basis sets, were used to determine the order of these two isomers. The relative energy differences are given in Table 4-4. Without ZVPE correction, the MP4 and CCSD(T)(full) with 6-31G* favor **4-5** over **4-7** by approximately 1 kcal/mol and 0.5 kcal/mol respectively. With ZPVE correction considered (using the MP2/6-31G* ZPVE correction), **4-5** and **4-7** are equal in energy at the CCSD(T)(full) level and **4-5** is 0.5 kcal/mol above **4-7** at MP4. With the 6-311G** basis set (except for MP2 and MP4SDTQ), all methods predicted that **4-7** is lower than **4-5**, although the difference is only about 0.3 kcal/mol. From these calculations, no definitive conclusion can be drawn about the relative stability of the epoxide and oxepin other than that these two isomers are close in energy. One should note that the

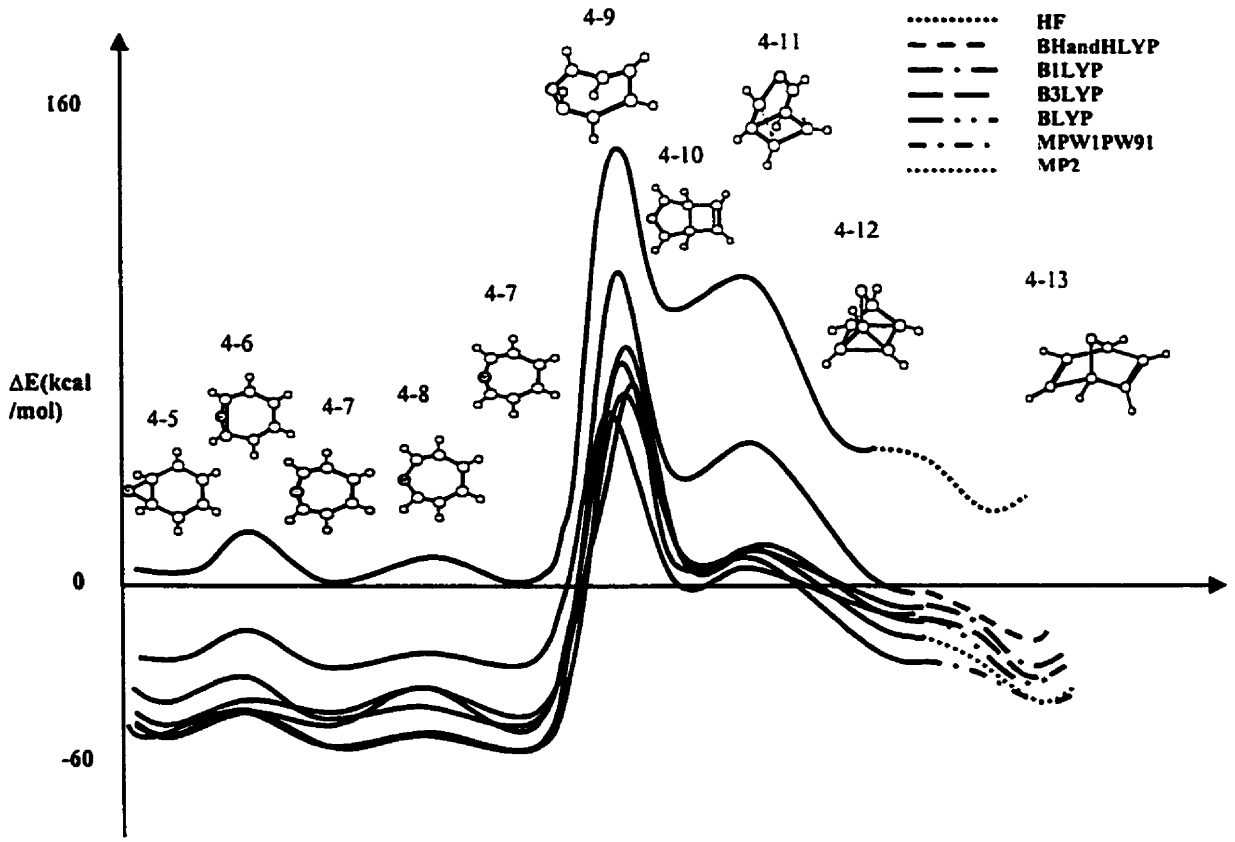

Figure 4-2 Isomerization pathway from epoxide to 7-Oxa-norbornadiene

experiments were carried out in solution and the solvent effect could be important in the case of such small energy differences [22]. To isomerize to **4-7**, **4-5** needs to overcome an 8.8 kcal/mol barrier through a transition state [20]. Except for HF, all methods predicted an energy barrier in reasonably good agreement with experiment. Among these predictions, the BHandHLYP and mPW1PW91 functionals give the best estimates of the barrier.

Table 4-4 Relative energies of the (C_s) epoxide 4-5 and (C_s) oxepin 4-7 (in kcal/mole) ($\Delta E=E_{oxepin}-E_{epoxide}$)

	MP2	MP3	MP4D	MP4DQ	MP4SDQ	MP4SDTQ	CCSD	CCSD(T)
6-31G*Aa	3.5	0.8	1.1	1.1	1.0	-	0.5	0.5
6-31G*Ab	3.0	0.3	0.6	0.5	0.5	-	0.0	0.0
6-311G**B	2.2	-0.6	-0.1	-0.2	-0.1	0.7	-0.3	-0.2

A: CCSD(T)(full) a: without ZVPE correction b: with ZVPE correction

B: MP4(SDTQ)(full), CCSD(T)(full)

At the MP2 optimized geometries

The structures of the isomers in Figure 4-2 are reported in Figures 4-2A and 4-2B. The epoxide resembles a diene rather than an aromatic compound if the CC bond lengths are considered. The CC bond in the epoxide ring and the two CC bonds connecting the CO bonds are single bonds judging from their lengths. The CC bond opposite the epoxide ring is a single bond as well (distance from 1.464Å at HF to 1.444Å at MP2). The remaining two equivalent CC bonds are double bonds (distance of 1.329Å at HF to 1.360Å at MP2). At the HF level, the formation of the epoxide is endothermic relative to reactants by 4.4 kcal/mol. The other methods predict that the formation of the epoxide is somewhat exothermic by approximately 40 to 50 kcal/mol.

The Hückel rule implies that the eight π-electron ring should distort to minimize the unfavorable anti-aromatic character in oxepin. The oxygen atom lies out of the carbon atom ring, which gives an overall boat shape to the oxepin. From the bond lengths, oxepin adopts a triene structure. The shape of oxepin does not change much compared with the epoxide structure as pointed out in a previous study [22]. The CC bond distance of the two carbon atoms connecting the oxygen atom lengthens from about 1.5Å in the epoxide to 2.3Å in the oxepin. These carbons are obviously bonded in the epoxide and nonbonded in the oxepin. In the transition state connecting the closed epoxide and the open oxepin structures, the distance between the two carbon atoms connecting oxygen lies between the epoxide and oxepin values (ranging from 1.819Å at HF to 1.902Å at MP2).

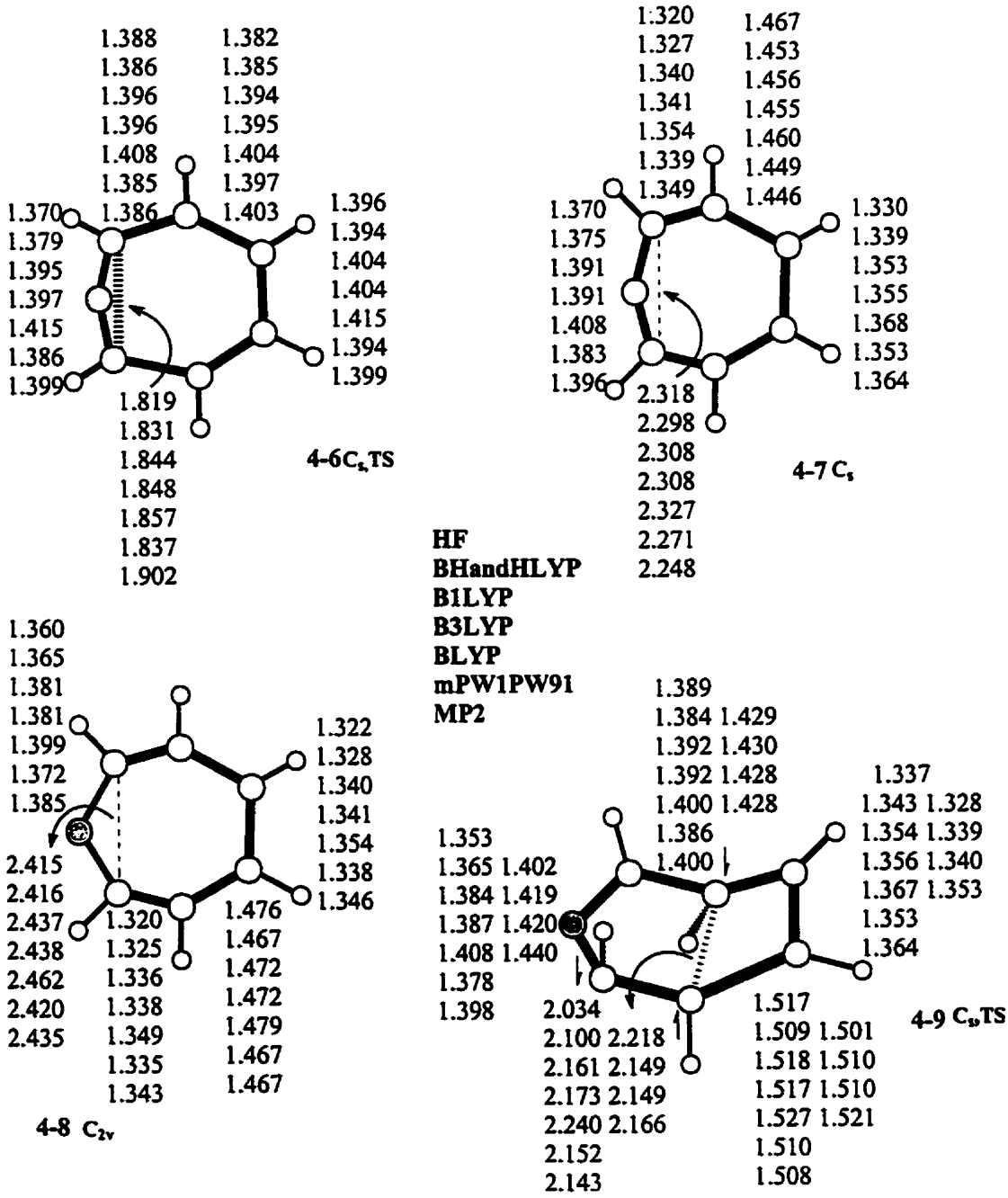

Figure 4-2A Geometries of oxepin 4-7 and transition states 4-6, 4-8 and 4-9 (for structure 4-9, the first column contains the closed shell singlet bond lengths and the second open shell singlet results)

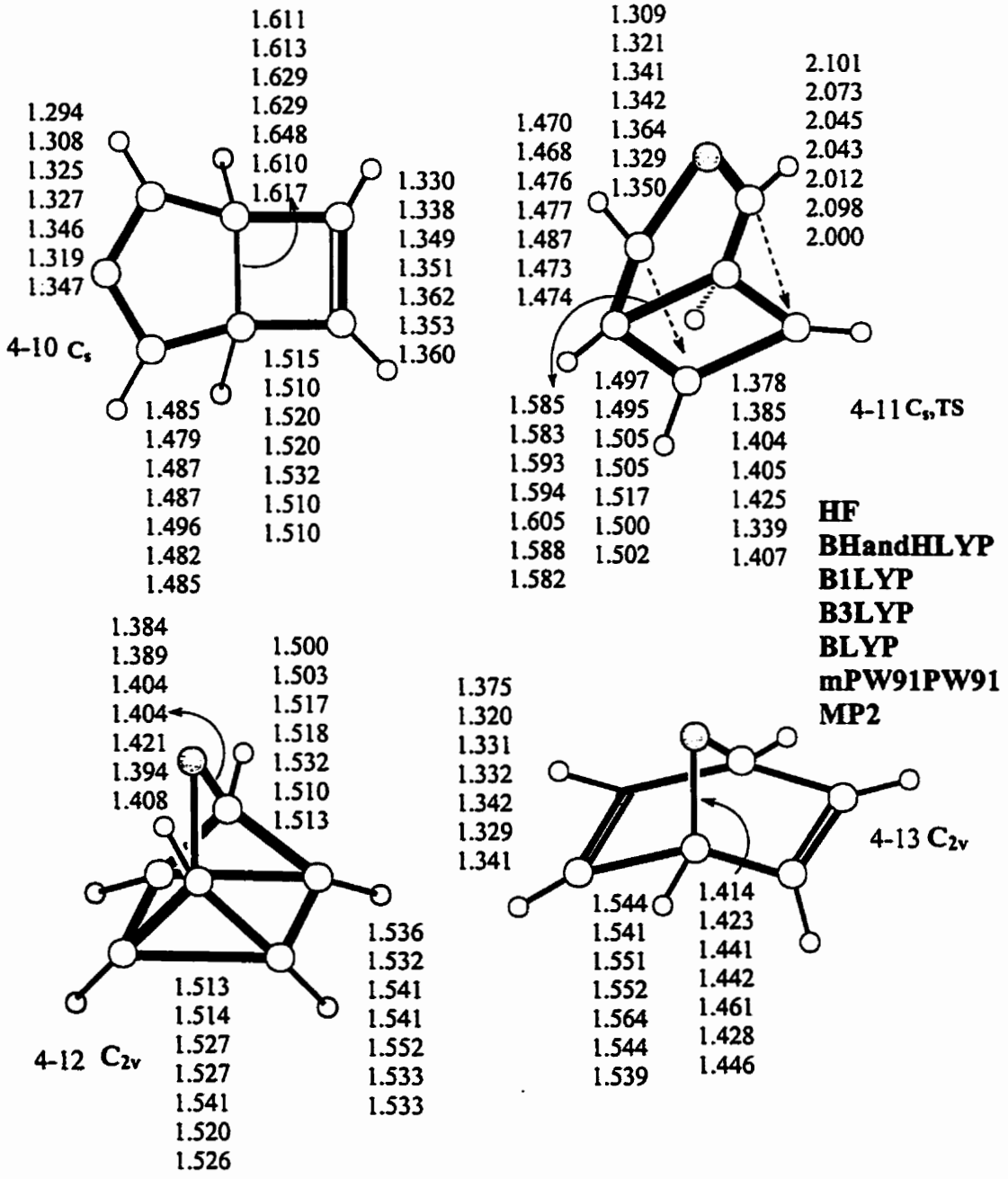

Figure 4-2B Geometries of (C_s) 3-Oxa-bicyclo[3.2.0]hept-6-ene, 4-10, transition state to 3-Oxa-quadricyclane, 4-12, and 7-Oxa-norbornadiene, 4-13

4.3.2.2 Isomerization of oxepin

Oxepin, can easily invert to an equivalent structure through a planar transition state **4-8** as illustrated in Figure 4-2. The inversion barrier of oxepin is predicted by the methods used to be about 3.0 kcal/mol. There are no large changes in the bond distances in the transition state compared with oxepin as would be expected given the small energy change. The imaginary vibrational mode involves merely the bending of the oxygen out of the molecular plane.

Oxepin could isomerize further by the bonding of two carbons in the seven-membered ring. The bonding of the two β carbon atoms results in a 4,5-membered ring compound (C_s)3-Oxa-bicyclo[3.2.0]hept-6-ene, **4-10**, through a transition state of C_s symmetry (**4-9**). (C_s)3-Oxa-bicyclo[3.2.0]hept-6-ene is also a possible adduct of furan and acetylene, in which the acetylene attacks the CC single bond in a 2,2-addition. The structure of **4-10** has more strain than oxepin since the formation of the four-membered ring requires that the CC bond angle be almost 90°. This calculation indicated that the formation of this structure from oxepin is endothermic. MP2 and the various functionals in DFT predicted that the system needs to absorb about 60 kcal/mol of energy in order to isomerize to **4-10** from oxepin (**4-7**). It is even more endothermic at the HF level (90 kcal/mol). The relative energies of the structures are reported in Table 4-5. The loss of the π electron conjugation due to formation of the four-membered ring also causes endothermicity as does the structural strain in the product. Compared with **4-7**, the structure in the five-membered ring of 10 changes greatly. The CC bonds in the five-membered ring change from double bonds to single bonds in **4-7**. The OC bonds become shorter due to the π electron conjugation of oxygen with its neighbouring carbons.

The transition state between **4-7** and **4-10** is similar in the four-membered ring region to that of **4-10** and similar in the oxygen portion to **4-7**. The CC bond-to-be in the transition state is about 2.1Å, lying between the corresponding values in **4-7** and **4-10**. Since the formation of **4-10** from **4-7** is highly endothermic, the activation barrier was expected to be large. The calculations with the restricted method predicted a barrier of 110 to 120 kcal/mol by MP2 and the various functional in DFTs. HF predicted the barrier to be as high as 173 kcal/mol as shown in Table 4-5 and Figure 4-2. Obviously, such a barrier rules out any chemical role for this pathway.

There may exist a lower energy solution that introduces multiconfiguration character for **4-9** due to the destruction of the π electron conjugation. Natural orbital analysis was employed to check the wavefunction at this point. Both unrestricted HF and unrestricted DFT calculations show that there exists an open shell singlet state lower in energy than the restricted singlet state at this point. With the unrestricted open shell wavefunction, all four DFT methods have been used to optimize the geometries of the open shell singlet structures. The $\langle S^2 \rangle$ values (listed in Table 4-6) indicate a large mixing of the triplet with the singlet electronic state. The HOMO-LUMO gaps of the α and β orbitals predicted by all methods used are equal in structure **4-9'**. As the mixture of exact exchange decreases, these gaps become smaller and smaller from UBHandhLYP to UBLYP as shown in Table 4-6. UMPW1PW91 predicts similar energy gaps to those of UB1LYP which indicates the importance of exact exchange in the prediction of this electronic property. The structures of both the closed shell and open shell singlet states are shown in Scheme 4-3. In the open shell singlet structure, the four-membered ring

Table 4-5. Relative energies of the isomers in the isomerization path from epoxide to 7-Oxa-norbornadiene (in kcal/mole)[$\Delta E=E_n-(E_{oxygen}+E_{benzene})$]

Isomers	HF	BHand HLYP	BHand HLYP*	B1LYP	B3LYP	BLYP	mPW1PW91	MP2
4-1	0.0	0.0	0.0	0.0	0.0	0.0	0.0	0.0
4-2	13.5	7.9	8.8	1.7	0.0	-6.3	1.4	35.4
4-3	3.7	-6.7	-5.1	-10.0	-11.2	-21.8	-12.9	18.1
4-4	52.7	5.1	4.6	-10.5	-15.9	-29.6	-13.2	-5.2
4-5	4.4	-38.7	-35.9	-47.4	-51.8	-58.2	-53.7	-51.1
4-6	17.3	-31.1	-29.1	-42.0	-46.7	-54.5	-47.1	-45.7
4-7	1.0	-40.0	-38.9	-49.0	-53.1	-60.0	-51.2	-48.3
4-8	4.0	-36.7	-35.4	-45.8	-49.9	-57.2	-47.5	-42.2
4-9	156.8	95.2	95.4	76.1	69.9	54.6	71.3	75.0
4-10	89.3	31.2	33.4	16.1	10.2	-0.9	7.6	4.9
4-11	94.0	34.7	37.5	20.9	14.8	5.7	8.9	10.3
4-12	42.9	-3.0	1.9	-7.7	-12.6	-14.2	-24.4	-16.1
4-13	21.8	-20.5	-18.5	-27.2	-31.3	-35.7	-35.4	-35.3
4-9′		69.8		62.1	58.6	50.4	63.2	

Basis set (except BH*): 6-31G*; BHandHLYP*: BHandHLYP/6-311++G**

4-9′: Open shell singlet; the structures of these isomers are shown in Figures 4-1 and 4-2.

Table 4-6 $<S^2>$ and HOMO-LUMO gaps (in a.u.) for the open shell singlet 4-9′

	UBHandHLYP	UB1LYP	UB3LYP	UBLYP	UMPW1PW91
4-9′	1.2452	1.1505	1.1242	1.0283	0.8756
α	0.24819	0.14905	0.12778	0.05288	0.15095
β	0.24819	0.14905	0.12778	0.05288	0.15095

$<S^2>$ (closed shell singlet)=0.0000

region shrinks while the five-membered ring including oxygen expands compared to the closed shell structure. The spin density distribution in the open shell singlet structure (as shown in Scheme 4-3) favors the formation of a new CC bond since the unpaired electrons on the two bonding carbons have opposite spin. Also for the open shell singlet state **4-9′** the barrier of the transition state corresponding to the closed shell species **4-9** is lowered by about **4-10** kcal/mol as shown in Table 4-5 and Scheme 4-3.

(C_s)3-Oxa-bicyclo[3.2.0]hept-6-ene, **4-10**, is high in energy on the potential surface as shown in Figure 4-2. It could isomerize to another minimum. The formation of the four- and five-membered rings in **4-10** implies sp^3 hybridization of the carbon atoms shared between the four- and five-membered rings. This hybridization renders the dihedral angle between these two rings smaller, which could facilitate ring closure of other carbons to form 3-Oxa-quadricyclane (isomer **4-12**). The transition state **4-11** between these two isomers resembles **4-10** except for the smaller dihedral angle along the reaction coordinate. The distance between the bonding carbons ranges from 2.0 Å to 2.1 Å with the methods employed. Other geometric data in the transition state are similar to those in isomer **4-10**. To overcome this transition state to reach **4-12**, isomer **4-10** needs to absorb

only several kcal/mole of energy (1.3 kcal/mol predictably at mPW1PW91, 6.3 kcal/mol by BLYP).

The formation of **4-12** from **4-10** is exothermic. 20 to 30 kcal/mol energy should be released upon reaction. **4-12** has C_{2v} symmetry. All the CC bonds in **4-12** are single bond. Isomer **4-12** is stable compared with the reactants ($O(^3P)$ + benzene). Different relative stability of **4-11** and **4-12** is predicted by B1LYP, B3LYP and mPW1PW91. mPW1PW91 predicts that **4-12** is lower in energy than **4-11** than do B1LYP and B3LYP do. mPW1PW91 predicts isomer **4-12** is more stable by 4 kcal/mol.

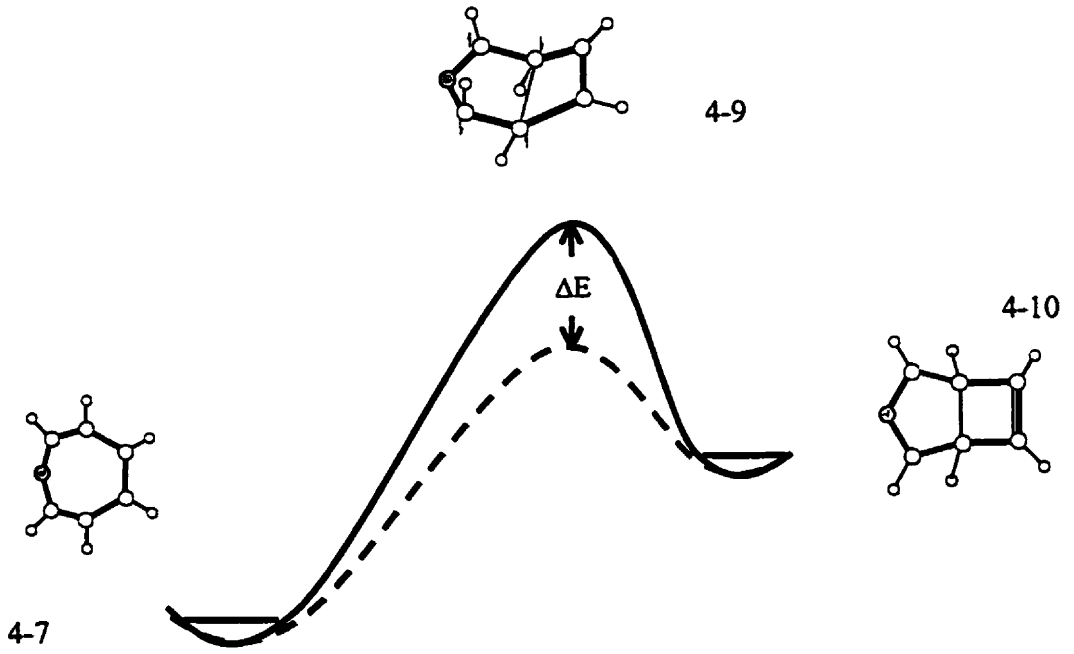

Dashed line is the potential curve for the open shell singlet

Scheme 4-3 Reaction pathways from oxepin to isomer 4-10 and an illustration of the spin distribution in the open shell singlet structure (C_s, TS)

Breaking of the two bridging CC bonds in **4-12** results in the formation of the 7-Oxa-norbornadiene (**4-13**). The calculations predict that the formation of **4-13** releases about 20 kcal/mol energy due to relaxation of geometric strain in **4-12**. The valence isomerization in these two isomers is similar to that of the norbornadiene-quadricyclane system. At the CCSD(T) level with the MP2 optimized geometry, the formation of quadricyclane from norbornadiene releases 24 kcal/mol energy [50]. The inter-conversion of these two isomers could involve excited states and intersystem crossing (or intersection) [50,51].

Photolysis and pyrolysis experiments on 3-Oxa-quadricyclane (isomer **4-12**) were performed more than twenty years ago by Prinzbach and Babsch [51]. Upon photolysis, **4-12** isomerizes to 7-Oxa-norbornadiene (**4-13**). In an acidic solution, **4-12** isomerizes to another isomer (isomer **4-20** in our study). Structure **4-12** isomerizes to oxepin (and there was an equilibrium between oxepin and benzene epoxide)[51] without acidic solution. An intermediate was assumed connecting **4-12** and oxepin in this experiment. The present theoretical study supports the proposed mechanism in this experiment for the photochemistry connecting oxepin to 7-Oxa-norbornadiene and 3-Oxa-quadricyclane system [51] and locate the reaction pathway by finding one minimum (isomer **4-10**) and two transition states (transition states **4-9** and **4-11**).

4.3.3 Isomerization pathway from epoxide to Dewar benzene oxide

Epoxide **4-5** could isomerize in a similar manner to **4-7** as that described above. **4-5** looks like a diene in the carbon ring region and the diene skeleton in **4-5** is planar. The two middle carbon atoms can bond to each other in transition state **4-14** and this bonding is similar to the ring closure in butadiene [52] as shown in Figure 4-3. The ring closure in **4-5** results in another epoxide (**4-15**) (a Dewar benzene oxide). Although the isomers connecting this transition state have C_s symmetry, the transition state has only C_1 symmetry which could be due to the geometric strain caused by the epoxide. The difference of the two OC bonds in the transition state is about 0.015Å (to 0.020 Å). The distance between the two bonding carbons is about 2.1 Å, similar to that in the transition state for the closure of butadiene [52b]. The structures of the isomers in Figure 4-3 are reported in Figure 4-3A. Compared with the cyclization of butadiene, the barrier for the ring closure in **4-5** is much higher than that of butadiene (43.8 kcal/mol for butadiene [52], about 80 kcal/mol for benzene oxide). The location of this transition state provides theoretical support for **4-15** isomerizing to **4-5** [53]. The relative energies of the isomers in Figure 4-3 are reported in Table 4-7.

The formation of **4-15** from **4-5** requires about 50 kcal/mol of energy. **4-15** becomes more bent than **4-10**. The interaction between the two carbons in the epoxide part causes strong bonding in **4-15**, this CC bond length is about 1.46~1.47 Å. Also the CC bonds next to this CC bond becomes longer. The bending in **4-15** renders the migration of oxygen from one side to the other possible. A transition state **4-16** has been located (for most methods) connecting the two identical isomers of **4-15** for oxygen migration. **4-16** has C_{2v} symmetry and the oxygen lies above the Dewar benzene.

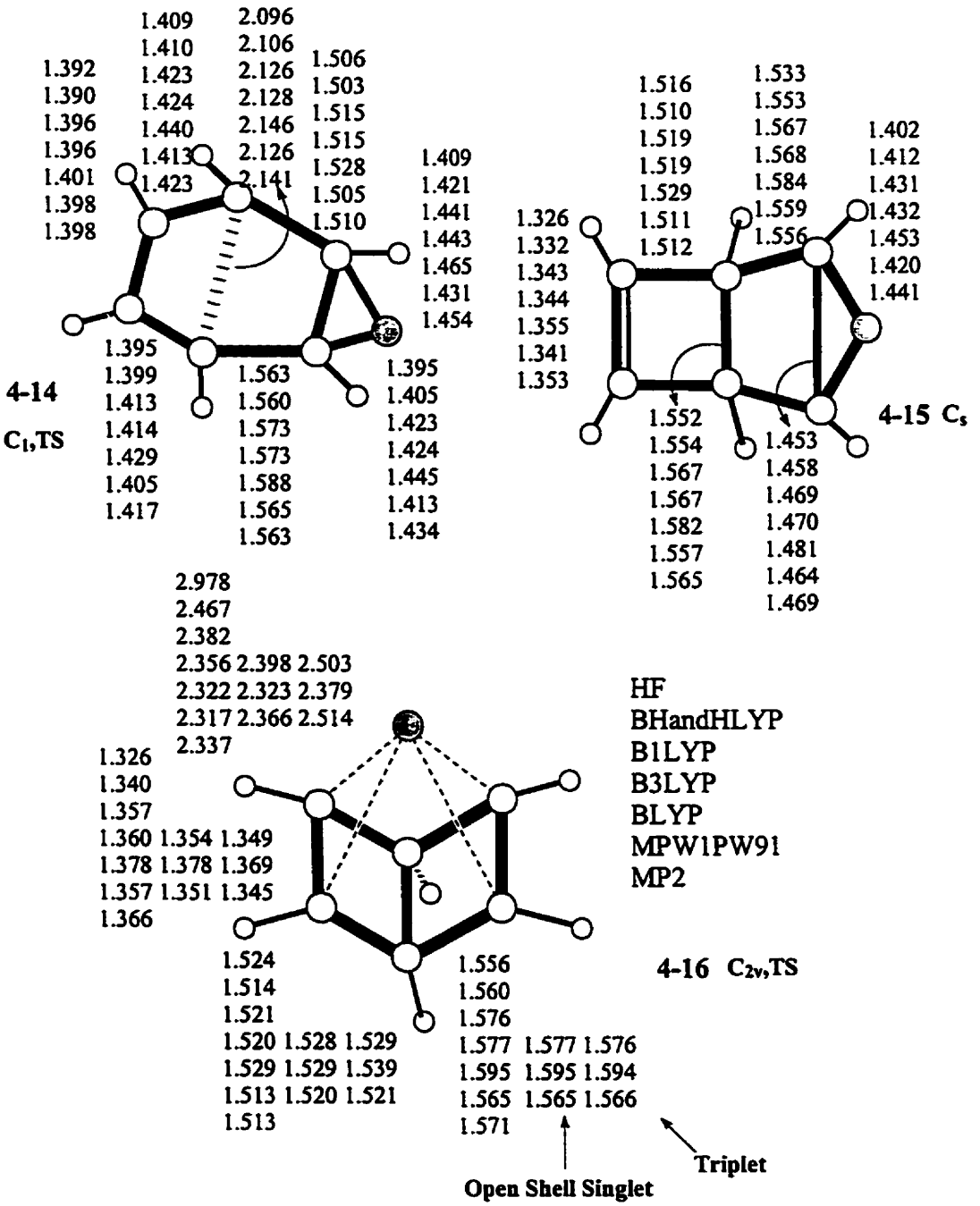

Figure 4-3 Geometries of Dewar benzene epoxide 4-15, transition states 4-14 and 4-16

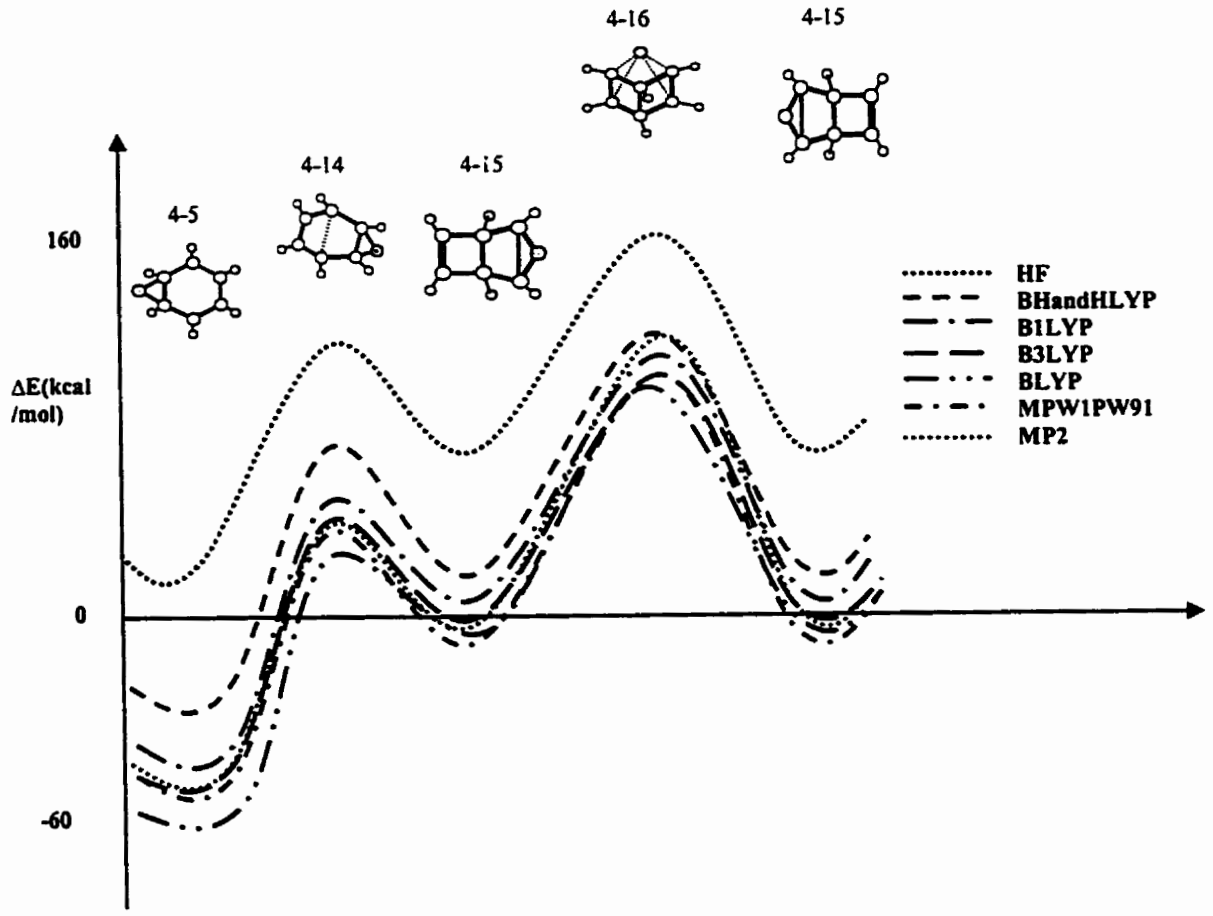

Figure 4-3A Isomerization pathway from epoxide to Dewar benzene oxide

Table 4-7. Relative energies of the isomers in the isomerization pathway from epoxide to Dewar benzene oxide (in kcal/mole)[$\Delta E=E_n-(E_{oxygen}+E_{benzene})$]

Isomers	HF	BHand HLYP	BHand HLYP*	B1LYP	B3LYP	BLYP	mPW1PW91	MP2
4-1	0.0	0.0	0.0	0.0	0.0	0.0	0.0	0.0
4-14	105.4	53.0	55.5	39.9	34.4	24.4	30.5	33.4
4-15	58.0	12.8	17.1	4.7	-0.04	-5.3	-7.2	-2.7
4-16	162.2	134.3	134.2	121.1	116.2	101.1	117.2	132.9
4-16[a]					88.1	77.9	86.3	
4-16[b]					75.8	68.1	73.0	

Basis set (except BHandHLYP*): 6-31G*

BHandHLYP*: BHandHLYP/6-311++G**

4-1 is the reactant of benzene with triplet oxygen atom; 4-16[a]: open shell singlet optimized geometry 4-16[b]: triplet optimized geometry

van Tamelen and co-workers synthesized a similar complex of Dewar benzene with palladium dichloride [53] to transition state **4-16**. In this experiment, the olefinic bond in Dewar benzene is prone to interact with an electron-deficient species while retaining a cyclobutadiene unit despite the availability of an aromatization pathway [53]. Although

oxygen is rich in electrons, its electronegativity allows it to accept additional electrons from another species. The analysis indicated that there was a small charge transfer from Dewar benzene (mainly from the four carbons of the double bonds) to oxygen in 16. The distance from oxygen to the four carbons of the double bonds is about 2.3 Å (2.5 Å at BHandHLYP and 3.0 Å at HF).

Among the methods employed (with the 6-31G* basis set), HF, BHandHLYP, B1LYP and MP2 predicted **4-16** to be a transition state. The harmonic vibrational frequency calculations yield only one negative eigenvalue for the Hessian matrix. The symmetry of the mode with a negative eigenvalue is b_1, involving the migration of the oxygen from one side to another out of the symmetry plane containing the middle carbon carbon bond. B3LYP, BLYP and mPW1PW91 predicted this structure to be a second order saddle point (SOSP). Even more tightly optimizing the geometry did not qualitatively change the results. The smaller negative eigenvalue is a b_2 mode involving the rocking of the oxygen within the symmetry plane mentioned above. Increasing the basis set to 6-311G** and tightening the geometry optimization caused the SOSP to become a transition state at the B3LYP and mPW1PW91 levels. Tighter optimization with BLYP/6-311G** predicated that this structure is a third order saddle point (TOSP). Addition of diffuse functions did not change this prediction. The symmetry of the mode (a_2) of the new negative eigenvalue involves bonding of oxygen with the two diagonal carbons.

The energy of **4-16** is much higher (about 110 kcal/mol) than **4-15**. The oxygen migration from one side to the other is difficult if it occurs at all as judged from the energetics. The discussion here is more theoretically interesting than of thermochemical

importance since different methods predict different natures for this stationary point. The loose complex of oxygen with the Dewar benzene in **4-16** could cause the wavefunction to be an open shell singlet that could mix the lowest triplet with the lowest singlet state. By the aid of natural orbital analysis, BLYP predicted this wavefunction to be an open shell singlet with two orbitals and two electrons in the active space. The release of the restriction on the α orbitals and β orbitals in the wavefunction should lower the energy of this stationary point. The single occupancy of the HOMO indicates that the weight of the triplet is large and suggests the closeness in energy of the lowest triplet state to the singlet in energy. Single point calculation of the open shell singlet (BHadnHLYP, B3LYP, BLYP and mPW1PW91) predicted that the open shell singlet is more than 30 kcal/mol (without ZPVE correction) lower in energy than the closed shell singlet.

Optimization of an open shell singlet state for **4-16** (by B3LYP, BLYP and mPW1PW91) indicated that the optimized open shell singlet is about 30 kcal/mol (or less) lower than the closed shell singlet. The $\langle S^2 \rangle$ ($\approx$1.000) are listed in Table 4-8 for the open shell singlet structures predicted by all three methods and indicates the mixing of the triplet and singlet states. The BLYP optimized open shell singlet geometry is almost identical to the closed shell structure in spite of the 23 kcal/mol energy difference. At UB3LYP and UMPW1PW91, the distance from oxygen to the top carbons in the open shell singlet geometry increases by 0.042Å and 0.049Å respectively. The change in CC

Table 4-8 HOMO-LUMO gaps Δ (in Hartree) of the closed shell singlet, open shell singlet and triplet of 16, $<S^2>$ for the open shell singlet and triplet of 4-16

	UBHandHLYP	UB1LYP	UB3LYP	UBLYP	UmPW1PW91
Δ	0.18584	0.08288	0.06290	-0.02465[C]	0.07831
$<S^2>^A$			1.0020	0.0000	1.0032
$\Delta\alpha^A$			0.13528	-0.02615[D]	0.16000
$\Delta\beta^A$			0.13528		0.16000
$<S^2>^B$			2.0058	2.0061	2.0057
$\Delta\alpha^B$			0.22980	0.14679	0.24881
$\Delta\beta^B$			0.15630	0.06065	0.18163

S^2(closed shell singlet)=0.0000

S^2(triplet)=2.0000

A=open shell singlet, B=triplet

C: Orbital Energy E_{25} = -0.12106, E_{26}= -0.14571

D: Orbital Energy E_{25} = -0.11909, E_{26}= -0.14524

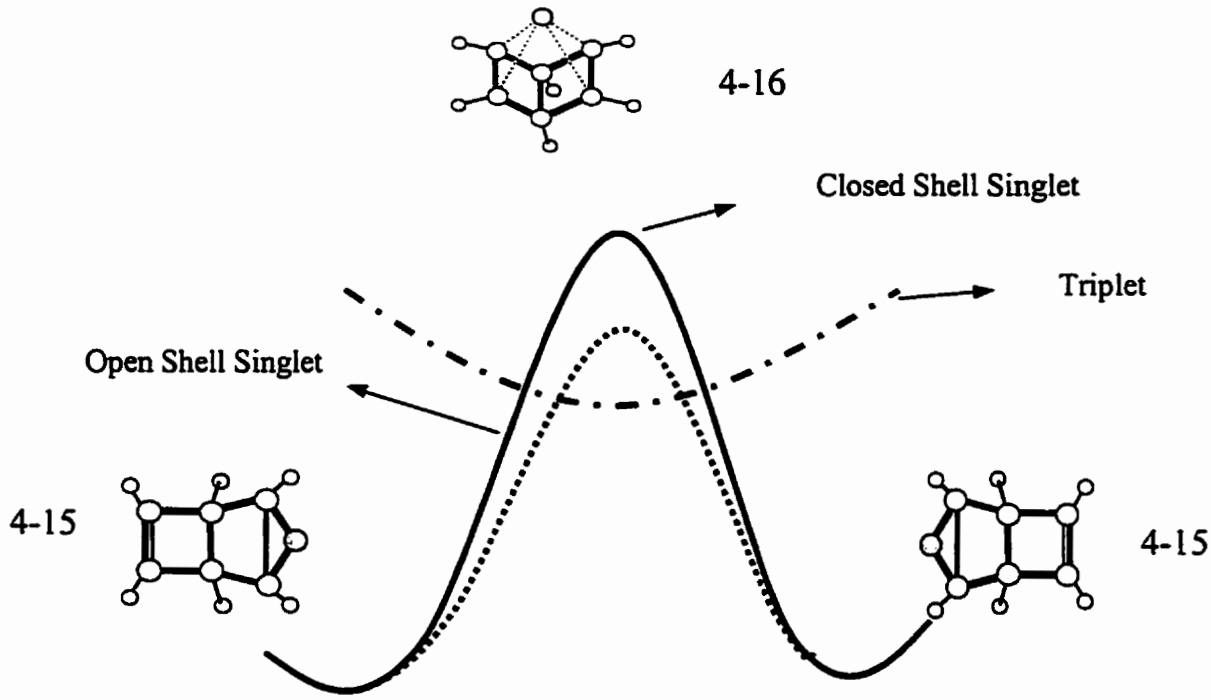

Scheme 4-4 Illustration of oxygen migration in Dewar benzene epoxide 4-15

bond length is not significant in this open shell singlet structure. Vibrational frequency analyses indicated that the open shell singlet is a transition state with all three methods used. The mode of the negative eigenvalue is a rocking of the oxygen within the symmetry plane containing the middle CC bond.

The triplet state was also optimized for **4-16** with B3LYP, BLYP and mPW1PW91 (since only these three methods located the open shell singlet geometry). In the triplet structure, the distance from oxygen to the top carbons becomes longer compared with the closed shell and open shell sinlget geometries. It increases by about by 0.15Å resulting in a still looser structure. The two end CC bonds closest to oxygen shorten about 0.01Å while the four equivalent CC bonds lengthen by 0.01Å. The structure of **4-16** is shown in Scheme 4-4. At the B3LYP and mPW1PW91 level, this triplet structure is a minimum. At BLYP, it is a transition state similar to the open shell singlet predicted by the same method, and also similar to intermediate **4-3**. The energetics predicted by the three methods indicate that the triplet state is more than 30 kcal/mol lower than the closed shell singlet state (10 kcal/mol lower in energy than the open shell singlet).

4.3.4 Isomerization path from oxepin to bicyclo[2.1.0]-2-pentene-5-carbaldehyde(4-20)

The first and fourth carbons in oxepin **7** can bond to form another isomer, 2-oxa-bicyclo[3,2,0]hepta-3,6-diene, **4-18**. 2-oxa-bicyclo[3,2,0]hepta-3,6-diene is well known as a product of the photolysis of oxepin in solution with visible light [3b,54]. A transition state **4-17** whose structure has been located between oxepin, **4-7**, and **4-18** is shown in Figure 4-4. **4-7** needs to absorb about 50 to 70 kcal/mol energy to overcome the barrier at

4-17 in order to form **4-18**. The isomerization pathway is shown in Figure 4-4A. The relative energies of the isomers in Figure 4-4 are reported in Table 4-9. The barrier is very high for a thermal reaction, although the formation of **4-18** from **4-7** was believed to proceed *via* a singlet process [55]. The distance between the two carbons which bond is about 2.3Å. In **4-18**, this distance decreases to 1.6Å, obviously approaching a single bond length. The structures of the isomers are reported in Figure 4-4A. The reverse reaction will not produce oxepin, **4-7**, due to the temperature required (150°-160° C) at which **4-7** could isomerize to another compound[3b]. Due to the ring strain and the destruction of electron conjugation, **4-18** is **15** kcal/mol higher in energy than **4-7**.

In acidic solution, 3-Oxa-quadricyclane, **4-12**, isomerizes to another compound similar to **4-20** [51] as shown in Figure 4-4. This reaction could involve protonation. Another reaction pathway was studied here for the formation of compound to Bicyclo[2.1.0]-2-pentene-5-carbaldehyde, **4-20**, from **4-18** involving cleavage of one CO bond and formation of a CC bond. The CO bond near the four membered ring breaks in the transition state and the distance between the bond-breaking carbon and oxygen ranges from 2.0 Å to 2.4 Å. During the breaking of the CO bond, another CC bond (C_2-C_6) is forming, while the C_2-C_5 bond remains unchanged. The distance between C_2 and C_6 is about 2.5 Å. Internal reaction coordinate (IRC) calculations on the transition state confirmed this mechanism. These bond breaking and bond forming processes require about 30 to 40 kcal/mol of energy.

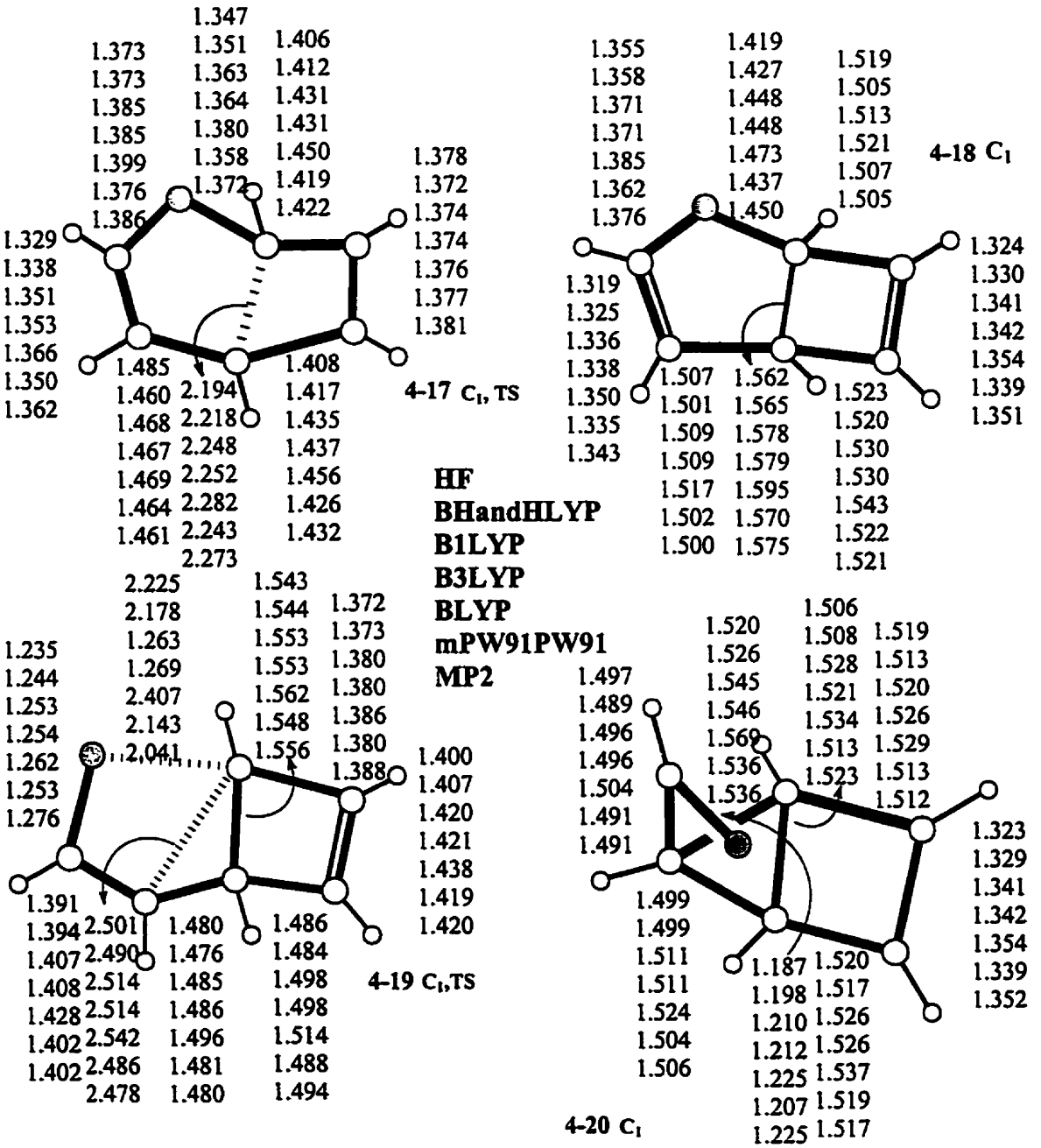

Figure 4-4 Geometries of 2-oxa-bicyclo[3,2,0]hepta-3,6-diene 18, transition states and bicyclo[2.1.0]-2-pentene-5-carbaldehyde(4-20)

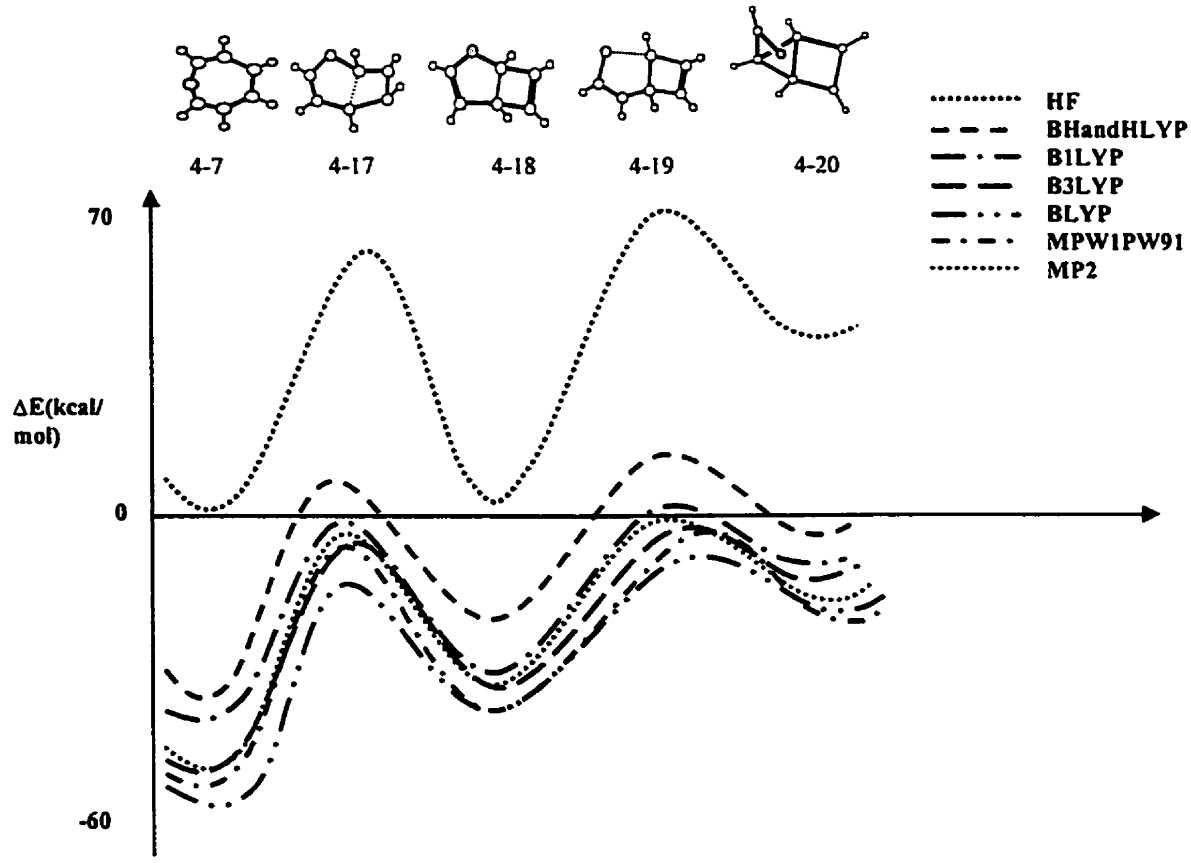

Figure 4-4A Isomerization path from oxepin to bicyclo[2.1.0]-2-pentene-5-carbaldehyde(4-20)

Table 4-9. Relative energies of the isomers in isomerization path from oxepin to bicyclo[2.1.0]-2-pentene-5-carbaldehyde (in Kcal/mole) [$\Delta E=E_n-(E_{oxygen}+E_{benzene})$]

Isomers	HF	BHand HLYP	BHand HLYP*	B1LYP	B3LYP	BLYP	mPW1 PW91	MP2
4-1	0.0	0.0	0.0	0.0	0.0	0.0	0.0	0.0
4-17	61.2	10.6	11.9	-2.6	-7.8	-18.1	-7.9	-6.4
4-18	16.2	-25.8	-23.2	-33.2	-37.4	-42.7	-40.7	-37.4
4-19	68.9	18.1	18.9	3.3	-2.2	-14.0	-3.1	-0.4
4-20	36.3	-4.3	-2.6	-13.0	-17.4	-23.6	-20.7	-20.4

Basis set (except BHandHLYP*): 6-31G*; BHandHLYP*: BHandHLYP/6-311++G**

4-1: reactant of benzene with triplet oxygen atom

Isomer Bicyclo[2.1.0]-2-pentene-5-carbaldehyde, **4-20**, has one three membered ring and one four membered ring, which causes great strain in this structure. The formation of Bicyclo[2.1.0]-2-pentene-5-carbaldehyde, **4-20**, from **4-18** is strongly endothermic. The system needs to absorb 20 kcal/mol energy. The CO group in **4-20** can rotate around the CC bond and there exists a transition state for this rotation. **4-20** also can break the CC bond between the three membered ring and the four membered ring to isomerize to another compound.

4.3.5 Isomerization path from epoxide to bicyclo[3.1.0]hex-3-en-2-one

Early photolysis experiments on the benzene oxide and oxepin system produced phenol and butadienylketene (BDK) [3c]. Cyclohexadienone was proposed as an intermediate in this reaction. Recent experiments on the benzene oxide and oxepin system [2] suggested that, through an intermediate, BDK (from cyclohexadienone) also has been obtained in gas phase photolysis.

The formation of cyclohexadienone from benzene oxide involves both hydrogen and oxygen migrations. Oxygen bonds to two carbons in benzene epoxide and it bonds to only one carbon through a CO double bond in cyclohexadienone. Each carbon is attached to a hydrogen in benzene oxide. In cyclohexadienone, one carbon has two bonded hydrogens and one of its neighboring carbons bonds only to oxygen without any hydrogen. A possibility involves one transition state connecting these two isomers with simultaneous migrations of hydrogen and oxygen.

A transition state **4-21**, as illustrated in Figure 4-5, has been located with all methods employed. The structures of the isomers are reported in Figures 5-5 and 5-5A. The structure of this transition state looks like the triplet intermediate **4-3** and the singlet transition state **4-4** for the "walk-around" of the oxygen on the benzene ring. The major difference in this structure from the other two is that this transition state has no symmetry. The bond lengths vary greatly compared with **4-3** and **4-4**. The bond angles of the hydrogen and oxygen with the carbons near oxygen are not identical as required by C_s symmetry. The OCC angle in **4-21** corresponding to that in **4-4** mentioned above and the HCC angles in the oxygen region are similar to those in **4-3**. In this structure, oxygen is on one side of the former C_s plane in **4-3** and **4-4** while hydrogen is on the other side.

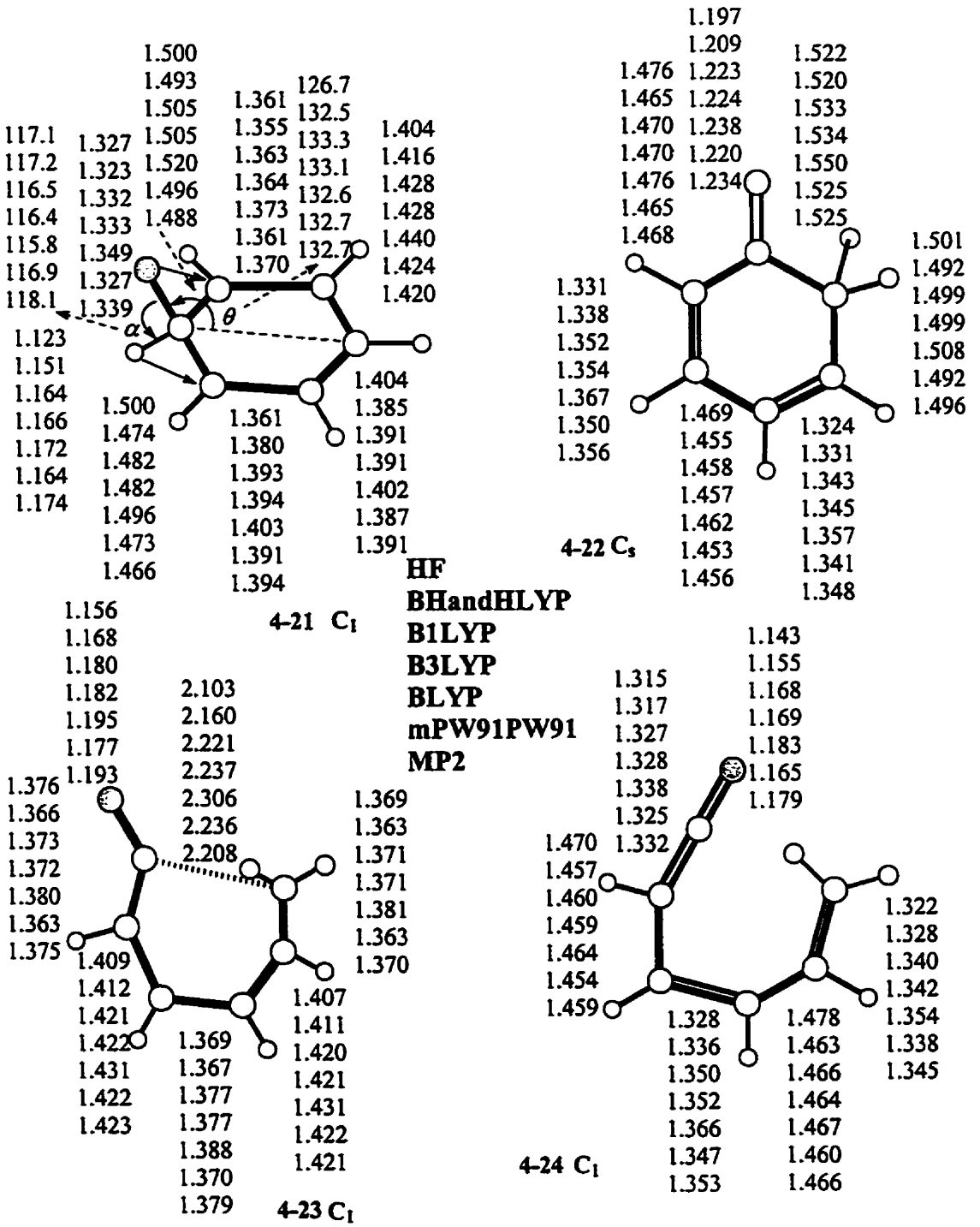

Figure 4-5 Geometries of cyclohexadienone 4-22, butadienylketene 4-24 and transition states 4-21 and 4-23

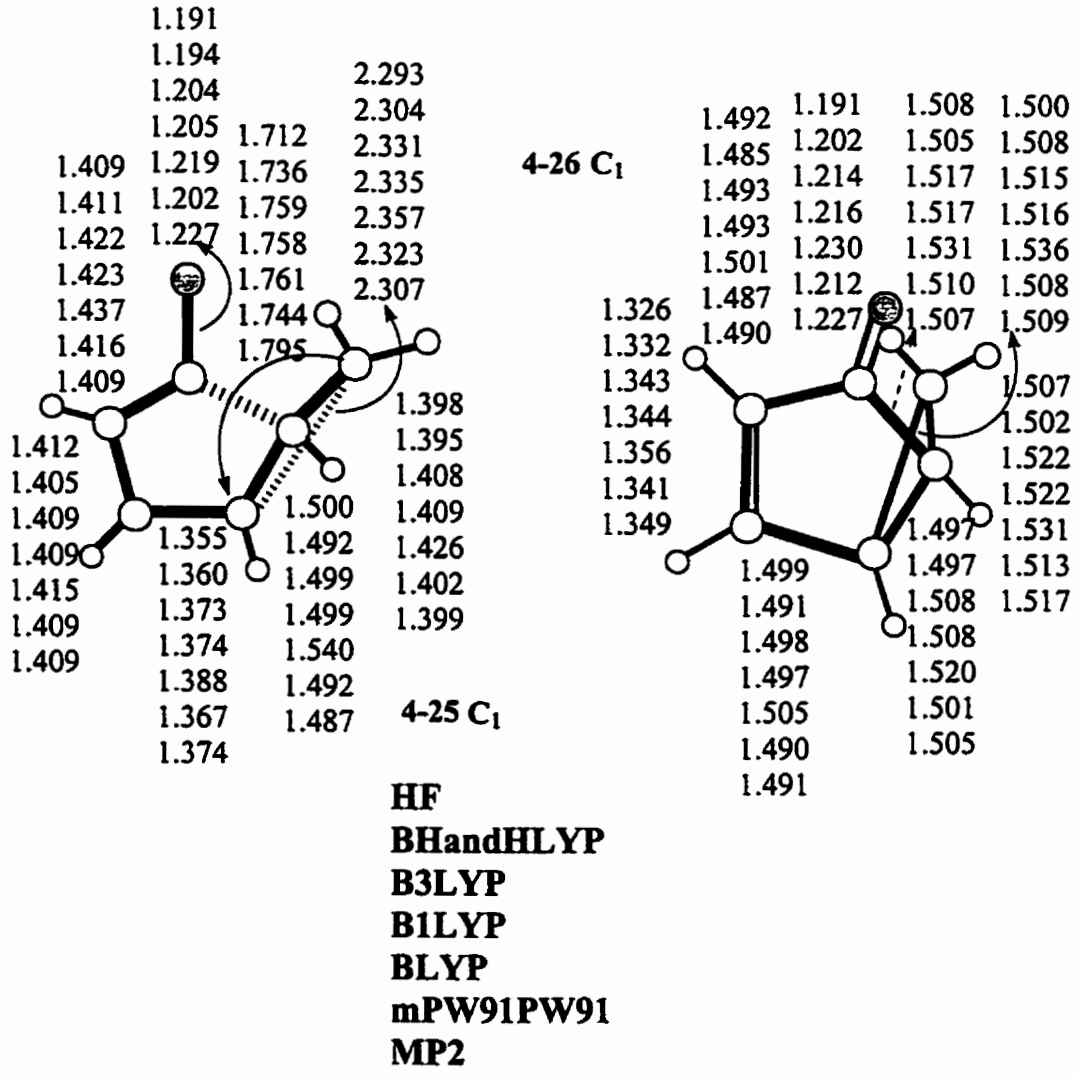

Figure 4-5A Geometries of bicyclo[3.1.0]hex-3-en-2-one 4-26 and its transition state 4-25

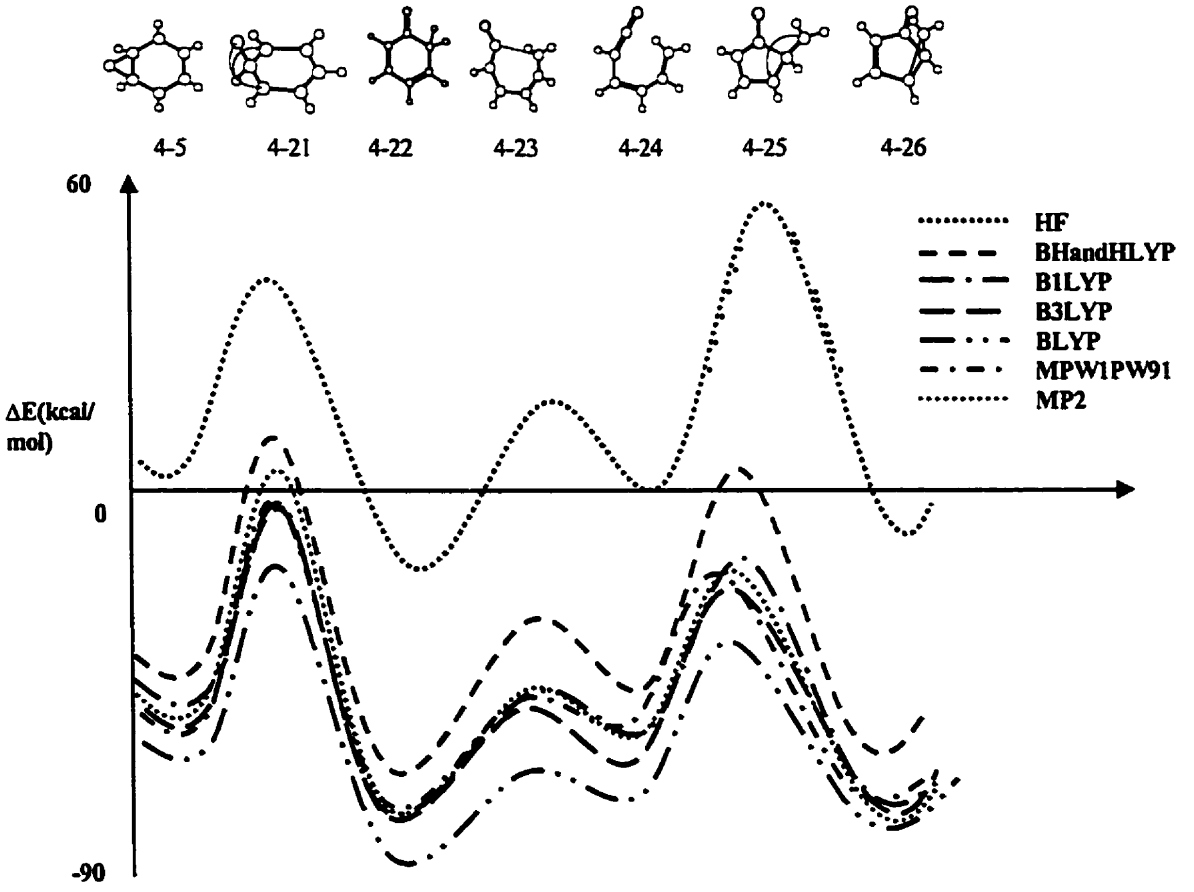

Figure 4-5B Isomerization path from epoxide to bicyclo[3.1.0]hex-3-en-2-one

The bond angles of oxygen with its neighboring carbons in **4-21** are about 120° and 100°, the corresponding angles of the hydrogen with carbons are about 95° and 105° respectively. This structure facilitates the bonding of oxygen with another carbon and migration of hydrogen to the carbon closest to it as illustrated for the motion of oxygen and hydrogen by the solid arrows in **4-21** in Figure 4-5. The dihedral angles of the carbon ring in this region also favor the motion of the oxygen and hydrogen. The dihedral angle D_{6123} (numbering of carbon starts from the oxygen side) is about −10°, and D_{2165} is about 2°.

The bond length in **4-21** also suggests the formation of benzene epoxide (**4-5**) and cyclohexadienone (**4-22**) from this transition state. Starting from the oxygen side (the side where the OCC angle is smaller (100°)), the CC bond lengths are approximately 1.47, 1.39, 1.38, 1.42, 1.36, and 1.49 Å. The CC bond length of 1.47Å is in the epoxide part of benzene epoxide **4-5**. The remaining CC bonds appear to be of single, double, single, and double character as in isomer **4-5**. The CH bond distance in the oxygen part is about 1.2 Å, much longer than a normal CH bond. This CH bond length indicates the migration of the hydrogen away from the carbon. IRC calculations on this transition state showed clearly that the two isomers connected by this transition state are **4-5** and **4-22**.

The isomerization pathway is illustrated in Figure 4-5B. The relative energies of the isomers in Figure 4-5B are reported in Table 4-10. The activation barrier of **4-21** relative to **5** is about 50 kcal/mol. The overall reaction from **4-5** to **4-22** is exothermic. The reverse reaction should be more difficult than the forward reaction judging from the reaction barrier, i.e. the migration of hydrogen is more efficient than the formation of the epoxide.

Table 4-10. Relative energies of the isomers for isomerization path from epoxide to bicyclo[3.1.0]hex-3-en-2-one (in kcal/mole)[$\Delta E=E_n-(E_{oxygen}+E_{benzene})$]

Isomers	HF	BHand HLYP	BHand HLYP*	B1LYP	B3LYP	BLYP	mPW1PW1	MP2
4-1	0.0	0.0	0.0	0.0	0.0	0.0	0.0	0.0
4-21	53.4	10.7	7.2	-3.6	-8.9	-22.2	-6.1	7.9
4-22	-29.8	-68.5	-67.2	-76.9	-80.9	-87.4	-80.1	-76.7
4-23	23.1	-25.3	-25.8	-40.7	-45.7	-58.2	-42.0	-39.6
4-24	1.4	-36.2	-38.0	-48.5	-52.6	-63.1	-47.7	-46.7
4-25	55.3	2.1	1.2	-15.6	-21.4	-36.0	-19.3	-16.4
4-26	-14.9	-54.4	-52.0	-61.3	-65.5	-70.0	-69.4	-66.7

Basis set (except BHandHLYP*): 6-31G*; BHandHLYP*: BHandHLYP/6-311++G**

4-1: reactant of benzene and triplet oxygen atom

Isomer **4-22** has C_s symmetry and thus all the atoms except the two hydrogens on the sp^3 hybridized carbon are in the symmetry plane. MP2 predicted this C_s structure to be a stationary point and the harmonic vibrational analyses yield a negative eigenvalue for the Hessian. So the C_s structure is predicted to be a transition state at MP2. The mode of the imaginary frequency involves a bending of the CO group. The distortion along this mode results in a minimum of C_1 symmetry. The C_1 structure does not differ much from the C_s one except for the loss of the symmetry plane. The interesting point is that the C_1 isomer is 0.12 kcal/mol higher than the C_s transition state when the ZPVE correction is included. Without the ZPVE correction, the C_1 form is 0.02 kcal/mol lower than the C_s transition state. The importance of the ZPVE is clear in this case (although the energy difference is very small). The problematic characteristics of MP2 in describing this system are obvious.

4-22 can further isomerize to another structure by bond breaking. Photochemical reaction of **4-22** resulted in the formation of BDK (**4-24**) by breaking the single CC bond of the CH_2 group closest to the oxygen in **4-22** [56]. The structure of the transition state **4-23** between **4-22** and **4-24** shows the forming and breaking of the CC single bond of this CH_2 group. The distance from the carbon in the CH_2 group to the carbon in the CO group is about 2.2 Å. The CO bond in **4-23** decreases and its neighboring CC bond develops into a double bond with a much shorter bond length which is characteristic of a ketene. Also the CC bond of the CH_2 group decreases to a double bond length and the neighboring CC bond becomes a single bond. To overcome the activation barrier from **4-22** to **4-24** requires about 35 kcal/mol of energy. It is possible for this reaction to take place through both photolysis and pyrolysis [54,56], although the formation of **4-24** from **4-**

22 is overall endothermic.

BDK **4-24** is a cumulenone with a cis conformation. The distance between the two carbons next to the end CH_2 group and that of the CO end is short enough for further bonding. A transition state **4-25** has been located for this reaction pathway. In structure **4-25**, the distance for the bonding carbons is about 1.8Å, leading on to the formation of the CC bond. During the formation of this CC bond, the CH_2 end bonds to the carbon next to it to form a three-membered ring with a distance of about 2.3Å between these bonding carbons in **4-25**. **4-25** is about 30 kcal/mol energy in energy above **4-24**.

An IRC calculation starting from **4-25** demonstrates the formation of bicyclo[3.1.0]hex-3-en-2-one (**4-26**). The formation of the five-membered and three-membered rings causes considerable strain in the newly formed isomer **4-26**. **4-26** is about 15 kcal/mol lower in energy than **4-24** and **4-24** can thermally arrange to **4-26**[54,56].

4.3.6 The isomerization pathway from hexadienone to 2,5-cyclo-hexadienone

Phenol is the product most often cited in the reaction of oxygen with benzene [7,13,14] and phenol also could be produced from benzene oxide [3,55]. It was proposed that the formation of phenol occurred through an open shell intermediate [3,7,19] in the reaction of oxygen with benzene or in the isomerization of benzene oxide. In the present study another mechanism has been proposed based on *ab initio* and DFT calculations.

The most probable path for the formation of phenol is the isomerization from **4-22** (cyclohexadienone) since these two structures are similar as shown in Figure 4-5 and Figure 4-6. Figures 6-6 and 6-6A report the geometries for the isomers in isomerization pathway in Figure 4-6B. Before the isomerization of **4-22** to phenol, **4-22** can rearrange in a degenerate manner to itself by migration of the hydrogen in the CH_2 group from one

side to the other through a transition state of C_s symmetry, **4-27**, as shown in Figure 4-6B. In **4-27**, the migrating hydrogen is about 1.5 Å away from the interacting carbons. The CO group bends out of the heavy atom skeleton. The barrier for this hydrogen migration is about 45 kcal/mol. The relative energies of the isomers in Figure 4-6 are reported in Table 4-11.

The isomerization of phenol **4-29** from **4-22** requires hydrogen migration from carbon to oxygen. The transition state **4-28** for this isomerization has no symmetry. One of the hydrogens in the CH_2 group in **4-28** is slightly below the benzene ring, another one is above the ring and lies between the carbon and oxygen in its migration to oxygen. The distance of the migrating hydrogen to the carbon to which it was formerly bonded is about 1.4Å. The corresponding distance of this migrating hydrogen from oxygen is also about 1.4Å. The CO bond length in this transition state is about 1.3Å, lying between that in **4-29** and **4-22**. The activation barrier for from **4-22** is about 50 kcal/mol. This barrier decreases significantly in aqueous solution [57].

From the reaction pathway from **4-22** to **4-29**, the mechanism of formation of phenol from benzene oxide is clear. Starting from **4-5**, through transition state **4-21**, **4-22** is formed. Then *via* transition state **4-28**, phenol **4-29** forms from **4-22**. In this mechanism, **4-22** (cyclohexadienone) serves as an intermediate as illustrated in Figure 4-6.

A rotation of 90° by the OH group in **4-29** about the CO bond results in transition state **4-30**. The barrier for this rotation is very low (about 3 kcal/mol). In transition state **4-30**, the HOC group is perpendicular to the plane of the benzene ring and this transition state has C_s symmetry.

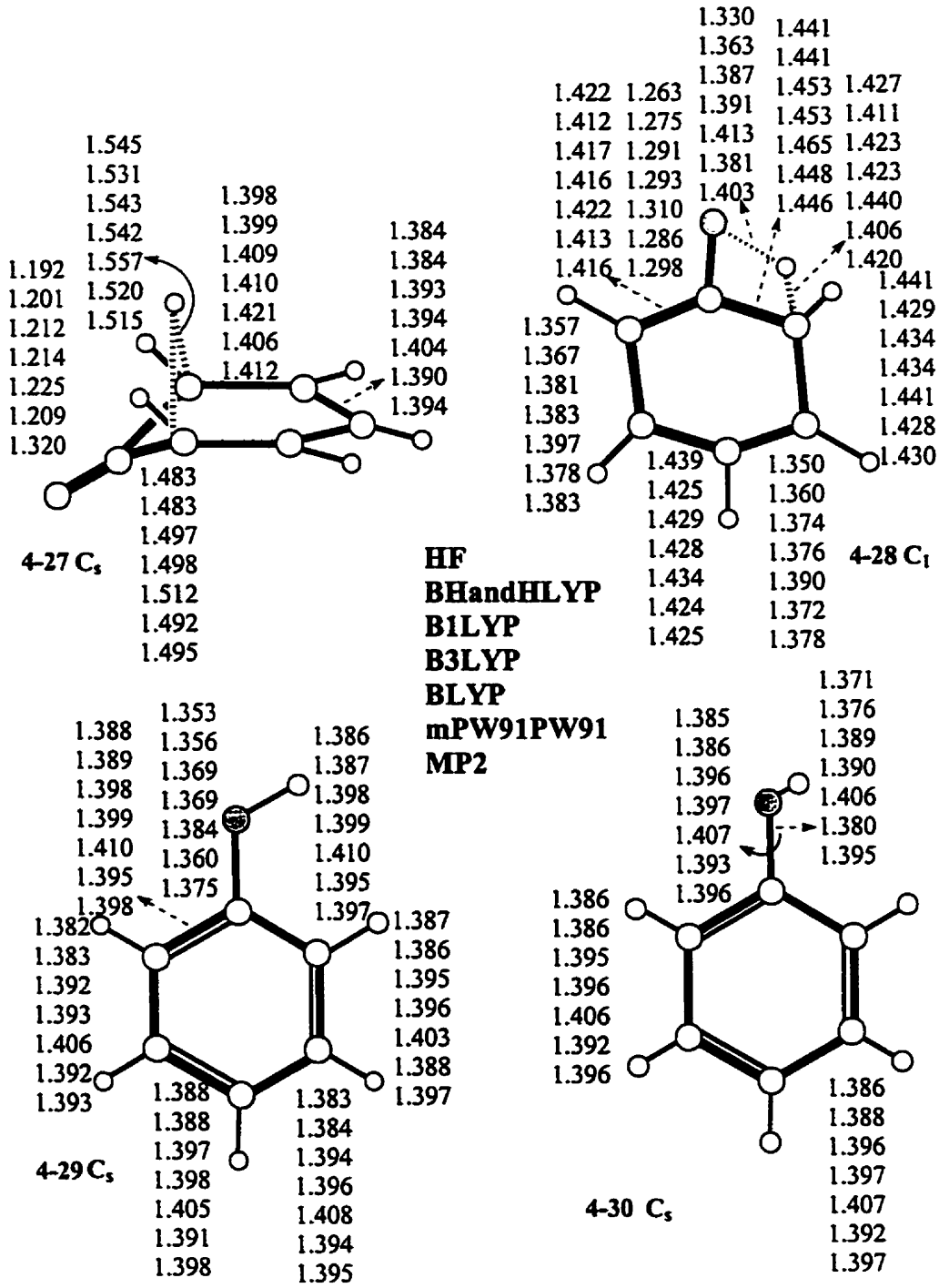

Figure 4-6 Geometries of phenol 29 and the related transition states

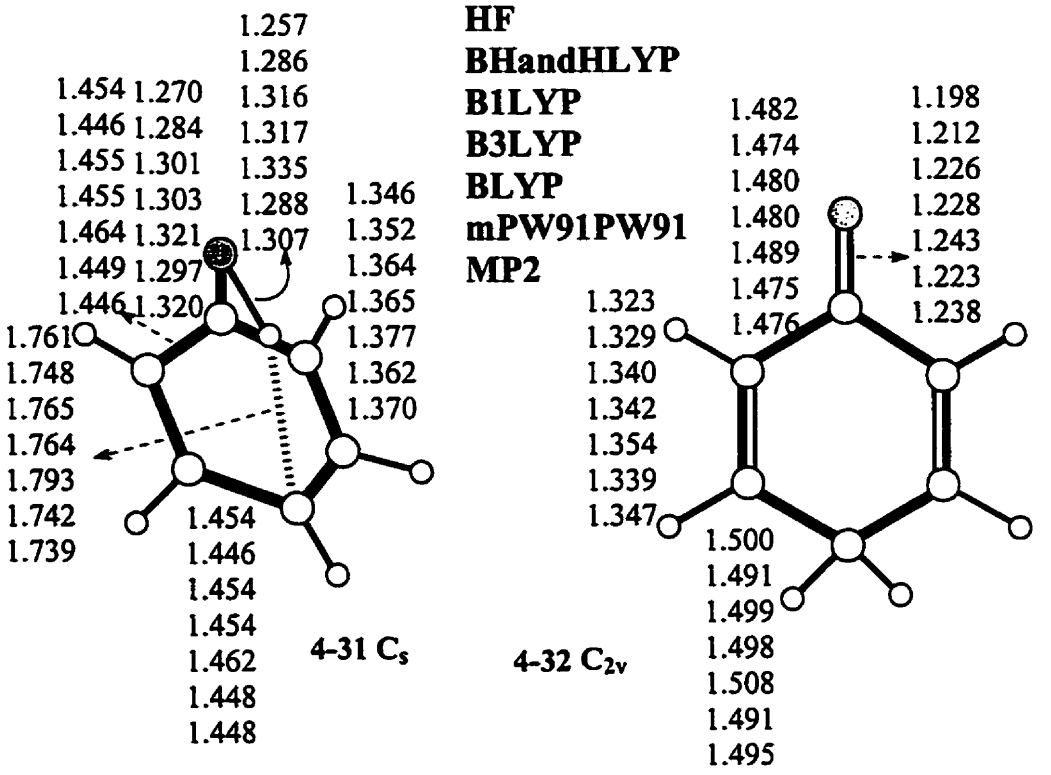

Figure 4-6A Geometries of 2,5-cyclo-hexadienone 4-32 and its related transition state 4-31

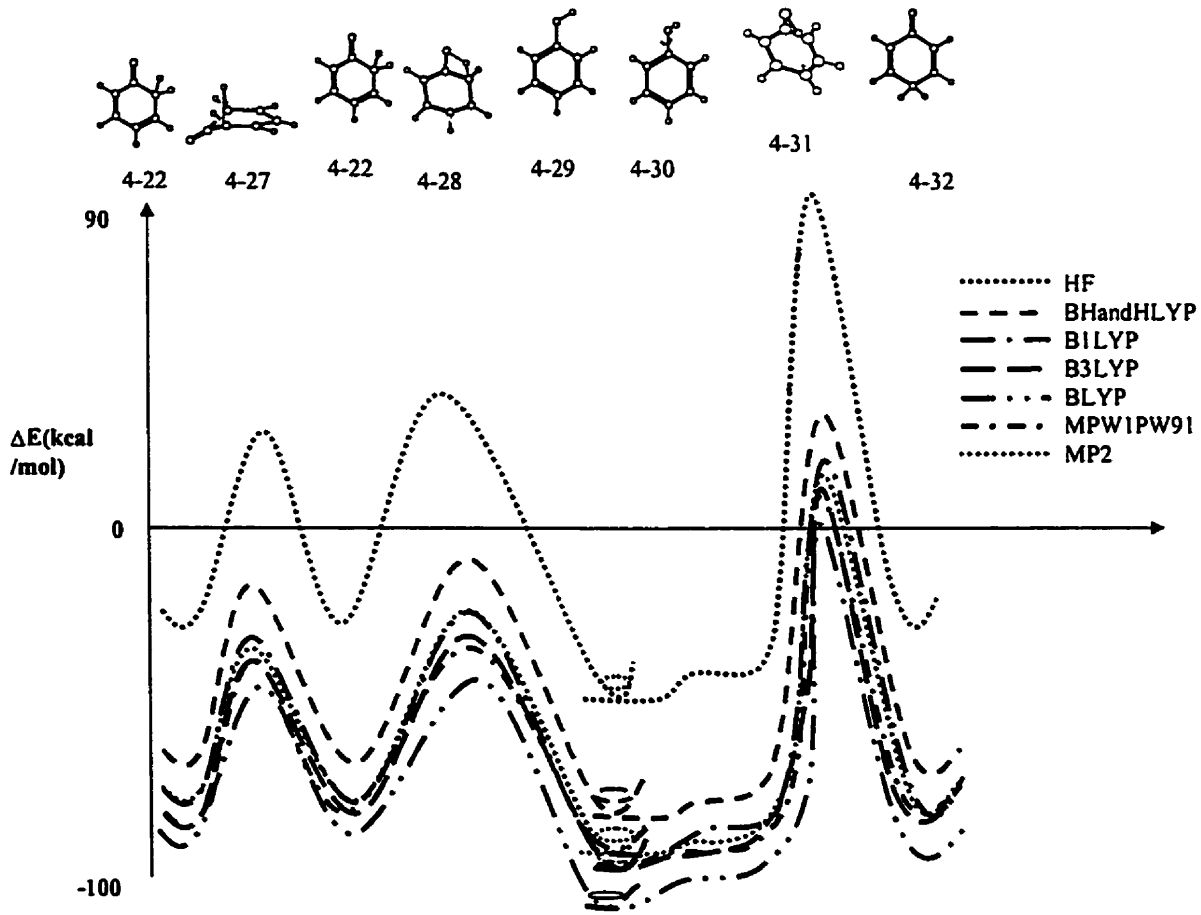

Figure 4-6B The isomerization pathway from hexadienone to 2,5-cyclo-hexadienone

Table 4-11. Relative energies of the isomers in isomerization pathway from hexadienone to 2,5-cyclo-hexadienone (in kcal/mole) [$\Delta E=E_n-(E_{oxygen}+E_{benzene})$]

Isomers	HF	BHand HLYP	BHand HLYP*	B1LYP	B3LYP	BLYP	mPW1PW91	MP2
4-1	0.0	0.0	0.0	0.0	0.0	0.0	0.0	0.0
4-22	-29.8	-68.5	-67.2	-76.9	-80.9	-87.4	-80.1	-76.7
4-27	28.7	-20.8	-21.8	-33.4	-38.5	-47.9	-39.7	-36.6
4-28	42.3	-10.2	-11.2	-24.7	-30.4	-41.8	-30.5	-24.5
4-29	-41.6	-83.5	-85.6	-91.1	-95.1	-99.9	-95.2	-93.7
4-30	-39.5	-80.7	-83.0	-87.8	-91.6	-96.0	-91.7	-90.6
4-31	90.4	36.4	34.3	21.9	16.2	4.8	15.3	17.6
4-32	-31.7	-69.8	-68.5	-77.9	-81.7	-87.9	-80.9	-77.7

Basis set (except BHandHLYP*): 6-31G*; BHandHLYP:* BHandHLYP/6-311++G**

4-1: reactant of benzene and triplet oxygen atom

In most cases, a transition state connects two minima on the potential energy surface. A transition state could connect another stationary point along some reaction pathway. One definition of a transition state is a stationary point which connects two lower energy stationary points. These two stationary points which are joined are not necessarily minima. In the present study, **4-31**, a transition state with C_s symmetry, has been located which connects transition state **4-30** and another minimum 2,5-cyclo-hexadienone (**4-32**) for migration of hydrogen from oxygen to the carbon across the benzene ring. In **4-31**, the migrating hydrogen is 1.3Å away from oxygen and 1.7(5)Å from the carbon to which it will bond. It is much higher in energy than both **4-30** and **4-32** at about 110 kcal/mol.

4.3.7 Isomerization path for C_2 benzene epoxide

Another possibility for the formation of a stable product from the reaction of oxygen with benzene occurs when oxygen approaches the benzene in the molecular plane between the two hydrogens. The oxygen bonds with two carbons but with the two hydrogens lying on different sides of the former molecular plane. In this case, a C_2 epoxide (**4-33**) forms as shown in Figure 4-7.

In **4-33**, the CC bond attacked by oxygen does not break during the reaction. This structure is similar to benzene oxide (C_s epoxide). It distorts greatly in the oxygen region in order to satisfy the sp^3 hybridization of the carbons. The butadiene part is still almost planar due to the conjugation of the π electrons. The formation of this C_2 isomer is endothermic. The reaction system needs to absorb several kcal/mol of energy to form this isomer.

The geometric strain in **33** due to the bonding of the two carbons connecting oxygen

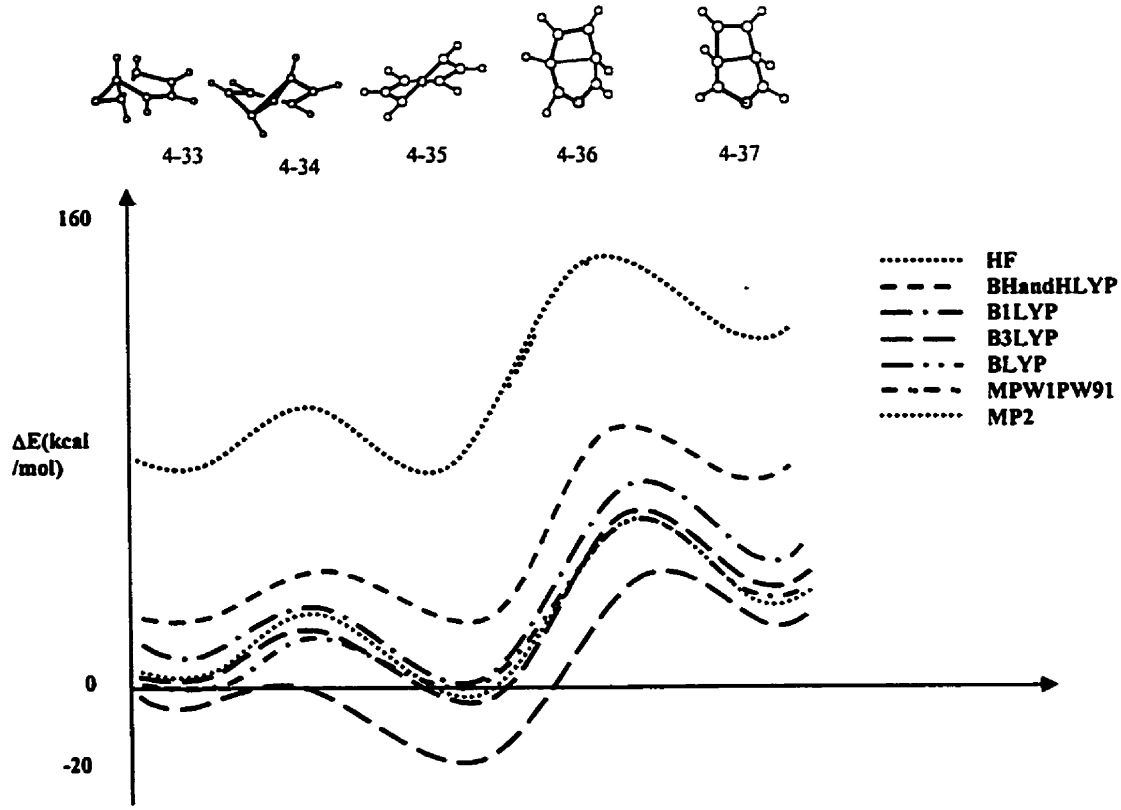

Figure 4-7 The isomerization pathway from C_2 epoxide to (C_2)3-Oxa-bicyclo-[3.2.0]hept-6-ene, 4-37

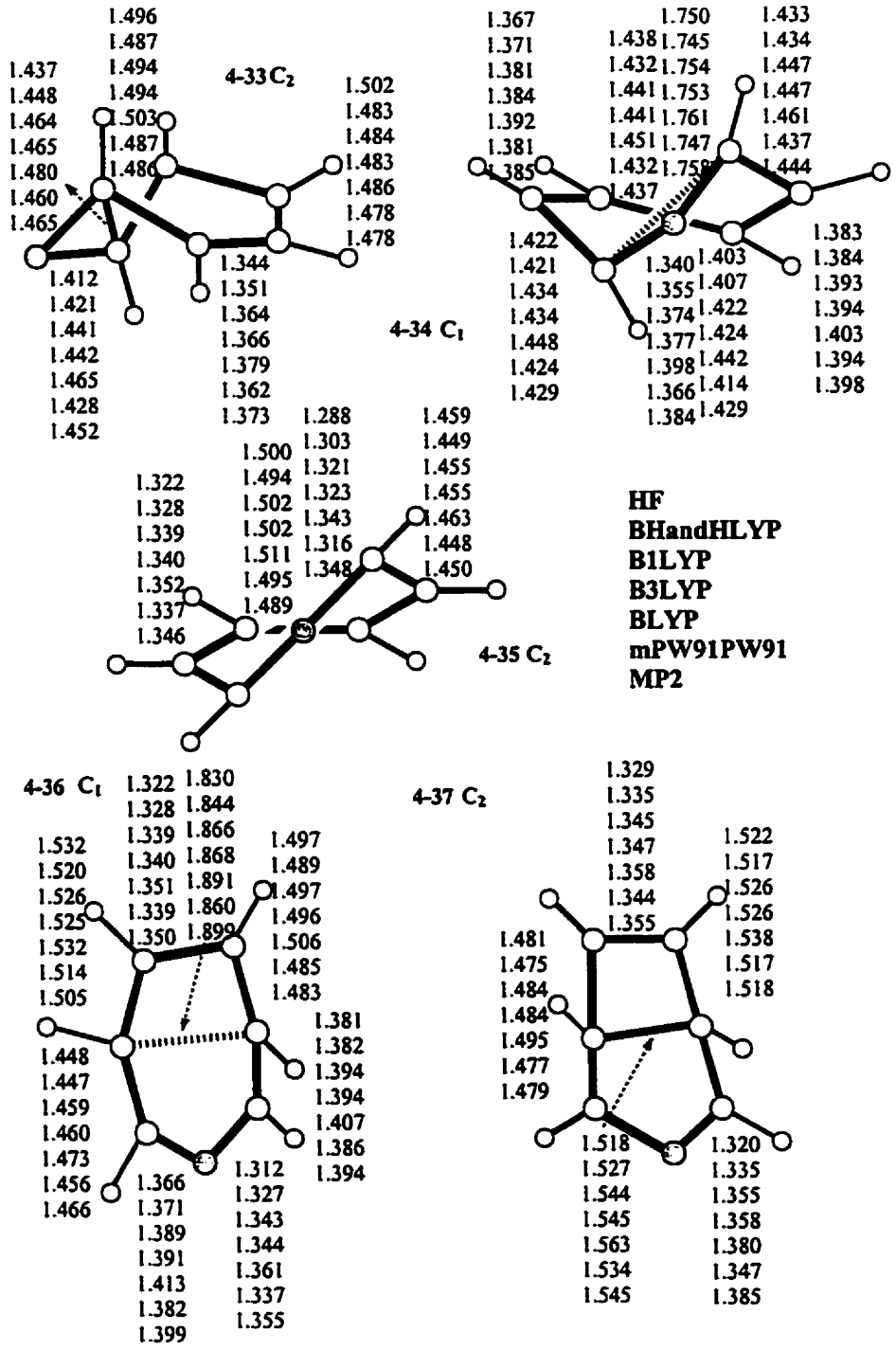

Figure 4-7A Geometries of C_2 epxoide 4-33, C_2 oxepin 35, (C_2) 3-Oxa-bicyclo-[3.2.0]hept-6-ene, 4-37, and related transition states

Table 4-12. Relative energies of the isomers in isomerization pathway from C_2 epoxide to (C_2)3-Oxa-bicyclo-[3.2.0]hept-6-ene, 4-37 (in kcal/mole) [$\Delta E=E_n-(E_{oxygen}+E_{benzene})$]

Isomers	HF	BHand HLYP	BHand HLYP*	B1LYP	B3LYP	BLYP	mPW1PW91	MP2
4-1	0.0	0.0	0.0	0.0	0.0	0.0	0.0	0.0
4-32	-31.7	-69.8	-68.5	-77.9	-81.7	-87.9	-80.9	-77.7
4-33	67.8	18.8	21.8	7.1	2.0	-6.9	-0.4	2.2
4-34	88.9	33.0	35.3	18.1	12.4	1.1	10.9	17.3
4-35	72.8	17.3	17.5	0.7	-4.9	-17.9	-1.5	-2.3
4-36	152.4	87.7	88.3	68.5	61.8	47.0	60.1	60.3
4-37	132.5	70.0	71.5	52.7	46.2	33.1	43.3	39.1

Basis set (except BHandHLYP*): 6-31G*; BHandHLYP*: BHandHLYP/6-311++G**

4-1: reactant of benzene with triplet oxygen atom

and the molecular symmetry facilitate the cleavage of this CC bond. Breaking of this CC bond results in a C_2 oxepin **4-35**. **4-35** is about 5 kcal/mol lower in energy than **4-33**. The relative energies of the isomers in Figure 4-7 are reported in Table 4-12. The distance between the carbons involved in the bond breaking is about 2.4Å. The structure of **4-35** is

a sort of a diene rather than a triene as in the C_s oxepin. The geometries of these isomers are reported in Figure 4-7A. In **4-35**, the two CO bonds (about 1.32Å) are shorter than that in C_s oxepin (about 1.39Å). The next CC bond length is about 1.45Å and the corresponding bond in the C_s oxepin is approximately 1.34Å in length. The CC bond perpendicular to the C_2 axis has a bond length of about 1.50Å, while this distance is 1.35Å in C_s oxepin.

The neighboring CC bond length is about 1.34Å, while the comparable distance in the C_s oxepin is 1.46Å. Based on the carbon bond lengths of **4-7** and **4-35**, the C_s oxepin is a triene while the C_2 oxpein is a diene. The structural characteristics of the C_2 oxepin indicate its two separate regions of π electron conjugation: one involving oxygen and its two neighboring carbons, and the other remaining heavy atoms.

Between the two C_2 isomers, a second order saddle point (SOSP) of C_2 symmetry has been located with all methods used. The order of these two modes with imaginary vibrational frequencies changes with the methods used. BHandHLYP and MP2 predicted the order as a, b (a is the larger mode), while B1LYP, B3LYP, BLYP and mPW1PW91 predicted the order as b, a (b is larger). The frequencies of these two modes are all close. The differences in wave numbers of these two modes vary with the methods. The smallest is $10cm^{-1}$ predicted by BHandHLYP the largest is $60cm^{-1}$ predicted by MP2 and mPW1PW91. The a mode involves mainly the CC bond breaking and formation between the two β carbons. The b mode is the rocking of hydrogens on the α carbons destroying the C_2 symmetry. Distortion along the b mode leads to a transition state **4-34** with C_1 symmetry. The imaginary vibrational mode is obviously the CC bond cleavage and formation in the epoxide portion of the molecule. The distance between these two

carbons is about 1.75Å. The bond length difference between two types of equivalent bonds in the heavy atoms as in **4-35** is about 0.01 to 0.03Å. The activation barrier from **4-33** to **4-34** is about 10 kcal/mol. The CC bond cleavage in **4-33** releases the geometric strain and stabilizes **4-35** by several kcal/mol.

In a similar mode to the oxepin isomerization path of epoxide in Figure 4-2, the two β carbons can bond to form a 4-5-membered-ring structure with C_2 symmetry ((C_2)3-Oxa-bicyclo-[3.2.0]hept-6-ene, **4-37**) through a transition state 36 with C_1 symmetry. **4-36** is about 65 kcal/mol higher in energy than **4-35**. This barrier makes the isomerization from **4-35** to **4-37** difficult because of the high energetic requirement. The bonding of the two β carbons increases the energy of **37** which is about 50 kcal/mol higher than **4-35**.

4.3.8 Performance of the functionals

In the present study, two exchange functionals B and mPW along with two correlation functionals have been used. The adiabatic connection mechanism (ACM) [58] rationalizes the mixing of exact exchange into the functionals, which results in these hybrid density functional methods. Besides the GGA BLYP, the hybrid DFTs - BHandHLYP, B1LYP, B3LYP and mPW1PW91 also were employed in the present study to analyze their performance in structural and energetic predictions.

4.3.8.1 Structure and property predictions

4.3.8.1.1 Benzene

Gauss and co-workers made structural predictions for benzene at CCSD(T)/cc-pVQZ level [45]. The predicted equilibrium CC bond length of benzene in best agreement with

experiment is 1.3911Å (the CC bond length from empirical fitting to experimental data is 1.3914Å) [45].

With the 6-31G* basis set, HF, BHandHLYP, B1LYP, B3LYP, BLYP, MPW1PW91 and MP2 predict the CC bond length in benzene as 1.386, 1.387, 1.396, 1.397, 1.407, 1.392 and 1.397Å respectively. For the B functional methods, as the weight of exact exchange decreases in the functional, the CC bond is predicted to be longer. A larger basis set 6-311++G(2df,2p), was used along with the BHandHLYP, B1LYP and mPW1PW91 functionals to check the effect of basis set on the structural prediction. With this triple zeta plus polarization and diffuse functions basis set, BHandHLYP predicts the CC bond length to be 1.382Å. mPW1PW91 predicts a value of 1.387Å. B1LYP predicts the carbon-carbon bond to be 1.391Å. B1LYP/6-311d(2df, 2pd) predicts benzene with a carbon-carbon bond length at 1.3942Å. mPW1PW91 gives the best result with 6-31G*. This excellent agreement of mPW1PW91 with experiment may be in part due to the fortuitous cancellation of basis set error and correlation effects since the larger basis set leads to a shorter CC bond length. GGA (BLYP) predicts longer bond lengths and the mixing of exact exchange attenuates this tendency. Comparison between mPW1PW91 and B1LYP (they have the same mixture of exact exchange) shows the effect of different functionals on structural prediction.

4.3.8.1.2 Triplet intermediate 4-3

The calculations on the symmetric triplet species **4-3** also reveal the different behaviors of the different functionals. Local (SVWN), hybrid (BHandHLYP, B1LYP, B3LYP and mPW1PW91) as well as conventional *ab initio* methods (HF, MP2)

predicted this structure to be a minimum on the potential surface. The GGAs (BLYP, G96LYP, mPWPW91 and PW91PW91) predicted this species to be a transition state. Even a small admixture of exact exchange (from zero up to 0.15) in BxHFyLYP (x+y=1.0, the Gaussian program allows the variation of the weight of the exchange density functional and of exact exchange) did not change the nature of this stationary point on the potential surface. This could be due to GGAs predicting small energy gaps of the HOMO and LUMO and mixing higher exited states. Exact exchange increases this energy gap. Analysis of the LUMO-HOMO gap confirms this observation. The LUMO-HOMO gaps predicted by BxLYP are reported in Table 4-13. When y=0, BxHFyLYP is BLYP. It is B1LYP when y=0.25. This behavior of the GGAs and hybrid DFTs with small amounts of exact exchange reveals an important role for exact exchange in the characterization of a stationary point on the potential surface.

Table 4-13 The HOMO- LUMO gaps (in Hartree) of the triplet intermediate 4-3 predicted by BxHFyLYP

	y=0.000	y=0.001	y=0.010	y=0.015	y=0.020	y=0.025
α gap	0.11765	0.11525	0.11803	0.14570	0.17637	0.19928
β gap	0.01969	0.02029	0.02435	0.06661	0.11641	0.14562

4.3.8.1.3 Region of the singlet intermediate, 4-4

There are several similar structures (**4-21** and **4-27**) to **4-4** on the singlet potential surface. **4-4** is a transition state with C_s symmetry for oxygen migration around the benzene ring and also probably for the ring closure after the ISC from the triplet potential surface. **4-21** is a transition state with C_1 symmetry connecting C_s benzene epoxide and cyclohexadienone. **4-27** is a C_s transition state for the hydrogen migration from one side to the other in cyclohexadienone. For **4-21**, HF predicts a very different wavenumber for the imaginary mode. The wavenumber predicted by other methods is about 800i cm^{-1}. HF predicts 200i cm^{-1} corresponding to this negative eigenvalue of the Hessian. The reason why HF predicts so different wavenumber for this frequency from DFT methods is not clear. The imaginary mode predicted by HF is a bending of the OCH group although the IRC calculations confirms this transition state is connecting the same minima as in the other methods. Restoring the C_s plane in which the OCH group lies results in a symmetric transition state for the HF method. The imaginary mode in this transition state is an in-plane bending which is the same as in **4-21**. It is interesting to note that IRC calculations on this transition state show that these two transition states connect the same isomers along the reaction pathway.

Starting from the optimized C_s transition state of the HF level, BHandHLYP has been used to reoptimize this structure. The calculation revealed that with BHandHLYP this optimized structure is a SOSP (**4-38**) as shown in Figure 4-8. The vibrational mode of the smaller negative eigenvalue (the solid vector in structure **4-38** of Figure 4-8) is an asymmetric (a") out-of-plane rocking of the OCH group destroying the symmetry plane. This mode connects the two equivalent transition states **4-21** (the dashed arrow in Figure

4-8A). The vibrational mode of the larger negative eigenvalue is a symmetric rocking of the OCH group (a') (the solid vector in structure **4-38** of Figure 4-8) within the symmetry plane. Distortion along one direction of this symmetric mode results in the formation of transition state **4-4** for the oxygen "walk-around" the benzene ring. Distortion along the other direction of this mode forms transition state **4-27** for the hydrogen migration from one side to the other in cyclohexadienone **4-22** (the solid arrow in Figure 4-8). So the SOSP associates the reaction pathways of Figure 4-1 with Figure 4-6 as shown in Figure 4-8. Among the methods used, only B1LYP and MP2 besides BHandHLYP located this SOSP with the 6-31G* basis set. The two imaginary frequencies are i743 cm^{-1} (a') and i320 cm^{-1} (a") at BHandHLYP, i677 cm^{-1} (a') and i210 cm^{-1} (a") at MP2. These two imaginary frequencies increase to i1957 cm^{-1} (a') and i1834 cm^{-1} (a") respectively at B1LYP. These increases are unusual since only the weight of exact exchange in the functionals varies from 0.5 in BHandHLYP [26] to 0.25 in B1LYP [36]. A closer examination of the orbital energies from these three methods reveals that the LUMO-HOMO gap of B1LYP (0.05a.u.) is much smaller than that of BHandHLYP (0.13 a.u.) and HF (0.31 a.u.). This difference could cause the wavenumber change in the imaginary frequency predicted by B1LYP. The small LUMO-HOMO gap at B1LYP could introduce a mixing of higher states that changes the nature of the stationary point. The Hessian is the second derivative of energy with respect to the nuclear coordinates, so vibrational frequency prediction is associated with orbital energy. The stability test on B1LYP solution indicated that it shows a RHF to UHF instability.

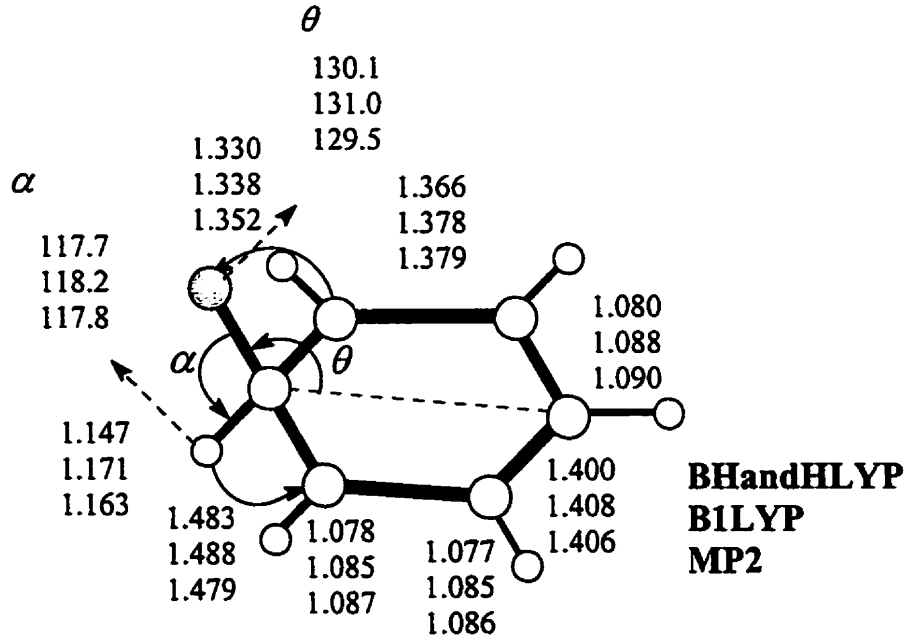

4-38 C_s(SOSP)

Figure 4-8 Geometries and imaginary vibrational modes for the two imaginary frequencies of 4-38

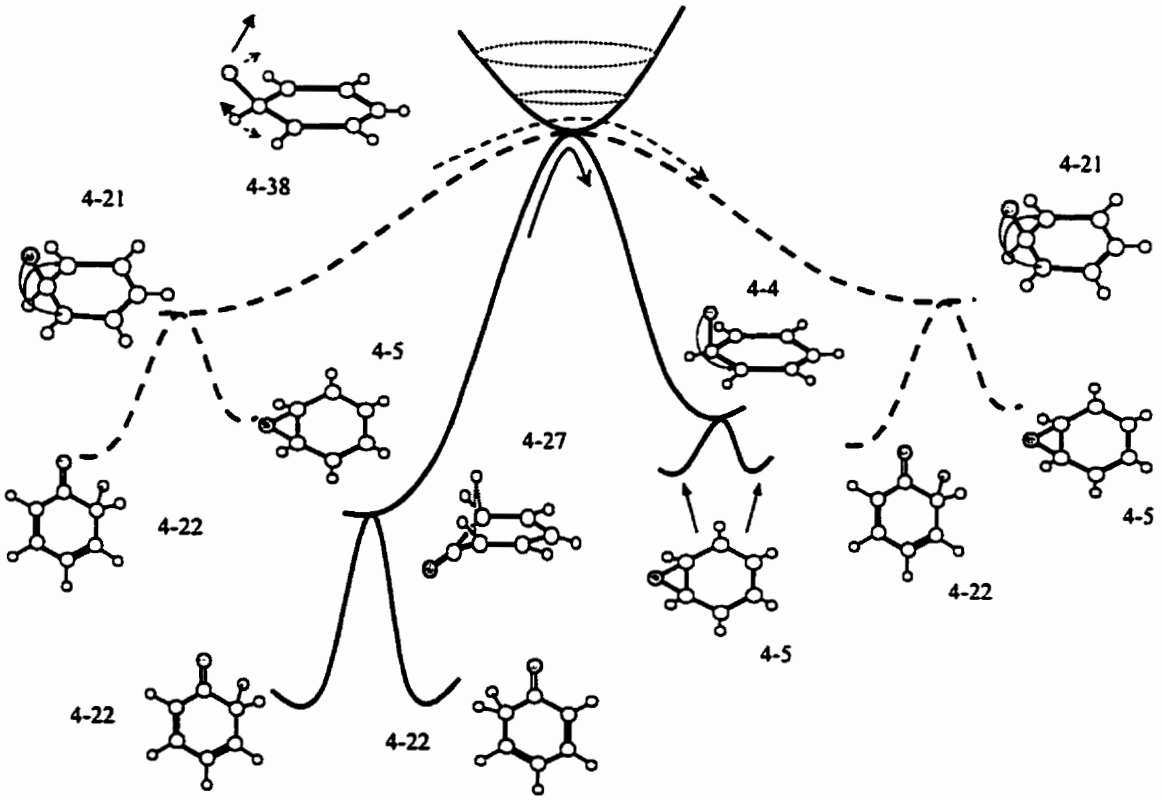

Solid and dashed lines (arrows) are for two different imaginary frequency modes of 38

Figure 4-8A The isomerization pathway near transition state 4-4

These transition states are low in energy relative to **4-38** (The relative energy of **4-38** to the reactants oxygen plus benzene was listed in Table 4-14). It is only 0.1 kcal/mol, 0.9 kcal/mol, and 0.5 kcal/mol above **4-21** (connecting to the C_s epoxide and cyclohexadienone) at BHandHLYP, B1LYP and MP2 respectively. It is about 8 kcal/mol (5.7 at BHandHLYP, 7.8 at B1LYP and 13.6 at MP2) higher in energy than 4 which is the transition state for the oxygen walk-around on the benzene ring. Compared with **4-21** and **4-4**, transition state **4-27** (for hydrogen migration in cyclohexadienone) is much lower in energy than **4-38** (31.6 kcal/mol at BHandHLYP, 36.1 kcal/mol at B1LYP and 45.0 kcal/mol at MP2). Comparison of the energetics of **4-28**, **4-27**, **4-21** and **4-4** reveals that the conversion among these critical points is very easy.

The geometry of **4-38** is similar to **4-21** and **4-3** especially in the angles about oxygen (the HCO angle and the OCC angle formed by the oxygen, the carbon to which it is bonded and the carbon across the benzene ring as shown in Figure1). This further confirms the mechanism suggested in Figure 4-8A. The similarity of **4-38** to **4-3** could suggest another mechanism for the initial reaction of triplet oxygen with benzene, namely, an intersystem crossing from **4-3** to **4-38** followed by the formation of the transition states **4**, **21** and **27**. The location of **38** by BHandHLYP, B1LYP and MP2 indicates the fine difference among the functionals in the structural characterization of this region of the potential surface.

Table 4-14 Relative energies of the stationary points near structure 4-38 (in kcal/mole) [$\Delta E=E_n-(E_{oxygen}+E_{benzene})$]

Isomers	HF	BHand HLYP	BHand HLYP*	B1LYP	B3LYP	BLYP	mPW1PW91	MP2
4-1	0.0	0.0	0.0	0.0	0.0	0.0	0.0	0.0
4-4	52.7	5.1	4.6	-10.5	-15.9	-29.6	-13.2	-5.2
4-5	4.4	-38.7	-35.9	-47.4	-51.8	-58.2	-53.7	-51.1
4-21	53.4	10.7	7.2	-3.6	-8.9	-22.2	-6.1	7.9
4-22	-29.8	-68.5	-67.2	-76.9	-80.9	-87.4	-80.1	-76.7
27	28.7	-20.8	-21.8	-33.4	-38.5	-47.9	-39.7	-36.6
38		10.8		-2.7				8.4

Basis set (except BHandHLYP*): 6-31G*; BHandHLYP*: BHandHLYP/6-311++G**

The re-optimization of **4-38** with unrestricted open shell wavefunctions results in another transition state **4-39** that involves the breaking and formation of one CO bond in 7-oxa-norbornadiene (**4-13**). The $<S^2>$ and the HOMO-LUMO gap of species **4-39** are listed in Table 4-15. The structure of **4-39** was shown in Figure 4-9. The structure of **4-39** resembles a boat in which oxygen bonds to one of the end carbons. The two middle carbon carbon bonds are double bonds. The two carbon carbon bonds next to oxygen are single bonds and the other two carbon bonds remote from the oxygen are intermediate in

length between single and double bond values. The distance between oxygen and carbon across the benzene ring is about 2.3Å. IRC calculations with UBHabdHLYP show that this transition state connects 7-oxa-norbornadiene (**4-13**) and an open shell singlet species **4-40**. Following the forward reaction path of **4-39**, the system changes symmetry to C_1. However the geometry almost retains the original C_s symmetry. Finally the system reaches the epoxide structure (**4-5**) at the end of the IRC calculation. Also the $<S^2>$ decreases to zero following the reaction pathway to the closed shell singlet. Thus it is a transition from an open shell singlet potential energy surface to a closed shell singlet potential energy surface. Optimization of one of the paths down the valley followed by the IRC with UBHandHLYP results in an open shell singlet intermediate (**4-40**) on the potential surface (The $<S^2>$ and HOMO-LUMO gap of species **4-40** were listed in Table 4-7.). Also the optimization of **4-4** by UBHadnHLYP reaches the same open shell singlet intermediate, **4-40**. The IRC calculations by UB1LYP yield the same final geometry as does UBHandLYP. The vibrational frequency analyses indicates that the open shell singlet intermediate is a transition state with UB1LYP that has the same reaction vector as transition state **4-4** i.e. a transition state for oxygen "walk-around" on the benzene ring. This open shell transition state is also obtained by a UB1LYP optimization of the transition state **4-4**. UmPW1PW91 produces the same results as UB1LYP. Calculations with UBLYP were not performed for this case since UBLYP predicts **4-39** to be a SOSP on the potential surface.

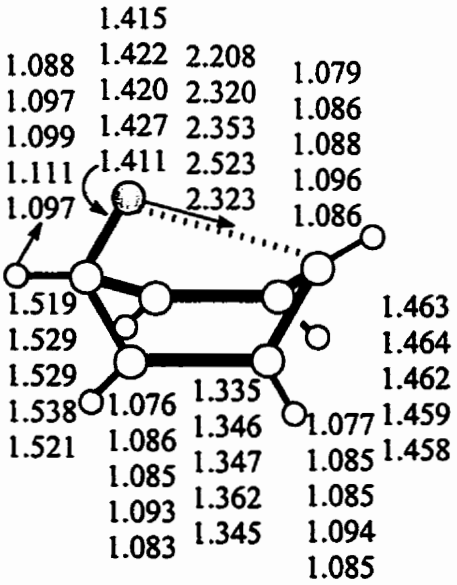

4-39 C_s(TS,open shellsinglet)

UBHandHLYP
UB1LYP
UB3LYP
UBLYP
UMPW1PW91

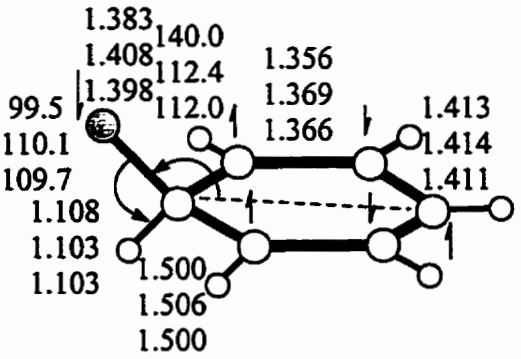

UBHandHLYP
UB1LYP
UMPW1PW91

4-40 C_s(TS,open shell singlet)

Figure 4-9 Geometries of open shell singlet transition states 4-39 and 4-40

Table 4-15 $<S^2>$ and HOMO-LUMO gaps (in a.u.) of the open shell singlet 4-39 and 4-40

	UBHandHLYP	UB1LYP	UB3LYP	UBLYP	UMPW1PW91
$<S2>^a$	0.7460	0.6573	0.6280	0.5726	0.7416
α^a	0.24352	0.14491	0.12233	0.03310	0.14808
β^a	0.23023	0.12444	0.10248	0.01354	0.12603
$<S2>^b$	1.1021	0.7463	0.5045		0.7981
α^b	0.18672	0.16164	0.08728		0.09531
β^b	0.26350	0.09694	0.11946		0.15638

<S2> (closed shell singlet)=0.0000

a: Structure **4-39** b: Structure **4-40**

α: HOMO-LUMO gap of α KS orbitals

β: HOMO-LUMO gap of β KS orbitals

The backward IRC in the other direction with UBHandHLYP shows that **4-39** proceeds downhill to reach 7-Oxa-norbornadiene as the $<S^2>$ value decreases to zero along the reaction path.

Based on these calculations by unrestricted DFT, the reaction pathway for **4-39** was illustrated in Figure 4-9A. The open shell singlet species **4-39** goes down on one side to

isomer **4-13** through an inter-section between the open shell singlet and closed shell singlet surface. On the other side two possiblities exist. One is that **4-39** goes downhill through conversion from the open shell singlet to the closed shell singlet and onto the closed shell singlet transition state **4-4**, followed by oxygen migration around the benzene ring. The other is that **4-39** goes downhill to the open shell singlet transition state **4-40** (except for the UBHandHLYP results), then returns to the closed shell singlet potential surface by approaching benezene epoxide as illustrated by the dashed curve in Figure 4-9A.

The different behavior of UBHandHLYP and UB1LYP from UB1LYP, UB3LYP and UMPW1PW91 for the potential curves of **4-39** further indicate the necessity to be cautious in the choice of functionals in potential surface characterization.

The location of the open shell singlet transition state **4-40** further confirms the plausibility of the ISC mechanism for the initial reaction from the triplet potential surface. The energy of 40 is lower than both **4-3** and **4-4** (a few kcal/mol lower in energy than **4-4**). The relative energies of the structures in Figure 4-9A are reported in Table 4-16. The spin density distributions of **4-3** and **4-40** are shown in Figures 6-1 and 6-9 and confirm this assumption. Only the spin orientations on oxygen in **4-3** and **4-40** are different, which indicates that the ISC most probably involves oxygen. Triplet **4-3** decreases in energy to the open shell singlet **4-40** through ISC, followed by conversion to a closed shell sinlget **4-4**. It is possible for the triplet **3** to proceed directly from triplet potential surface to **4-4** on the closed shell singlet potential surface by ISC.

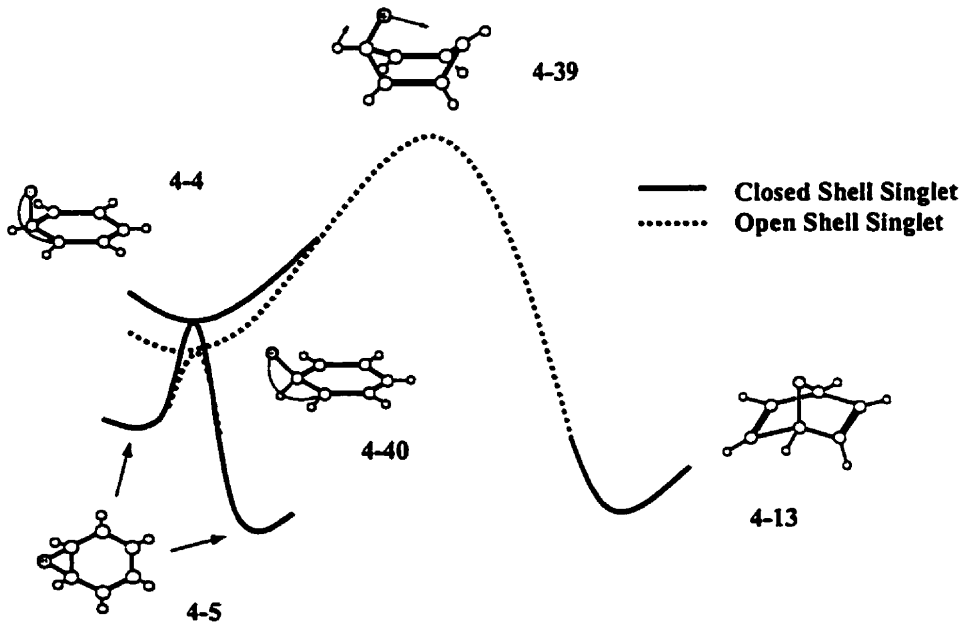

Figure 4-9A The reaction pathway from the "walk" transition states 4-4 and 4-40 to 7-oxa-norbornadiene 4-13

Table 4-16. Relative energies of the isomers in reaction pathway from the "walk" transition states 4-4 and 4-40 to 7-oxa-norbornadiene 4-13 (in kcal/mole) [$\Delta E=E_n-(E_{oxygen}(^3P)+E_{benzene})$]

Isomers	HF	BHandHLYP	BHandHLYP*	B1LYP	B3LYP	BLYP	mPW1PW91	MP2
4-1	0.0	0.0	0.0	0.0	0.0	0.0	0.0	0.0
4-4	52.7	5.1	4.6	-10.5	-15.9	-29.6	-13.2	-5.2
4-5	4.4	-38.7	-35.9	-47.4	-51.8	-58.2	-53.7	-51.1
4-13	21.8	-20.5	-18.5	-27.2	-31.3	-35.7	-35.4	-35.3
4-39		21.3		13.2	9.6	-1.3	9.2	
4-40		-10.2		-14.1	-17.5		-16.6	

Basis sets (except BHandHLYP*): 6-31G*; BHandHLYP*: BHandHLYP/6-311++G**

4-1: reactant of benzene and triplet oxygen atom

4.3.8.2 Electronic properties

Tables 4-6, 4-8 and 4-15 list the HOMO-LUMO gap Δ and $<S^2>$ of the open shell species of **4-9**, **4-16**, **4-39** and **4-40** as predicted by various methods. The magnitude of Δ and the $<S^2>$ decrease proceeding from BHandHLYP, UB1LYP, UB3LYP to UBLYP. This decrease is due to the different weight of exact exchange mixed into these functionals. The more exact exchange that is included in a functional, the larger the HOMO-LUMO gap Δ and the larger the value of $<S^2>$ that are predicted. This increase in Δ is to be expected considering the largest gaps predicted by HF. It is unusual that the LUMO energy as predicted by BLYP is lower than the HOMO in both the closed shell singlet and the open shell singlet of **4-16**. This ordering violates the Aufbau principle [59]. Also the delicate role of local correction, gradient correction (and exact exchange possibly) can be seen from the fine differences between the α and β gaps of **4-40** predicted by UB1LYP and UB3LYP as listed in Table 4-7. The order of the α and β gaps switches from UB1LYP to UB3LYP. UBHandHLYP and UB1LYP predict α gap is larger than β gap, while UB3LYP has the opposite trend. The accurate prediction of HOMO-LUMO gaps is very important for DFT when applied to the prediction of band gaps in conducting materials, it is also useful for ionization potential (IP), electron affinity (EA) prediction and application in excitation energy prediction.

4.4 Concluding Remarks

4.4.1 Chemical applications

The reaction of an oxygen atom (^3P) with benzene where oxygen attacks carbon from above goes through a transition state to a triplet intermediate, followed by an inter-system crossing (ISC) which is necessary for the formation of a stable singlet product. This initial reaction (formation of benzene epoxide) is exothermic. The location of the open shell singlet transition state (**4-40**) helps to explain the mechanism for the reaction of oxygen with benzene producing different products. After the initial reaction (formation of the triplet intermediate **4-3**), one possible pathway was mentioned just above (the formation of benzene epoxide). Another possible pathway proceeds through a second order saddle point (SOSP), **4-38**, from the triplet potential surface down to three different transition states forming benzene epoxide and cyclohexadienone as illustrated in Figure 4-8.

The present study rationalizes the isomerization pathway from 3-Oxa-quadricyclane (**4-12**) to oxepin and another isomer (**4-20**). The isomerization from 3-Oxa-quadricyclane to oxepin is easier than the reverse isomerization based on the barriers. There exists a lower energy open shell singlet pathway for the isomerization as well as the closed shell singlet one, which lowers the activation energy slightly (by about 10 kcal/mol). Isomerization from oxepin to 3-Oxa-quadricyclane is more probable photochemically rather than thermally judged from the activation barriers. This is the first time benzene epoxide (**4-5**) has been connected to 7-Oxa-norbornadiene (**4-13**) by the transition states **4-39**, **4-40** and **4-4**. The isomerization from benzene epoxide (**4-5**) to 7-Oxa-norbornadiene (**4-13**) is thermochemically feasible.

The isomerization from benzene epoxide (**4-5**) to Dewar benzene oxide (**4-15**) is endo-thermic. The large activation barrier makes this reaction difficult under thermal conditions. Also Dewar benzene oxide (**4-15**) can isomerize to its equivalent isomer by oxygen migration from on side to another side but only through a very high barrier about 110 kcal/mol in a closed shell singlet pathway. There exists an open shell singlet pathway with a slightly lower barrier for this oxygen migration.

The reaction pathway from oxepin (**4-7**) to 2-oxa-bicyclo[3.2.0]hepta-3,6-diene (**4-18**) confirmed the need for photolysis in solution since the oxepin (**4-7**) requires 50 to 70 kcal/mol energy to overcome the barrier. 2-oxa-bicyclo[3.2.0]hepta-3,6-diene (**4-18**) can further isomerize to another compound **4-20**. This combination of mechanisms for the isomerization of oxepin (**4-7**) to 3-Oxa-quadricyclane (**4-12**) explained the possible pathway from 3-Oxa-quadricyclane (**4-12**) to 20 in experiment [51].

The present study confirms the proposed reaction mechanism to form butadienylketene (BDK) (**4-24**) through the photochemical reaction of oxygen (^3P) with benzene. Two possible pathways have been located for the formation of the proposed intermediate cyclohexadienone (**4-22**). One follows from benzene epoxide (**4-5**). The other involves a second order saddle point (SOSP) (**4-38**) through a transition state (**4-27**) that connects equivalent cyclohexadienones by hydrogen migration from one side to the other. The pathway from the SOSP (**4-38**) is probable since this SOSP is very close in energy to the initial triplet intermediate while it is lower than the reactants. BDK (**4-24**) can further isomerize to bicyclo[3.1.0]hex-3-en-2-one if an additional 30 kcal/mol of energy is available.

In the present study, for the first time the hydrogen migration between two equivalent

cyclohexadienones has been examined. The process involves a barrier of more than 4-40 kca/mol. Also this is the first study on the isomerization from cyclohexadienone to phenol which help to confirm the mechanism in acidic solution [57]. Following the rotation of the OH group in phenol, the hydrogen of the OH group can migrate to the carbon across the benzene ring to form a dienone. This hydrogen migration can only be achieved photochemically due to the very high activation barrier of about 110 kcal/mol.

For the first time in the present study a C_2 symmetric benzene epoxide (4-33) and C_2 symmetric oxepin (4-35) have been located, and a mechanism provided for the isomerization of these two structures. Judging from the thermodynamics and symmetry, this reaction is not likely to take place as a result of the reaction of triplet oxygen (^3P) with benzene.

4.4.2 Performance of the density functional methods

Among the methods used in characterizing the reaction of oxygen with benzene and isomerization of benzene oxides, the hybrid exchange-correlation functionals: BHandHLYP, B1LYP, B3LYP and mPW1PW91 and especially BHandHLYP and B1LYP are the best tools for chemical reaction characterization. BHandHLYP is not the best for accurate structural and energetic characterizations due to the large component of exact exchange in the functional. B1LYP has been improved for structural description and energy characterization and it has similar performance to that of B3LYP even better than B3LYP in barrier prediction.

In the regions with multi-configuration characteristics, single determinant based methods even CCSD(T) and MPn (up to fourth order) are not really suitable for energy

differences between different electronic states. The inclusion of both dynamic and non-dynamic electron correlation in DFT makes unrestricted DFT capable of describing such critical points on the potential surface. A large admixture of exact exchange worsens the performance of BHandHLYP for the relative energy between the triplet and singlet electronic states especially for conjugated systems. This poor behavior may be due to considerable mixing of higher multiplicity state i.e. spin contamination.

BLYP underestimates the activation barrier. This underestimation may be due to GGAs such as BLYP overestimating conjugation especially in the bond-breaking-bond-forming intermediate and the transition state. Over-stabilization for such structures decreases the energy differences between the stable isomer and the saddle point. Also BLYP predicts different natures for certain stationary points on the potential surface from the hybrid functionals. For some stationary points it violates the Aufbau principle [59]. Mixing of exact exchange improve the shortcomings of GGAs as proven by the performance of the hybrid exchange-correlation functionals (BHandHLYP, B1LYP, B3LYP and mPW1PW91).

B1LYP, B3LYP and mPW1PW91 are of approximately the same quality as MP2 for potential surface characterization. Apparently a reasonable admixture of exact exchange has been included in these hybrid methods. B1LYP gives essentially similar results for structure and energy to B3LYP. B1LYP is better than B3LYP for location of critical points on the potential surface. The different weight of local, gradient correction and exact exchange in B1LYP and B3LYP could change the property for some delicate points on the potential surface because of the change of electronic property.

4.5 References

1. T. H. Lay, J. W. Bozzelli, and J. H. Seinfeld, J. Phys. Chem., **100**, 6543 (1996)
2. B. Klotz, I. Barnes, K. H. Becker, and B. T. Golding, J. Chem. Soc., Faraday Trans., 93(8), 1507 (1997)
3. a) F. Sondheimer, and A. Shani, J. Am. Chem. Soc., **86**, 3168 (1964); b) E. Vogel, and F. –G. Klärner, Angew. Chem. Int. Ed., **7**, 374 (1968); c) D. M. Jerina, B. Witkop, C. L. McIntosh, O. L. Chapman, J. Am. Chem. Soc., **96**, 5578 (1974)
4. U. Zoller, E. Shakkour, I. Pastersky, Š. Sklenak, and Y. Apeloig, Tetrahedron **54**, 14283 (1998)
5. J. R. Kanofsky, and D. Gutman, Chem. Phys. Lett., **15**, 236 (1972)
6. J. R. Kanofsky, D. Lucas, F. Pruss, and D. Gutman, J. Phys. Chem., **78**, 311 (1974)
7. I. Mani and M. C. Sauer, Jr., Adv. Chem. Ser., **82**, 142 (1968)
8. L. I. Avramenko, R. V. Kolesnikova, and G. I. Savinova, Isv. Akad. Nauk. SSSR Ser. Khim., 1, 28 (1965)
9. R. A. Bonanno, P. Kim, J. -H. Lee, and R. B. Timmons, J. Chem. Phys., **57**, 1377 (1972)
10. S. Furuyama and N. Ebara, Int. J. Chem. Kinet., **7**, 689 (1975)
11. R. Atkinson and J. N. Pitts, Jr., J. Phys. Chem., **78**, 1780 (1974)
12. A. J. Colussi, D. L. Singleton, R. S. Irwin, and R. J. Cvetanović, J.Phys. Chem., **79**, 1900 (1975)
13. T. M. Sloane, J. Chem. Phys., **67**, 2267 (1977)
14. S. J. Sibener, R. J. Buss, P. Casavecchia, T. Hirooka, and Y. T. Lee, J. Chem. Phys., **72**, 4341 (1980)

15. F. Tabarés, V. S. Rábanos, and A. G. Ureña, J. Chem. Soc., Faraday Trans. **1**, **78**, , 3679 (1982)

16. A. G. Ureña, S. M. A. Hoffmann, D. J. Smith, and R. Grice, J. Chem. Soc., Faraday Trans. **2**, **82**, 1537 (1986)

17. R. F. W. Bader, M. E. Stephens and R. A. Gangi, Can. J. Chem., **55**, 2755 (1977)

18. R. J. Cvetanović, Adv. Photochem., **1**, 115 (1963)

19. J. K. Parker, and S. R. Davis, J. Am. Chem. Soc., **121**, 4271 (1999)

20. E. Vogel, and H. Günther, Angew. Chem. Int. Ed., **6**, 385 (1967)

21. A) D. M. Hayes, S. D. Nelson, W. A. Garland, and P. A. Kollman, J. Am. Chem. Soc., **102**, 1255 (1980); b) J. M. Schulman, R. L. Disch, M. L. Sabio, J. Am. Chem. Soc., **106**, 7696 (1984); c) D. Cremer, B. Dick, and D. Christeu, J. Mol. Struct. (Theochem), **110**, 277 (1984); d) C. W. Bock, P. George, J. J. Stezowski, J. P. Glusker, Struct. Chem., **1**, 33 (1989)

22. C. C. Pye, J. D. Xidos, R. A. Poirier, and D. J. Burnell, J. Phys. Chem. A, **101**, 3371 (1997)

23. Gaussian 94, Revision B.1, M. J. Frisch, G. W. Trucks, H. B. Schlegel, P. M. W. Gill, B. G. Johnson, M. A. Robb, J. R. Cheeseman, T. Keith, G. A. Petersson, J. A. Montgomery, K. Raghavachari, M. A. Al-Laham, V. G. Zakrzewski, J. V. Ortiz, J. B. Foresman, J. Cioslowski, B. B. Stefanov, A. Nanayakkara, M. Challacombe, C. Y. Peng, P. Y. Ayala, W. Chen, M. W. Wong, J. L. Andres, E. S. Replogle, R. Gomperts, R. L. Martin, D. J. Fox, J. S. Binkley, D. J. Defrees, J. Baker, J. J. P. Stewart, M. Head-Gordon, C. Gonzalez, and J. A. Pople, Gaussian, Inc., Pittsburgh PA, 1995

24. Gaussian 98 (Revision A.5 and A.7), M. J. Frisch, G. W. Trucks, H. B. Schlegel, G. E. Scuseria, M. A. Robb, J. R. Cheeseman, V. G. Zakrzewski, J. A. Montgomery, R. E. Stratmann, J. C. Burant, S. Dapprich, J. M. Millam, A. D. Daniels, K. N. Kudin, M. C. Strain, O. Farkas, J. Tomasi, V. Barone, M. Cossi, R. Cammi, B. Mennucci, C. Pomelli, C. Adamo, S. Clifford, J. Ochterski, G. A. Petersson, P. Y. Ayala, Q. Cui, K. Morokuma, D. K. Malick, A. D. Rabuck, K. Raghavachari, J. B. Foresman, J. Cioslowski, J. V. Ortiz, B. B. Stefanov, G. Liu, A. Liashenko, P. Piskorz, I. Komaromi, R. Gomperts, R. L. Martin, D. J. Fox, T. Keith, M. A. Al-Laham, C. Y. Peng, A. Nanayakkara, C. Gonzalez, M. Challacombe, P. M. W. Gill, B. G. Johnson, W. Chen, M. W. Wong, J. L. Andres, M. Head-Gordon, E. S. Replogle and J. A. Pople, Gaussian, Inc., Pittsburgh PA, 1998

25. C. Adamo, and V. Barone, in Recent Advances in Density Functional Methods, Part II, D. P. Chong ed. World Scientific Co. Pte. Ltd., Singapore, 1997, p115

26. Æ. Frisch, and M. J. Frisch, Gaussian 98 User's Reference, Gaussian Inc., Pittsburgh, PA, 1998

27. A. D. Becke, J. Chem. Phys., **98**, 5648 (1993)

28. C. Lee, W. Yang, and R. G. Parr, Phys. Rev. **B 37**, 785 (1988)

29. M. Nendel, K. N. Houk, L. M. Tolbert, E. Vogel, H. Jiao, and P. v. R. Schleyer, J. Phys. Chem. **A 102**, 7191 (1998)

30. J. L. Durant, Chem. Phys. Lett., **256**, 595 (1996)

31. A. D. Becke, J. Chem. Phys., **98**, 1372 (1993)

32. B. M. Rice, S. V. Pai, and C. F. Chabalowski, J. Phys. Chem. **A 102**, 6950 (1998)

33. H. M. Sulzbach, M. S. Platz, H. F. Schaefer III, and C. M. Hadad, J. Am. Chem.

Soc., **119**, 5682 (1997)

34. A. D. Becke, J. Chem. Phys., **104**, 1040 (1996)

35. J. P. Perdew, and M. Ernzerhof, J. Chem. Phys., **105**, 9982 (1996)

36. C. Adamo, and V. Barone, Chem. Phys. Lett., **274**, 242 (1997)

37. C. Adamo, and V. Barone, J. Chem. Phys., **108**, 664 (1998)

38. A. D. Becke, Phys. Rev. **A 38**, 3098 (1988)

39. C. Møller, and M. S. Plesset, Phys. Rev., **46**, 618 (1934)

40. J. A. Pople, M. Head-Gordon and K. Raghavachari, J. Chem. Phys., **87**, 5968 (1987)

41. X. Li, and J. Paldus, Int. J. Quant. Chem., **77**, 281 (2000)

42. a) B. G. Johnson, and M. J. Frisch, Chem. Phys. Lett., **216**, 133 (1993); b) B. G. Johnson, and M. J. Frisch, J. Chem. Phys., **100**, 7429 (1994)

43. A. A. Jarzęcki, J. Gajewski, and E. R. Davidson, J. Am. Chem. Soc., **121**, 6928 (1999)

44. S. Knuts, B. F. Minaev, O. Vahtras, and H. Ågren, Int. J. Quant. Chem., **55**, 23 (1995)

45. J. Gauss, and J. F. Stanton, J. Phys. Chem., **104**, 2865 (2000)

46. R. A. King, T. D. Crawford, J. F. Stanton, and H. F. Schaefer III, J. Am. Chem. Soc., **121**, 10788 (1999)

47. J. Olsen, O. Christiansen, H. Koch, and P. Jørgensen, J. Chem. Phys., **105**, 5082 (1996)

48. J. D. Goddard, X. Chen, and G. Orlova, J. Phys. Chem. **A 103**, 4078 (1999)

49. J. D. Goddard, and G. Orlova, J. Chem. Phys., **111**, 7705 (1999)

50. R. D. Bach, I. L. Schilke, and H. B. Schlegel, J. Org. Chem., **61**, 4845 (1996)

51. V. H. Prinzbach, and H. Babsch, Angew. Chem., **87**, 772 (1975)

52. a) J. Breulet, and H. F. Schaefer III, J. Am. Chem. Soc., **106**, 1221 (1984) b) D. C. Spellmeyer, and K. N. Houk, J. Am. Chem. Soc., **110**, 3412 (1988)

53. E. E. van Tamelen, and D. Carty, J. Am. Chem. Soc., **89**, 3922 (1967)

54. M. Klessinger, and J. Michl, in Excited States and Photochemistry of Organic Molecules, VCH Publishers, Inc., New York, 1995, p326

55. J. M. Holovka, and P. D. Gardner, J. Am. Chem. Soc., **89**, 6390 (1967)

56. G. Quinker, F. Cech, E. Kleiner, and D. Rehm, Angew. Chem. Int. Ed. Engl., **18**, 557 (1979)

57. M. Capponi, I. G. Gut, B. Hellrung, G. Persy, and J. Wirz, Can. J. Chem., 77, 605 (1999)

58. J. Harris, Phys. Rev., **A 29**, 1648 (1984)

59. P. R. T. Schipper, O. V. Gritsenko, E. J. Baerends, Theo. Chem. Acc., **99**, 329 (1998)

Chapter 5

Numerical Examination of Density Functional Methods: Aspects of the Exchange and Correlation Potentials

5.1 Introduction

The evaluation of the results from density functional theory based methods for chemical reaction energies and structural characterizations in Chapters 3 and 4 support the conclusion that the popular density functional methods, especially hybrid density functional methods, are good tools for applied quantum chemistry. Among the density functionals employed, BHandHLYP gave the highest reaction barriers, while BLYP gave the lowest ones and sometimes even predicted a negative reaction barrier. The amount of exact (Hartree-Fock) exchange modifies the nature of some stationary points on the potential energy surface. For example, the triplet intermediate in the reaction of triplet oxygen with benzene is a transition state when the component of exact exchange is increased from 0.000 to 0.150, while it becomes a minimum when the exact exchange component is set at 0.200. We also note that the B1LYP and mPW1PW91 functionals predict different results for some species in the study of the oxygen atom reacting with benzene.

The underestimation of the reaction barrier by a GGA method (as shown in Chapter 4) was attributed to the self-interaction error (SIE) intrinsically rooted in the approximate density functional. It is their SIE that cause widely used DFT methods to give the wrong dissociation curve for H_2^+ [1]. The mixture of exact exchange improves the performance of density functionals for such a dissociation as indicated in Yang's work [1].

Based on such observations, the role of exact exchange in density functionals methods will be studied in the first part of this chapter. The analysis will be based on consideration of the total, kinetic, potential and electron-electron interaction energies for the simple atoms and ions of H, He and Li as well as for the one-electron molecular cation H_2^+.

The exchange portion of the usual exchange-correlation functionals accounts for most (about 90%) of the exchange-correlation energy [2]. Thus in most cases the behavior of the exchange functional is much more important to the energy prediction than is the correlation functional. In some delicate cases, for example the very flat potential energy surfaces of linear molecules such as H_2C_3O and H_2C_3S, correlation is critical to obtaining qualitatively correct results for the structure and relative energies.

A newer DFT method, mPW1PW91, including the modified PW91 exchange functional combined with the PW91 correlation functional along with 0.25 of the exact exchange was shown to be a very efficient computational tool and comparable in accuracy to B3LYP, and in some cases it gives even better performance than B3LYP [3]. In the second part of this chapter, this new combination of exchange correlation functionals, mPW1LYP, was tested on the reduced G2 data [4] as well as on some weakly interacting systems to examine the role of the correlation functional in the prediction of molecular properties.

5.2 The Role of Exact Exchange and of the Self-Interaction Error: Numerical Examination of the Atoms and Ions of H, He, Li and of Ion-Molecular Ion H_2^+

5.2.1 Theoretical background

5.2.1.1 Adiabatic connection mechanism, ACM

The local density approximation, the basis of Kohn-Sham theory, was derived from the homogeneous electron gas – a non-interacting system. The rapid change of electron density in the chemical bond requires a non-local treatment of the phenomenon of

bonding. The general gradient approximation (GGA) is such an approach although it is still local in terms of the mathematical definitions of local and non-local, since the GGA includes the gradient correction only at the reference point. GGAs have shown considerable success in many chemical problems and have become popular tools for chemical application [4]. However, in the region of bond formation and breaking, GGAs are now known not to be the best choice.

The mixture of exact exchange into the functional improved the performance of DFT methods significantly [5,6]. In fact, Becke's three-parameter hybrid protocol serves as a "standard" method for the application of current density functional theory. The B3 model was fit to the G2 data set of the structures and thermodynamics of molecules to determine any adjustable parameter. Thus, given the results from that fitting process, there was no precise explanation why approximately 20% exact exchange is appropriate for the best overall performance of this protocol. Of course, the fundamental basis of the mixing of the exact exchange arises from the adiabatic connection mechanism (ACM) [7].

In ACM, the Hamiltonian was written as

$$\hat{H}^{\lambda} = \hat{T} + \lambda \hat{V}_{ee} + \hat{V}_{ext}^{\lambda} \qquad (5.1)$$

$\hat{T}$ is the kinetic energy term. $\hat{V}_{ee}$ is the electron-electron interaction, and λ is an electron-electron coupling parameter ranging from 0 to 1. At λ=0, the system (the electrons) is in the noninteracting Kohn-Sham reference state, and at λ=1, the system is in the fully interacting state. $\hat{V}_{ext}^{\lambda}$ is the external potential felt by the system at coupling strength λ and it is mainly the electron-nuclear attraction if no other perturbation is added to the system.

The electron-electron interaction energy E_{ee} can be found by integrating $\hat{V}_{ee}$

$$E_{ee} = \int_0^1 \lambda \hat{V}_{ee} \, d\lambda \qquad (5.2)$$

For convenience, it can be rewritten as [6]:

$$E_{XC} = \int_0^1 U^{\lambda}_{xc} \, d\lambda \qquad (5.3)$$

E_{XC} is the exchange-correlation energy (here the electron-electron repulsion energy was excluded from V_{ee} as described in (5.2) since the greatest concern here is the exchange-correlation) and U^{λ}_{XC} is the exchange-correlation potential energy at coupling strength λ. ACM "connects" the non-interacting Kohn-Sham reference system (λ=0) to the fully interacting real system (λ=1) by a continuous partially interacting system with coupling strength λ ($0 \leq \lambda \leq 1$) sharing a common density ρ of the real, fully interacting system.

At λ=0, the system corresponds to the non-interacting Kohn-Sham reference system, i.e. no correlation between the electrons is considered. Exchange results from the fact that the Kohn-Sham orbitals are are arranged in Slater determinants. This situation resembles the conventional Hartree-Fock method (this pure exchange energy is essentially equal in value to the Hartree-Fock exchange energy). The exchange energy at this point was designated E_X – the Kohn-Sham exchange energy [6]. ACM rationalizes the essential role of exact exchange (in practical computation, the E_X is the Hartree-Fock exchange although E_X is not the Hartree-Fock exchange by definition) in density functional theory for highly accurate performance in property prediction as shown by the B3LYP protocol. The B3 scheme can be generalized as:

$$E_{XC}^{hyb} = E_{XC}^{LSD} + a_0(E_X - E_X^{LSD}) + a_x(E_X^{GGA} - E_X^{LSD}) + a_c(E_C^{GGA} - E_C^{LSD}) \qquad (5.4)$$

E_{XC}^{LSD} is the local exchange correlation functional, E_X is the exact exchange, E_X^{LSD} is

the local exchange, E_X^{GGA} is exchange with gradient correction, E_X^{LSD} is local exchange, E_C^{GGA} is correlation with gradient correction and E_C^{LSD} is the local correction. The fitting of the numerical results of the B3 scheme to the G2 thermodynamic data results in the optimal parameters for exact exchange (E_X), a_0= 0.20, local exchange (E_X^{LSD}), gradient correction to local exchange (LSDA) E_X^{GGA}, B_X^{88}(Becke's 1988 exchange functional), a_x=0.72, and correlation E_{Corr}(E_C^{GGA}+-E_C^{LSD}), PW91(Perdew's 91 correlation functional), a_c= 0.81. The original correlation used in the B3 scheme was the 1991 gradient correction for the correlation of Perdew and Wang [8], while the most popular correlation functional is LYP, the gradient correction for the correlation functional developed by Lee, Yang and Parr[9].

5.2.1.2 **Rationale of exact exchange in the exchange-correlation functional**

It is well known that local density functional methods and GGAs are physically inappropriate near the λ=0 exchange-only limit in molecular bonds due to incorrect localized and nonstatic "left-right" correlation. This physical defect causes the overbinding tendency of LSDA and GGAs. Further simplification of the B3 scheme leads to Becke's one-parameter protocol [10]

$$E_{XC} = E_{XC}^{DFT} + a_0(E_X^{Exact} - E_X^{DFT}) \qquad (5.5)$$

in which the DFT pure exchange part with qualitatively incorrect behavior near λ=0 was replaced by the exact exchange of the Kohn-Sham determinant which is correct near λ=0 and thus can properly represent the λ=0 region in the ACM. In practical applications, Hartree-Fock (HF) exchange was employed to replace the exact exchange of the Kohn-Sham determinant. In this thesis, HF exchange is used for the exact exchange of the

Kohn-Sham determinant unless otherwise specified.

The fitting to the G2 data resulted in the value of a_0 in equation (5). This value is 0.16 or 0.28 depending on the choice of DFT and DFT-GGA combination in Becke's work [10]. The new one-parameter scheme is much simpler and appears to yield results of higher quality than the three-parameter scheme [6,10].

Based on observations of the performance of Half-and-Half (HandH) [5], three-parameter [6] and one-parameter [10] protocols within the ACM, Perdew and co-workers [11] rationalized the optimal weight of HF exchange in the hybrid scheme with the aid of perturbation theory.

A simple model for the hybrid coupling constant dependence was proposed [11]:

$$E_{XC,\lambda}^{hyb}(n) = E_{XC,\lambda}^{DFT} + (E_X - E_X^{DFT})(1-\lambda)^{n-1} \qquad (5.6)$$

Integrating the energy density results in

$$E_{XC}^{hyb} = \int_0^1 d\lambda \; E_{XC,\lambda}^{hyb} = E_{XC}^{DFT} + \frac{1}{n}(E_X - E_X^{DFT}) \qquad (5.7)$$

n was proposed to be 4, the lowest order of perturbation theory which provides a realistic description of the shape of the λ-dependence of the exact $E_{XC,\lambda}$,

$$E_{XC,\lambda} \approx e^2(c_0 + c_1\lambda + \cdots + c_{n-1}\lambda^{n-1}) \quad (0 \le \lambda \le 1) \qquad (5.8)$$

So equation (7) can be rewritten as

$$E_{XC}^{hyb} = \int_0^1 d\lambda \; E_{XC,\lambda}^{hyb} = E_{XC}^{DFT} + \frac{1}{4}(E_X - E_X^{DFT}) \qquad (5.9)$$

The rationale of the role and of the weight of HF exchange inspired new combinations of functionals: B1LYP, B1PW91 [12] and mPW1PW91 [3]. These methods have similar performance to or even better performance than B3LYP [12,3] in practical calculations. The behavior of density functional methods with the change in the amount of HF

exchange in the hybrid methods is still not entirely clear.

5.2.1.3 Self-interaction error, SIE

The total energy of the electronic ground state is a functional of the electron density ρ(r). In Kohn-Sham density functional theory,

$$E[\rho(r)] = T_S[\rho] + V_{Ne}[\rho] + J[\rho] + E_{XC}[\rho] \qquad (5.10)$$

An electron can interact coulombically with other electrons but not with itself. Violation of this principle yields the self-interaction error (SIE).

In the Hartree-Fock approximation, the electron-electron repulsion term J is

$$J=\frac{1}{2}\int d^3r \int d^3r' \frac{|\varphi(r)|^2|\varphi(r')|^2}{|r-r'|} \qquad (5.11)$$

and the exchange term E_X is

$$E_X = -\frac{1}{2}\sum_{\sigma}\sum_{\alpha,\alpha'} f_{\alpha\sigma} f_{\alpha'\sigma} \int d^3r \int d^3r' \frac{\varphi^*_{\alpha\sigma}(r)\varphi^*_{\alpha'\sigma}(r')\varphi_{\alpha'\sigma}(r)\varphi_{\alpha\sigma}(r')}{|r-r'|} \qquad (5.12)$$

f is the occupation number orbital φ. When $\alpha=\alpha'$, E_X cancels J and there is no self-interaction in the HF approximation, i.e. the HF approximation is self-interaction free. In the case of a one-electron system, $J[\rho] + E_{XC}[\rho]=0$ and an SIE free method results.

In current density functional schemes, the electron repulsion term is independent of the exchange-correlation term, so a self-interaction free result is not expected. Even for the hydrogen atom, exchange functionals such as LSDA, B, and the correlation functionals VWN, P86, PW91 are not SI free [13].

For a q-electron system, with $0 < q \leq 1$, Zhang and Yang [1] derived a scaling relation required if the E_{XC} is to be SIE free:

$$E_{XC}[q\rho_1] = q^2 E_{XC}[\rho_1] \qquad (5.13)$$

where ρ_1 is the density for a one-electron system.

Usually the SIE is negative [1], i.e. SIE decreases the total energy of the system. For many-electron systems, the SIE might also be negative for a fractional number of electrons for example in transition states or intermediates where the number of electrons in a orbital is not integral. In general, SIE will increase for a system with a fractional number of electrons. The resulting total energy of such a system would be too negative [1]. For transition states and intermediates where bond-breaking and bond-forming take place, the SIE is more serious than it is in the region near a stable equilibrium geometry.

5.2.2 Previous studies

5.2.2.1 Exchange functionals

Lacks and Gordon [14] calculated the exchange energy contribution (ΔE_X) for pairs of helium and neon atoms with the exchange functionals B86A[15], B86B[16], B88(B)[17], PW86[18] and PW91[8] for the Hartree-Fock electron density. These results compared with the corresponding HF exchange energy contributions to the atomic interactions of a dimer of inert atoms. The ΔE_X is dominated by the small-density-large-gradient regions between the two inert atoms. Correct large-gradient behavior of functional is necessary if density-functional theory is applied to a weakly interacting system where weak attractive interactions play important roles.

In that work, the authors concluded that PW86 and B86B were the best functionals in the large-gradient regions, as these two functionals were the only exchange functionals they found which accurately predicted ΔE_X for the internuclear separations of interest. The PW91 functional, reparameterized from PW86, which satisfies theoretical constraints of an exact exchange functional, did poorly in this case, as did B88. This is the first work

which studied extensively the behavior of existing exchange functionals on weakly interacting systems. Based on the observations of the performance of the exchange functionals on the total exchange energy and the exchange-energy contribution to the total interaction (compared with the HF exchange energy contribution) for the helium and neon dimers, the authors proposed a new exchange functional Lack-Gordon (LG), which gives good results for both the total exchange energy and the exchange-energy contribution (ΔE_X).

Through the one-parameter progressive (OP) correlation functional [19], the conventional exchange functionals, (LSD (Slater exchange) [20], B88, PW91, G96 [21], PBE [22]) were examined [23]. In that work, 11 physical conditions were introduced for exchange functionals. The 11 conditions require that the exchange functionals should satisfy the following relations:

a: The exchange functionals are limited to an energetic region. The exchange functional is scaled to a constant under coordinate-scaling and should have a lower bound [24].

b: The exchange functional should reproduce the local density approximation of exchange for constant density and is for slowly-varying density can be expanded to a definite term.

c: The exchange functionals should be self-interaction free.

d: The exchange functional should decay asymptotically to reproduce the correct behavior of the exchange energy.

For the exchange functionals studied, LSD (Slater exchange), B88, PW91, G96, PBE and B88 do not scale to a constant under coordinate-scaling. All the functionals studied produce SIE. Only B88 decays asymptotically correctly for an exponentially decaying

density. B88 and G96 do not have the correct lower bound and do not satisfy the expansion in the slowly varying limit ($x_\sigma \to 0$) of density. Note that these exchange functionals (except LSD), despite the theoretical limitations noted, behave very well in predicting the chemical properties of the molecules in the G2 data set.

5.2.2.2 **Correlation functionals**

In contrast to exchange, correlation is not determined by simple dimensionality and scaling rules. Becke selected the following four simple "minimal" requirements for correlation in his work on a one-parameter scheme [25],

(1) attainment of the exact uniform electron gas limit,

(2) distinct treatment of opposite-spin and parallel-spin correlation,

(3) perfectly self-interaction free,

(4) a good fit to the exact correlation energies of atomic systems.

Tests of the conventional correlation functionals LYP [9] and PW91[8] showed that LYP does not satisfy requirements (1) and (2), PW91 does not satisfy requirement (3). LYP does not attain the exact uniform electron gas limit and does not take into account of the parallel-spin correlation. PW91 is not self-interaction free. In the present work, only the LYP and PW91 correlation functionals are discussed since only these two correlation functionals were employed in the computations of this work. In earlier work on the OP functional [19], LYP and PW91 were found not to be negative or zero for any density. LYP also does not scale properly under several conditions while PW91 does.

5.2.3 Computational details

Self-consistent field (SCF) calculations were carried out with the Gaussian 98 A.7 program [26] on a Silicon Graphics Origin 2000 server at the University of Waterloo. The following scheme [27] was employed:

$$E = P_2E_X^{HF} + P_1(P_4E_X^{Slater} + P_3\Delta E_X^{non\text{-}local}) + P_6E_C^{local} + P_5\Delta E_C^{non\text{-}local} \quad (5.14)$$

E_X^{HF} is the HF-exchange, E_X^{Slater} is the Slater local exchange, $\Delta E_X^{non\text{-}local}$ is the gradient correction (not exactly non-local correlation) to the local exchange (here B, PW91, G96, mPW91 and LG were used). E_C^{local} is the local correlation and $\Delta E_C^{non\text{-}local}$ is the gradient correction to the correlation. The coefficients (P_5 and P_6) for correlation were fixed at 1 or 0 depending on whether correlation was employed or not. The LYP and PW91 correlation functionals were employed in this work. For the coefficients of the exchange functionals, P1, P2, P3 and P4, we chose P3=P4=1 and P1 + P2 =1. P1(P2) was increased (or decreased) from 0.00 (1.00) to 1.00 (0.00) by 0.01 changes. Equation 5.14 could be written as:

$$E = P_2E_X^{HF} + P_1(E_X^{Slater} + \Delta E_X^{non\text{-}local}) + (E_C^{local} + \Delta E_C^{non\text{-}local}) \quad (5.15)$$

in this expression, $(E_C^{local} + \Delta E_C^{non\text{-}local})$ is the gradient corrected correlation functional E_C^{GGA}.

Without correlation, it is,

$$E = P_2E_X^{HF} + P_1(E_X^{Slater} + \Delta E_X^{non\text{-}local}) \quad (5.16)$$

Actually $(E_X^{Slater} + \Delta E_X^{non\text{-}local})$ is the GGA functional for the exchange functional, so Equation 16 can be written as:

$$E = P_2E_X^{HF} + P_1E_X^{GGA} \quad (5.17)$$

Equations 5.16 and 5.17 can be rewritten as:

$$E = xE_X^{GGA} + yE_X^{HF} + E_C^{GGA} \qquad (5.18)$$

and

$$E^X = xE_X^{GGA} + yE_X^{HF} \qquad (5.19)$$

E^X is the energy without a contribution from the correlation functional.

$$x + y = 1 \qquad (5.20)$$

If E_X^{GGA} in Equations 5.18 and 5.19 is replaced by the exchange GGAs, B, G96, PW91, mPW91 and LG, the scheme described by Equation 5.19 becomes BxHFy, G96xHFy, PW91xHFy, mPW91xHFy and LGxHFy respectively.

The basis set used for all atoms is Dunning's cc-pv5Z (for Li, the cc-pv5Z was obtained from the PNNL web page) [28]. This set was chosen to be as consistent as possible for H, He and Li since the largest basis set available for Li from this web page is cc-pv5Z. For comparison, HF, CCSD-T (or CISD) with cc-pv5Z were employed to predict energies for the systems considered.

5.2.4 Results and discussion

5.2.4.1 Formulas of exchange and correlation functionals

5.2.4.1.1 Exchange functionals

The exchange functionals studied here are B[17], PW91[8], LG[14], G96[21] and mPW91[3].

The B exchange functional was constructed on semi-empirical grounds[16],

$$E_X = E_X^{LSDA} - \zeta \sum_\sigma \int \rho_\sigma^{4/3} \frac{\chi_\sigma^2}{(1 + 6\zeta\chi_\sigma \sinh^{-1}\chi_\sigma} d^3r \qquad (5.21)$$

ζ: was determined by a least squares fit to exact atomic Hartree-Fock exchange energy

ζ=0.0042 is for a best fit to the six noble gas atoms helium to radon. σ is electron spin either "up" or "down".

$$\chi_\sigma = \frac{|\nabla \rho_\sigma|}{\rho_\sigma^{4/3}}$$

$$E_X^{LSDA} = -C_X \sum_\sigma \int \rho_\sigma^{4/3} d^3r \qquad C_X = \frac{3}{2}\left(\frac{3}{4\pi}\right)^{1/3}$$

Exchange functionals can be rewritten in the following general form,

$$E_X = -\sum_\sigma \int \rho_\sigma^{4/3} K_\sigma d^3r \qquad (5.22)$$

and K_σ is the exchange functional kernel.

Then the kernel for the exchange functional B is,

$$K_\sigma^{B} = K_\sigma^{LSDA} + \zeta \frac{\chi_\sigma^2}{1 + 6\zeta\chi_\sigma \sinh^{-1}\chi_\sigma} \qquad (5.23)$$

and

$$K_\sigma^{LSDA} = \frac{3}{2}\left(\frac{3}{4\pi}\right)^{1/3} \qquad (5.24)$$

is the kernel of the Slater local density approximation.

Starting from the form of the B functional, the PW91 exchange functional was modified to satisfy the Levy scaling inequalities and the local Lieb-Oxford bound with the following form. At small χ_σ, it reduces to the gradient expansion with the correct value $10C_X/7$ where C_X is the Sham coefficient (in order to be compared to other functionals, each functional was rewritten as the sum of a local term and the gradient correction term),

$K_\sigma^{PW91} = K_\sigma^{LSDA} +$

$$\frac{(0.2743-0.1508e^{-100\chi_\sigma^2/(48\pi^2)^{2/3}})\chi_\sigma^2/(48\pi^2)^{2/3}-0.004\chi_\sigma^d/(48\pi^2)^{2/3}}{1+6\zeta\chi_\sigma\sinh^{-1}\chi_\sigma+0.004\chi_\sigma^d/(48\pi^2)^{4/3}}K_\sigma^{LSDA} \qquad (5.25)$$

ζ is 0.0042 both in the B and PW91 functionals and d is 4 in PW91.

The LG fit to the total exchange energy and exchange-energy contribution to the total interaction (compared with the HF exchange energy contribution) of the helium and neon dimers and cast in the form of PW86, has the following form [14],

$$K_\sigma^{LG}=\frac{[1+(10^{-8}+0.1234)S^2/b+a_4S^4+a_6S^6+a_8S^8+a_{10}S^{10}a_{12}S^{12}]^b}{1+10^{-8}S^2}K_\sigma^{LSDA} \qquad (5.26)$$

$S=\frac{\chi_\sigma}{(48\pi^2)^{1/3}}$, b=0.024974, a_4=29.790, a_6=22.417, a_8=12.119, a_{10}=1570.1, a_{12}=55.94

Without applying a fundamental constraint, Gill's 96 exchange functional (G96) [21] has performance comparable with the B functional but with much greater simplicity. The author fit the one parameter to the HF exchange energy for the Ar atom using the HF/6-311++G density. G96 has the following form,

$$K_\sigma^{G96}=K_\sigma^{LSDA}+\chi_\sigma^{3/2}/137 \qquad (5.27)$$

In Lacks and Gordon's work [14], it was found that the arbitrary choice of the coefficient and exponent of the χ^d term in the PW91 exchange functional which makes the functional obey the Levy scaling inequality and the Lieb-Oxford bound, does not affect significantly the total atomic energy. This choice does determine the behavior of the exchange functional in the low-density and large-gradient regions far from the nuclei. Based on such an observation, the exponent of the χ^d term in the PW91 exchange functional was modified to be d=3.73 resulting in the modified PW91 exchange functional, mPW91 [3]. In this mPW91 exchange functional, the ζ value was set to 0.0046 rather then the original value of 0.0042.

Based on the above analysis, all the exchange functional kernels can be written in the following general form,

$$K_\sigma^{GGA} = K_\sigma^{LSDA} + \Delta K_\sigma^{GGA} \qquad (5.28)$$

and ΔK_σ^{GGA} is the General Gradient Approximation Correction to LSD.

5.2.4.1.2 Correlation Functionals

LYP[9], one of the most popular correlation functionals, is a "second-order gradient expansion" to the Colle-Salvetti correlation functional [29] which was fit to the correlation energy of the helium atom in order to determine the parameters,

$$E^C = -a\int \frac{1}{1+d\rho^{-1/3}}\{\rho + b\rho^{-2/3}[C_F\rho^{5/3} - 2t_W + (\frac{1}{9}t_W + \frac{1}{18}\nabla^2\rho)]e^{-c\rho^{-1/3}}\}dr \qquad (5.29)$$

a=0.049, b=0.132, c=0.2533 and d=0.349,

$$t_W = \frac{1}{8}\frac{|\nabla\rho(r)|^2}{\rho(r)} - \frac{1}{8}\nabla^2\rho \text{ and } C_F = \frac{3}{10}(3\pi^2)^{2/3}$$

In practical computation, the $\nabla^2\rho$ term in (5.29) was eliminated [9b].

Starting from the VWN correlation functional [2], a spin-interpolation formula for the correlation functional (kernel) (local part) was proposed by Perdew and Wang [8b] which is:

$$\varepsilon_C(r_S,\zeta) = \varepsilon_C(r_S,0) + \alpha_C(r_S)\frac{f(\zeta)}{f''(0)}(1-\zeta^4) + [\varepsilon_C(r_S,1) - \varepsilon_C(r_S,0)]f(\zeta)\zeta^4 \qquad (5.30)$$

$$f(\zeta) = \frac{[(1+\zeta)^{4/3} + (1-\zeta)^{4/3} - 2]}{(2^{4/3} - 2)} \qquad (5.31)$$

$f(0)=0$, $f(1)=1$, and $f''(0)=1.709921$, $\alpha_C(r_S) = f''(0)[\varepsilon_C(r_S,1) - \varepsilon_C(r_S,0)]$ and

r_S is density parameter,

$$r_S=[\frac{3}{4}\pi(\rho_\alpha+\rho_\beta)]^{1/3} \qquad (5.32)$$

ρ_α is the electron density with α spin and ρ_β is the electron density with β spin, ζ is the relative spin polarization,

$$\zeta=(\rho_\alpha-\rho_\beta)/(\rho_\alpha+\rho_\beta) \qquad (5.33)$$

There was another gradient correction term H combined with this kernel $\varepsilon_C(r_S,\zeta)$ in the PW91 correlation energy [8c],

$$H=H_0+H_1 \qquad (5.34)$$

$$H_0=g^3\frac{\beta^2}{2\alpha}\ln[1+\frac{2\alpha}{\beta}\frac{t^2+At^4}{1+At^2+A^2t^4}], \qquad (5.35)$$

$\alpha=0.009$, $\beta=\nu C_C(0)$, $\nu=(16/\pi)(3\pi^2)^{1/3}$, $C_C(0)=0.004235$, $C_X=-0.001667$,

$$A=\frac{2\alpha}{\beta}\frac{1}{e^{-2\alpha\varepsilon_C(r_S,\zeta)/(g^3\beta^2)}-1} \qquad (5.36)$$

$$H_1=\nu[C_C(r_S)-C_C(0)-3C_X/7]g^3t^2\exp[-100g^4(k_S^2/k_F^2)t^2] \qquad (5.37)$$

$t=|\nabla\rho|/2gk_S\rho$ (5.38) is the scaled density gradient,

$g=[(1+\zeta)^{2/3}+(1-\zeta)^{2/3}]/2$ (5.39)

This correlation functional was fit to Green's-function Monte Carlo data at high and low density for the uniform electron gas to obtain the correct behavior [8b].

5.2.4.2 One-electron systems – H, He^+, H_2^+

For a one-electron system, there is no electron-electron interaction but the kinetic energy and nuclear-electron attraction terms remain. Such systems can be used to check the self-interaction error of the functionals.

5.2.4.2.1 H and He^+

With the schemes outlined by Equations 5.15 to 5.19, the energy of the hydrogen atom was calculated self-consistently by BxHFy, G96xHFy, PW91xHFy, mPW91xHFy and LGxHFy. If the correlation functionals (LYP and PW91) are included, two new protocols BxHFyLYP and PW91xHFyPW91 are created. Since the real exchange-correlation functional is not known, there is no systematic way to improve the total energy of the system, nor is there a minimum energy bound for a system. It is meaningless to focus on the total energy itself, as it is not comparable to the conventional *ab initio* energy. If such a comparison was made, it gives only a general idea about the behavior of the functional for energy prediction (fortunately the energy difference rather than the energy itself is more important in chemistry). The comparison of the energy predicted by DFTs with *ab initio* methods (for example the full CI (configuration interaction) or CC (coupled cluster)) provides only this rough idea of the closeness of the DFT energy (and correlation energy) to its counterpart from conventional *ab initio* theory.

Following equations 5.18 (or 5.19), and 5.20, there are 101 calculations with one protocol for one system if y (or x) changes by 0.01 in each step from 1.00 to 0.00. The curves of total energy for the hydrogen atom *vs.* y (ratio of HF exchange) predicted by these protocols are shown in Figure 5-1. The total energy is in Hartree (for discussion mH, i.e. milliHartree or 10^{-3} Hartree will also be used).

Since the starting point (y=1.00) is the energy predicted by HF, all the curves begin at a common point. The energy predicted by the pure GGA exchange functional without any HF exchange lies at the end point of the curve (y=0.00). All the curves appear to be straight lines with different slopes as shown in Figure 5-1. Among the curves of the

functionals tested, G96xHFy has the smallest slope and PW91xHFy has the largest slope. The order of the slopes is:

$$G96xHFy < LGxHFy < BxHFy < mPW91xHFy < PW91xHFy \qquad (5.40)$$

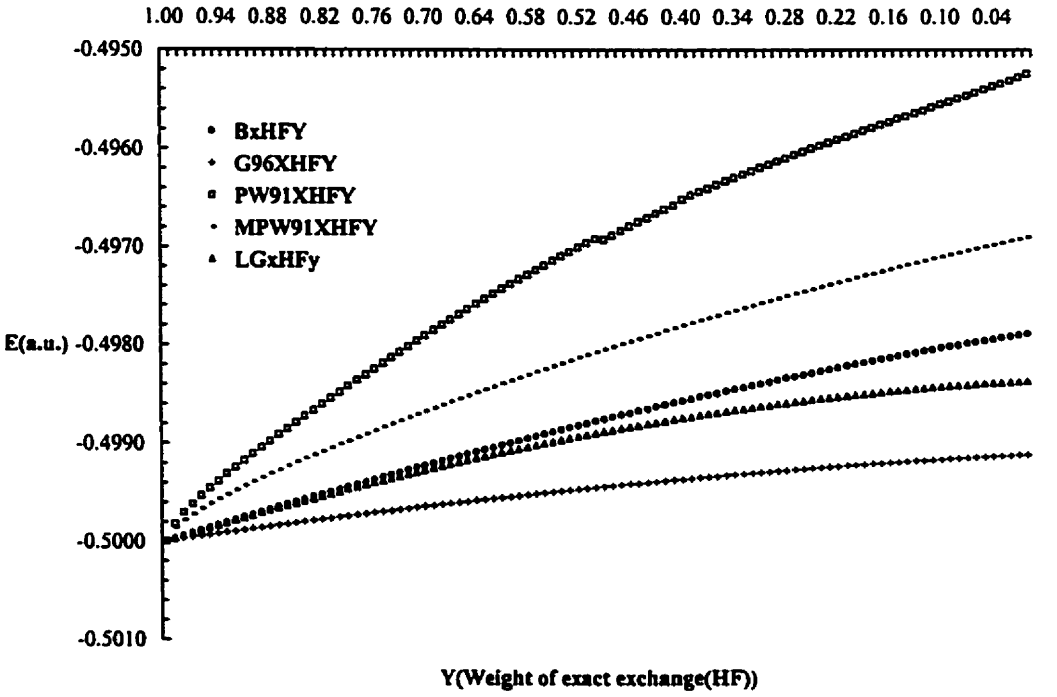

Figure 5-1 Energy of H predicted by BxHFy, G96xHFy, PW91xHFy, mPW91xHFy and LGxHFy

Equation 5.19 can be rewritten as,

$$E^X = E_X^{HF} + (1-y)E_X^{GGA} = E_X^{GGA} + y(E_X^{HF} - E_X^{GGA}) \qquad (5.41)$$

The slope of the curve ($E_X^{HF} - E_X^{GGA}$) indicates the energy difference between HF and pure GGA. The largest difference of energy predicted by GGAs from HF is that by PW91xHFy. It is about 5mH (3kcal/mol). The comparable energy difference for G96 from HF is only about 1mH (0.6kcal/mol). All the energies predicted by hybrid protocols and GGAs are higher than those from HF. Since there is only one electron in hydrogen, the energy predicted by CI or CC should be the same as by HF. The HF energy with cc-pv5Z for hydrogen is -0.499994522 Hartree.

Among the curves in Figure 1, PW91xHFy is far from the other curves with the largest slope. The modification of the parameters in PW91 decreases the slope as shown by the curve of mPW91xHFy. The BxHFy and LGxHFy curves are close to each other. Around the y = 0 starting point, these two curves overlap each other up to almost y = 0.75. After that point, the LGxHFy curve deviates from BxHFy bending slightly downward.

All the curves should be straight lines as required by Equation 41. The deviation from a straight line indicates the non-linear relation between the HF exchange and exchange functional. This non-linear relation does not satisfy equation 5.41. Among the five curves, PW91xHFy and LGxHFy show greater nonlinearity than the other three.

The plots of energies *vs.* the component of HF exchange of He^+ predicted by the five functionals are similar to their counterparts for H in shapes and relative order of the slopes as shown in Figure 5-2. The energy differences between HF and GGAs results become larger. Such a difference of HF and PW91xHFy is about 10mH (6.5kcal/mol). It

is 2mH (1.3kcal/mol) for HF and G96xHFy. For the high accuracy required in chemistry, such an error is still relatively large since the system (hydrogen) is the smallest normally considered in chemistry.

Figure 5-2 Energy of He^+ predicted by BxHFy, G96xHFy, PW91xHFy, mPW91xHFy and LGxHFy

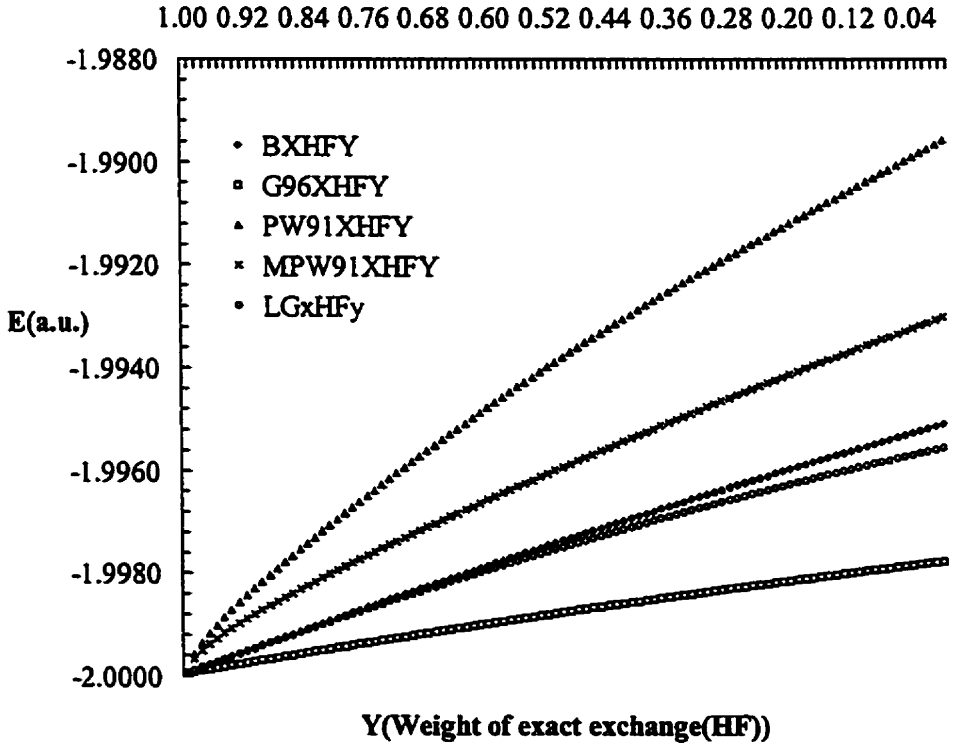

In order to obtain deeper insight into the behavior of the functional, the total energies of H and He^+ by all methods are decomposed into the kinetic and potential energies. There is no electron-electron interaction in these one-electron systems. The kinetic and potential energies of H and He^+ are plotted *vs.* the weight of HF exchange in Figures 5-3 to 5-6.

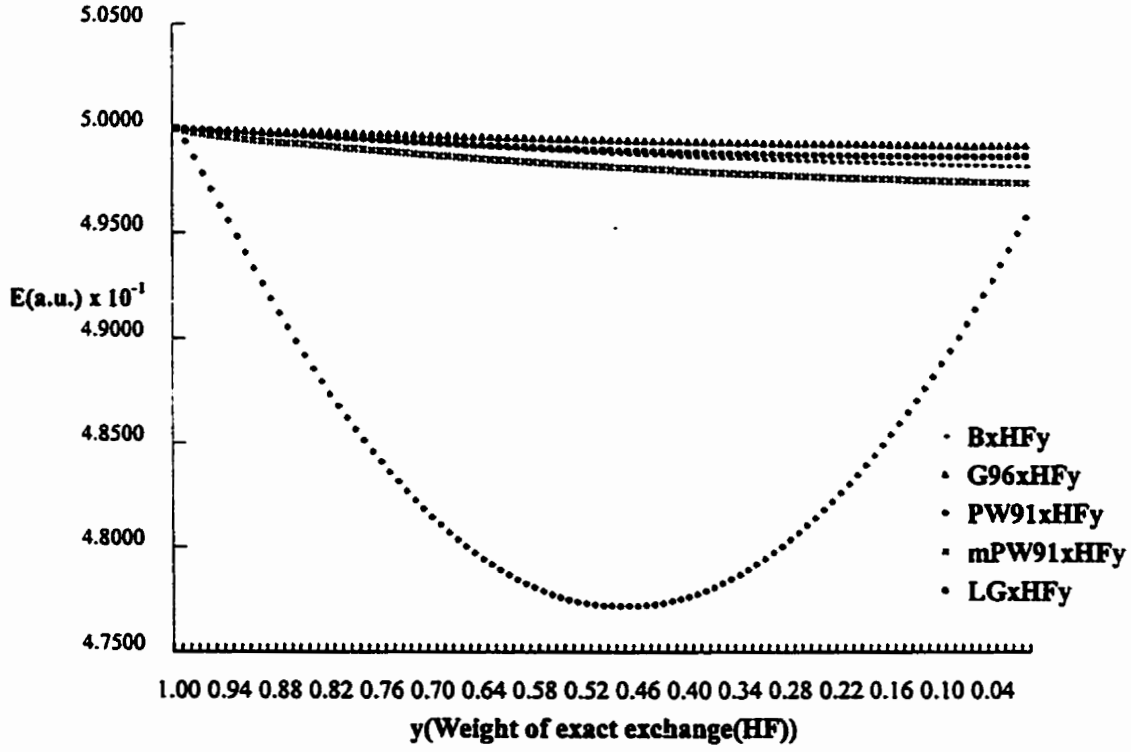

Figure 5-3 Kinetic Energy of H predicted by BxHFy, G96xHFy, PW91xHFy, mPW91xHFy and LGxHFy

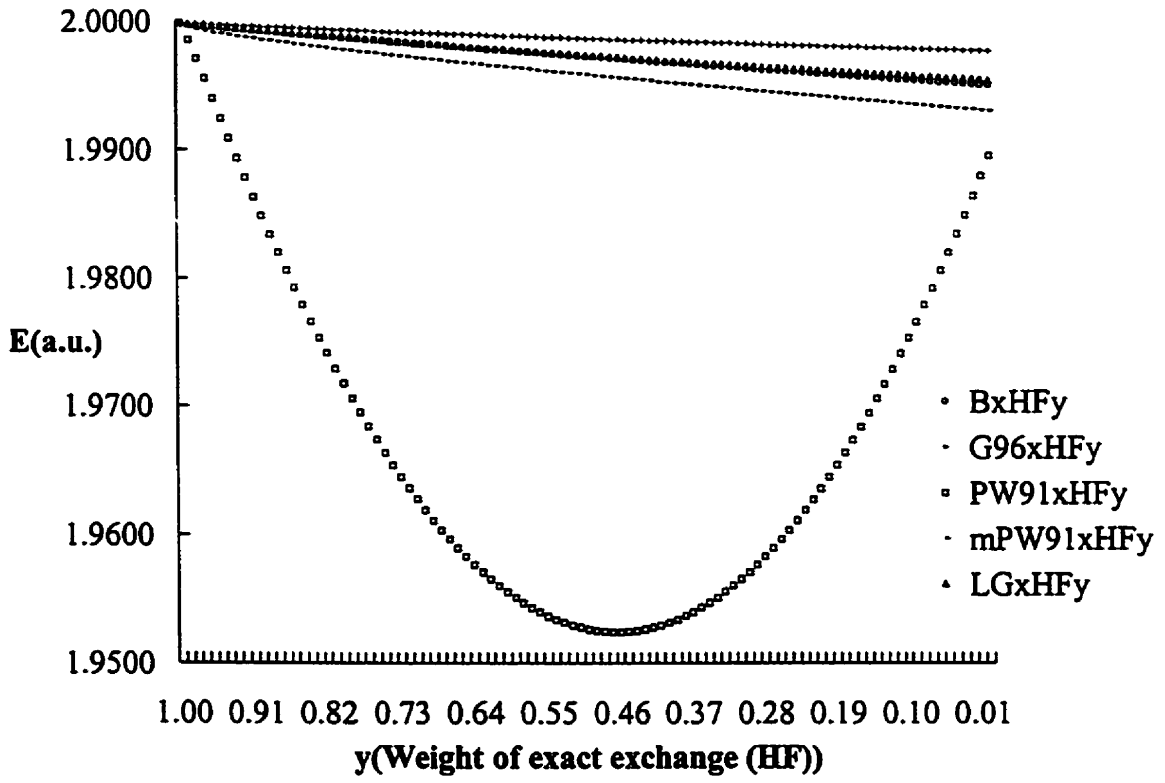

Figure 5-4 Kinetic energy of He^+ predicted by BxHFy, G96xHFy, PW91xHFy, mPW91xHFy and LGxHFy

Figure 5-3 shows the kinetic energy of the hydrogen atom. The curves for BxHFy, G96xHFy, mPW91xHFy and LGxHFy have similar shapes. These straight lines have a very small and negative slope. The kinetic energies are slightly lower than that from HF. The results from these functionals are similar to those from HF exchange (the largest absolute error is 26mH, within 0.6% of HF value). The order of these four curves switches compared with the order for the total energies by these methods. The shape of the PW91xHFy curve is striking as it resembles the second half of a plot of the sine

function with a minimum around y=0.50. The reason of the difference of the shape of PW91xHFy from those of the other methods is unclear. The kinetic energy plots for He^+ (in Figure 5-4) are similar to those for H. The error from BxHFy, G96xHFy, mPW91xHFy and LGxHFy is much smaller for He^+ than that of H. The PW91xHFy curve is still sine like with a minimum near y=0.50.

Figures 5-5 and 5-6 are plots of the potential energies, V_{ne}, of H and He^+ predicted by the five methods. In contrast to the curves for the kinetic energies, the slopes of the first four curves (BxHFy, G96xHFy, mPW91xHFy and LGxHFy) are slightly positive with the same ordering as the curves for the total energy. In this case, the PW91xHFy curve resembles the positive portion of a sine function.

It is understandable that the slopes of the total energies predicted by all the methods vary in the same way as the potential energies. The viral theorem requires

$$-\frac{V}{T} = 2 \qquad (5.42)$$

for an atomic system or a molecule in a bound stationary state [30,31]. V is the potential energy and T is the kinetic energy of the system. So the potential energy determines the shape of the curve for the total energy. The adherence to the viral theorem is the reason the overall curves of the total energy of H and He^+ predicted by PW91xHFy are straight lines although the kinetic and potential energies have a parabolic shape. The different trends in the potential and kinetic energy curves predicted by PW91xHFy cancel to cause the total energy curve to be flat. The total energy curve does show the same tendency as the potential curve.

The linear relationship of potential and kinetic energies to the weight of exact exchange predicted by PW91xHFy will be discussed later.

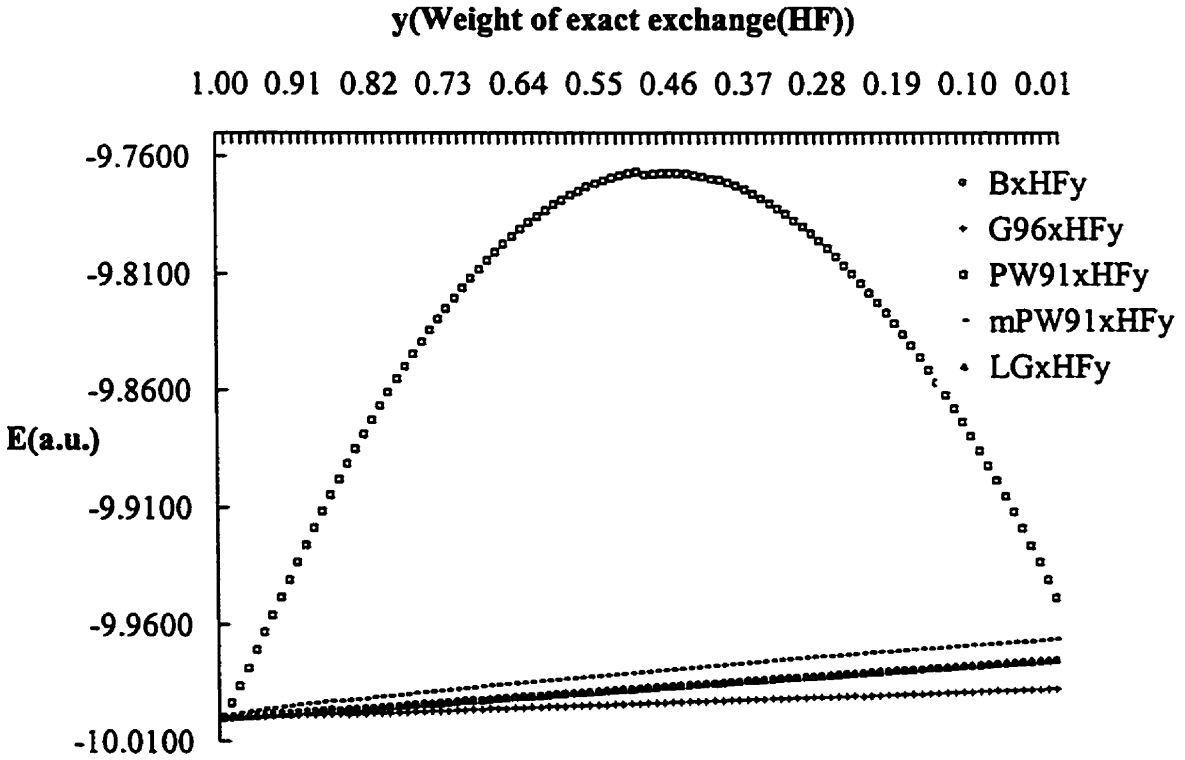

Figure 5-5 Potential Energy of H predicted by BxHFy, G96xHFy, PW91xHFy, mPW91xHFy, LGxHFy

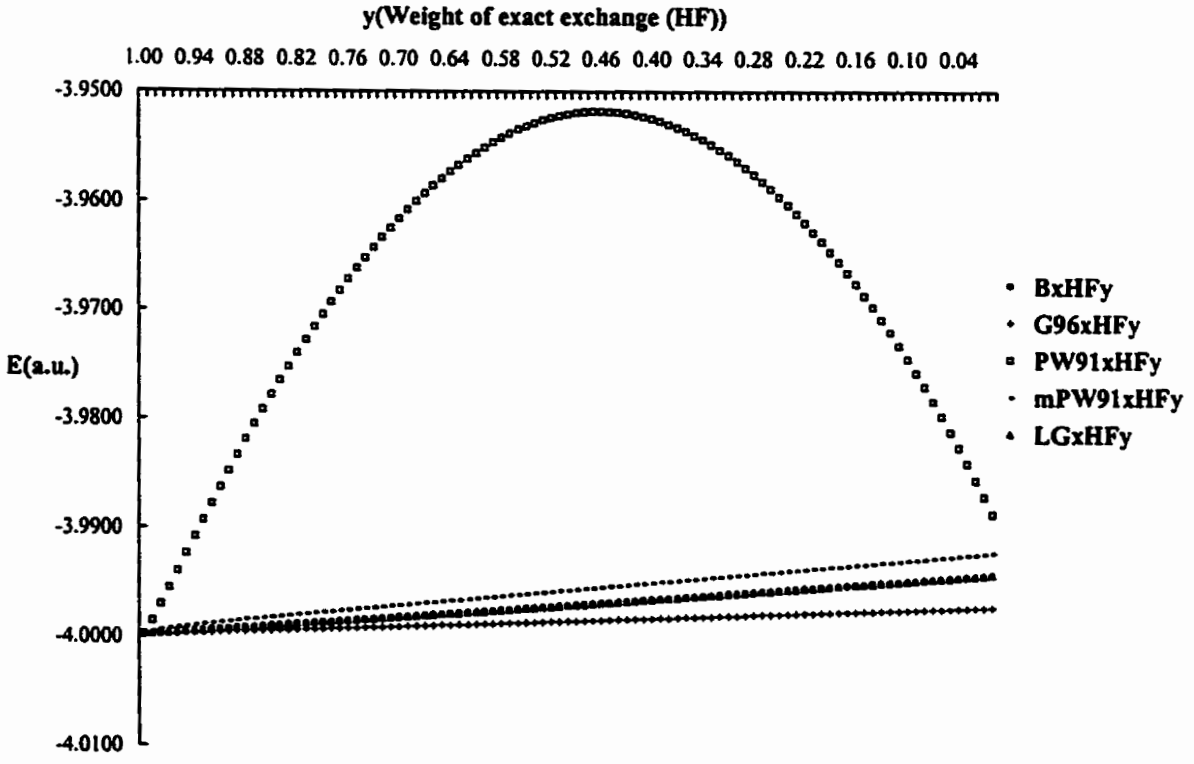

Figure 5-6 Potential energy of He^+ predicted by BxHFy, G96xHFy, PW91xHFy, mPW91xHFy and LGxHFy

5.2.4.2.2 H_2^+

The bond distance in H_2^+ is chosen to be 4 Å, since at this point, the self-interaction error of the method employed was very clear in Yang's earlier work [1]. This simplest molecular system excludes other effects.

Figure 5-7 presents plots of the total energy of H_2^+ *versus* the weight of HF exchange as predicted by the five methods. All five curves are straight lines with slightly different slopes. The ordering of these curves (for the total energy) is:

$$G96xHFy < LGxHFy \approx BxHFy < mPW91xHFy < PW91xHFy \qquad (5.43)$$

In contrast to the energy curves of H and for H_2^+, He^+ predicted by the same methods, the slopes predicted by all five methods for He^+ total energy are negative i.e. the total energies predicted by all the GGAs are lower than those from HF. The largest energy difference between the GGAs and HF is about 71mH. This difference is significant if the total energy of H (0.499994522 Hartree by HF) and H_2^+ (0.503229541Hartree by HF) are taken into account. The major physical difference in this case from H and He^+ is that H_2^+ has a nuclear-nuclear repulsion term. However all methods must predict the same nuclear-nuclear interaction energy for a fixed nuclear geometry. Thus there may still be different behaviors of the potential and kinetic energy curves since these two terms contribute together to the total energy of He^+.

Figures 5-8 and 5-9 illustrate the kinetic and potential energy curves for H_2^+ predicted with the five methods. In Figure 5-8, all the curves have positive slopes, i.e. all GGAs predict higher kinetic energies than does HF. Except for PW91xHFy, the other four methods have similar curves with slightly different slopes. The curve predicted by PW91xHFy is much flatter than the comparable one for H and He^+ and is concave. On

the other hand, the potential curves for H_2^+ have negative slopes. Similar to the kinetic energy curves, all methods except for PW91xHFy predict nearly straight lines with very similar slopes. PW91xHFy predicts a flat curve with the convex character and yields the highest energy. The concavity in kinetic energy and convexity in potential energy curves (as predicted by PW91xHFy) cancel each other so that the total energy is a straight line as shown in Figure 5-7.

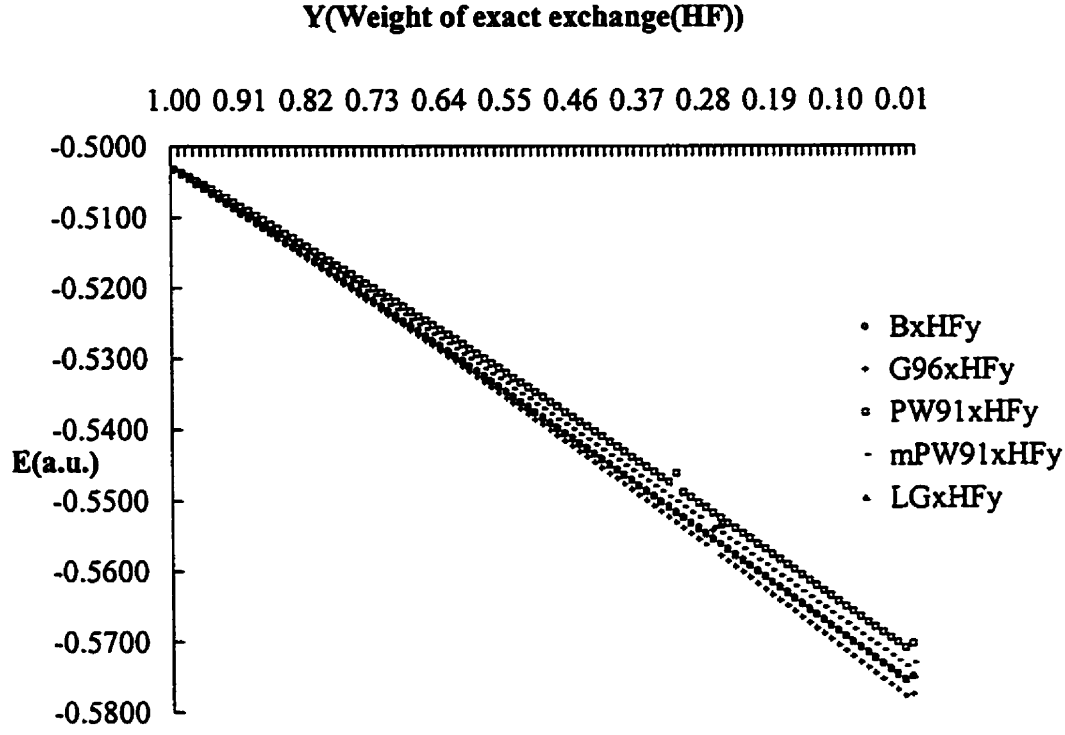

Figure 5-7 Energy of H_2^+ at 4 Å predicted by BxHFy, G96xHFy, PW91xHFy, mPW91xHFy and LGxHFy

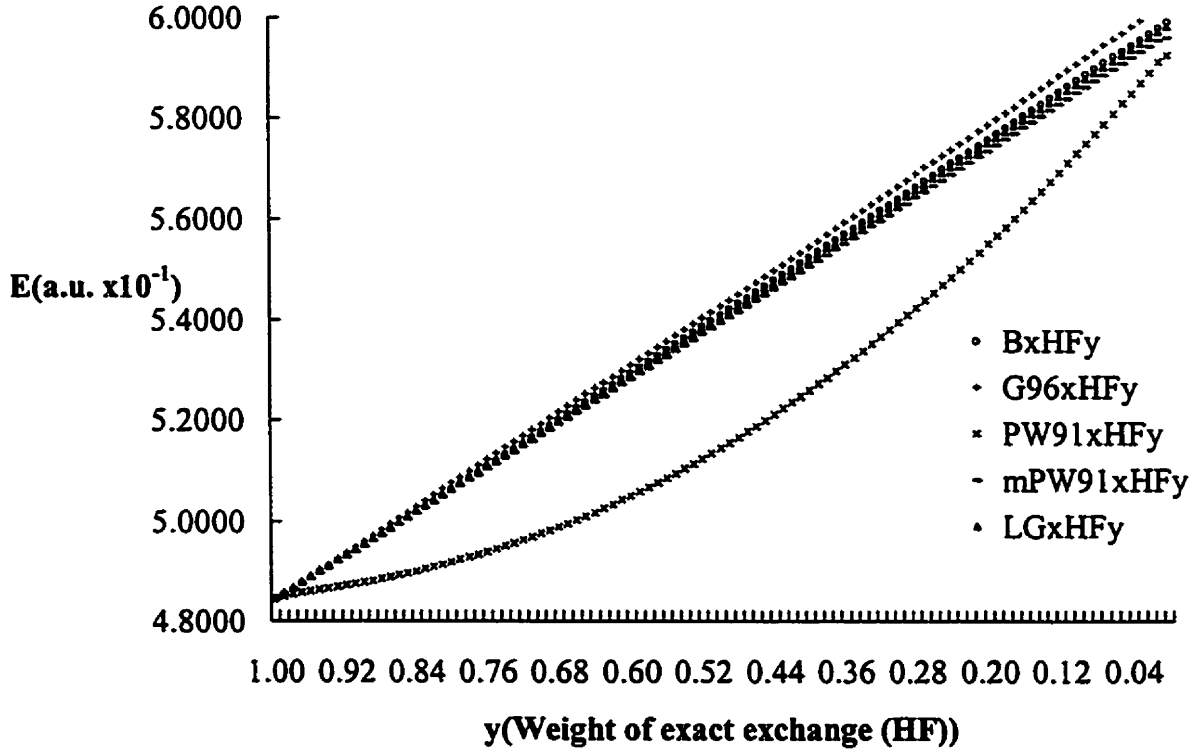

Figure 5-8 Kinetic energy of H_2^+ (R=4Å) predicted by BxHFy, G96xHFy, PW91xHFy, mPW91xHFy and LGxHFy

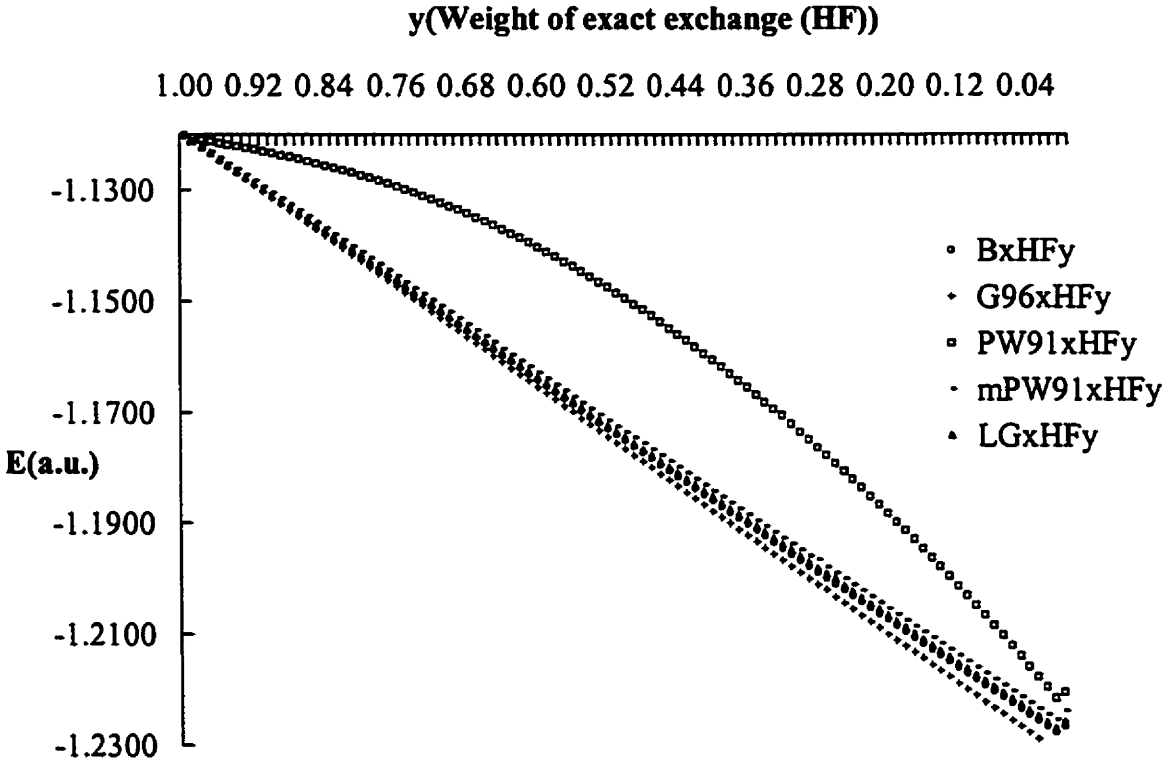

Figure 5-9 Potential energy of H_2^+ (R=4Å) predicted by BxHFy, G96xHFy, PW91xHFy, mPW91xHFy and LGxHFy

5.2.4.2.3 Self-interaction error, SIE

Since there is no electron-electron interaction in a one-electron system, self-interaction error must be the cause of any electron-electron term which is not zero. The study on the B exchange functional based methods with H_2^+ showed that H_2^+ is a good system for testing SIE [1]. For H_2^+, as the HH distance increases, the electron density on each nucleus should be half of an electron and the "halves" of the one electron should not interact with each other. Thus H_2^+ can be employed to test for SIE with various exchange functionals: B, G96, PW91, mPW91 and LG. The correlation functionals LYP and PW91 also are to be tested. Furthermore, H, and He^+ are also used to test these functionals to see if there is any SIE for these systems with an integral number of electrons in an orbital.

The SIE of the five methods employed for H_2^+ at R=4Å are reported in Figure 5-10. The SIE of HF exchange is zero as shown at the starting point (y=1.00). All plots are straight lines. As the weight of HF exchange decreases, the SIE increases (more negative). Based on such observations, the role of exact exchange and the behavior of the density can be discussed. The order of (absolute value) SIE increase as,

$$PW91 < mPW91 < B \approx LG < G96 \qquad (5.44)$$

The smallest SIE is –74.6mH (46.8kcal/mol) by PW91 exchange functional and the largest is –82.7 mH (51.9kcal/mol) by G96. The BxHFy curve in Figure 5-10 confirms the order of the SIE for BHandHLYP, B3LYP and BLYP for SIE in Yang's work [1]. The HF component reduces the SIE in hybrid DFT since HF exchange is free of SIE. Figure 5-10 clearly shows the existence of the SIE in DFT functionals for systems with non-integral electrons. The reason why there are discontinuity of curves at y=0.30 and the increase of energy for PW91PW91 and PW91(exchange only) in Figure 5-10 is unclear.

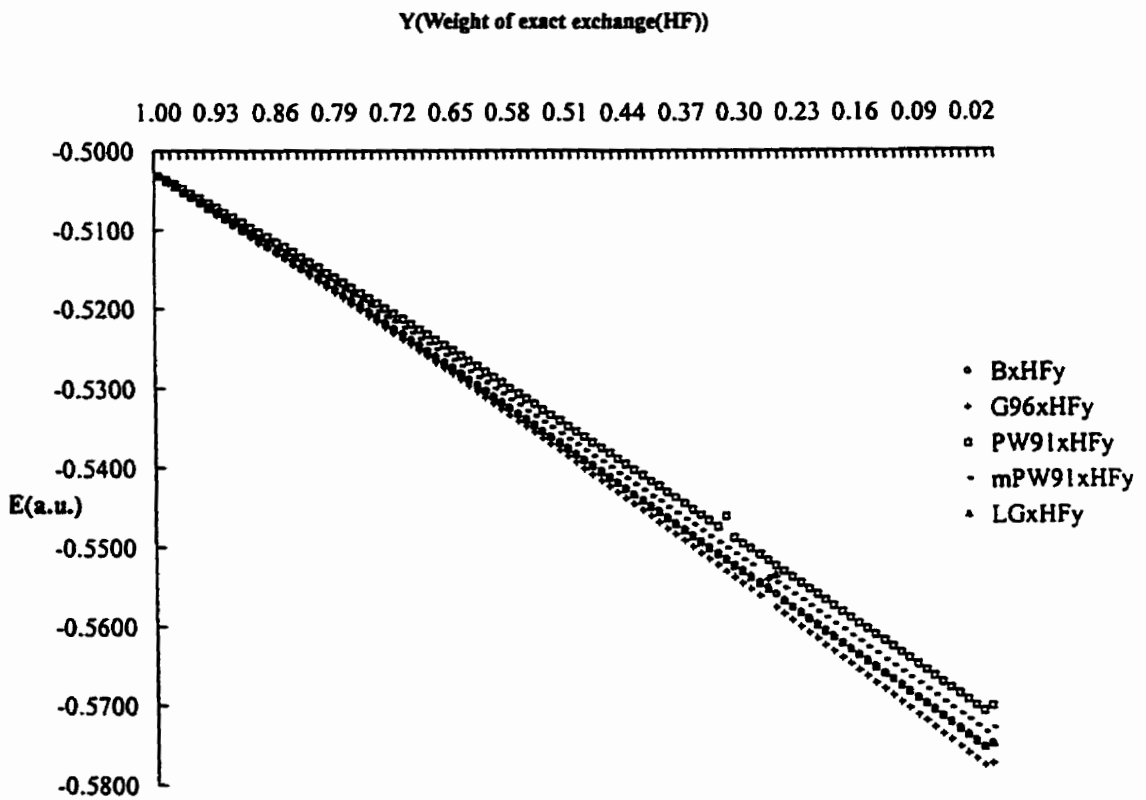

Figure 5-10 Self-interaction error of H_2^+ (R=4Å) predicted by BxHFy, G96xHFy, PW91xHFy, mPW91xHFy and LGxHFy

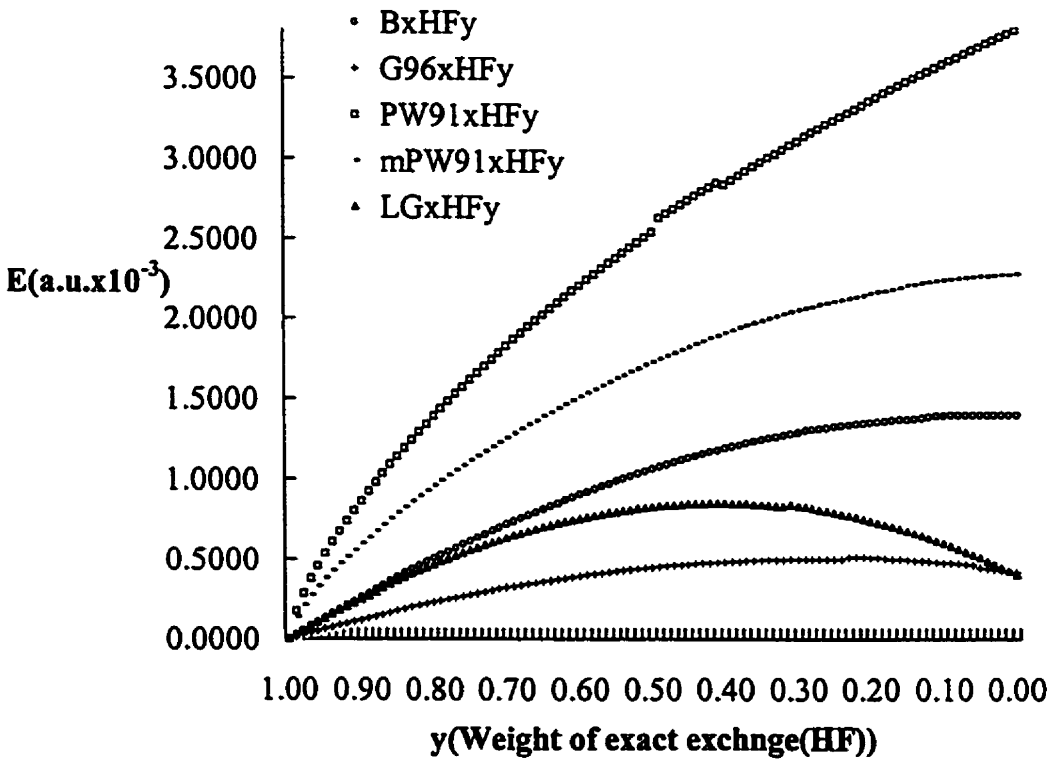

Figure 5-11 Self-interaction error of H predicted by BxHFy, G96xHFy, PW91xHFy, mPW91xHFy and LGxHFy

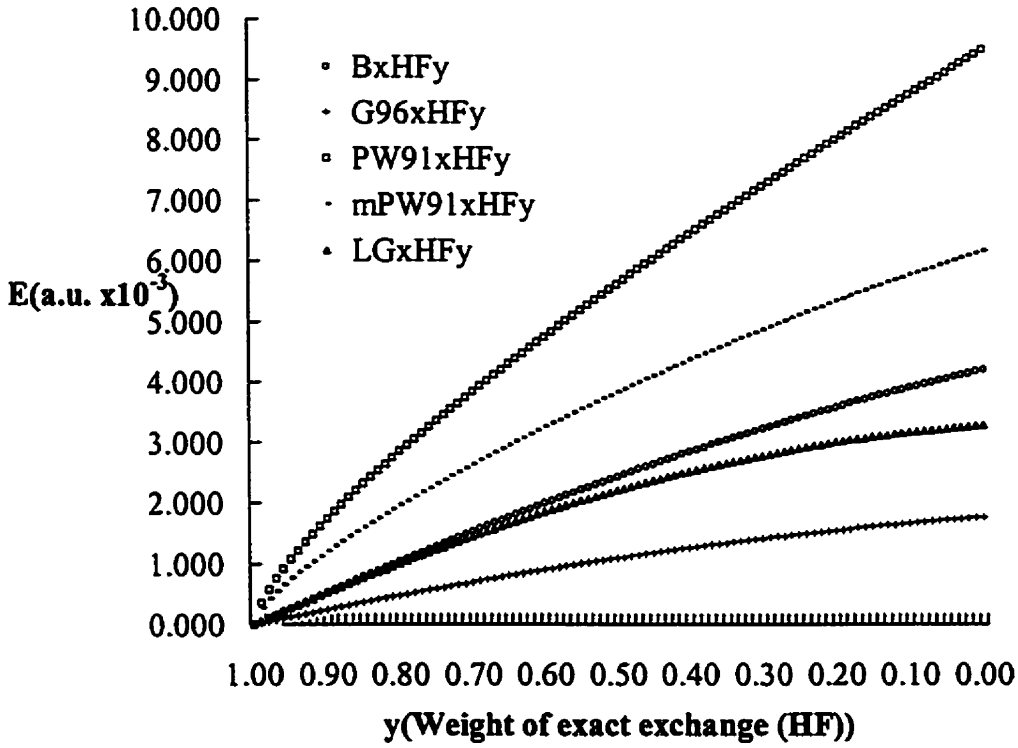

Figure 5-12 Self-interaction error in He^+ predicted by BxHFy, G96xHFy, PW91xHFy, mPW91xHFy and LGxHFy

The SIE for H and He^+ also were calculated by these methods and are reported in Figures 5-11 and 5-12. Figure 5-11 reports the SIE of the five methods for H. It is also unclear why there is discontinuity in the curve around y=0.50 in Figure 5-11 predicted by PW91xHFy. In contrast to the SIE in H_2^+, the SIE in H as predicted by all five methods is positive rather than negative (as in H_2^+). SIE increases in the order (absolute value),

$$G96 < LG < B < mPW91 < PW91 \qquad (5.45)$$

The magnitude of the SIE with all methods for H is much smaller than that in H_2^+. The largest SIE is predicted by PW91, 3.8mH (2.4kcal/mol) and the smallest is 0.4mH(0.3kcal/mol) by G96. The SIE of these methods for He^+ has similar curves to those for H. All the SIEs in He^+ predicted by these methods are positive and the same order of magnitude as for H. This is one reason that these DFT methods predict higher energy of H and He^+ than HF does. Usually DFT methods predict lower energy for system than HF does. The largest SIE for He^+ is 9.5mH (6.0kcal/mol) for PW91 and the smallest is 1.8mH (1.1kcal/mol) for G96.

The contribution from the LSD also is analyzed to check the contribution from the gradient correction in GGAs. In GGAs, the LSD accounts in large part for the total energy as manifested by equations 21 to 28. LSD also accounts for about one quarter of the total SIE (–26mH ≈16.6kcal/mol) in H_2^+ indicating that the SIE in GGA is largely (ca. 75%) due to the gradient correction. Surprisingly, the LSD contribution is much higher. The order of magnitude of the total SIE of all methods in H and He^+ is 10^{-3}. However, it is 10^{-2} Hartree for the LSD contribution in these systems. In H, the LSD contribution to the SIE is 41.4mH (25.6kcal/mol) while the total SIE for PW91 exchange is only 3.8mH(2.4kcal/mol). In He^+, the contribution from LSD to SIE is 85.9mH

(53.9kcal/mol), approximately a factor of nine greater than the total SIE from PW91 exchange for He^+.

The most notable observation is the difference in the behaviors of the functionals on H_2^+, H and He^+ with regards to the SIE. One observation is that the SIE of the functionals is greater for the systems with fractional electrons than that with integral electrons. The other observation is that LSD has larger SIE for a system with integral electrons (for example in the cases of He^+ and H). It may be that LSD is important in the region with high electron density while the gradient correction is important in the region with large electron density gradient i.e. a large variation in the electron density. In H_2^+, there exists a region with large electron density gradient due to the bonding, while the electron density in H is regularly and more densely distributed in space. In DFT, the electron repulsion term is essentially independent of the exchange-correlation term (as shown in Equation 10) especially when only the exchange term is applied. It is expected that the SIE may be reduced if an appropriate exchange functional is combined with a suitable correlation functional in order to cancel the error.

The SIE for some correlation functionals are also examined. The LYP functional earlier was found to be SIE free by theoretical analysis [1]. The identical energies of BxHFy and BxHFyLYP in the present study confirm such a conclusion. Figure 5-13 reports the energies of H_2^+ predicted by PW91xHFy and PW91xHFyPW91 at a bond length of 4Å. The PW91xHFyPW91 curve is lower in energy than that of PW91xHFy by a constant amount. The constant is the self-interaction error of the PW91 correlation functional for H_2^+. The value is 4.4mH (2.7kcal/mol) and much smaller than that for the PW91 exchange functional, 74.6mH (46.8kcal/mol). It is reasonable since the exchange

energy is much larger than the correlation energy in atoms and molecules.

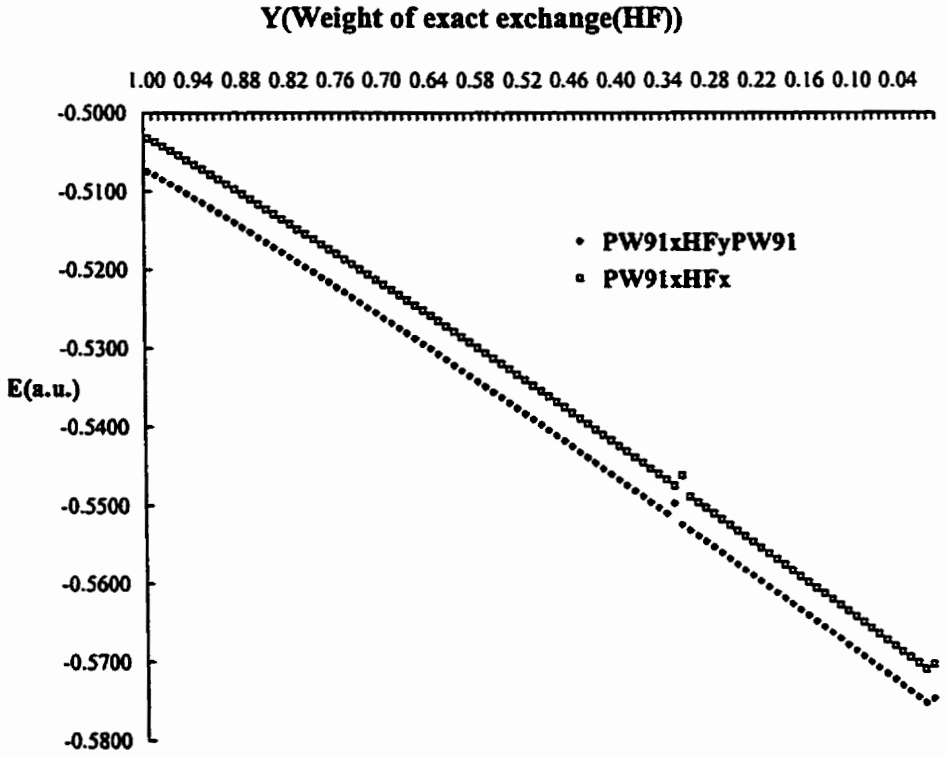

Figure 5-13 Self-interaction error in H_2^+ (R=4Å) predicted by PW91xHFy and PW91xHFyPW91

5.2.4.3 Two-electron systems – H^-, He, Li^+

Electron-electron interactions exist once the system has more than one electron. A two-electron system is obviously the simplest multielectron system. There are two possibilities for the relative spin orientations of the two electrons: parallel and antiparallel.

The system with only parallel electrons (for example the lowest triplet state of the helium atom) has a Fermi hole indicating a region in which the probability of finding another electron with the same spin is small. A Coulomb hole is a region in which the probability of finding another electron with opposite spin is small. For the parallel case, HF treats the system well enough that the conventional electron correlation for triplet Helium is relatively small (approximately 0.001598a.u.=1kcal/mol from the CCSD(full) model with a cc-pv5Z basis set). For parallel electrons, HF includes some electron correlation based on exchange.

For a system with only antiparallel electron, for example singlet helium, HF cannot treat this electronic interaction of antiparallel (electron correlation) properly. The integration of the antiparallel electrons over the spin orbitals disappears and thus there is no exchange term. Only the coulombic interaction is taken into account at the HF level. So the conventional electron correlation energy (the difference between the energy of HF limit and the non-relativistic energy of the system) is significant in systems with antiparallel electrons (electron correlation will be discussed in the next section using mPW1LYP). The correlation energy (E(CISD(full))-E(HF)) of singlet helium with the cc-pv5Z basis set is 41.5mH (26.1kcal/mol).

5.2.4.3.1 H^-

There is a well-known failure of the local-spin-density approximation (LSDA). Negative ions are not bound and this can cause the GGAs to have this intrinsic failure [6]. In spite of this obvious difficulty, the energy of H^- is calculated by all methods employed to illustrate the energy change with the change of the HF component and the different behaviors of the functionals.

The total energies of H^- predicted by all methods are plotted in Figure 5-14. Except for the energy predicted by PW91xHFy, all other energies decrease as the weight of HF exchange decreases. This means that GGAs (without correlation functional) predict lower energies than does HF. The PW91xHFy curve rises slowly up to a point around y=0.50, then decreases slowly. This is different from the monotonic decrease of the other curves. All these calculations show that the extra electron does bind to H in this hydrogen anion. However, this binding is an artifact due to the limited basis set. The Gaussian basis set confines the electron to the space around the hydrogen atom since the basis functions do not extend to infinity. It is the limited basis set which requires that the electron remain near and thus bond to the nucleus. Numerical calculations with complete basis set would change the curves shown in Figure 5-14 [32].

Figure 5-15 shows the energy of the highest occupied orbital as predicted by all exchange functionals. The curves for all the methods except PW91xHFy overlap each other and are nearly straight lines. This agrees with the linear relation expected between HF exchange and the GGA exchange functional as described by Equations 5.19 and 5.41. All curves have positive slope i.e. HF exchange lowers the energy of the highest occupied orbital in hybrid density functional methods. The overlap of these lines indicates that B,

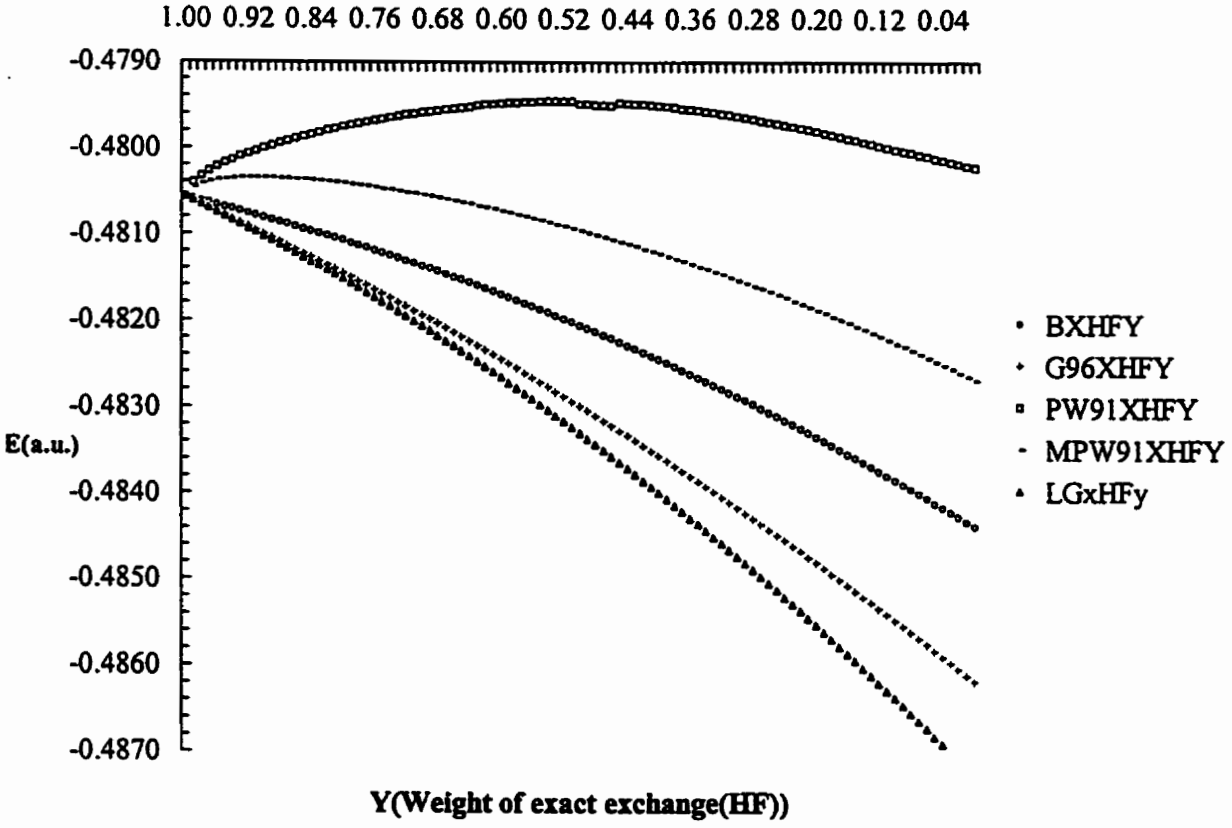

Figure 5-14 Energy of H^- predicted by BxHFx, G96xHFy, PW91xHFy, mPW91xHFy and LGxHFy

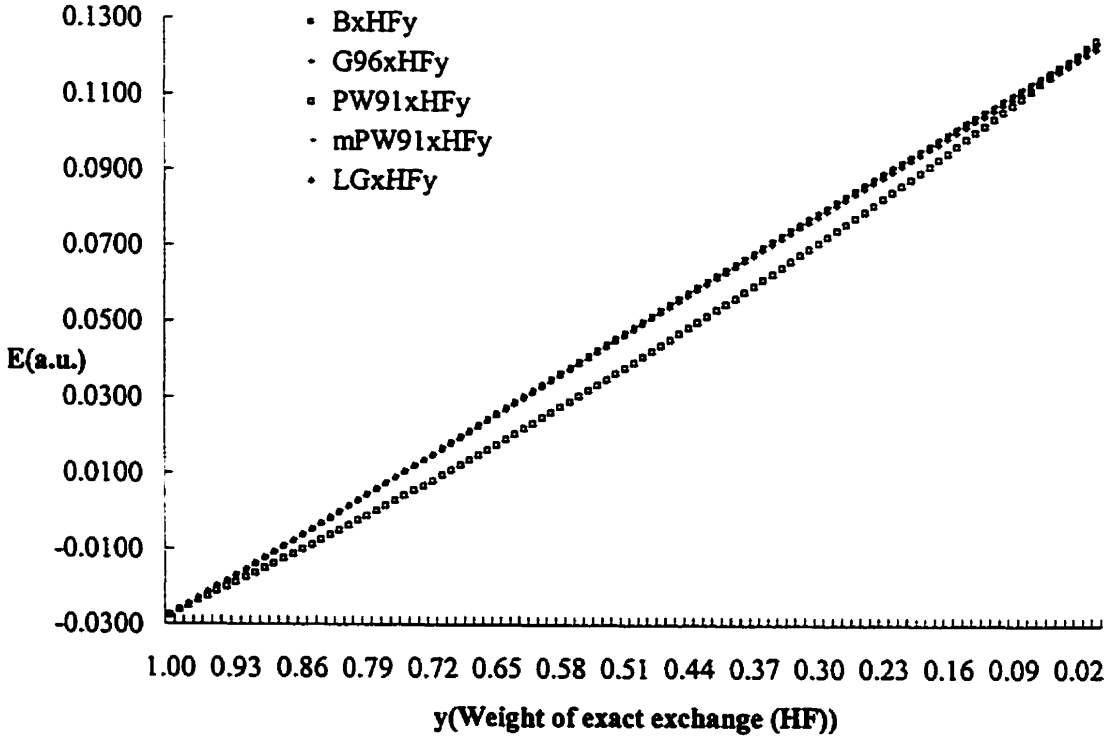

Figure 5-15 Energy of the highest occupied orbital of H^- predicted by BxHFy, G96xHFy, PW91xHFy, mPW91xHFy and LGxHFy

G96, mPW91 and LG show very similar behavior in predicting this electronic property. PW91xHFy deviates slightly from and is lower than the other lines slightly from y=0.75 to y=0.25. HF predicts the occupied orbital energy as –0.2744H. As the component of the HF exchange decreases in the hybrid method, the highest occupied orbital energy increases, at approximately y=0.82, this orbital energy becomes positive i.e. unbound. When y=0.00 i.e. in the case of pure GGA, the highest occupied orbital energy is about 0.123H which is very definitely positive and thus not binding.

Figure 16 reports the highest occupied orbital energy of H^- for the BxHFy and BxHFyLYP methods. These two straight lines (BxHFyLYP is lower) have a constant difference at 17.99mH and this value is due to the contribution of the LYP correlation functional. The corresponding difference for the highest occupied orbital energy of H^- between PW91xHFy and PW91xHFyPW91 which is larger than that between BxHFy and BxHFyLYP. The difference is 24.46mH as shown in Figure 5-17. In Figure 5-15, the PW91 exchange functional predicts lower orbital energy than does BxHFy. Overall PW91PW91 (and its hybrid methods) may predict lower orbital energies than does BLYP (and presumably its corresponding hybrid methods).

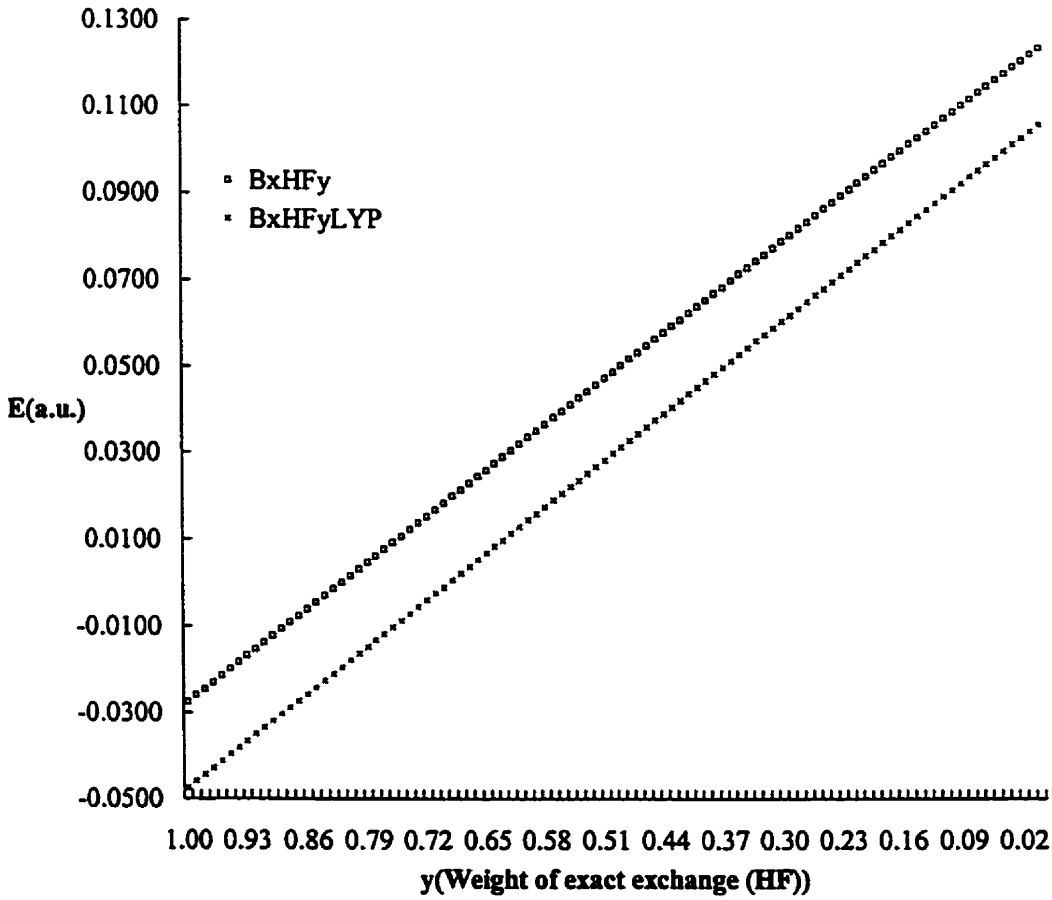

Figure 5-16 Energy of the highest occupied orbital of H^- predicted by BxHF and BxHFyLYP

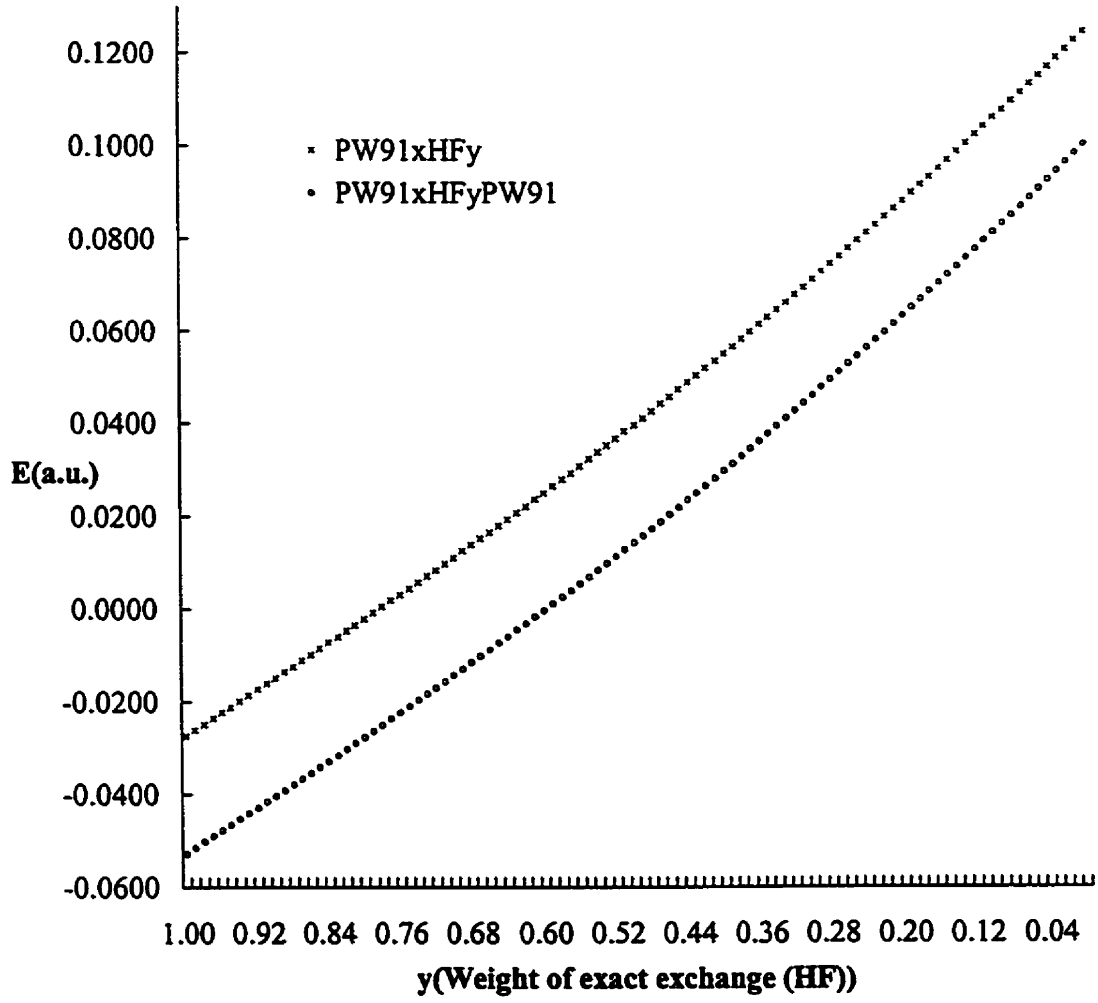

Figure 5-17 Energy of the highest occupied orbital of H^- predicted by PW91xHFy and PW91xHFyPW91

5.2.4.3.2 Singlet helium

5.2.4.3.2.1 Total energy of He

Helium is one of the smallest neutral systems with only anti-parallel electrons in its lowest singlet state. It is a good model for studying correlation of antiparallel electrons. The total energies of He predicted by all methods are plotted against the amount of HF exchange in Figure 5-18. Compared with the curves in Figures 5-1 and 5-2 for H and He^+, the slopes of the curves in Figure 5-18 are small. Except for the curves for the PW91xHFy and mPW91xHFy methods, the other curves have negative slopes i.e. the GGAs (B, G96 and LG) predict slightly lower energy than does HF. The slope of BxHFy is close to zero and the slopes from G96xHFy and LGxHFy are slightly more negative than that from BxHFy. Exchange functionals not only determines the exchange energy but also partially the correlation energy. However, in an atomic system especially such as He, the HOMO-LUMO gap is too large to allow for the introduction of non-dynamic correlation. The exchange functionals (especially non-local exchange) mainly account for non-dynamical electron correlation [25]. The energy gap can serve as a criterion for the occurrence of non-dynamic correlation in general. Another possible reason exists for the different behaviors of the exchange functional in the prediction of total atomic energy, for example the exchange functional fitting procedure. The order of these curves (slopes of the energy curves) is,

$$\text{LGxHFy}<\text{G96xHFy}<\text{BxHFy}<\text{mPW91xHFy}<\text{PW91xHFy} \qquad (5.46)$$

The curves of LGxHFy and G96xHFy are close to each other. All the curves are essentially straight lines although PW91xHFy deviates from a straight line slightly more than the other curves.

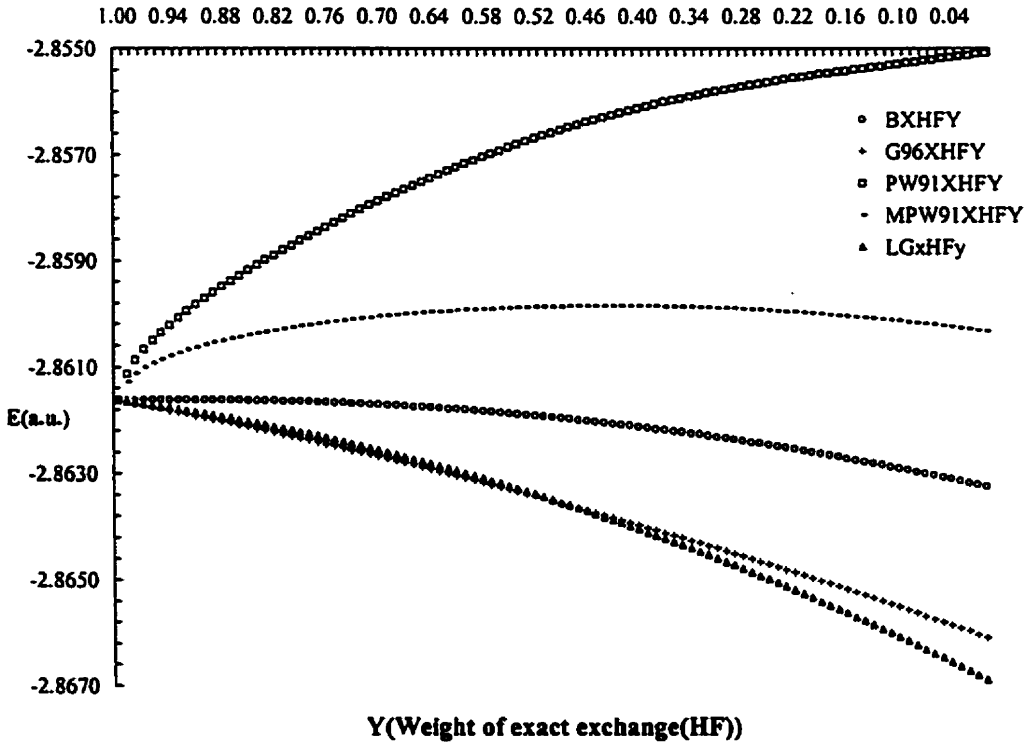

Figure 5-18 Energy of He Predicted by BxHFy, G96xHFy, PW91xHFy, mPW91xHFy and LGxHFy

5.2.4.3.2.2 Decomposition of the total energy of helium

Considering the electronic Hamiltonian, the total energy can be decomposed into potential, kinetic, electron-electron Coulomb repulsion, exchange and correlation energies. In He, there are only two anti-parallel electrons and the LUMO-HOMO gap is large (1.32461H by CISD(full)/cc-pv5Z). There are no exchange energies and parallel electron correlation energies for this system. The electron-electron interaction includes only the Coulomb repulsion and the anti-parallel electron correlation. Thus the energy difference between that predicted by HF and full CI for He is the anti-parallel pair electron correlation. The total energy curves of He in Figure 5-18 indicate the different behaviors of the functional from those in the H and He^+ cases. In addition, the total energies of He are decomposed into potential, kinetic and electron-electron interaction energies to study the effects of the functionals on each energy component.

The kinetic energy and potential energy of He are plotted versus the weight of HF exchange in Figures 5-19 and 5-20. The slopes of the curves of potential energy and kinetic energy of He are slightly positive while the slope of the total energy curves are slightly negative. Such a result may be due to the contribution from electron-electron interaction. The curves in Figures 5-18, 5-19 and 5-20 predicted by PW91xHFy are not straight lines. The kinetic energy curve resembles the second half of a sine curve and the potential curve appears to be the first half of the sine curve. In both Figures 5-19 and 5-20, BxHFy, G96xHFy and mPW91xHFy have a slight discontinuity between y=0.45 and y=0.15. The reason for the discontinuity is not clear. The order of the curves of potential energy is the same as that of the total energy as shown in Equation 46, so do the kinetic energy curves.

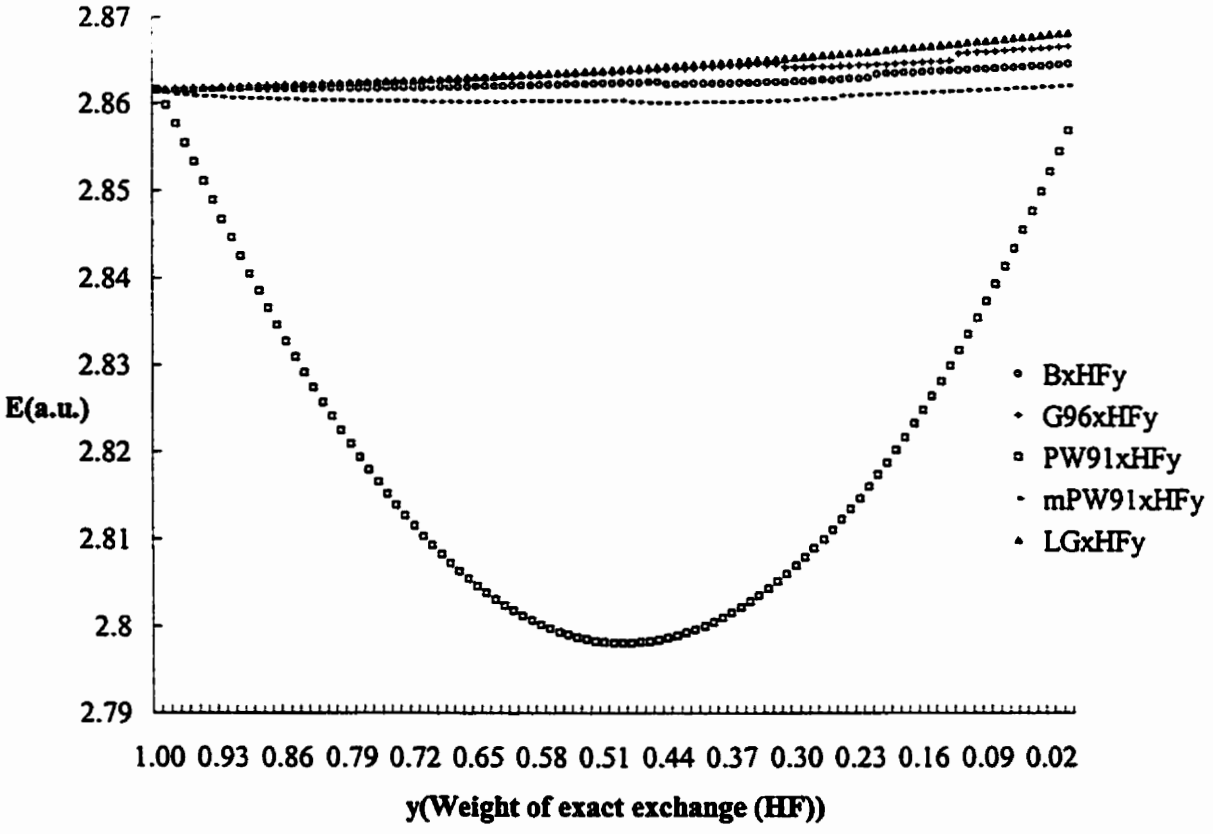

Figure 5-19 Kinetic energy of He predicted by BxHFy, G96xHFy, PW91xHFy, mPW91xHFy and LGxHFy

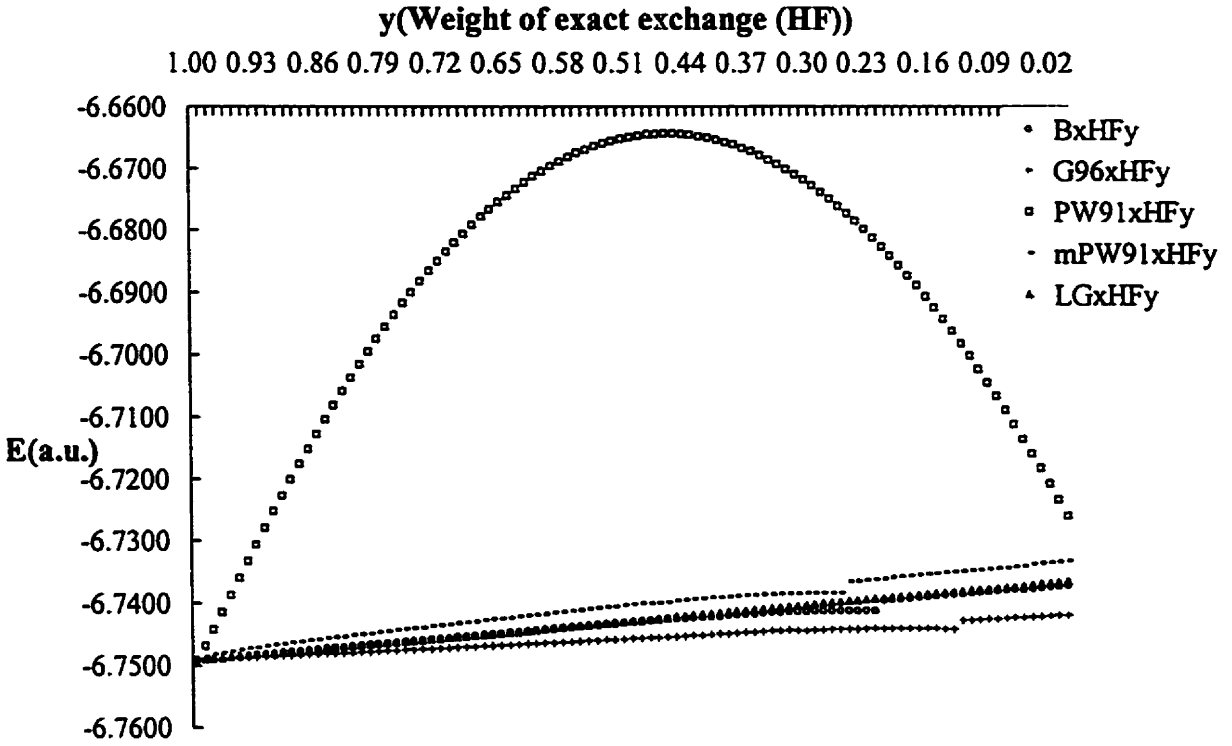

Figure 5-20 Potential energy of He predicted by BxHFy, G96xHFy, PW91xHFy, mPW91xHFy and LGxHFy

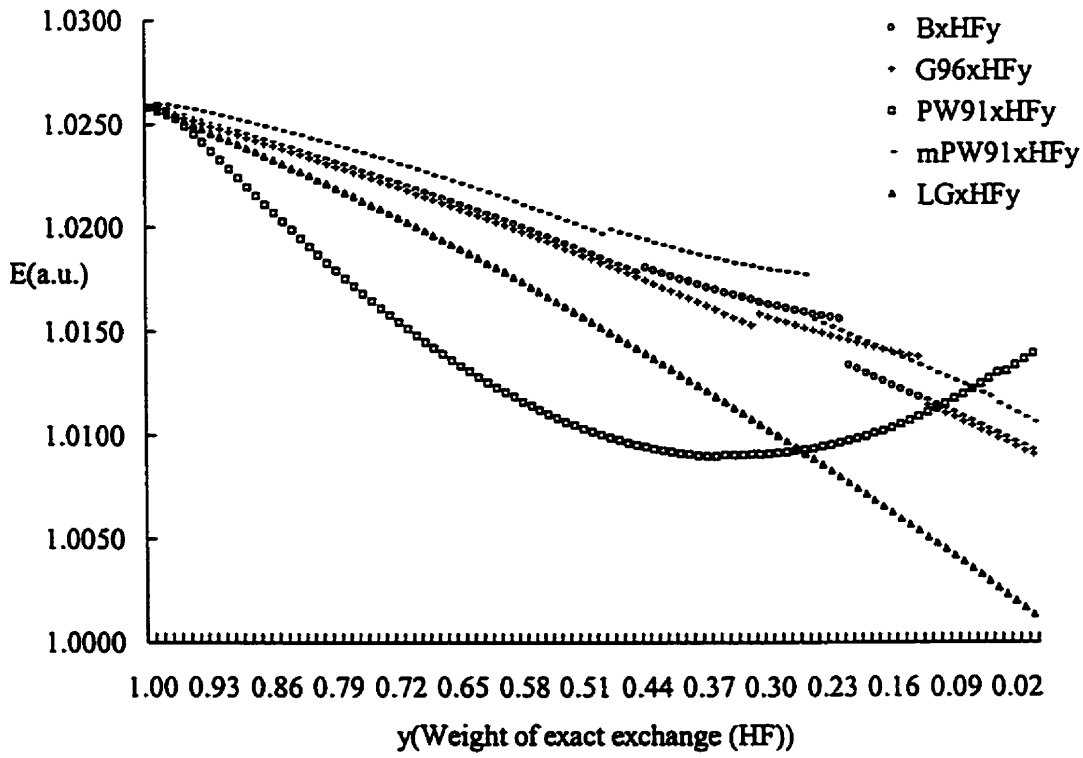

Figure 5-21 Electron-electron interaction energy of He predicted by BxHFy, G96xHFy, PW91xHFy, mPW91xHFy and LGxHFy

The electron-electron interaction curves of He are plotted in Figure 5-21. All GGAs predict lower energies than HF. This explains why the total energies of He predicted by GGAs are lower than for HF although the potential and kinetic energies are slightly

higher than from HF. The electron-electron interaction energy difference between GGAs and HF is larger than the corresponding sum of the potential and kinetic energy differences. In Figure 5-21, there are discontinuities from y=0.50 to y=0.15 for all curves except for LGxHFy. The PW91xHFy curve is not linear. It is unclear for these phenomena in Figure 5-21.

5.2.4.3.2.3 The energetic contributions from the correlation functionals

The correlation functional is mainly designed to account for dynamic correlation [25] and LYP was fit to the electron correlation energy of Helium [9]. The electron-electron interaction in He from LYP is obtained by subtracting the electron-electron interaction of B from the electron-electron interaction of BLYP. The same procedure is employed to calculate the electron-electron interaction predicted by the PW91 correlation functional for He i.e. subtracting the electron-electron interaction of the PW91 exchange functional from the electron-electron interaction of PW91PW91 exchange-correlation functionals in He. The results are reported in Table 5-1.

Table 5-1 The electron-electron interaction in He predicted by B, BLYP, PW91 and PW91PW91(in a.u.) with the cc-pv5Z basis set

	B	BLYP	LYP	$PW91_X$	PW91PW91	$PW91_C$
EE	1.00898	0.96771	-0.04121	1.01395	0.97513	-0.03882

E (HF)= -2.86162, E(CISD)= -2.90315, ΔE(CISD-HF)=-0.04153

$PW91_X$: PW91 exchange functional, $PW91_C$: PW91 correlation functional

It is not surprising that LYP predicts the correlation energy very close to the conventional *ab initio* correlation energy since LYP was fit to the correlation energy of He. The error in the correlation energy predicted by the PW91 correlation functional is 7% if the correlation energy from the CISD calculation is adopted as a reference.

Since the components of the energy are not independent, they may correlate with each other. Thus the energetic contribution from the correlation functional is not completely correlation energy. The correlation functional also may effect the potential and kinetic energy of the system due to the self-consistent field procedure employed in the energy optimization. Starting from this assumption, the possible contribution to the total potential and kinetic energy of the system from the correlation functional is analyzed. Table 5-2 reports the potential and kinetic energies predicted by the B, BLYP, PW91 exchange and PW91PW91 exchange-correlation functionals.

Table 5-2 The kinetic and potential energy of He predicted by the B, BLYP, PW91 and PW91PW91 functionals (in a.u.) with the cc-pv5Z basis set

	B	BLYP	LYP	PW91X	PW91PW91	PW91C
KE	2.86466	2.87487	0.01021	2.85697	2.86416	0.00719
PE	-6.73688	-6.74955	-0.01267	-6.72601	-6.73921	-0.01320

KE(HF)= 2.86162, PE(HF)= -6.74916, PW91X: PW91 exchange functional, PW91C: PW91 correlation functional

From Table 5-2, the contribution to the kinetic and potential energy of a system from the correlation functional is obvious.

From Figure 5-15, the effect of HF exchange on the energy of the highest occupied orbital is evident from the energy curves. Figure 5-22 displays the curve of the highest occupied orbital energy versus the weight of HF exchange in the hybrid methods. All the methods have very similar curves to each other. All the GGA exchange fucntionals predict higher occupied orbital energy than does HF i.e. exchange functionals destabilize the He atom although the GGA exchange functionals (except for PW91 exchange) predict lower total energies for He than does HF. The decrease in the highest occupied orbital energy of approximately 0.37H (roughly 10 e.v.) from HF to GGA significantly effects the overall electronic structure of He. From Figures 5-15 and 5-22, an important conclusion may be drawn that the nonbinding for anions with GGAs may be a more general behavior.

The calculations show similar results for Li^+ as those for He, and will not be discussed here.

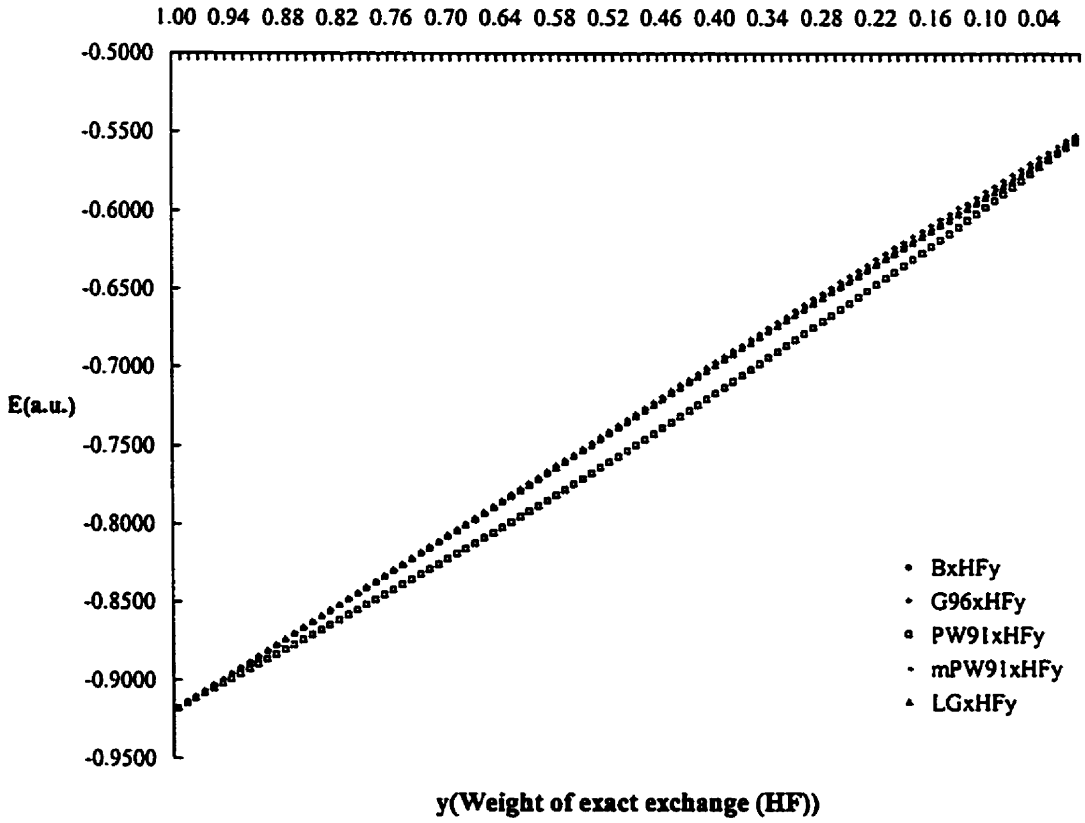

Figure 5-22 The highest occupied orbital energy of He predicted by BxHFy, G96xHFy, mPW91xHFy, PW91xHFy and LGxHFy

5.2.4.3.3 Triplet helium

In He, only anti-parallel electron correlation exists. If one electron in 1s He is excited into the 2s orbital and its spin changed, then only parallel electron correlation (a Fermi hole) exists in this triplet helium atom. The difference between the electron correlation strengths (anti-parallel and parallel) can be analyzed by studying the electron-electron interaction in He in its singlet ground state and first excited triplet state.

5.2.4.3.3.1 Total energy of triplet He

The total energies of triplet He predicted by the exchange based methods were plotted in Figure 5-23. Except for PW91xHFy, all the methods predict that the total energy decreases as the weight of HF exchange decreases. The total energy predicted by PW91xHFy changes slightly compared to other methods as the weight of HF exchange varies, and the curve is close to a straight line. The energetic order of the curves is:

$$G96xHFy < LGxHFy < BxHFy < mPW91xHFy < PW91xHFy \qquad (5.47)$$

In Figure 5-23, the curves for LGxHFy and G96xHFy are closer to each other than the other curves. The energies predicted by the PW91 and mPW91 exchange functionals are closer to those from HF than the other methods.

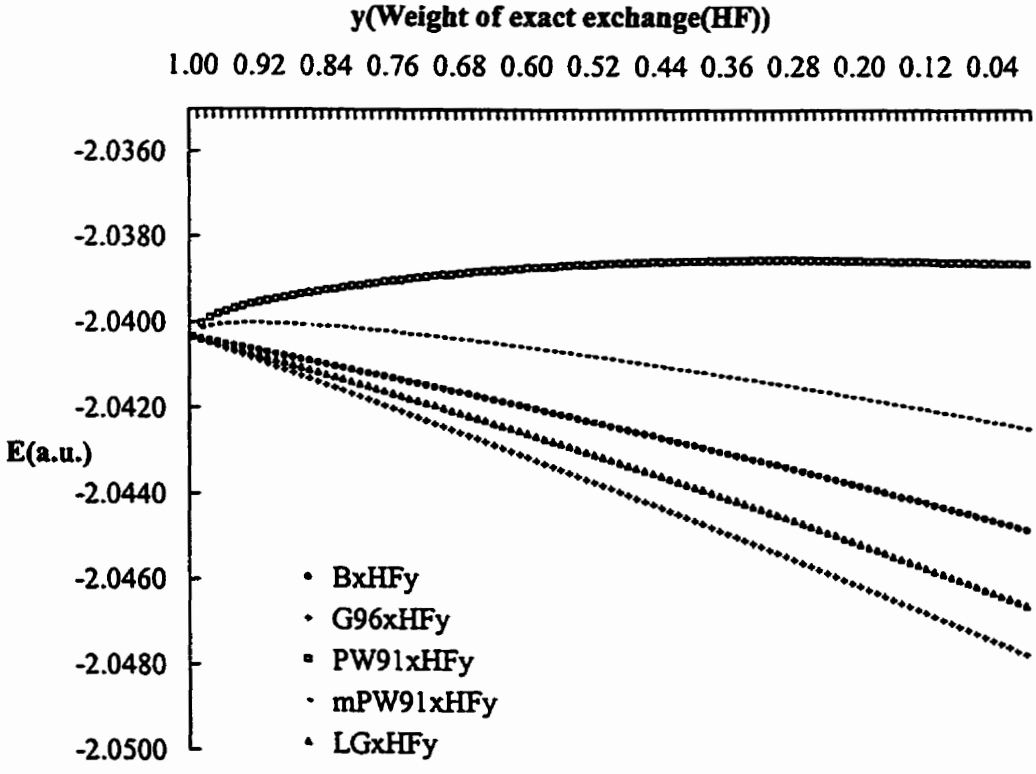

Figure 5-23 Total energy of triplet He predicted by BxHFy, G96xHFy, PW91xHFy, mPW91xHFy and LGxHFy

5.2.4.3.3.2 The decomposition of the total energy of triplet helium

Figures 5-24, 5-25 and 5-26 present curves for the kinetic, potential and electron-electron interaction energies of triplet He.

Unlike the kinetic energy curves of singlet He, the kinetic energy curves for triplet He in Figure 5-24 have slightly negative slopes indicating that the GGA exchange functionals predict lower kinetic energy than does HF. The curves predicted by BxHFy and mPW91xHFy nearly overlap and the mPW91xHFy curve is slightly lower than that from BxHFy. PW91xHFy still predicts a curve with a minimum around y=0.47.

Figure 5-25 presents the potential energy curves for triplet He. The order of the energies predicted by the methods employed is opposite to that of the kinetic energy in Figure 5-24. The order (in energy) is,

$$\text{LGxHFy} < \text{BxHFy} < \text{mPW91xHFy} < \text{G96xHFy} < \text{PW91xHFy} \qquad (5.48)$$

All the curves except for PW91xHFy are close to straight lines and have positive slopes. PW91xHFy predicts a curve with a maximum around y=0.47. The end point of this curve is close to the other curves. In Figure 5-25, the BxHFy and mPW91xHFy curves almost overlap.

In He, the shape of the total energy is determined not only by the kinetic and potential energies, but also by the electron-electron interactions which are significant to the total energy. The effect of electron-electron interaction on the slope of the total energy curves predicted by the methods is confirmed in Figure 5-18 for singlet He. Figure 5-26 shows plots of the electron-electron interaction in triplet He as predicted by these methods. All the exchange GGAs predict lower electron-electron interactions in triplet He than does HF. A comparison with the electron-electron interactions of He in its singlet ground state

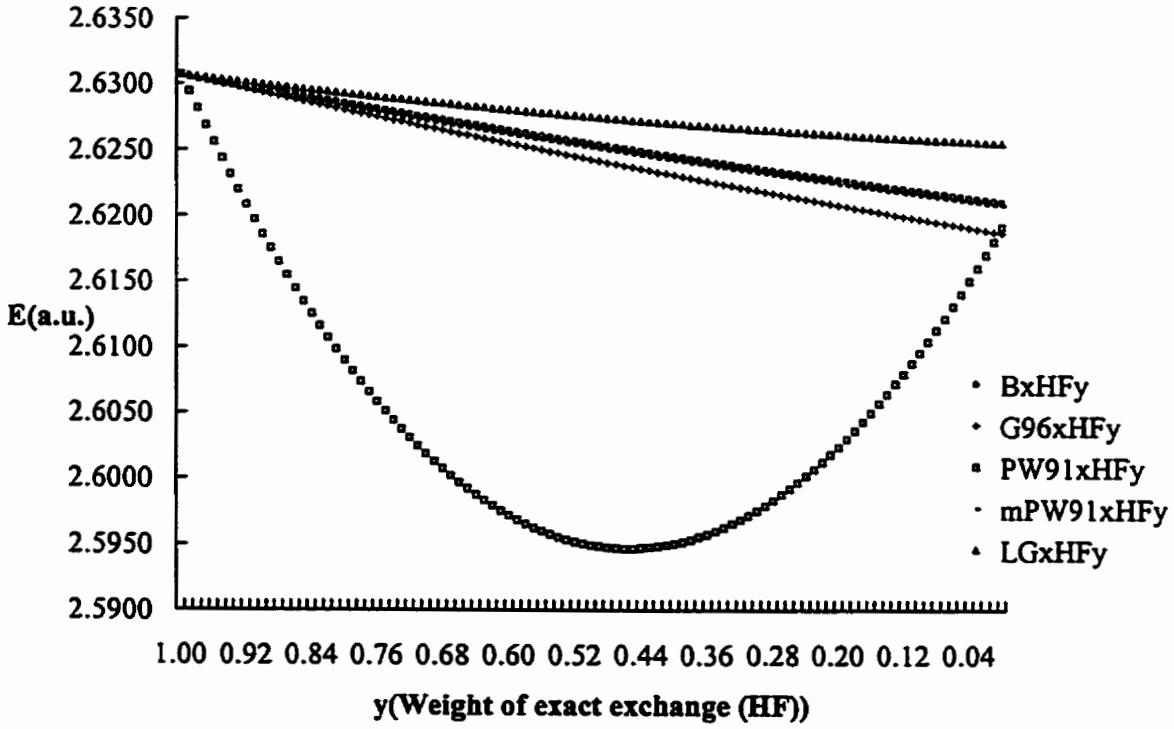

Figure 5-24 Kinetic energy of triplet helium predicted by BxHFy, G96xHFy, PW91xHFy, mPW91xHFY and LGxHFy

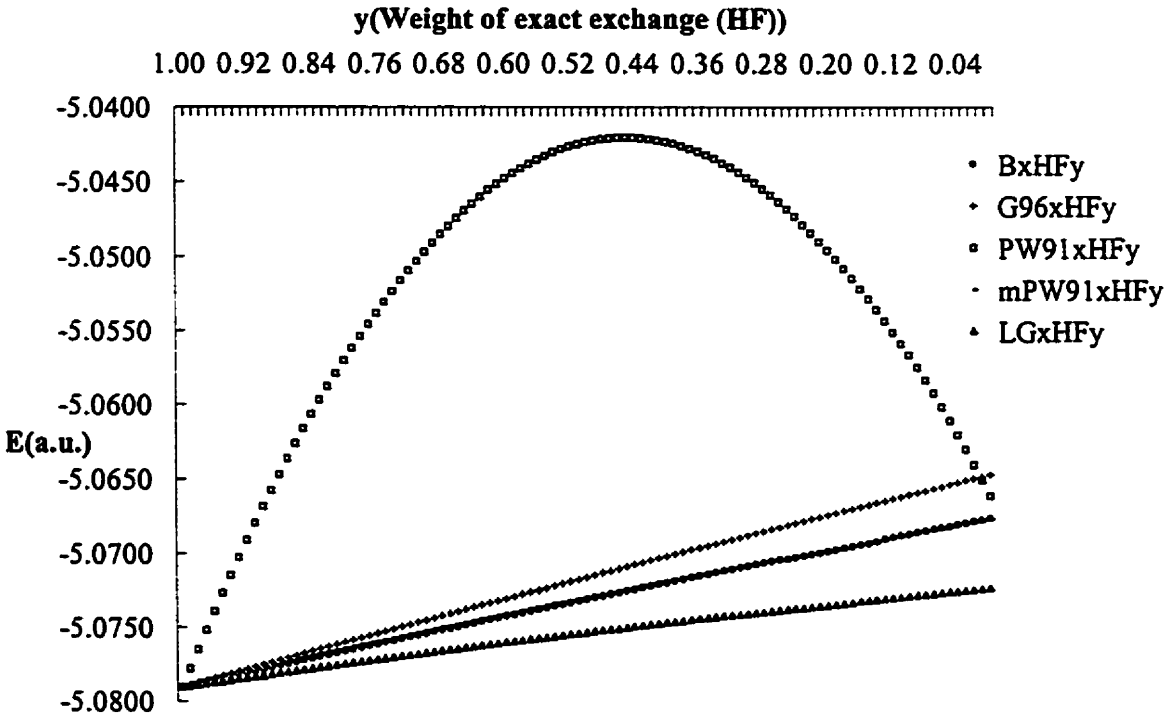

Figure 5-25 Potential energy of triplet helium predicted by BxHFy, G96xHFy, PW91xHFy, mPW91xHFy and LGxHFy

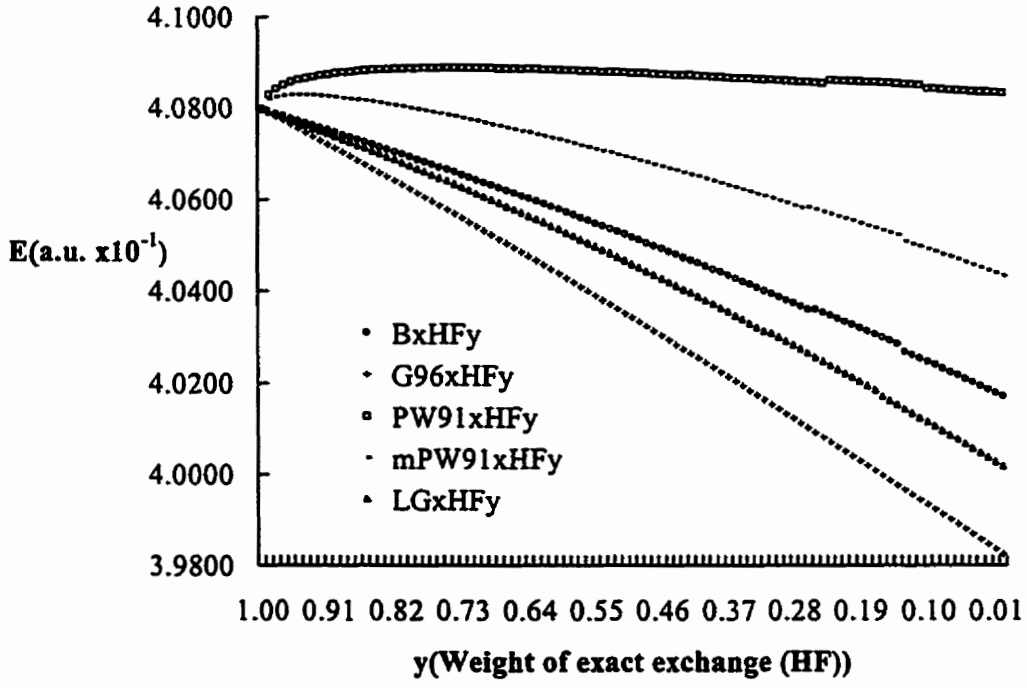

Figure 5-26 Electron-electron interaction energy in He predicted by BxHFy, G96xHFy, PW91xHFy, mPW91xHFy and LGxHFy

is shown in Figure 5-21, the electron-electron interaction energy difference for triplet He among the predictions of HF and GGAs (about 0.08H for LGxHFy) is larger than its counterpart in singlet He (about 0.025H). Also the electron-electron interaction in triplet He is about 4 times that in singlet He. The electron correlation in singlet He is larger than that in triplet He and the correlation energy stabilizes the singlet system more. The CI calculations indicate that the Coulomb correlation in singlet He is much larger than the Fermi correlation in triplet He. The kinetic energies of both singlet and triplet He predicted by GGAs are shown in Figures 5-19 and 5-24 and are closer to the HF results than the corresponding electron-electron interactions. The GGA exchanges predicts much lower electron-electron interactions than does HF. This lower electron electron repulsion is the main cause of the lower energetic prediction for a system usually observed with GGAs. The result is reasonable in SCF methods since only the electron electron interaction part is different in HF and DFT. It is worth noting that PW91 exchange predicts the electron-electron interaction in triplet He to be close to that of HF. The curve for PW91xHFy in Figure 5-26 is close to a straight line. In Figure 5-21, the PW91xHFy electron electron interaction curve is more curved with a minimum around y=0.38.

5.2.4.3.3.3 The energetic contribution from correlation functionals

The singlet ground state of He is a very good test case to check the performance of the correlation functional for Coulomb correlation. The triplet state of He is a test of the performance of correlation functionals for Fermi correlation. Comparing the performance of the correlation functionals on these two cases should provide insight into the overall performance for electron correlation.

LYP was fit to the Coulomb correlation (anti-parallel correlation) and it does not take the parallel correlation into account as mentioned in Becke's work [25]. The present calculations with BxHFy and BxHFyLYP indicate that these two methods give identical curves i.e. LYP does not account for parallel correlation. Also the contributions to the kinetic and potential energies from the LYP functional are zero as shown in Table 5-3.

Figure 5-27 presents for the total energy curves of triplet He predicted by PW91xHFy and PW91xHFyPW91. There is a constant gap between the two curves in Figure 5-27. It can be identified with the energy contribution from the PW91 correlation functional. This gap is about 0.018H (11.1kcal/mol). The correlation energy in triplet He predicted by CISD/cc-pv5Z is 0.0016H (1.0kcal/mol). Obviously the PW91 correlation functional overestimates parallel electron correlation in triplet He. The possibilities of including the self-interaction error and the contributions from the kinetic and potential parts can not be excluded. Compared with the case of singlet He, the electron correlation is much smaller in triplet He from both conventional *ab initio* calculations and from DFT. Thus LYP may still be good in energy predictions even though it does not consider the parallel electron correlation. As the system gets larger, the parallel correlation may become more important to the total energy (for example nitrogen atom or transition metals). From

Table 5-3, the contribution of kinetic and potential energy from PW91 correlation is obvious. Compared to the contribution of electron-electron interactions, the kinetic and potential contributions from the correlation functional are relatively small but comparable to the correlation energy predicted by CISD.

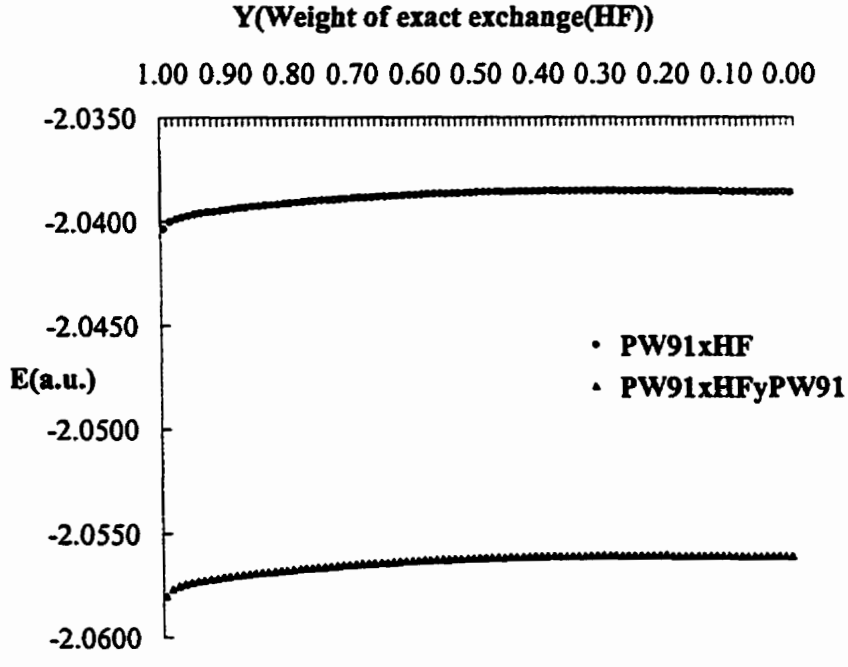

Figure 5-27 Total energy of triplet He predicted by PW91xHFy and PW91xHFyPW91

Table 5-3 Kinetic, potential and electron-electron interaction energies in triplet He predicted by B, BLYP, PW91 and PW91PW91 (in a.u.) with the cc-pv5Z basis set

	B	BLYP	LYP	PW91X	PXPC	PW91C
KE	2.62109	2.62109	0	2.61917	2.61798	-0.00119
PE	-5.06764	-5.06764	0	-5.06613	-5.06502	0.00111
EE	0.40172	0.40172	0	0.40836	0.39091	-0.01745

KE(HF)= 2.63072, PE(HF)= -5.07904, EE(HF)= 0.40799, EE(CISD-HF)=-0.0016

PW91X: PW91 exchange functional PXPC: PW91PW91, PW91C: PW91 correlation functional

5.2.4.4 Three-electron systems: He^- and Li

The He^- shows similar results to those from H^-. Due to the problematic behaviors of DFT methods on anions, this system will not be discussed.

Figure 5-28 shows the total energies of Li predicted by all methods. Except for the LG exchange functional, all GGA exchange functionals predict higher total energies for Li than does the HF method. G96 predicts the total energy of Li close to that from HF. The PW91 exchange functional predicts the highest energy for Li among all the methods. The order of the energies for Li predicted by these methods is,

$$\text{LGxHFy} < \text{G96xHFy} < \text{BxHFy} < \text{mPW91xHFy} < \text{PW91xHFy} \qquad (5.49)$$

All the curves are close to straight lines.

Figure 5-29 shows the predicted kinetic energies of Li. The order of the curves is,

$$\text{PW91xHFy} < \text{mPW91xHFy} < \text{BxHFy} < \text{LGxHFy} < \text{G96xHFy} \qquad (5.50)$$

The relative order of LGxHFy and G96xHFy switch as compared to the total energy as shown in Equation 5.49. Except for PW91xHFy, these methods predict the curves to be straight lines. PW91xHFy predicts the curves with a minimum around y=0.47. This curve looks like a parabola. The order in Figure 5-30 for the potential energies of Li is the reverse of the order in Figure 5-29. In Figure 5-30, PW91xHFy predicts a maximum around y=0.47, the shape of this curve is the reverse of the corresponding kinetic energy curve. Figure 5-31 shows the electron-electron interaction energies for Li. Essentially, the electron-electron interaction energy curves are similar to those of the kinetic energy curves both in the relative order, shapes and slopes. PW91xHFy still predicts the electron-electron interaction curve to resemble the second half of the sine triangonometric function. PW91 predicts the electron-electron interaction

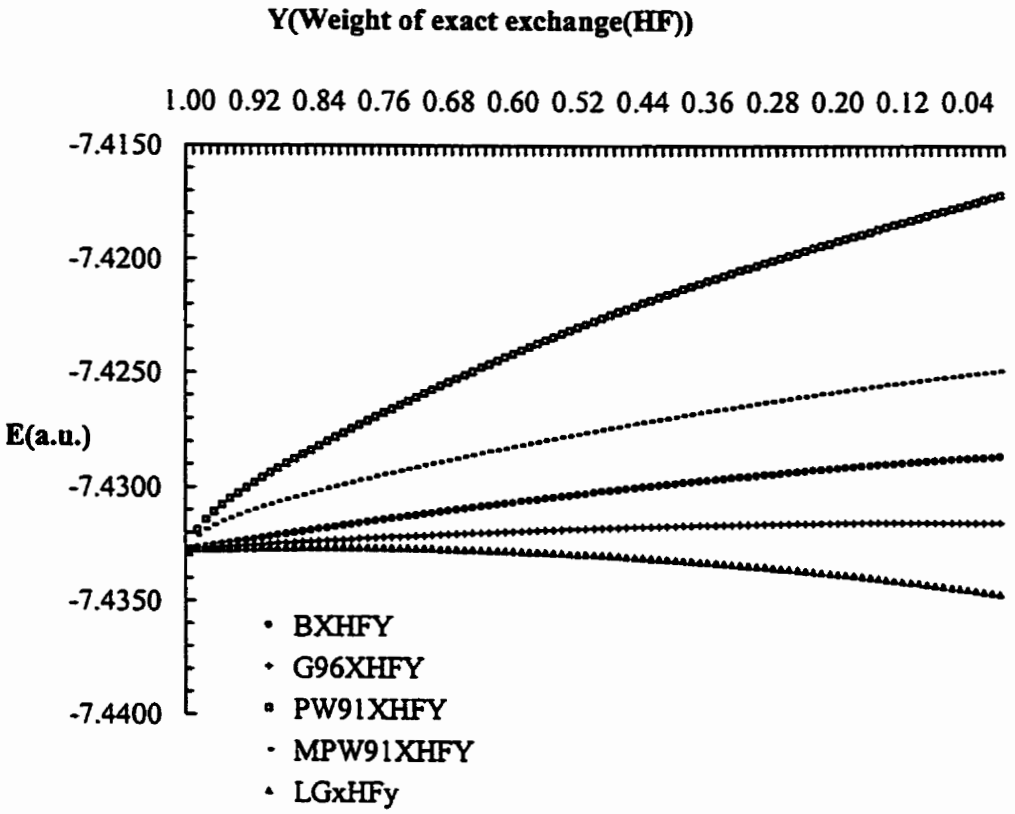

Figure 5-28 Total energies of Li Predicted by BxHFy, G96xHFy, PW91xHFy, mPW91xHFy and LGxHFy

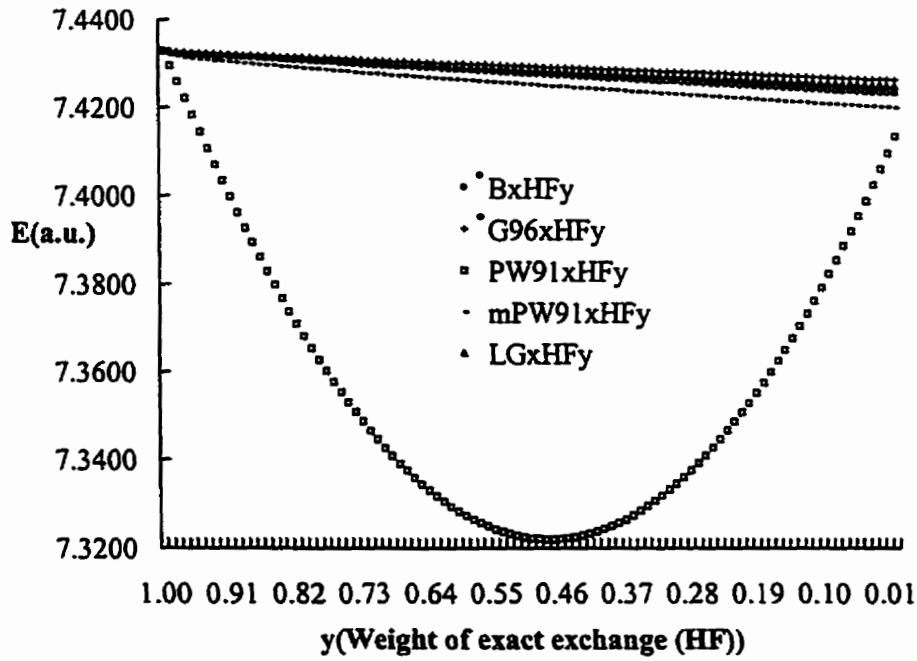

Figure 5-29 Kinetic energies of Li predicted by BxHFy, G96xHFy, PW91xHFy, mPW91xHFy and LGxHFy

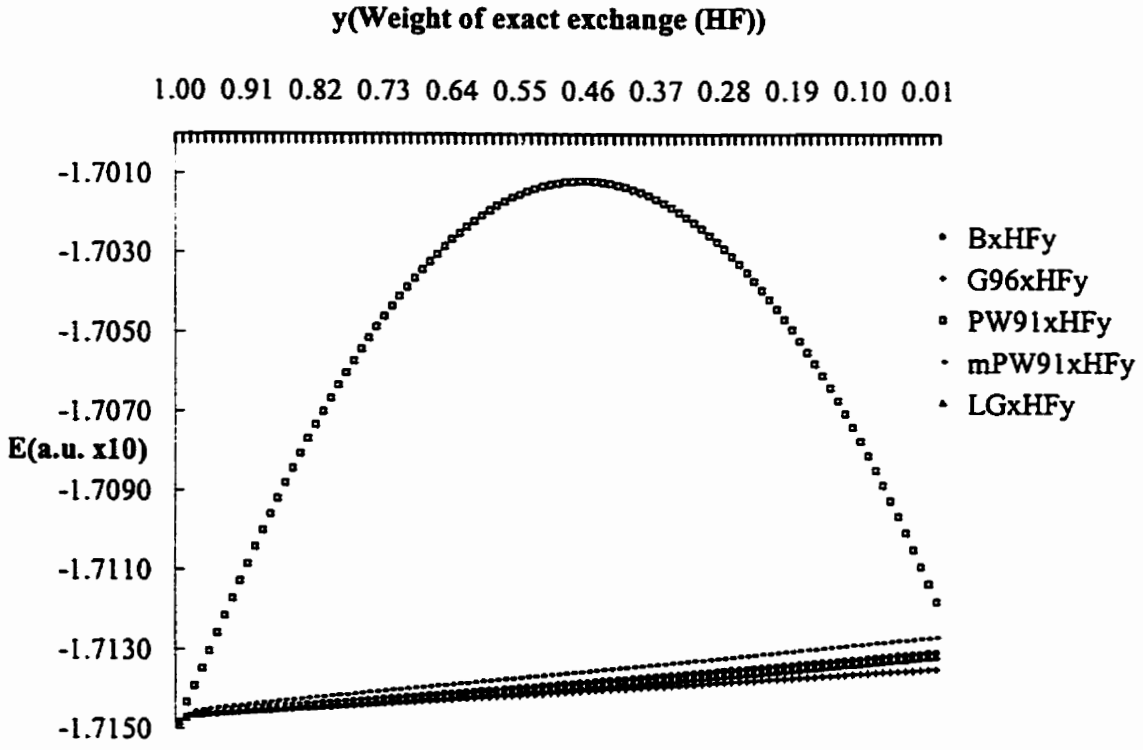

Figure 5-30 Potential energies of Li predicted by BxHFy, G96xHFy, PW91xHFy, mPW91xHFy and LGxHFy

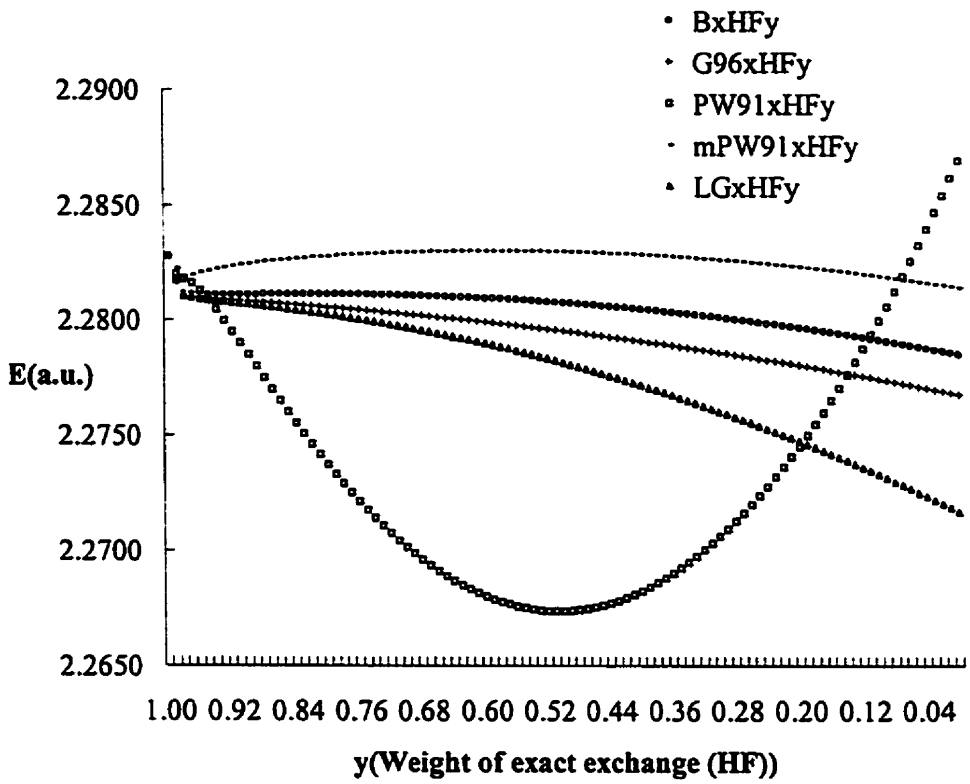

Figure 5-31 Electron-electron interaction energies of Li predicted by BxHFy, G96xHFy, PW91xHFy, mPW91xHFy and LGxHFy

energies to be slightly higher than does HF. mPW91 predicts a similar electron-electron interaction energy as HF. B and G96 make slightly lower predictions than HF. LG predicts the lowest electron-electron interaction energy among all the exchange functionals employed.

The energy differences in the electron-electron interaction among HF and GGAs are not as large as the individual kinetic and potential energy difference between HF and GGAs. Thus the total energy curves of Li in Figure 5-28 (except for PW91) follow the shape of the potential energy though the slopes of the curves change slightly due to the contribution from electron-electron interaction predicted by GGAs.

5.2.4.5 Contributions to kinetic and potential energy from the correlation functionals

Table 5-4 reports the total, potential, kinetic and electron-electron interaction energies predicted by B, BLYP, HF, PW91 and PW91PW91. For comparison, the corresponding energies predicted by HF and correlation energy predicted by CCSD(T) also are reported in Table 5-4.

The energy differences from the HF and the GGAs exchange functionals are relatively small, but chemically significant. The B functional predicts energies closer to those of HF than does the PW91 exchange functional. The LYP and PW91 correlation functionals not only contribute to the electron-electron interaction (mainly electron correlation), but also to the kinetic and potential energies of Li. The electron-electron interaction contributions from the LYP and PW91 correlation functionals are larger than the electron correlation energies predicted by CCSD(T). The electron-electron repulsion from the PW91

correlation functional may include some self-interaction error although it still overestimates the electron-electron correlation in Li. LYP definitely overestimates the electron correlation in Li since LYP is known to be self-interaction free. The LYP functional contains no parallel electron correlation and thus it overestimates the anti-parallel correlation in Li. From the energy contribution of the LYP and PW91 correlation functionals, we note that the correlation contribution from the correlation functionals can not be compared directly to the results from conventional *ab initio* methods. The energy overestimation from the LYP and PW91 correlation functionals may be one of the reasons that DFT methods systematically overestimate the energies of a system.

Table 5-4 The total energy, potential, kinetic, and electron-electron interaction energies predicted by the B, BLYP, HF, PW91, and PW91PW91 (in a.u.) with the cc-pv5Z basis set

	HF	B	BLYP	LYP	PW91X	PW91PW91	PW91C
E	-7.43274	-7.42863	-7.48256	-0.05393	-7.41715	-7.47405	-0.05690
KE	7.43288	7.42348	7.43911	0.01563	7.41366	7.42521	0.01155
PE	-17.14844	-17.13060	-17.15860	-0.02800	-17.11778	-17.13892	-0.02114
EE	2.28282	2.27850	2.23693	-0.04157	2.28698	2.23966	-0.04732
E(CCSD(T)-HF)=-0.02717							

PW91X: PW91 exchange functional, PW91C: PW91 correlation functional

5.2.5 The contributions from LSDA (local spin density approximation)

As shown in Equations 5.23, 5.25, 5.26 and 5.27, all of the five exchange functionals (B, G96, PW91, mPW91 and LG) can be decomposed into a local part (LSDA) and a gradient correction portion. To check the effect of the gradient correction on the total energy of a system, a hybrid method consisting of LSDA with HF exchange is also examined with H, He and Li to check the behavior of LSDA changing with the weight of HF exchange in the hybrid method.

Figures 5-32, 5-33 and 5-34 plot the total energies of H, He and Li predicted by SxHFy, (Slater local exchange with an admixture of HF exchange) respectively.

All three curves have similar shapes (straight lines) with positive slopes i.e. LSDA underestimates the total energy of the three atoms. Comparing these figures with those of the GGAs, the primary conclusion that may be reached is that the underestimation of the energy of a system by the GGAs arises from the gradient correction.

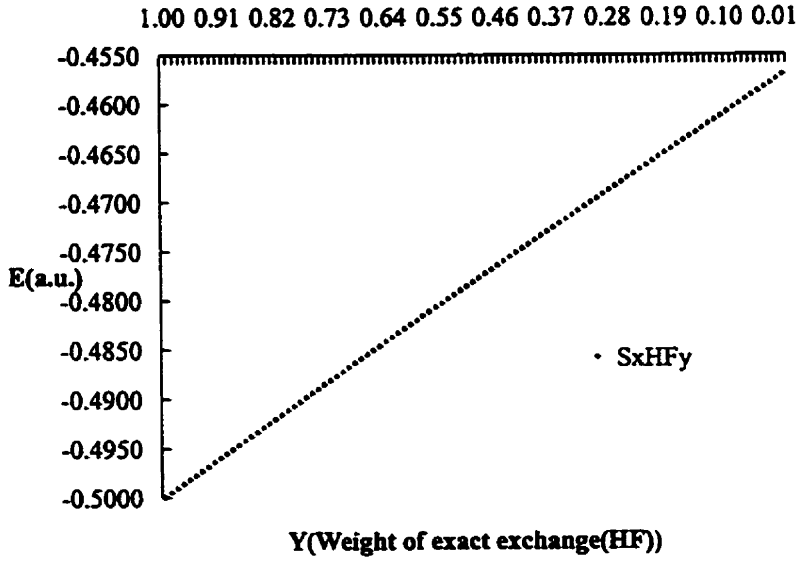

Figure 5-32 Energy of H predicted by SxHFy

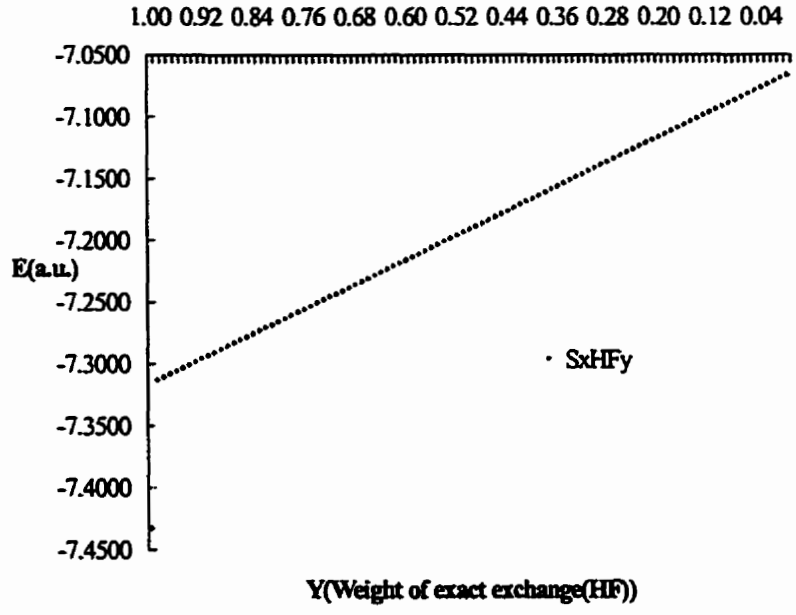

Figure 5-33 Energy of He predicted by SxHFy

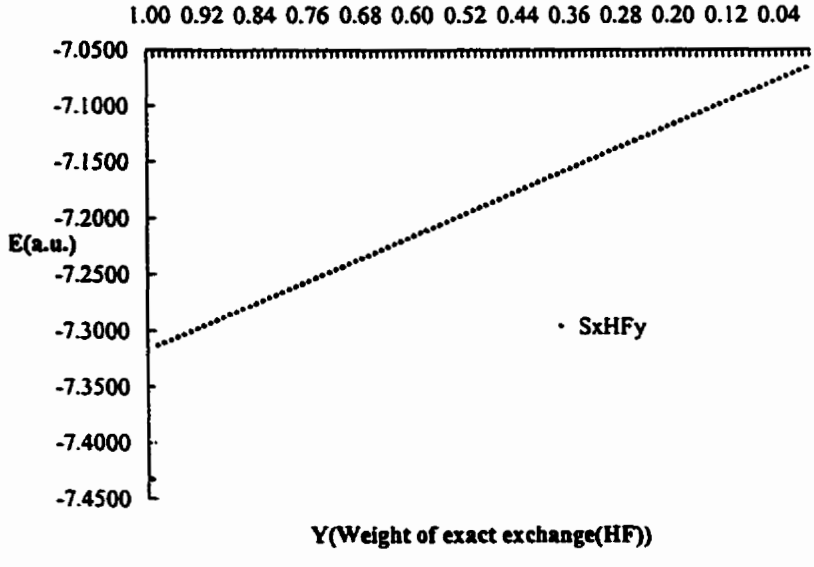

Figure 5-34 Energy of Li predicted by SxHFy

5.2.6 Concluding remarks

5.2.6.1 Exchange functionals

Through the calculation of one-electron systems (H, He^+ and H_2^+), all the exchange functionals (B, G96, PW91, mPW91 and LG) are shown not to be self-interaction error free. The self-interaction error even exists in system with integral electrons in a system such as H and He^+. The self-interaction error is more serious in the case with fractional electrons such as transition states and reaction intermediates rather than stable minima [1]. Except for the PW91 exchange functional, all the exchange functionals show a nearly linear relation between the various energies and the weight of HF exchange in the hybrid method. Alhough the total energy curves of the systems predicted by the PW91 exchange functional are close to straight lines i.e. the PW91 exchange functional shows a nearly linear relation between the total energy and the weight of HF exchange in the hybrid method. However, PW91 does not show a linear relation between the weight of HF exchange and the energy components (kinetic, potential and electron-electron interaction energies).

Nearly all the GGA exchange functionals predict lower energies for a system than does HF. The order is:

$$LG < B < G96 < mPW91 < PW91$$

which implies that PW91 predicts the highest total energy among the exchange functionals. One possible reason is that these functionals are not self-interaction free. This overestimation may be due to the gradient correction portion of the functionals. It is anticipated that this order will be applicable to molecular systems as well.

The modification of the two parameters in PW91 which generates the mPW91

functional [3] improves its dependence on the percentage of HF exchange in hybrid method in the energy prediction.

All the exchange functionals destabilize a system by increasing the energy of the highest occupied orbital energy. The mixing of HF exchange lowers the energy of this HOMO.

5.2.6.2 Correlation functionals

LYP is self-interaction free but it does not take parallel electron correlation into account as shown for triplet helium. Both the LYP and PW91 correlation functionals overestimate the electron correlation energy compared to conventional *ab initio* computations of the correlation energy. Correlation functionals contribute not only the electron-electron interaction energy but also to the kinetic and potential energies. The correlation energy for DFT should not be compared directly to that for conventional *ab initio* methods since the two methods have different reference systems. Correlation functionals lowers the highest occupied orbital energy and the total energy of a system as illustrated by the result using the LYP and PW91 functionals.

Overall, some deficiencies were revealed in both the exchange and correlation functionals which were examined. The mixing of HF exact exchange generally improves the energy predictions and the prediction of the highest occupied orbital energy. The present study can guide future of the modeling the existing functionals in hybrid method. Although mixing about one quarter of the HF exchange with the hybrid method is the general choice (e.g. B3), different exchange-correlation functionals need fine tuning with respect to the weight of HF exchange. The appropriate mixing of HF exchange and

proper combination (in order to cancel the errors in the functionals) of exchange and correlation functionals is critical to the better performance of hybrid methods.

5.3 The Role of Correlation: Numerical Examination of a New Exchange-Correlation functional mPW1LYP

5.3.1 Introduction

The application of hybrid methods such as B3LYP [33] and BHandHLYP [34] in chemical reactions involves the mixing of exact exchange (HF exchange) into the DFT functionals. A one-parameter protocol has been extensively studied with different functionals [3,12,35] since the rationalization of the appropriate mixing of exact exchange (HF exchange) in hybrid methods [11] and the earlier developments by Becke [25]. These one-parameter based methods (e.g. B1LYP, B1PW91 [12], PW1PW91, mPW1PW91 [3] and LG1LYP [35]) have been tested on the reduced G2 data set [4] for molecular geometries, atomization energies, and vibrational frequencies. These methods also have been examined for some noncovalent interactions, for reaction barriers and for interaction energies. mPW1PW91 was found to be one of the best methods for such chemical applications [3]. Although the combination of the PW exchange functional with the PW correlation functional has been assumed to yield a cancellation of errors from the exchange and the correlation functionals, there is no theoretical basis or any non-numerical evidence for this assumption. LYP has been shown to provide improved results [12,36,37]. A new combination of exchange and correlation functionals within the one-parameter protocol – namely mPW1LYP is examined in the present work. Numerical

tests are carried out on the reduced G2 data set. Molecular geometries, atomization energies, dipole moments and vibrational frequencies were examined in detail. The dimers of inert atom, He_2 and Ne_2, are studied with mPW1LYP. The water dimer and the complex between ethylene and the chlorine molecule are examined as examples of hydrogen bonding and of weak intermolecular interactions. Proton transfer in malonaldehyde and the initial reaction barriers of triplet oxygen with ethylene and benzene were studied to check the performance of the mPW1LYP method for conjugated systems and for low barriers to reaction. An examination of the Walden inversion process in $[ClCH_3Cl]^-$ is used to test further the performance of mPW1LYP in the case of another small reaction barrier. Finally the electronic spectra of some small molecules are calculated to check how mPW1LYP performs for electronic excitation energies in comparison with experiment and with other theoretical methods. All these test cases taken together form a good standard for the validation of new methods. [3,4,12,35]

5.3.1.1 A modified PW91 exchange functional and the performance of mPW1PW91

As introduced in section 5.2.4.1.1, the modified PW91 exchange functional (mPW91) yields an improved description of weakly interacting systems. Two parameters have been modified in the mPW91 functional. The first one is ζ (in Equation 34). The original value for this parameter in PW91 which was 0.0042 came from a fit of the total atomic exchange energies within 1% of the exact (HF) exchange energies and was changed slightly to 0.0046 [3]. The second parameter d was modified in the exponent χ in equation 34. This d value has been reduced from 4 to 3.73 by fitting the different exchange

energies of the rare-gas dimers to HF values [3] in the region of Van der Waals interactions. Calculations using mPW1PW91 on the G2 data set, on noncovalent interacting systems such as rare gas dimers, hydrogen-bonded sytems(water dimer), and charge transfer complexes ($C_2H_4\cdots Cl_2$), barrier sensitive organic reactions (e.q. proton transfer process in malonaldehyde, the gas phase Walden inversion) show that the mPW1PW91 protocol generally provides similar or even better results than B3LYP and does especially well in the field of weakly interacting systems. The very good performance of mPW1PW91 inspires us to look for another combination of the modified PW91 exchange functional with another correlation functional with even better performance in chemical application.

5.3.1.2 The reduced G2 data set

The reduced G2 data set contains all neutral molecules comprised of only first-row atoms plus H_2. It contains 15 diatomic and 17 polyatomic molecules. Chemical properties studied for these molecules include equilibrium geometries, dipole moments, harmonic vibrational frquencies, and total atomization energies [4]. There are experimental data available for all species in the reduced G2 data set. The geometries of molecules in the reduced G2 data set are taken from the web pages of Argonne National Laboratory: http://chemistry.anl.gov/compmat/g2theory.htm

5.3.1.3 Basis set superposition error (BSSE)

Basis set superposition error (BSSE) involves an artificial lowering of the energy of each monomer as the dimer forms [38] due to the use of limited basis set. The

intermolecular interaction energy is calculated as the difference between the total energy on the combined system and its fragments. The intermolecular interaction energy is small compared to the total energy especially in a very weakly interacting system such as an inert gas dimer. In this case, the BSSE can be large relative to the intermolecular interaction energy. BSSE first appears when the monomers approach closely enough that the basis set on one monomer can overlap with that on the other. Thus the basis set of one monomer "artificially" improves the basis set of the second monomer (providing more functional freedom for the electrons on the other monomer [38]). An extra stabilization results. The BSSE decreases as the basis set becomes larger. There would be no BSSE if a complete basis set were employed [38].

The most popular procedure for BSSE correction was introduced by Boys and Bernardi and is known as the counterpoise procedure (CP)[38,39]. This procedure is summarized by the following formula,

$$E_{int} = E_{tot} - (E_{mon1} + E_{mon2}) \qquad (51)$$

The interaction energy of a dimer is obtained as the difference between the dimer and monomer energies with all these energies calculated using the same basis set. Thus, the energy of the isolated monomer is calculated with a basis set consisting of both the monomer's basis set and its partner's basis functions. The partner's nuclei are replaced with nuclei without charge. In other words, only the basis set is added for the second monomer. Its nuclei or electrons will not be present in the calculation of the first monomer's energy. This procedure is employed in the present work to correct the interaction energies of the inert gas dimers and of the weak complexes.

5.3.2 Computational details

Most of the calculations were carried out with the Gaussian 98 package version A.7[26] on the Origin 2000 server at the University of Waterloo and the Pentium II 300 Personal Computer with the Linux (Mandrake 6.0) operating system. For comparison to the earlier mPW1PW91 results [3], the basis sets for the G2 data set and other systems have been chosen as in that earlier study [3]. The basis sets are specified in detail in each section.

5.3.3 Results and discussion

5.3.3.1 The reduced G2 data set

Tables 5-5 and 5-6 report the bond lengths of the molecules in the reduced G2 data set. For the diatomic molecules, mPW1LYP gives a similar prediction as mPW1PW91 for the bond lengths. Both mPW1LYP and mPW1PW91 predict the same bond length for Li_2, which is one of the most difficult molecules to calculate using DFT methods. In Li, the 2s and 2p orbital are nearly degenerate, which makes it difficult to predict accurately an bond length for this molecule. Both of these functionals yield better distances than do B1PW91 and mPW3PW91. mPW1LYP frequently gives very nearly the same prediction as mPW1PW91 for the geometries of the polyatomic molecules in the reduced G2 data set. However, there are several exceptions. For the carbon-carbon single bond length in CH_3CH_3, the nitrogen-nitrogen bond distance and HNNH torsion angle in H_2NNH_2, and the oxygen-oxygen bond and HOOH torsion angle in HOOH, mPW1LYP yields better results than mPW1PW91, B1PW91 and mPW3PW91. mPW1LYP gives a poorer result for the NNH angle in H_2NNH_2 than does mPW1PW91. All geometric predictions from mPW1LYP are very close to the experimental values.

Table 5-7 reports the atomization energies predicted by mPW1LYP in comparison with other methods and experiment. The mean average deviation of the atomization energies with mPW1LYP for the 32 molecules is 3.2 kcal/mol. This deviation is larger than that from the mPW3PW91 method but smaller than that from the mPW1PW91 approach. For the maximum deviation in atomization energies from experiment, mPW1LYP predicted a similar value to that from mPW3PW91, which is slightly larger than the maximum deviation from mPW1PW91. mPW1LYP does perform better than B1PW91 when both the mean average deviation and the maximum deviation for atomization energies are considered.

Table 5-8 summarizes the mean absolute deviation for the bond lengths, atomization energies, dipole moments and harmonic vibrational frequencies from the mPW1LYP functionals in comparison with other methods. mPW1LYP appears to be among the best methods for the prediction of molecular property. For bond lengths predictions, mPW1LYP produces the same quality prediction as from a three-parameter scheme such as B3LYP. For the atomization energies, mPW1LYP yields only slightly inferior results to the results from B3LYP, mPW3PW91 and B1LYP, but better than the other three-parameter method (B3PW91) and the one-parameter methods (B1PW91 and mPW1PW91) which were tested. For the dipole moments, mPW1LYP produces slightly inferior results to those from the other three-parameter and one-parameter methods. mPW1LYP yields better predictions for the vibrational frequency with much smaller deviation than all the methods as listed in Table 5-8, both conventional *ab initio* and other DFT methods (LSDA, GGAs and hybrid). Thus the mPW1LYP method gives reliable predictions of atomization energies (with the ZPVE correction included since it is one

part of the total energy). Judging from the results collected in Table 5-8, mPW1LYP is one of the best methods for both thermodynamic and harmonic vibrational frequency predictions.

We also should note that the absolute deviation predicted by mPW1LYP from an experimentally observed vibrational frequency is very large (242 cm^{-1} for the hydrogen symmetric stretch in H_2NNH_2). Quantum chemical methods usually do not take the anharmonicity into account. The largest deviation from a harmonic vibrational frequency predicted by mPW1LYP is 110 cm^{-1} for the stretches of F_2. The harmonic vibrational frequency for the F_2 stretch is 891cm^{-1}, while mPW1LYP predicts it to be 1001cm^{-1}.

Table 5-5. Theoretical and experimental geometries of the diatomic molecules in the reduced G2 data set. Bond lengths in angstroms. All theoretical values were obtained with the 6-311G(d,p) basis set

Molecule	B1PW91[a]	mPW1PW91[a]	mPW3PW91[a]	mPW1LYP	Exp.[a]
H_2	0.744	0.744	0.746	0.743	0.742
LiH	1.600	1.591	1.599	1.591	1.595
BeH	1.349	1.342	1.349	1.343	1.343
CH	1.127	1.126	1.129	1.126	1.120
NH	1.040	1.043	1.043	1.043	1.045
OH	0.971	0.973	0.973	0.974	0.971
FH	0.915	0.919	0.918	0.919	0.917
Li_2	2.742	2.700	2.731	2.700	2.67
LiF	1.565	1.553	1.560	1.555	1.564
CN	1.163	1.163	1.165	1.163	1.172
CO	1.125	1.125	1.126	1.125	1.128
N_2	1.093	1.093	1.095	1.093	1.098
NO	1.142	1.146	1.145	1.146	1.151
O_2	1.194	1.202	1.198	1.202	1.207
F_2	1.338	1.402	1.395	1.403	1.412
Avg. abs. error	0.011	0.007	0.009	0.006	
Max error	0.072(Li_2)	0.030(Li_2)	0.061(Li_2)	0.030(Li_2)	

a: From C. Adamo, and V. Barone, J. Chem. Phys. 108 (1998), 664 and G. J. Laming, V. Termath, and N. C. Handy, J. Chem. Phys. 99 (1993), 8765.

Table 5-6. Theoretical and experimental geometries of the polyatomic molecules in the reduced G2 data set. Bond lengths in angstroms, angles in degree. All theoretical values were obtained with the 6-311G(d,p) basis set

Molecules	Parameter	B1PW91[a]	mPW1PW91[a]	mPW3PW91[a]	mPW1LYP	Exp.[a]
CH_2	r(CH)	1.079/1.115	1.079/1.113	1.080/1.116	1.079/1.113	1.075/1.107
$(^3B_1)/(^1A_1)$	α(HCH)	134.3/101.1	134.7/101.2	134.6/100.8	1.347/101.2	133.9/102.4
CH_3	r(CH)	1.080	1.079	1.081	1.079	1.079
CH_4	r(CH)	1.090	1.090	1.091	1.090	1.086
NH_2	r(NH)	1.028	1.029	1.030	1.030	1.024
	α(HNH)	102.2	102.3	102.1	102.2	103.4
NH_3	r(NH)	1.013	1.015	1.015	1.014	1.012
	α(HNH)	106.4	106.5	106.4	106.5	106.0
OH_2	r(OH)	0.958	0.961	0.960	0.961	0.957
	α(HOH)	103.9	103.9	103.8	103.9	104.5
HCCH	r(CC)	1.198	1.197	1.199	1.196	1.203
	r(CH)	1.063	1.063	1.064	1.062	1.062
H_2CCH_2	r(CC)	1.325	1.325	1.326	1.326	1.334
	r(CH)	1.085	1.084	1.086	1.084	1.081
	α(HCH)	116.6	116.6	116.6	116.5	117.4
H_3CCH_3	r(CC)	1.511	1.510	1.516	1.529	1.526
	r(CH)	1.095	1.094	1.094	1.093	1.088
	α(HCH)	108.2	108.3	108.2	107.5	107.4
HCN	r(CN)	1.147	1.147	1.149	1.147	1.153
	r(CH)	1.066	1.066	1.067	1.065	1.065
HCO	r(CO)	1.174	1.170	1.176	1.172	1.175
	r(CH)	1.125	1.124	1.126	1.126	1.122
	α(HCO)	124.5	124.4	124.3	124.1	124.6
H_2CO	r(CO)	1.194	1.196	1.198	1.198	1.203
	r(CH)	1.107	1.109	1.111	1.108	1.099
	α(HCH)	115.6	115.6	115.5	115.6	116.4

H_3COH	r(CO)	1.410	1.409	1.412	1.419	1.421
	$r(CH_a)$	1.090	1.090	1.092	1.090	1.093
	$r(CH_b)$	1.099	1.098	1.099	1.097	1.093
	r(OH)	0.956	0.957	0.959	0.960	0.963
	$\alpha(OCH_a)$	107.1	107.1	107.0	106.9	107.0
	α(COH)	107.8	107.8	107.7	107.9	108.0
	$\alpha(H_0CH_0)$	108.5	108.5	108.4	108.6	108.5
H_2NNH_2	r(NN)	1.420	1.420	1.423	1.435	1.447
	r(NH)	1.012	1.015	1.012	1.010	1.008
	α(NNH)	109.5	109.4	109.5	112.1	109.2
	α(HNH)	113.5	113.4	113.6	107.7	113.3
	d(HNNH)	87.3	87.3	87.6	90.2	88.9
HOOH	r(OO)	1.431	1.430	1.438	1.449	1.475
	r(OH)	0.961	0.962	0.964	0.964	0.950
	α(OOH)	100.6	100.6	100.4	100.2	94.8
	d(HOOH)	117.9	118.0	118.3	120.3	120.0
CO_2	r(CO)	1.156	1.156	1.159	1.158	1.160

a: From C. Adamo, and V. Barone, J. Chem. Phys. 108 (1998), 664 and G. J. Laming, V. Termath, and N. C. Handy, J. Chem. Phys. 99 (1993), 8765.

Table 5-7. Theoretical and experimental atomization energies (kcal/mol) for the 32 molecules in the reduced G2 data set. All theoretical values were obtained with the 6-311G++G(3df,3pd) basis set at the 6-311G(d,p) geometries. The atomization energies include ZPVE corrections for the molecules.

Molecule	B1PW91[a]	mPW1PW91[a]	mPW3PW91[a]	MPW1LYP	Exp.[a]
H_2	99.0	98.7	100.8	102.3	103.3
LiH	50.8	51.3	53.2	55.8	56.0
BeH	53.5	53.6	54.3	54.4	46.9
CH	78.4	78.9	80.0	80.7	79.9
$CH_2(^3B_1)$	181.6	182.8	184.5	179.7	179.6
$CH_2(^1A_1)$	165.1	165.8	168.8	168.7	170.6
CH_3	290.8	289.5	293.1	289.0	289.2
CH_4	386.5	389.1	393.9	389.6	392.5
NH	79.8	80.3	80.8	82.6	79.0
NH_2	169.3	170.7	174.1	174.2	170.0
NH_3	270.3	272.7	277.9	276.3	276.7
OH	99.6	100.3	102.5	101.7	101.3
OH_2	211.9	213.6	218.0	214.8	219.3
FH	131.8	131.3	133.9	131.9	135.2
Li_2	17.3	18.8	19.5	21.7	24.0
LiF	130.2	131.1	134.3	134.5	137.6
HCCH	381.9	385.5	388.7	382.4	388.9

H_2CCH_2	525.5	530.0	535.7	527.0	531.9
H_3CCH_3	654.8	660.0	668.0	659.7	666.3
CN	171.5	173.5	177.7	172.8	176.6
HCN	296.2	299.0	303.4	299.5	301.8
CO	249.1	250.5	255.2	249.3	256.2
HCO	268.7	271.4	276.6	269.2	270.3
H_2CO	351.7	355.1	356.6	353.2	357.2
H_3COH	472.0	477.3	484.7	475.2	480.8
N_2	216.9	219.2	223.8	222.3	225.1
H_2NNH_2	397.1	402.8	411.4	405.8	405.4
NO	146.5	148.7	153.4	148.8	150.1
O_2	117.8	119.9	124.6	117.3	118.0
HOOH	241.7	245.8	253.5	245.4	252.3
F_2	22.6	31.3	35.4	31.0	36.9
CO_2	369.1	382.7	389.1	375.7	381.9
mean avg. dev.	5.4	3.5	2.7	3.2	
max dev.	11.5(14.3)	6.5(6.7)	6.6(7.4)	7.5	

a: From C. Adamo, and V. Barone, J. Chem. Phys. 108 (1998), and G. J. Laming, V. Termath, and N. C. Handy, J. Chem. Phys. 99 (1993), 8765. The correct maximum deviation for B1PW91, mPW1PW91 and mPW3PW91 should be the values in brackets which were re-calculated in the present work.

Table 5-8. Mean absolute deviations of different methods for properties of the 32 molecules in the G2 data set. Bond lengths (Å), and harmonic frequencies (cm^{-1}) are computed using the 6-311G(d,p) basis set, atomization energies (D_0) (kcal/mol) and dipole moments (μ) are evaluated with the 6-311++G(3df,3pd) basis set

Method	Bond length	D_0	μ	Harmonic frequency
HF[a]	0.022	82.0	0.29	144
MP2[a]	0.014	23.7	0.28	99
CCSD[T][a]	0.005	11.5	0.10	31
LSD[a]	0.017	43.5	0.25	75
BPW91[a]	0.014	6.0	0.11	69
PW91PW91[a]	0.012	8.6	0.12	66
BLYP[a]	0.014	9.6	0.10	59
mPW91PW91[a]	0.012	6.7	0.11	65
B3LYP[a]	0.004	2.4	0.08	31
B3PW91[a]	0.008	4.8	0.08	45
mPW3PW91[a]	0.008	2.7	0.08	37
B1LYP[a]	0.005	3.1	0.08	33
B1PW91[a]	0.010	5.4	0.10	48
mPW1PW91[a]	0.010	3.5	0.10	39
mPW1LYP	0.008	3.2	0.11	23

a: From C. Adamo, and V. Barone, J. Chem. Phys. 108 (1998), 664, HF, CCSD[T] and MP2 from B. G. Johnson, P. M. W. Gill, and J. A. Pople, J. Chem. Phys. 98 (1993), 5612, LSD from A. D. Becke, J. Chem. Phys. 104 (1996), 1040.

5.3.3.2 Noncovalent interactions (inert gas dimers, the water dimer, and the ethylene-chlorine complex $C_2H_4\cdots Cl_2$)

Table 5-9. Bond lengths and interaction energies for He_2 and Ne_2 using the modified cc-pV5Z basis set

Dimer	Method	r(Å)	D_{int}(eV)
	PW91PW91[a]	2.78	0.010
	mPW91PW91[a]	3.14	0.003
He_2	mPW3PW91[a]	2.97	0.002
	mPW1PW91[a]	3.11	0.002
	mPW1LYP	2.53	0.003
	Exact[b]	2.97	0.001
	PW91PW91[a]	2.94	0.014
	mPW91PW91[a]	3.25	0.004
Ne_2	mPW3PW91[a]	3.16	0.003
	mPW1PW91[a]	3.23	0.003
	mPW1LYP	2.80	0.010
	Exact[b]	3.09	0.004

a: From C. Adamo, and V. Barone, J. Chem. Phys. 108 (1998), 664 and S. F. Boys; b: From F. Bernardi, Mol. Phys. 19 (1970), 553.

Usually there is not a great difference among the results from the various functionals in the region of the equilibrium geometry of a molecule. Many functionals give satisfactory predictions for stable structures. In the region of the equilibrium geometry of a system, the electron density is sufficiently large to lessen the role of the electron density gradient correction. A different case arises in the weakly interacting region, where the electron density is low and the change of electron density is rapid i.e. the density gradient is much more significant. The different performance of the different methods should be more evident in this region of weak interaction. The B functional has been shown not to predict a Van der Waals interaction. BHandHLYP shows a very slight weak interaction for the inert gas dimer [40] that is related to the large amount of HF exchange mixed into this functional. In the present work, we compare the results from mPW1LYP for two dimers of inert gases, the water dimer, and a charge transfer complex between ethylene and chlorine ($C_2H_4\cdots Cl_2$) with the results from Ref. [3].

Table 5-9 reports the results on the He and Ne dimers obtained with mPW1LYP and corrected for the basis set superposition error (BSSE). The basis set used is the modified cc-pV5Z [3]. In Reference [3], the methods involving the B exchange functional predicted no binding for these dimers. All the PW91 and mPW91 based methods predict a minimum for both dimers. mPW1PW91 predicts slightly longer bond lengths for the two dimers while the interaction energies for the two inert gas dimers are predicted to be close to the exact value [3]. With the LYP correlation functional, mPW1LYP overestimates the attractive interactions in these dimers. mPW1LYP predicts a bond length for He_2 that is 0.44 Å shorter than the exact bond length and the predicted interaction energy for He_2 by mPW1LYP (0.003eV) is slightly larger than the exact

interaction energy (0.001eV). For the Ne dimer(Ne_2), mPW1LYP predicts a slightly shorter bond length and larger interaction energy(0.010eV). The exact value of the interaction is 0.04eV for Ne dimer. Examining these predictions of distance and interaction energies for He_2 and Ne_2, the role of the correlation functional is significant. The lower energy and shorter bond length predicted by LYP (compared to the PW91 correlation functional) is neither the result of the self-interaction error in PW91 nor the deficiency in parallel correlation in LYP. This behavior may be systematic for these correlation functionals as was demonstrated for the behaviors of exchange functionals with regard to the total energies of the atoms H, He and Li. Note that the description of weakly interacting systems such as charge transfer complexes or hydrogen bonded systems by the B exchange functional may not be attributed from dispersion effects which are not predicted by this method.

A further comparison of the results using mPW1LYP with other methods is carried out for the water dimer, a hydrogen bonded system. Strong anharmonic effects make a precise experimental estimate of the equilibrium geometry of the water dimer difficult. The best estimated O-O distance from experiment was 2.952Å[41] and the binding energy was 5.44±0.7kcal/mol [42a], more recent experimentally derived value is 4.91kcal/mol[42b]. The equilibrium geometry of the water dimer is described accurately by many density functional methods. BPW91, PW91PW91, mPW19PW91, mPW3PW91 and mPW1PW91 with the 6-311G** basis set predict an O-O distance close to 2.87Å. With the 6-311G** basis set, the mPW1LYP functional predicts a water-dimer stationary point similar in geometry to that from other DFT approaches to be a transition state. Increasing the basis set to 6-311++G** changes the nature of this stationary point from transition

state structure to a minimum. The O-O distance is predicted to be 2.89Å at mPW1LYP/6-311++G**, which is slightly shorter than but very close to 2.90Å, the value from mPW1PW91 with the 6-311G** basis set. At 6-311G**, mPW1PW91 predicts a binding energy of 7.0kcal/mol [3], extension of the basis set to 6-311++G(3df,3pd) lowers this value to 4.5kcal/mol (with both BSSE and ZPVE corrections included). Including BSSE and ZPVE correction, mPW1LYP/6-311++G(3df,3pd) predicts a binding energy of 2.8 kcal/mol. From the geometry and the binding energy, mPW1LYP appears to be giving a similar description to the water dimer as does mPW1PW91.

The description of charge transfer (CT) complexes has been shown to be a stringent test for both density functional [43] and conventional *ab initio* methods [44]. The complex between ethylene and chlorine, $C_2H_4\cdots Cl_2$, is studied to evaluate the performance of the mPW1LYP functional. The methods using the B exchange functional predict too short an intermolecular distance and too large an interaction energy for such complexes [3,43]. There are several conformations for the $C_2H_4\cdots Cl_2$ complex, only the most stable conformation (the axial-perpendicular structure) is considered here. In the axial-perpendicular structure, the Cl-Cl bond is perpendicular to the C-C bond and the ethylene plane and the complex has C_{2v} symmetry. The intermolecular distance manifests the strength of interaction between Cl_2 and C_2H_4 in the complex. This intermolecular distance is directly related to the σ-π electron transfer from chlorine to ethylene. This electron transfer weakens the Cl-Cl bond, which results in a much lower Cl-Cl stretching frequency than in the free chlorine molecule.

Table 5-10 reports selected geometrical parameters, the Cl-Cl stretching frequency and the interaction energy in the $C_2H_4\cdots Cl_2$ complex. For the intermolecular distance,

mPW1LYP predicts a better value than the remaining density functional methods except for B1LYP. PW91PW91 obviously overestimates the interaction and predicts a much shorter intermolecular distance. mPW1PW91, B1LYP and mPW1LYP predict this distance (2.834Å, 2.890 Å and 2.871 Å respectively) somewhat closer to the experimental value (3.128 Å). For the Cl-Cl stretching frequency prediction, mPW1LYP ($437cm^{-1}$) does better than PW91PW91 ($390cm^{-1}$) and mPW91PW91 ($379cm^{-1}$), and slightly worse than the results from the other three hybrid methods. Consequently, mPW1PW91 predicts a slightly stronger interaction energy (9.3kcal/mol) than mPW1PW91 (5.9kcal/mol) and B1LYP (5.0kca/mol). PW91PW91 and mPW91PW91 obviously overestimate this interaction energy as indicated in Table 5-10. These interaction energies are corrected for both BSSE and ZPVE effects. mPW1LYP predicts a value very close to experiment. Overall, the mPW1LYP functional is comparable to mPW1PW91 and B1LYP in predictions on this complex.

Table 5-10. Selected geometrical parameters (Å), harmonic Cl-Cl frequencies (cm^{-1}) and the binding energy (kJ/mol) of the C_2H_4····Cl_2 complex

	MP2[a]	PP[a]	mPP[a]	mP1P[a]	mP3P[a]	B1[a]	mP1L	Exp.[a]
d(Cl···plane)	3.003	2.599	2.627	2.834	2.792	2.890	2.871	3.128
d(ClCl)	2.044	2.151	2.149	2.062	2.079	2.093	2.097	
ν(Cl-Cl)	506	390	379	467	450	450	437	527
ΔE_{comp}	-6.7	-23.2	-13.3	-5.9	-11.7	-5.0	-9.3	-7.1/ -11.3

The energies are computed at the 6-311++G(3df,3pd) level with 6-311G(d,p), and are corrected for BSSE and ZPVE effect.

a: From C. Adamo, and V. Barone, J. Chem. Phys. 108 (1998), 664, experimental data from H. I. Bloemink, K. Hinds, A. C. Legon, and J. C. Thorn, J. Chem. Soc. Chem. Commun. 1321 (1994), H. I. Bloemink, K. Hinds, A. C. Legon, and J. C. Thorn, Chem. Phys. Lett. 223 (1994), 162, and A. G. Bowmaker and P. D. Boyd, J. Chem. Soc. Faraday Trans. 83 (1987), 2211, and MP2 from E. Ruiz. D. R. Salahub, and A. Vela, J. Phys. Chem. 100 (1996), 12265

PP: PW91PW91; m PP: PW91PW91; mP1P: mPW1PW91; mP3P: mPW3PW91; B1: B1LYP; mPL: mPW1LYP

5.3.3.3 Proton transfer in malonaldehyde

Table 5-11. Selected geometrical parameters (Å) and relative energies (kJ/mol) for the minimum (M) and saddle points (SP) of the malonaldehyde rearrangement

	MP2[a]		mPW91PW91[a]		mPW1PW91[a]		mPW3PW91[a]		mPW1LYP		Exp.[b]
	M	SP	M	SP	M	SP	M	SP	M	SP	
d(O···O)	2.581	2.355	2.518	2.387	2.539	2.353	2.534	2.359	2.587	2.362	2.55
d(O···H)	1.678	1.197	1.561	1.217	1.632	1.200	1.620	1.203	1.703	1.206	
d(OH)	0.991	1.197	1.034	1.217	1.001	1.200	1.006	1.203	0.993	1.206	
ΔE	0.0	11.7	0.0	3.8	0.0	12.0	0.0	8.2	0.0	12.0/14.5	

The relative energies are computed at the 6-311++G(3df,3pd) level with 6-311G(d,p) geometries

a: From C. Adamo, and V. Barone, J. Chem. Phys. 108 (1998), 664

b: From M. D. Harmony, V. W. Laurie, R. L. Kwczkowski, R. H. Schwendeman, D. A. Ramsay, J. Lovas, W. J. Lafferty, and A. G. Maki, J. Phys. Chem. Ref. Data 8 (1979), 694

Density functional methods have some difficulty in describing proton transfer reactions and usually underestimate the activation energy for proton transfer. This low barrier has been ascribed to an overestimation of the correlation energy that yields excessive conjugation in the molecular skeleton [3,45]. Study on the H_2^+ molecular cation showed that such underestimation of an activation barrier can be caused by the self-interaction error and is thus rooted in the functional [1]. The present studies on simple atoms indicate that all functionals except for LYP are not self-interaction error free. This

SIE may cause different exchange functionals created with the same protocol to show similar behavior in characterizing the proton transfer in malonaldehyde [3]. For example BPW91 compared with mPW91PW91 and B3PW91 compared with mPW3PW91.

One should note that in experiment the structure of malonaldehyde is an average of the C_{2v} saddle point and the C_s minimum since only the C_{2v} structure has been observed in experiment [46]. The average O-O distance observed in experiment is 2.55Å [46]. Experiment also indicated that the barrier for this proton transfer is very low.

Table 5-11 reports selected geometrical parameters and the proton transfer activation energy predicted by mPW1LYP along with the other predictions from Ref. [3]. mPW1LYP predicts the minimum energy geometry closest to that from MP2 especially for the longest O-O distance. MP2 predicts this O-O distance to be 2.581 Å and mPW1LYP finds a value of 2.587 Å. mPW1PW91 yields an O-O distance of 2.539Å which is the next closest to the MP2 value. For the transition state (first order saddle point), mPW1LYP predicts an O-O distance of 2.362Å. mPW1LYP predicts a slightly higher energy barrier (14.5 kJ/mol) than mPW1PW91 (12.0 kJ/mol). Other density functional methods predict lower barriers for this proton transfer. We believe the reaction barrier reported in Ref. [3] has not been corrected for the ZPVE effects. This was confirmed by repeating calculations with the mPW1PW91 functional on both the minimum and transition state. The ZPVE corrected reaction barrier predicted by mPW1PW91 should be 9.6 kJ/mol rather than 12.0 kJ/mol. The barrier of 12.0 kJ/mol for mPW1LYP is corrected for ZPVE, while this barrier is 14.5kJ/mol without being corrected for ZPVE. It is in agreement with experiment for this reaction barrier to be low since only C_{2v} structure rather than C_s has been observed in experiment [46]. The observed

structure might be average of the two equivalent C_s isomers. For this proton transfer reaction, mPW1LYP give a similar description of the structure and energies to mPW1PW91. The mixture of HF exchange improves the performance of the exchange functional (decreases the self-interaction error).

5.3.3.4 The Walden inversion reaction

The Walden inversion (S_N2 reaction) is another stringent test for density functional methods [3]. This S_N2 reaction is also important in organic chemistry. In the Walden inversion, one chloride anion attacks the carbon in CH_3Cl from one side, and the Cl in this molecule is displaced by the attacking Cl^- and leaves as an anion. In the gas phase, this reaction starts from a C_{3v} pre-reaction complex, passes through a D_{3h} transition state (first order saddle point) and proceeds to a post-reaction complex identical to the pre-reaction complex. The complexation energy of the ion-molecule adduct ($Cl^-\cdots CH_3Cl$) ΔE_{comp}, the activation energy relative to reactants $\Delta E^{\#}$, and the overall activation energy ΔE_{ovr} (difference between the complexation energy and the activation energy) are the important thermodynamic quantities for this reaction. The most significant geometrical parameter is the distance of the attacking Cl^- to the carbon in methyl chloride.

The geometries of the pre-reaction complex and the transition state are reported in Table 5-12. Compared with the MP2 results, mPW1LYP gives the best prediction for the longer C-Cl distance in the complex. MP2 predicts the C-Cl distance to be 3.270Å and mPW1LYP predicts it to be 3.177Å. Also mPW1LYP predicts other geometrical parameters very close to those from MP2. For the transition state, mPW1LYP predicts C-Cl distances of 2.369Å, which are the longest among all predicted values. The C-Cl

distance in the transition state predicted by MP2 is 2.317 Å. The effect of the correlation functional on the geometry of the critical point is important judging from the change in the C-Cl distance at the saddle point in changing from mPW1PW91 to mPW1LYP.

Table 5-13 reports the thermodynamic quantities for the Walden inversion reaction. The experimental values for the complexation energy and activation energy are over 50 kJ/mol. The overall activation energy is relatively low with a large range of experimental uncertainty. The MP2 prediction is not reliable for these energies which has large values as shown by G2+ prediction [3]. mPW1LYP gives the best predictions of all three energies. mPW1PW91 is the next most accurate method for these energy predictions. The GGAs (BPW91 and MPW91PW91) make the poorest predictions and the overall activation energies predicted by these two methods are negative. Among the density functional methods listed in Table 5-13, mPW1PW91, B3PW91, mPW3PW91 and mPW1LYP perform relatively well for energetic predictions.

Table 5-12. Selected geometric parameters of the ion-complex $Cl^-\cdots CH_3Cl$ and the corresponding transition state for the Walden inversion. All values are obtained with the 6-311+G(d,p) basis set

Parameters	MP2 [a]	BP [a]	mPP [a]	mP1P [a]	B3P [a]	mP3P [a]	mP1L
			ion-complex				
d(C···Cl)	3.270	3.133	3.108	3.157	3.167	3.160	3.177
d(CCl)	1.810	1.870	1.870	1.828	1.836	1.835	1.856
d(CH)	1.085	1.090	1.089	1.083	1.084	1.084	1.081
α(ClCH)	108.8	107.9	107.9	108.5	108.4	108.4	107.9
			SP				
d(CCl)	2.317	2.366	2.362	2.328	2.339	2.336	2.369
d(CH)	1.073	1.079	1.079	1.072	1.073	1.073	1.070

BP: BPW91; mPP: mPW91PW91; mP1P: mPW1PW91; B3P: B3PW91; mP3P: mPW3PW91; mP1L: mPW11LYP; a: From C. Adamo, and V. Barone, J. Chem. Phys. 108 (1998), 664

Table 5-13. Complexation energies of the ion-molecule complex Cl^--CH_3Cl, ΔE_{comp}, activation energy $\Delta E^{\#}$ and overall activation energy relative to reactants ΔE_{ovr} for the Walden inversion

	G2+[a]	BP[a]	mPP[a]	mP1P[a]	B1L[a]	B3P[a]	mP3P[a]	mP1L	Exp.
ΔE_{comp}	44.3	39.2	43.8	42.0	40.8	39.2	39.8	44.7	51.0±8.4
$\Delta E^{\#}$	10.3	26.6	26.2	43.7	37.6	40.4	40.4	45.4	55.8±8.4
ΔE_{ovr}	54.6	-12.6	-17.6	1.7	-3.2	1.2	0.6	0.7	4.2±4.2

All values in kJ/mol are obtained with the 6-311+G(d,p) basis set corrected for BSSE and ZPE corrections.

G2+: G2+(MP2); BP: BPW91; mPP: mPW91PW91; mP1P: mPW1PW91; B1L: B1LYP; B3P: B3PW91; mP3P: mPW3PW91; mP1L: mPW11LYP

a: From C. Adamo, and V. Barone, J. Chem. Phys. 108,664 (1998); G2+(MP2) from M. N. Glukhovtsev, R. D. Bach, A. Pross, and L. Radom, Chem. Phys. Lett. 260,558 (1996); exp. from S. E. Barlow, J. M. van Doren, and V. M. Bierbaum, J. Am. Chem. Soc. 116, 10645 (1994).

5.3.3.5 Reaction barrier for the reaction of the oxygen atom (^3P) with benzene (C_6H_6) and ethylene (C_2H_4)

Our studies on the reaction of the triplet oxygen atom with benzene showed that different density functional methods (BHandHLYP, B3LYP, B1LYP, BLYP and mPW1PW91) predicted different activation barriers for the initial reaction in the triplet electronic state. That study elucidated the role of HF exchange in the energetic prediction. The attack of the triplet oxygen atom on the benzene disrupts the π electronic conjugation. The initial reactant benzene is aromatic and fully conjugated. This reaction may serve as a good test for density functional methods in reaction barrier prediction. The reaction barrier for this reaction is large enough that most methods may be capable of reproducing it and it is low enough to discriminate between different methods. Most of the data reported in Table 5-14 and 15 were reported in Figures 3-1 and 3-3 in Chapter 3 and Figure 4-1 and Table 4-1 in Chapter 4. We repeat data analysis here in comparison to results from the new combination of functionals mPW1LYP.

Table 5-14 reports the main geometric features of the triplet transition state for the initial reaction of a triplet oxygen atom with a singlet benzene molecule, the activation energy, and the carbon-carbon bond lengths in the reactant benzene. The carbon atom attacked by oxygen in the transition state is C1, the carbon atoms connected to C1 are C2, etc.. In the transition state, the most significant geometric parameters are the OC1 distance and the carbon-carbon bond lengths in the benzene ring. B1LYP predicts geometries of the transition state similar to mPW1LYP and B3LYP. B3LYP predicts a longer C-O distance (1.883Å) than B1LYP (1.870 Å) and mPW1LYP (1.870 Å). Except for the C-O distance, mPW3PW91 performs similarly to mPW1PW91 in structural

predictions for the transition state. mPW3PW91 predicts a slightly longer C-O distance (1.904 Å) than does mPW1PW91 (1.893 Å). The angle of attack (OC1C4) for the oxygen atom relative to the benzene ring is about 100° by all methods. The difference between correlation functionals is illustrated by the structure of the transition state predicted by mPW1PW91 and mPW1LYP. mPW1PW91 predicts a longer C-O distance (1.893 Å) and shorter C-C bond lengths than does mPW1LYP. The major difference in the structures of the transition states for all methods is this C-O distance. The C-C bond lengths in the benzene ring change along with the change in C-O distance. The similarity in the structural prediction by the methods also is reflected in the C-C bond length prediction in benzene. B1LYP and B3LYP predict similar C-C bond length for benzene (1.3934 and 1.3939 Å respectively). mPW1LYP predicts a slightly shorter C-C bond length (1.3928 Å). mPW1PW91 predicts the shortest C-C bond length for benzene (1.3898 Å). The best estimate of the equilibrium C-C bond length in benzene is 1.3915 Å [47]. Taking the basis set effect into account, B1LYP, B3LYP and mPW1LYP make the best prediction for the benzene C-C bond length although the difference among different methods is very small. The activation energies predicted by all methods also are reported in Table 5-14. The experimental value for the activation energy of this initial reaction of triplet oxygen with benzene is 17±2 kJ/mol [48]. Not all methods predict this quantity well. B1LYP does best but predicts the activation barrier to be 5.6 kJ/mol. B1LYP and mPW1PW91 predict a positive reaction barrier. mPW1LYP predicts a reaction barrier close to zero although very slightly negative. The two three-parameter protocols (B3LYP and mPW3PW91) predict negative reaction barriers for the initial reaction. The reaction barriers predicted by mPW1LYP and mPW1PW91 demonstrate the role of the correlation functional.

Table 5-14 Geometries of the transition state and activation barrier (kJ/mol) of C_6H_6 reacting with triplet oxygen atom. Bond length is in Å and bond angle is in degree. The activation energy (kJ/mol) are calculated by 6-311++G(3df,3pd) basis set at 6-311G geometries including ZPVE correction**

	CC[a]	B1	B3	mP3P	mP1P	mP1L	Exp.[b]
			TS(Geometries)				
O-C1		1.870	1.883	1.904	1.893	1.870	
C1-C2		1.431	1.429	1.422	1.422	1.430	
C2-C3		1.381	1.382	1.381	1.379	1.380	
C3-C4		1.401	1.401	1.397	1.396	1.400	
OC1C4		101.5	100.5	99.2	100.0	101.0	
			C_6H_6(Geometries)				
C-C	1.3915	1.3934	1.3939	1.3912	1.3898	1.3928	
ΔE		5.6	-2.4	-4.5	2.9	-0.4	17±2

a: the C-C bond length has been determined by CCSD(T)/cc-pVQZ in combination with the reanalysis of the experimental rotational constant in J. Gauss, and J. F. Stanton, J. Phys. Chem. A, **104**, 2865 (2000) b: from A. G. Ureña, S. M. A. Hoffmann, D. J. Smith, and R. Grice, J. Chem. Soc., Faraday Trans. 2, **82**, 1537 (1986)

Table 5-15 The main geometrical features of the C_2H_4O transition state and the activation barrier (kJ/mol) for C_2H_4 reacting with triplet oxygen using 6-311++G(3df,3pd) basis with ZPVE correction

	CBS[a]	BH	B1	mPHB	MPHC	mP1P	mP1L	Exp.
O-C1	1.996	2.030	2.179	2.075	2.022	2.431	2.096	
C1-C2	1.355	1.347	1.345	1.340	1.372	1.333	1.352	
O-C2	2.574	2.607	2.609	2.613	2.660	2.493	2.587	
ΔE	-2.1	7.3	-10.7	5.2	20.0	-10.5	-16.5	5±2

B1: B1LYP; BH: BHandHLYP; mPHB: mPW91HandHPW91 with local correlation; mPHC: mPW91HandHPW91 without local correlation; mP1P: mPW1PW91; mP1L: mPW1LYP

a: from B. S. Jursic, J. Mol. Struct. (THEOCHEM), **492**, 85 (1999)

Exp.: from R. E. Huie, and J. T. Herron, J. Phys. Chem. Ref. Data, **2** 267 (1973)

Another more stringent case for *ab initio* methods and density functional methods involving π electrons is the reaction of triplet oxygen (^3P) with ethylene. The activation energy for the initial reaction is 5±2 kJ/mol [50]. This reaction has been described by a spin uncoupling model followed by inter-system crossing from the triplet to the singlet electronic state [51]. The single point calculations for the singlet and triplet state of the open OCH_2CH_2 in Chapter 3 confirmed this reaction mechanism. In the triplet transition state, the two unpaired electrons are mainly on the oxygen atom, and the interaction

between oxygen with the π electrons causes partial electron transfer from the oxygen atom to the ethylene which causes the fractional occupancies of electrons in this transition state.

Table 5-15 reports the main geometric features (heavy atom bond lengths) and the activation barriers of the transition state in the initial reaction of triplet oxygen with ethylene. Density functional methods are compared with Petersson's Complete Basis Sset (CBSQ) method [49] and experiment [50]. The structure of the transition state for the CBSQ method has been optimized at the MP2/6-31G(d') level and the activation energy has been calculated at 298K by Jursic [49].

The three-parameter protocols (B3LYP and mPW3PW91) fail to locate this transition state. All three of the one-parameter protocols (B1LYP, mPW1PW91 and mPW1LYP) locate a transition state, B1LYP and mPW1LYP predict similar structures for this transition state while mPW1LYP predicts a slightly looser geometry i.e. the transition state is much closer to the separated reactants. From the predicted structure of the transition state from B1LYP, mPW1LYP (also MP2 in Chapter 3), the oxygen atom obviously attacks a terminal carbon. The vibrational frequency calculations confirm this mechanism. The structure predicted by mPW1PW91 resembles one for transfer of an oxygen atom from one carbon atom to the other, and the two C-O distances are close to each other even started from the structure as other methods. This transition state is different from the one described in Chapter 3 by other methods. Location of this transition state by mPW1PW91 indicates that different methods yield different potential surfaces for the system. Examination of the eigenvector for the imaginary mode in the vibrational frequency calculation confirms this analysis (a', i34cm^{-1}) for mPW1PW91.

MPW1PW91 failed to locate a similar transition state to that predicted by B1LYP and mPW1LYP. The fine difference between correlation functionals in transition state structure characterization is revealed again by this case. Among the three one-parameter protocols, B1LYP makes the best prediction of the transition state judging from the structure and the activation energy. In accordance with Hammond's postulate for an exothermic reaction [52], the energy for the transition state is close to that of the reactants and the transition state structure is similar to the reactants. Experiment confirms the very small activation barrier [50]. The negative activation barriers from CBSQ and other methods support at least a very low reaction barrier. For comparison, BHandHLYP, mPWHandHPW91 were employed to study the activation barrier. In one of the mPWHandHPW91 protocols, local correlation is omitted to examine the role of local correlation on the prediction of the transition state. BHandHLYP and mPWHandHPW91 (mPWHB with both local correlation and gradient correction) reproduce the activation barrier very well. These two methods also predict similar transition structures to that from B1LYP and other methods. BHandHLYP predicts the activation energy to be 7.3kJ/mol and mPWHandHPW91 (mPWHB) predicts a 5.2 kJ/mol barrier. The half-and-half approach is not as reliable for structural predictions and vibrational frequency calculations as for the prediction of the activation energy [12]. This scheme usually is recommended for very low reaction barriers. Judging from the overall performance of the half-and-half protocol, this functional is still qualitatively useful. Another half-and-half protocol mPWHandHPW91 (mPHC in Table 5-15 without local correlation, the original PW91 contains both local correlation and gradient correction) is employed here to examine the role of local correlation. Without local correlation, mPHC predicts a stronger

interaction between oxygen and ethylene, which results in a shorter C-O distance. Also mPHC predicts a much higher activation energy for this reaction than mPWHB (with local correlation) and other methods. This change manifests the role of the correlation functional in lowering the activation energy.

In comparison, in the case of the oxygen atom reacting with ethylene, mPW1LYP performs slightly better than mPW1PW91 for the prediction of low barrier reactions.

5.3.3.6 Electronic spectra

The most popular functionals contain parameters fit to geometric or thermodynamic experimental data (for example the B exchange functional) or are constructed to include physical constraints (for example the P86 and PW91 exchange functionals). None of these functionals has been developed explicitly for excitation energies. Most functionals have been developed within a time-independent formalism and an excitation energy is an example of a time-dependent property. The Hohenberg-Kohn existence theorem [53] and Kohn-Sham theory [54] hold for the ground state of a system and most functionals are based on these two theorems. The formal foundation for time-dependent density functional theory (TD-DFT) by Gross [55] gives a sound and practical way for the application of density functional theory in time-dependent examples if the exchange-correlation functional for the time-dependent problem is known. Applications of time-independent functionals in predicting the excitation energies gave promising results for molecular systems, [56,57] which indicate that the functional for a ground state is a good approximation to the time-dependent functional. The implementation of TD-DFT in the Gaussian 98 package [58] allows the calculation of the excitation energies of a molecule.

Thus predictions of the mPW1LYP method for the excitation energies of formaldehyde (H_2CO), acetaldehyde (H_3CHCO) and acetone (CH_3COCH_3) are examined and compared with results from other density functional methods [59]. CIS gives poor excitation energies for acetone and TD-DFDT has been shown to be better than CIS in this case [59]. The minimum basis set required for satisfactory results for excitation energies from TD-DFT has been shown to be 6-311++G** [59].

Table 5-16 reports the excitation energies of formaldehyde predicted by mPW1LYP with the 6-311++G** basis set. Compared to experiment and the predictions by other methods, mPW1LYP does the worst for the excitation energies in formaldehyde. All the predicted values from mPW1LYP are lower than those from other methods and from experiment. The largest deviation from experiment is the $^3A_1$ (n-π^*) excitation, mPW1LYP predicts to occur at 5.18eV and the experimental value is 6.0 eV. All the excitation energies predicted from mPW1LYP are significantly lower than experiment.

Table 5-17 reports the excitation energies of acetaldehyde predicted by mPW1LYP and other methods. The predictions from mPW1LYP are close to experiment and are comparable with B3P86 which is the best method in predicting excitation energies for the three molecules, and is even better than B3P86 for some excitation energies for example for all the triplet excitations and most of the singlet excitations. For most of the excitation energies, mPW1LYP predicts the energies slightly higher than experiment.

The excitation energies of acetone are reported in Table 5-18 for mPW1LYP along with other methods and experimental values. For the higher excitations, mPW1LYP predicts very close to the higher excitation energies compared with experiment. At the lower end, mPW1LYP still underestimates the excitation energies compared to the

Table 5-16 Transition energies (in eV) of formaldehyde (H_2CO) predicted with the 6-311++G basisi set**

State	Methods						
	B3LYP[a]	B1LYP[a]	B3PW91[a]	B3P86[a]	mP1PW[a]	mP1L	Obs[b]
Singlets:							
$^1A_2$ (n-π^*)	3.93	3.96	3.95	3.95	3.96	3.90	4.1
$^1B_2$	6.58	6.66	6.76	6.98	6.78	6.49	7.13
$^1A_1$	7.35	7.64	7.71	7.93	7.74	7.46	8.14
$^1B_2$	7.67	7.73	7.89	8.09	7.82	7.48	7.98
$^1A_2$	8.37	8.44	8.57	8.81	8.50	8.21	
$^1B_1$	9.18	9.21	9.22	9.23	9.26	8.98	
Triplets:							
$^3A_2$ (n-π^*)	3.25	3.27	3.23	3.25	3.23	3.16	3.5
$^3A_1$ (n-π^*)	5.50	5.36	5.44	5.49	5.30	5.18	6.0
$^3B_2$	6.45	6.53	6.59	6.82	6.59	6.34	7.09
$^3A_1$	7.42	7.50	7.53	7.81	7.55	7.34	8.14
$^3B_2$	7.52	7.57	7.72	7.91	7.63	7.33	7.92
$^3B_1$	7.89	7.92	7.88	8.09	7.91	7.77	
$^3A_2$	8.37	8.44	8.56	8.82	8.52	8.21	

mP1PW: mPW1PW91; mP1L: mPW1LYP. a: M. E. Casida, C. Jamorski, K. C. Casida, and D. R. Salahub, J. Chem. Phys., **108**, 4439 (1998); b: J. B. Forsman, M. Head-Gordon, J. A. Pople, M. J. Frisch, J.Phys. Chem., **96**, 135 (1992).

Table 5-17 Transition energies (in e.V.) of acetaldehyde (H_3CHCO) predicted with the 6-311++G**

State	Methods						
	B3LYP[a]	B1LYP[a]	B3PW91[a]	B3P86[a]	mP1PW[a]	mP1L	Obs[b]
Singlets:							
$^1A''$ (n-π*)	4.49	4.32	4.28	4.29	4.31	4.11	4.28
$^1A'$ (n-π*)	6.35	6.45	6.55	6.76	6.55	6.76	6.82
$^1A'$	6.88	6.88	7.06	7.29	7.11	7.25	7.46
$^1A''$	7.26	7.36	7.41	7.70	7.42	7.26	
$^1A'$	7.52	7.60	7.72	7.89	7.68	8.22	7.75
$^1A'$	8.00	8.10	8.17	8.35	8.21	8.28	8.43
$^1A'$	8.42	8.53	8.65	8.76	8.64	8.51	8.69
$^1A''$	8.55	8.71	9.03	9.30	8.99	8.90	
Triplets:							
$^3A''$ (n-π*)	3.67	3.69	3.63	3.65	3.65	3.45	3.97
$^3A'$ (n-π*)	5.73	5.63	5.68	5.72	5.58	6.09	5.99
$^3A'$	6.17	6.27	6.36	6.58	6.35	6.64	6.81
$^3A'$	6.77	6.88	6.99	7.16	6.96	7.18	7.44
$^3A''$	7.24	7.34	7.41	7.67	7.42	7.68	
$^3A'$	7.45	7.52	7.64	7.89	7.56	8.11	7.80

mP1PW: mPW1PW91; mP1L: mPW1LYP. a: from M. E. Casida, C. Jamorski, K. C. Casida, and D. R. Salahub, J. Chem. Phys., **108**, 4439 (1998); b: M. E. Robin, Higher Excited States of Polyatomic Molecules, Vol. 3, Academic Press, New York, 1985

Table 5-18 Transition energies (in e.V.) of acetone (H_3CCOCH_3) predicted with the 6-311++G basis set**

State	Methods						
	B3LYP[a]	B1LYP[a]	B3PW91[a]	B3P86[a]	mP1PW[a]	mP1L	Obs[b]
Singlets:							
$^1A_2$ (n-π*)	4.44	4.48	4.49	4.41	4.47	4.40	4.43
$^1B_2$	6.11	5.96	6.09	6.28	6.08	5.73	6.36
$^1A_1$	6.83	6.94	7.01	7.26	7.06	6.71	7.41
$^1A_2$	6.96	7.07	7.16	7.43	7.15	6.84	7.36
$^1B_2$	7.21	7.31	7.40	7.67	7.39	7.36	7.49
$^1A_2$	7.47	7.58	7.72	7.89	7.70	8.29	8.09
Triplets:							
$^3A_2$ (n-π*)	3.86	3.89	3.82	3.84	3.85	3.75	4.18
$^3A_1$ (n-π*)	5.84	5.75	5.79	5.82	5.70	5.42	5.88
$^3A_2$	5.80	5.91	6.03	6.23	6.08	6.81	6.26
$^3A_1$	6.68	6.78	6.86	7.13	6.90	7.57	
$^3A_2$	6.95	7.05	7.14	7.60	7.30	8.14	7.90

mP1PW: mPW1PW91; mP1L: mPW1LYP. a: from M. E. Casida, C. Jamorski, K. C. Casida, and D. R. Salahub, J. Chem. Phys., **108**, 4439 (1998); b: from M. E. Robin, Higher Excited States of Polyatomic Molecules, Vol. 3, Academic Press, New York, 1985; and C. M. Hadad, J. B. Foresman, K. B. Wiberg, J. Phys. Chem., **97**, 4293 (1993).

experimental values. Other TD-DFT methods display similar trends as shown in the three tables.

Overall, mPW1LYP gives satisfactory predictions for the excitation energies for all three molecules. Generally TD-DFT methods underestimate the excitation energies at lower energy and slightly overestimates excitation energies at higher energy.

5.3.4 Concluding remarks

The numerical examination of mPW1LYP on the reduced G2 data shows that this new combination of functionals does well for geometries, vibrational frequencies, and energetic predictions for ground state molecules. The performance of mPW1LYP on inert gas dimers, charge-transfer complexes, the proton transfer reaction in malonaldehyde, the Walden inversion reaction and the initial reaction barriers of triplet oxygen atom with ethylene and benzene, indicates that mPW1LYP can describe weaker interactions but slightly overestimates the interaction energy. The slight overestimation is mainly due to the role of the particular functional, LYP. mPW1LYP can locate the transition state for the initial reaction of triplet oxygen atom with ethylene due to this overestimation of the interaction. This method is recommended for systems in which the weak interaction is important.

The calculations on the electronic spectra of formaldehyde, acetaldehyde, and acetone reveal that mPW1LYP can give satisfactory excitation energies. In acetaldehyde the results are slightly inferior to these from other density functional methods. mPW1LYP (and other density functional methods) underestimate the lower excitation energies and overestimate the higher excitation energies.

5.4 References

1. Y. Zhang, and W. Yang, J. Chem. Phys., **109**, 2604 (1998)
2. S. Vosko, L. Wilk, and M. Nusair, Can. J. Phys., **58**, 1200 (1980)
3. C. Adamo, and V. Barone, J. Chem. Phys., **108**, 664 (1998)
4. B. G. Johnson, P. M. W. Gill, and J. A. Pople, J. Chem. Phys., **98**, 5612 (1993)
5. A. D. Becke, J. Chem. Phys., **98**, 1372 (1993)
6. A. D. Becke, J. Chem. Phys., **98**, 5648 (1993)
7. J. Harris, and R. O. Jones, J. Phys. **F, 4**, 1170 (1974); O. Gunnarsson, and B. I. Lundqvist, Phys. Rev. **B 13**, 4274 (1976); D. C. Langreth, and J. P. Perdew, Phys. Rev. **B, 15**, 2884 (1997); J. Harris, Phys. Rev. **A, 29**, 1648 (1984)
8. a) J. P. Perdew, in Electronic Structure of Solids, edited by P. Ziesche and H. Eschrig, Akademie Verlag, Berlin, 1991; b) J. P. Perdew, and Y. Wang, Phys. Rev. **B, 45**, 13244 (1992); c) J. P. Perdew, J. A. Chevary, S. H. Vosko, K. A. Jackson, M. R. Pederson, D. J. Singh, and C. Fiolhais, Phys. Rev. **B, 46**, 6671 (1992)
9. a) C. Lee, W. Yang, R. G. Parr, Phys. Rev. **B, 37**, 785 (1988); b) B. Miehlich, A. Savin, H. Stoll, and H. Preuss, Chem. Phys. Lett., **157**, 200 (1989)
10. A. D. Becke, J. Chem. Phys., **104**, 1040 (1996)
11. J. P. Perdew, M. Ernzerhof, and K. Burke, J. Chem. Phys., **105**, 9982 (1996)
12. C. Adamo, and V. Barone, Chem. Phys. Lett., **274**, 242 (1997)
13. W. Koch, and M. C. Holthausen, A Chemist's Guide to Density Functional Theory, Wiley-VCH, Weinheim, 2000
14. D. J. Lacks, and R. G. Gordon, Phys. Rev. **A, 47**, 4681 (1993)

15. A. D. Becke, J. Chem. Phys., **85**, 7184 (1986)

16. A. D. Becke, J. Chem. Phys., **84**, 4524 (1986)

17. A. D. Becke, Phys. Rev. **A, 38**, 3098 (1988)

18. J. P. Perdew and Y. Wang, Phys. Rev. **B, 33**, 8800 (1986)

19. T. Tsuneda, T. Suzumura, and K. Hirao, J. Chem. Phys., **110**, 10664 (1999)

20. J. C. Slater, *Quantum Theory of Molecules and Solids. Vol. 4: The Self-Consistent Field for Molecules and Solids*, McGraw-Hill, New York, 1974

21. P. M. W. Gill, Mol. Phys., **89**, 433 (1996)

22. J. P. Perdew, K. Burke, and M. Ernzerhof, Phys. Rev. Lett., **77**, 3865 (1996)

23. T. Tsuneda, T. Suzumura, and K. Hirao, J. Chem. Phys., **111**, 5656 (1999)

24. E. H. Lieb, and S. Oxford, Int. J. Quantum Chem., **19**, 427 (1981)

25. A. D. Becke, J. Chem. Phys., **104**, 1040 (1996)

26. Gaussian 98, Revision A.7, M. J. Frisch, G. W. Trucks, H. B. Schlegel, G. E. Scuseria, M. A. Robb, J. R. Cheeseman, V. G. Zakrzewski, J. A. Montgomery, Jr., R. E. Stratmann, J. C. Burant, S. Dapprich, J. M. Millam, A. D. Daniels, K. N. Kudin, M. C. Strain, O. Farkas, J. Tomasi, V. Barone, M. Cossi, R. Cammi, B. Mennucci, C. Pomelli, C. Adamo, S. Clifford, J. Ochterski, G. A. Petersson, P. Y. Ayala, Q. Cui, K. Morokuma, D. K. Malick, A. D. Rabuck, K. Raghavachari, J. B. Foresman, J. Cioslowski, J. V. Ortiz, A. G. Baboul, B. B. Stefanov, G. Liu, A. Liashenko, P. Piskorz, I. Komaromi, R. Gomperts, R. L. Martin, D. J. Fox, T. Keith, M. A. Al-Laham, C. Y. Peng, A. Nanayakkara, C. Gonzalez, M. Challacombe, P. M. W. Gill, B. Johnson, W. Chen, M. W. Wong, J. L. Andres, C. Gonzalez, M. Head-Gordon, E. S. Replogle, and J. A. Pople, Gaussian, Inc.,

Pittsburgh PA, 1998

27. Æ. Frisch, and M. Frisch, *Gaussian 98 User's Reference*, Gaussian Inc. Pittsburgh PA, 1998

28. K. A. Peterson, D. E. Woon and T. H. Dunning Jr., J. Chem. Phys., **100**, 7410 (1994), PNNL at http://www.emsl.pnl.gov:2080/forms/basisform.html

29. R. Colle, and D. Salvetti, Theo. Chim. Acta, **37**, 329 (1975)

30. I. N. Levine, *Quantum Chemistry*, 4th Ed. Prentice-Hall, Inc. Englewood Cliffs 1991

31. R. G. Parr, and W. Yang, *Density-Functional Theory of Atoms and Molecules*, Oxford University Press, New York, 1989

32. Discussion with Dr. Axel D. Becke at the 4th Canadian Computational Chemistry Conference in Lennoxville in Quebec, 2000.

33. J. Baker, J. Andzelm, M. Muir and P. R. Taylor, Chem. Phys. Lett., **237**, 53 (1995)

34. H. M. Sulzbach, M. S. Platz, H. F. Schaefer III, and C. M. Hadad, J. Am. Chem. Soc., **119**, 5682 (1997)

35. C. Adamo, and V. Barone, J. Comput. Chem., **19**, 418 (1998)

36. G. J. Laming, V. Termath, and N. C. Handy, J. Chem. Phys., **99**, 8765 (1993)

37. B. G. Johnson, P. M. W. Gill, and J. A. Pople, J. Chem. Phys., **97**, 7846 (1992)

38. N. R. Kestner, and J. E. Combariza, P99 in *Reviews in Computational Chemistry*, **13**, Edited by K. B. Lipkowitz, and D. B. Boyed, Wiley-VCH, John Wiley and Sons, Inc., New York, 1999

39. S. F. Boys, and F. Bernardi, Mol. Phys., **19**, 553 (1970)

40. J. M. Pérez-Jordà, and A. D. Becke, Chem. Phys. Lett., **233**, 134 (1995)

41. J. A. Odutola, and T. R. Dyke, J. Chem. Phys., **72**, 5062 (1980)

42. a) L. A. Curtiss, D. J. Frurip, and M. Blander, J. Chem. Phys., **71**, 2073 (1979); b) R. S. Fellers, C. Leforestier, L. B. Braly, M. G. Brown, R. J. Saykally, Science **284**, 945-948 (1999)

43. E. Ruiz, D.R. Salahub, and A. Vela, J. Phys. Chem., **100**, 12265 (1996)

44. A. E. Reed, F. Weinhold, L. A. Curtiss, and D. J. Pochatko, J. Chem. Phys., **84**, 5687 (1986)

45. V. Barone, and C. Adamo, J. Chem. Phys., **105**, 11007 (1996)

46. From M. D. Harmony, V. W. Laurie, R. L. Kwczkowski, R. H. Schwendeman, D. A. Ramsay, J. Lovas, W. J. Lafferty, and A. G. Maki, J. Phys. Chem. Ref. Data **8**, 694 (1979)

47. J. Gauss, and J. F. Stanton, J. Phys. Chem., **A, 104**, 2865 (2000)

48. A. G. Ureña, S. M. A. Hoffmann, D. J. Smith, and R. Grice, J. Chem. Soc., Faraday Trans. **2, 82**, 1537 (1986)

49. B. S. Jursic, J. Mol. Struct. (THEOCHEM), **492**, 85 (1999)

50. R. E. Huie, and J. T. Herron, J. Phys. Chem. Ref. Data, **2** 267 (1973)

51. R. F. W. Bader, M. E. Stephens and R. A. Gangi, Can. J. Chem., **55**, 2755 (1977)

52. G. S. Hammond, J. Am. Chem. Soc., **77**, 334 (1955)

53. P. Hohenberg, and W. Kohn, Phys. Rev., **136**, B864 (1964)

54. W. Kohn, and L. J. Sham, Phys. Rev., **140**, A1133 (1965)

55. E. Runge, and E. K. U. Gross, Phys. Rev. Lett., **52**, 997 (1984)

56. R. Bauernschmitt, and R. Ahlrichs, Chem. Phys. Lett., **256**, 454 (1996)

57. M. E. Casida, C. Jamorski, K. C. Casida, and D. R. Salahub, J. Chem. Phys., **108**, 4439 (1998)

58. R. E. Stratmann, G. E. Scuseria, and M. J. Frisch, J. Chem. Phys., **109**, 8218 (1998)

59. K. B. Wiberg, R. E. Stratmann, and M. J. Frisch, Chem. Phys. Lett., **297**, 60 (1998)

60. J. B. Forsman, M. Head-Gordon, J. A. Pople, M. J. Frisch, J.Phys. Chem., **96**, 135 (1992)

61. M. E. Robin, Higher Excited States of Polyatomic Molecules, Vol. 3, Academic Press, New York, 1985

62. C. M. Hadad, J. B. Foresman, K. B. Wiberg, J. Phys. Chem., **97**, 4293 (1993)

Chapter 6

Conclusions

6.1 Chemical Applications

6.1.1 The reactions of a triplet oxygen atom with C_{60} fragments

The structures of the C_{60} fragments are more constrained as they become larger. They are weakly aromatic molecules judging from the NICSs (nucleus independent chemical shifts). The addition of an oxygen atom to the carbon-carbon double bond affects the aromaticity in the region which was attacked. The formation of oxides of the C_{60} fragments from the reaction of a triplet oxygen atom is exothermic. Comparison of the heat of formation and the reaction barrier for the oxides of the C_{60} fragments indicates that the largest fragment studied, $C_{26}H_{12}$, has a similar reactivity to that of C_{60}. The reaction barriers and heats of formation for these oxides are similar to those for ethylene oxide. A preliminary conclusion is that the double bond in C_{60} is a constrained carbon-carbon double bond rather than an aromatic carbon-carbon bond.

6.1.2 The reaction of a triplet oxygen atom, $O(^3P)$, with benzene and the isomerization of benzene oxides

6.1.2.1 Reaction of a triplet oxygen atom, $O(^3P)$, with benzene

Among the several initial possible paths for reaction of a triplet oxygen atom (^3P) with benzene, the pathway to form benzene epoxide as shown in Figure 6-1 proceeds through a triplet transition state (**4-2**) with a reaction barrier of about 4 kcal/mol to form a triplet intermediate (**4-3**). In the transition state (**4-3**), the oxygen atom attacks one carbon atom in the benzene ring. This intermediate connects *via* an inter-system crossing (ISC) from the triplet electronic state of the intermediate to the singlet ground state (**4-4**). A transition state (**4-4**) which involves the "walk-around" of the oxygen atom on the

benzene ring is formed followed by formation of the benzene epoxide (**4-5**). This reaction mechanism supports the experimental observations. The triplet transition state (**4-2**), the triplet intermediate (**4-3**) and the singlet transition state (**4-4**) have similar structures involving a singly bonded oxygen atom to one carbon of the benzene. There exists an open shell singlet transition state (**4-40**), with a structure similar to that of the triplet intermediate (**4-3**) and a closed shell singlet transition state (**4-4**). Both of them are transition states for the oxygen "walk" on the benzene ring and for the epoxide ring closure. The open shell transition state (**4-40**) and the closed shell singlet transition state (**4-4**) have similar force vectors for the reaction coordinate. The existence of this open shell singlet transition state (**4-40**) indicates a lower reaction pathway for ring closure from the triplet intermediate (**4-3**) to the benzene epoxide (**4-5**). Starting from the open shell singlet transition state (**4-40**) or the closed shell singlet transition state (**4-4**) but proceeding through another open shell singlet transition state (**4-39**), the oxygen atom migrates from the initially attacked carbon atom across the benzene ring to form a bridge with the fourth carbon atom. Thus, 7-Oxa-norbornadiene (**4-13**) is formed. The system requires approximately 20 kcal/mol of energy to form this 7-Oxa-norbornadiene (**4-13**). This reaction provides an example where a "transition state" connects stationary points but not necessarily connect two minima on the potential energy surface.

From the closed singlet transition state (**4-4**), which is the critical point for the "walk around" of the oxygen atom on the benzene ring, an additional 15 kcal/mol is required to reach a second order saddle point (**4-38**) leading to the other transition state (**4-21**) and the eventual formation of benzene oxide (**4-5**) or cyclohexadienone (**4-22**). This second order saddle point (**4-38**) has a similar structure to the triplet intermediate (**4-3**) and the

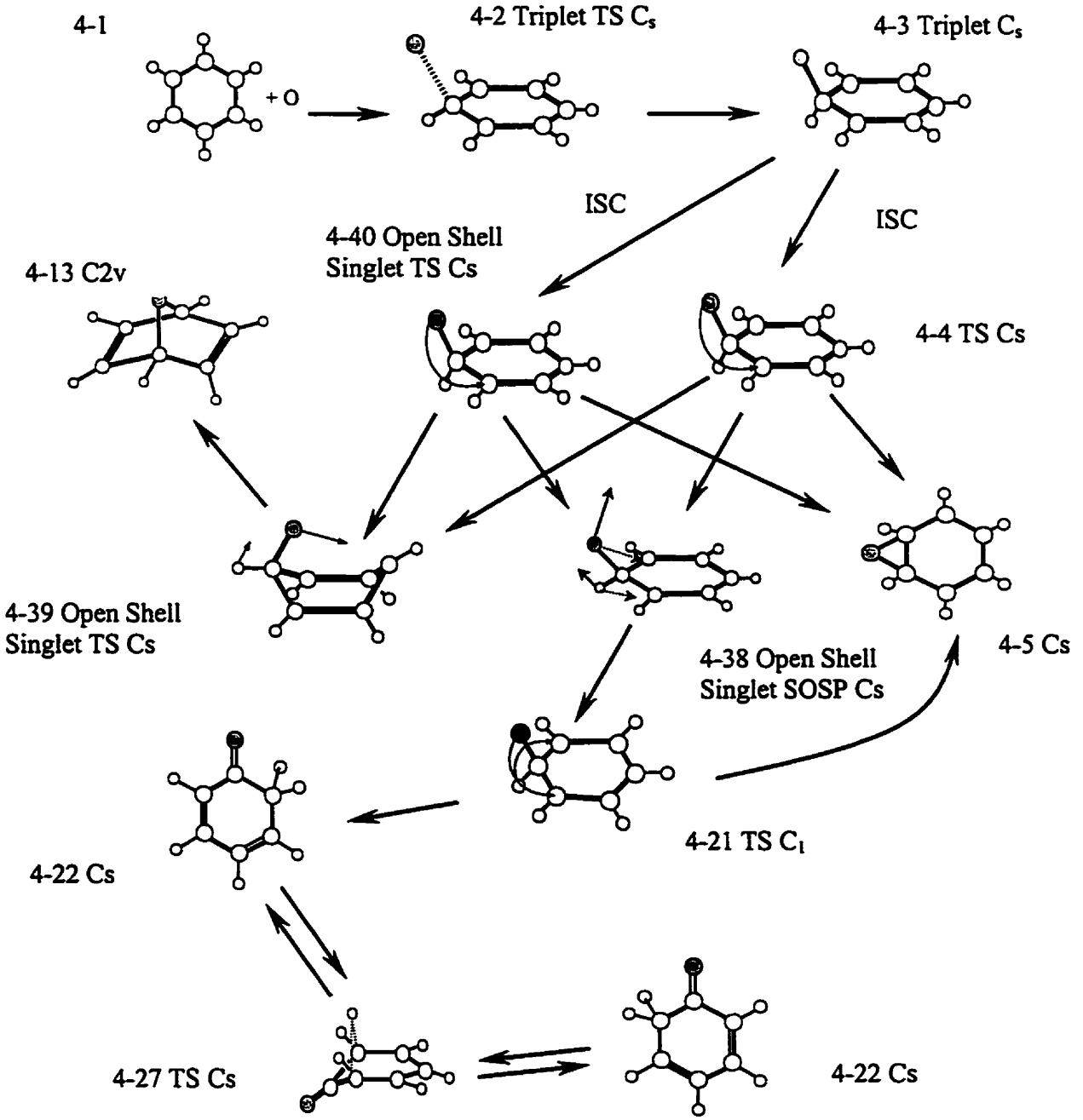

Figure 6-1 Illustration of the initial reaction of triplet oxygen atom (^{3}P) with benzene

open shell singlet transition state (**4-40**). The similarity of these stationary points suggests the complicated nature of the potential energy surface in this region.

6.1.2.2 Isomerizations of benzene oxides

The major isomerization pathways of benzene oxides are summarized in Figure 6-2. Benzene epoxide (**4-5**) isomerizes to other structures by the breaking and formation of carbon-oxygen or carbon-carbon bonds. The carbon-carbon bond in the epoxide structure (**4-5**) breaks to form an oxepin structure (**4-7**) through a transition state (**4-6**) with a low reaction barrier of approximately 5 kcal/mol. Oxepin (**4-7**) inverts to its symmetry-equivalent isomer through a planer transition state (**4-8**) even at low temperature and the activation barrier is predicted to be only 3 kcal/mol.

The formation of four and five membered ring structures (**4-10**) from oxepin by bonding of two β carbons (counting from the oxygen) requires a large amount of energy (ca. 120 kcal/mol) and thus is impossible thermally. It may be photochemically feasible. An open shell singlet reaction pathway through **4-9′** for this isomerization has a barrier which is lower by approximately 10 kcal/mol. This four and five membered ring isomer (**4-10**) could further isomerize to 3-Oxa-quadricyclane (**4-12**) by two carbon-carbon bond formations. The activation energy is less by about 10 kcal/mol. The reverse isomerization from 3-Oxa-quadricyclane (**4-12**) to oxepin (**4-7**) is more thermochemically feasible due to a less activation energy. The two β carbons (counting from the oxygen) in benzene epoxide (**4-5**) bond to form a "Dewar benzene oxide" (**4-15**) with two four-membered rings and one three-membered ring through a transition state (**4-14**) with C_1 symmetry requiring 80 kcal/mol of activation energy. The oxygen atom could migrate from one side

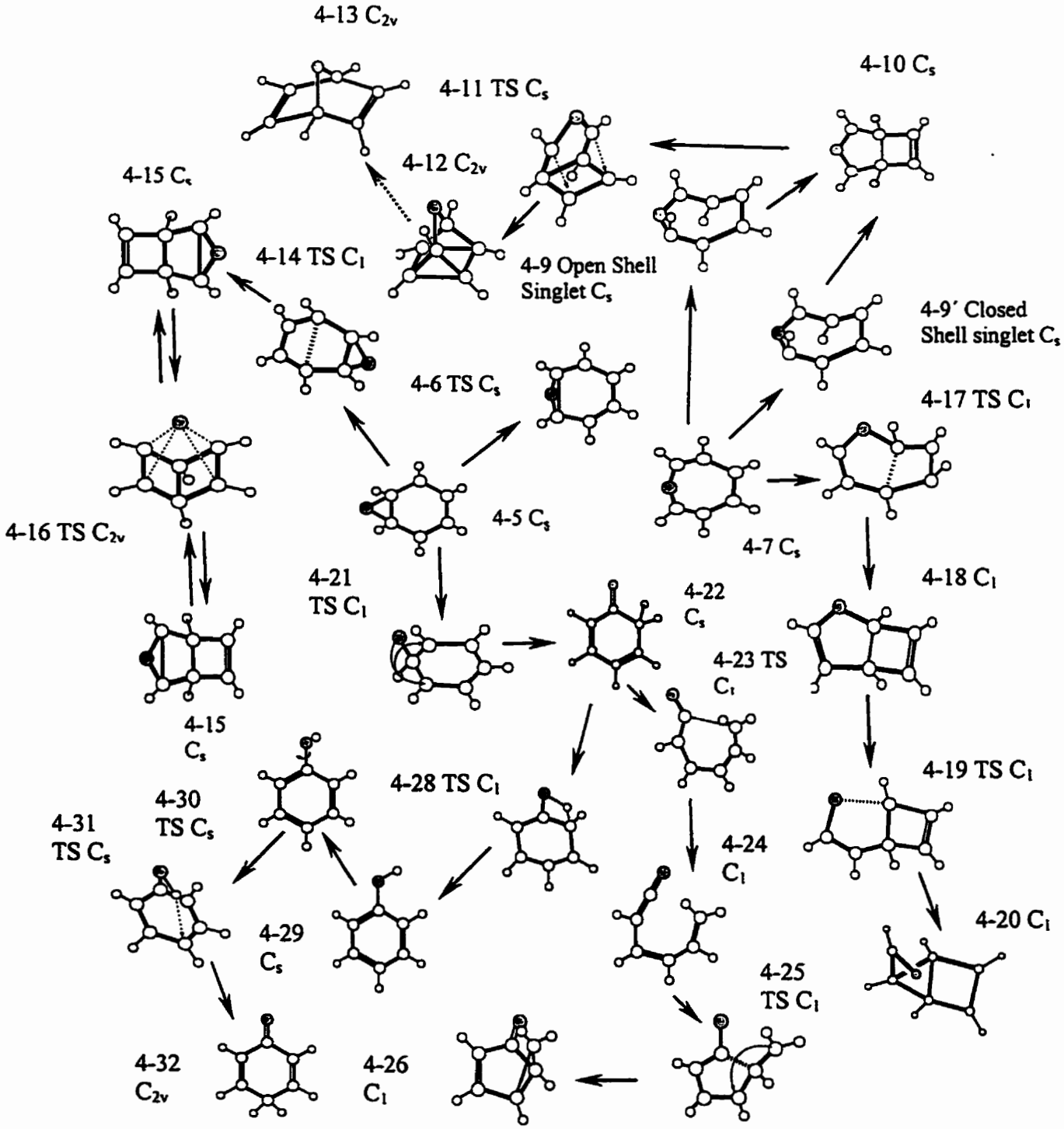

Figure 2 Illustration for the isomerization pathways of benzene oxides

to the other in Dewar benzene oxide (**4-15**) , however, there is a very high activation energy (ca. 120 kcal/mol).

The α carbon on one side of the oxepin (**4-7**) could bond to the β carbon on the other to form a furan derivative: 2-oxa-bicyclo[3,2,0]hepta-3,6-diene (**4-18**) through a transition state (**4-17**). The path obviously involves bond breaking and forming between the α carbon on one side and the β carbon on the other. The activation energy for this isomerization is about 60 kcal/mol. The carbon-oxygen bond closest to the four membered ring in 2-oxa-bicyclo[3,2,0]hepta-3,6-diene (**4-18**) could break to form bicyclo[2.1.0]-2-pentene-5-carbaldehyde (**4-20**) through a transition state (**4-19**) with an activation energy of about 35 kcal/mol.

Cyclohexadienone (**4-22**) could result from the rearrangement of benzene epoxide (**4-5**) through a transition state (**4-21**) with an activation barrier of about 35 kcal/mol. The structure of this transition state (**4-21**) (of C_1 symmetry) is similar to that of the transition state (**4-4**) for the oxygen "walk-around" on the benzene ring and to that of the second order saddle point (**4-38**). The CC bond between the CO and the CH_2 group in cyclohexadienone (**4-22**) breaks to form a butadienylketene (BDK) (**4-24**) over a barrier of approximately 40 kcal/mol. The existence of this pathway rationalizes the experimental observation of BDK (**4-24**) from the reaction of triplet oxygen atom with benzene in an argon matrix. BDK (**4-24**) could further isomerize to a bicyclic three and four membered ring ketone: bicyclo[3.1.0]hex-3-en-2-one (**4-26**) through a transition state (**4-25**) with an activation energy of approximately 30 kcal/mol.

Cyclohexadienone (**4-22**) could isomerize to a symmetry equivalent isomer by the migration of the hydrogen on one CH_2 group from one side to the other through a

transition state with C_s symmetry (**4-27** in Figure 6-1). Another possibility is that one hydrogen in the CH_2 group in cyclohexadienone (**4-22**) migrates to oxygen and forms phenol (**4-29**) through a transition state (**4-28**) with an activation barrier of 50 kcal/mol. The rotation of the OH group in phenol requires little energy to reach a transition state (**4-30**) connecting two equivalent phenol rotamers. This transition state (**4-30**) for OH rotation serves as a stationary point which can be relevant to the hydrogen migration from the oxygen atom to the carbon atom across the benzene ring to form 2,5-cyclo-hexadienone (**4-32**). Before the system reaches 2,5-cyclo-hexadienone (**4-32**), there is a transition state (**4-31**) between the transition state (**4-30**) for OH rotation and that for rearrangement to 2,5-cyclo-hexadienone (**4-32**). This hydrogen migration has a very high activation energy of 110 kcal/mol and thus is not chemically feasible. The transition state (**4-31**) as shown in Figure 6-2 for hydrogen migration is another example of a "transition state" that does not necessarily connect two minima.

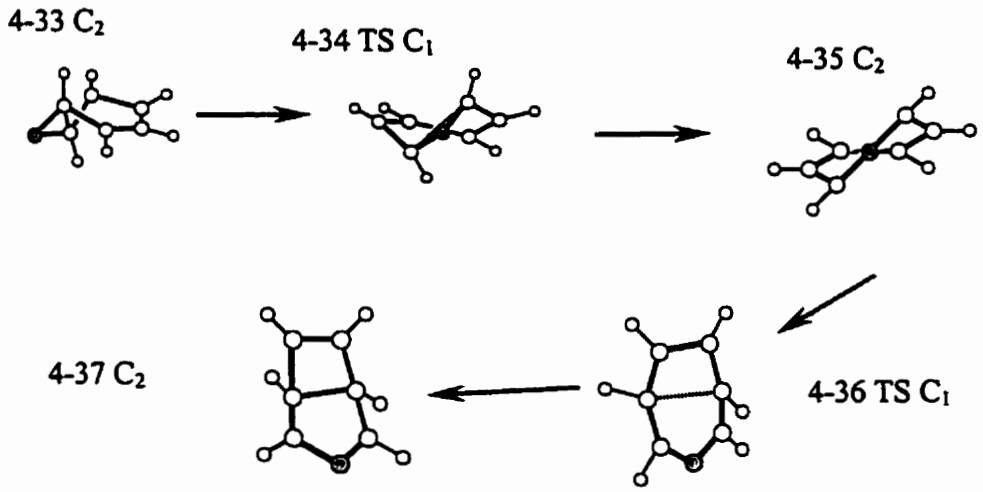

Figure 6-3 Illustration of the isomerization pathway for benzene oxide with C_2 symmetry

A benzene epoxide (**4-33**) of C_2 symmetry could result from the reaction of a triplet oxygen atom with benzene. This C_2 benzene epoxide is about 50 kcal/mol higher in energy than the benzene epoxide of C_s symmetry. In a similar manner to the C_s benzene epoxide, the C_2 benzene epoxide can isomerize to an oxepin (**4-35**) of C_2 symmetry through a C_1 transition state (**4-34**) with an activation barrier of approximately 10 kcal/mol. The two β carbon atoms could bond to form a bicyclo ring structure with a four and five membered ring (**4-37**) with C_2 symmetry through a C_1 transtion state (**4-36**) with an activation barrier of 65 kcal/mol. This isomerization pathway shows that the transition state does not necessarily have the same symmetry as the reactant and product even though the reactant and product are of the same symmetry.

6.2 Evaluation of Exchange-Correlation Functionals

6.2.1 The evaluation of the predictions of various exchange-correlation for chemical reactions

Several hybrid density functionals (BHandHLYP, B1LYP, B3LYP and mPW1PW91) as well as other methods (BLYP, HF, MP2 and CCSD(T)) were employed in the study of the reaction of the triplet oxygen atom with C_{60} fragments and with benzene. Increased HF exchange was found to increase the reaction barrier and to change the nature (i.e. minimum or saddle point) of some critical points. BHandHLYP gives the best performance for the reaction barrier and transition state characterization especially for reactions with low activation barriers. With similar amounts of HF exchange, the hybrid methods (B1LYP, B3LYP and mPW1PW91) give comparable performance to MP2 for the potential energy surface characterization both for energies and structures. For some

reaction pathways involving an open shell singlet, B1LYP has the best performance among these three hybrid methods with a similar percentage of HF exchange. The general gradient approximation (GGA) based methods (for example BLYP, G96LYP, mPWPW91 and PW91PW91) sometimes predict different some stationary points (minimum or saddle point) than those from other methods (LSDA, hybrid and conventional *ab initio* methods). These GGA methods can even predict a virtual orbital energy lower than an occupied orbital energy which is un-physical. On the basis of the performance of density functional methods, B1LYP is recommended for chemical reaction modeling. For some chemical reactions with very low reaction barriers, BHandHLYP may be recommended.

6.2.2 Detailed analysis of exchange and correlation functionals

The performance of exchange correlation functionals on the atomic systems H, He and Li was studied. Most functionals (Slater exchange, B, PW91 exchange and correlation, G96, LG and mPW) are not self-interaction free. The correlation functional LYP is self-interaction free but does not take parallel electronic correlation into account.

In hybrid methods (i.e. the exchange functional has HF exchange included), mPW91 exchange, B, G96 and LG, there is a linear relationship between the weight of the HF exchange and the total energy and the energy components (kinetic, potential and electron-electron interaction energy) as well. PW91 exchange does not vary linearly with the weight of HF exchange especially for the energy components. The reason is unclear. For the orbital energy, exchange functionals tend to destabilize the occupied orbital energy and decrease the HOMO-LUMO energy gap. The inclusion of HF exchange and the

addition of a correlation functional lowers the occupied orbital energy. This is especially conspicuous in the prediction of the orbital energies of anions. The anion is unbound with the use of pure density functional methods. For neutral systems, density functional methods still predict occupied orbital energies which are far too high. All the exchange functionals show similar performance in predicting orbital energies.

6.2.3 A new hybrid exchange-correlation functional, mPW1LYP

The geometric and thermodynamic predictions on the reduced G2 data set with mPW1LYP demonstrate that this method is one of the best hybrid density functional approaches for structures and energies. The predictions on Van der Waals and weakly interacting complexes indicates mPW1LYP does model the Van der Waals interaction and slightly overestimates this term thus predicting shorter bond distances and larger interaction energies. The location of a transition state and the reproduction of the low reaction barrier in selected chemical reactions reveal that mPW1LYP is capable of predicting low activation barriers. mPW1LYP is satisfactory for the prediction of electronic excitation energies as indicated by the results on formaldehyde, acetaldehyde and acetone. This functional is recommended if the chemical reaction has a low activation energy or if van der Waals interactions are important.

6.3 General Conclusions and Suggestions for the Improvement of Density Functional Methods

Inclusion of exact exchange (HF exchange in term of the computation) in density functional methods, yielding the various schemes, improves their overall performance in

chemical modeling. The one-parameter hybrid methods perform better than the MP2 model in the prediction of chemical reactions, structures, and properties with MP2 requiring greater computational resource. The inclusion of HF exchange in the hybrid method should take the properties of the exchange and correlation functional into account. All available exchange and correlation functionals are approximations to the exact functionals and are fit to physical constraints or chemical data in their construction. One reason for the improvement caused by the inclusion of HF exchange in hybrid methods is that most of the exchange correlation functionals are not self-interaction error free. HF exchange itself is free from the self-interaction error and one way to improve the hybrid density method is to reduce this error. All the exchange functionals show similar behavior in the prediction of the highest occupied orbital energies.

Improvements to and creation of new density functionals are necessary for more accurate application of density functional methods in chemistry. One direction involves the inclusion of higher order gradient corrections [1]. Numerical difficulties must be solved for these higher order corrections (≥2) and there seems to be little improvement in chemical predictions [2]. Kinetic energy density dependent approximations to the exchange energy [3] may be an alternative to, and an improvement over, the present exchange functionals.

All quantum chemical methods describe the same physical system from different, but related, points of view [4]. The combination of different methods with their respective strengths may result in new, more promising methods [4a]. The hybrid density functional in practice is a combination of a density functional based approach with the HF method, although this combination has a physical origin [5]. Another combination involves

Hartree-Fock exchange with a correlation functional [6] but takes the electron density from a high level *ab initio* coupled cluster computation[7]. In density functional methods, the exchange functional mainly considers the non-dynamic correlation and the correlation functional determines the dynamic correlation. A perturbation correction to the exchange functional is another way to take dynamic correlation into account, and may have advantages over MP2 due to the smaller spin contamination in density functional methods.

Although unrestricted density functional methods may simulate the multi-configuration problem, multi-configuration based methods are still preferable in such a situation. Such a combination of density functional methods with multi-configuration methods yields the CAS-DFT [8] or DFT-MRCI [9] methods. These methods are also good for the accurate prediction of electronic excitation energies.

Although static density functionals has been shown to be a good approximation in time-dependent problems, the new functionals including the time-dependent effect are expected to give improved descriptions of excitation energies and photochemical reactions. This field is relatively new but a promising one for the application of density functional theory.

6.4 References

1. H. L. Schmider, and A. D. Becke, J. Chem. Phys., **109**, 8188 (1998)
2. R. Neumann, and N. C. Handy, Chem. Phys. Lett., **266**, 16 (1997)
3. M. Ernzerhof, and G. E. Scuseria, J. Chem. Phys., **111**, 911 (1999)
4. a) L. Künne, Int. J. Quant. Chem., **74**, 55 (1999). b) V. Sahni, Phys. Rev. **A, 55**, 1846 (1997)
5. J. Harris, and R. O. Jones, J. Phys. **F, 4**, 1170 (1974); O. Gunnarsson, and B. I. Lundqvist, Phys. Rev. **B, 13**, 4274 (1976); D. C. Langreth, and J. P. Perdew, Phys. Rev. **B, 15**, 2884 (1997); J. Harris, Phys. Rev. **A, 29**, 1648 (1984)
6. S. Baroni, and E. Tuncel, J. Chem. Phys., **79**, 6140 (1983); Q. Zhao, R. C. Morrison, and R. G. Parr, Phys. Rev. **A, 50**, 2138 (1994)
7. G. K-L. Chan, D. J. Tozer, and N. C. Handy, J. Chem. Phys., **107**, 1536 (1997)
8. B. Miehlich, H. Stoll, and A. Savin, Mol. Phys., **91**, 527 (1997); J. Gräfensten, and D. Cremer, Chem. Phys. Lett., **316**, 569 (2000)
9. S. Grimme, and M. Waletzke, J. Chem. Phys., **111**, 5645 (1999)

Appendices

Total energies of the systems studied in Chapter 3 (with BHandHLYP/6-31G* otherwise specified) and Chapter 4 (with B1LYP/6-31G*) are list below.

Chapter 3(BHandHLYP/6-31G* unless otherwise specified)

Compounds	Energy (in a.u., including zero-point vibration energy)
3-1a	-153.518861
3-1b	-153.518819
3-2	-153.560928
3-3	-153.561347
3-4	-153.633691
3-5	-231.995864
3-6	-307.026989
3-7	-307.050197
3-8	-307.101205
3-9	-307.089039
3-10	-307.103275
3-11	-385.498884
3-12	-460.519676
3-13(C_s/C_1)	-460.531164/-460.530864
3-14	-460.571382
3-15(HF/6-31G*)	-457.945860

3-16	-460.586604
3-17	-460.571880
3-18	-537.753436
3-19(C_s/C_1)	-612.783051/-612.782602
3-20	-612.800909
3-21(UB3LYP/6-31G*)	-613.195802
3-22	-612.841581
3-23	-692.405971
3-24	-767.448173
3-25(UB3LYP/6-31G*)	-767.928684
3-26	-767.431306
3-27	-767.481630
3-28	-997.090808
3-29	-997.099667
3-30(C_s/C_1)	-1072.174089/ -1072.173543
3-31	-1072.139782
3-32	-1072.223454

Chapter 4 (B1LYP/6-31G*)

Compounds	Energy (in a.u., including zero-point vibration energy)
4-1 (benzene/triplet oxygen)	-232.011644/-75.045153
4-2	-307.054049
4-3	-307.072718
4-4	-307.073573
4-5	-307.132397
4-6	-307.123707
4-7	-307.134840
4-8	-307.129805
4-9	-306.935512
4-10	-307.031119
4-11	-307.023522
4-12	-307.069125
4-13	-307.100107
4-14	-306.993240
4-15	-307.049299
4-16	-306.863669
4-17	-307.060970
4-18	-307.109631
4-19	-307.051552
4-20	-307.077548
4-21	-307.062596

4-22	-307.179416
4-23	-307.121595
4-24	-307.134113
4-25	-307.081661
4-26	-307.154453
4-27	-307.110000
4-28	-307.096180
4-29	-307.201925
4-30	-307.196664
4-31	-307.021966
4-32	-307.180897
4-33	-307.045448
4-34	-307.028015
4-35	-307.055741
4-36	-306.947656
4-37	-306.972887
4-38	-307.061159
4-39	-307.035713
4-40	-307.079198